A Velocity Prediction Procedure for Sailing Yachts with a hydrodynamic Model based on integrated fully coupled RANSE-Free-Surface Simulations

Christoph Böhm

A Velocity Prediction Procedure for Sailing Yachts with a hydrodynamic Model based on integrated fully coupled RANSE-Free-Surface Simulations

Proefschrift

ter verkrijging van de graad van doctor
aan de Technische Universiteit Delft,
op gezag van de Rector Magnificus prof. ir. K. C. A. M. Luyben,
voorzitter van het College voor Promoties,
in het openbaar te verdedigen op woensdag 8 oktober 2014 om 10:00 uur

door

Christoph Böhm

Diplom-Ingenieur (Fachhochschule) Schiffbau
geboren te Essen, Duitsland.

Dit proefschrift is goedgekeurd door de promotor:

Prof. dr. ir. R.H.M. Huijsmans

Copromotor: Dr. ir. M. Gerritsma,

Samenstelling promotiecommissie:

Rector Magnificus,	voorzitter
Prof. dr. ir. R. H. M. Huijsmans,	Technische Universiteit Delft, promoter
Dr. ir. M. I. Gerritsma,	Technische Universiteit Delft, copromotor
Prof. dr. F. Fossati,	Politecnico di Milano
Prof. dr. K. Graf,	University of Applied Sciences Kiel
Dr. ir. J. A. Keuning,	Technische Universiteit Delft
Prof. dr. ir. T. J. C. van Terwisga,	Technische Universiteit Delft
Prof. dr. P. A. Wilson,	University of Southampton
Prof. dr. ir. J. J. Hopman,	Technische Universiteit Delft, reservelid

An electronic version of this dissertation is available at
http://repository.tudelft.nl/.

To my whole family for their support and patience,
especially to my wife Bettina and my sons Maximilian and Felix Alexander.

TABLE OF SYMBOLS

LATIN LETTERS

$(1+k)$	Form factor	$[-]$
$A_S ails$	Sail area	$[\mathrm{m}^2]$
AR	Wing aspect ratio	$[-]$
AWS	Apparent wind speed	$[\mathrm{m/s}]$
B	Bias component of uncertainty U	$[-]$
C_D	Drag coefficient	$[-]$
C_{D0}	Drag coefficient at zero lift	$[-]$
C_{Di}	Induced drag coefficient	$[-]$
C_{Ds}	Separation drag coefficient	$[-]$
C_F	Force coefficient	$[-]$
C_k	Correction factor	$[-]$
C_L	Lift coefficient	$[-]$
C_M	Moment coefficient	$[-]$
C_T	Total resistance coefficient	$[-]$
CFL	Courant number	$[-]$
CV	Control volume of a grid cell	$[\mathrm{m}^3]$
e, CE	Efficiency coefficient	$[-]$
E	Comparison error	$[-]$
f_H	Heeling force coefficient	$[-]$
$\frac{\partial f_H}{\partial \beta}$	Heeling force gradient	$[-]$
f_{H0}	Heeling force coefficient at zero leeway	$[-]$
$\mathbf{F}_S$	Sail force vector	$[\mathrm{N}]$
F_H	Heeling force perpendicular on flow direction and span	$[\mathrm{N}]$
Fn	Froude number	$[-]$
$\mathbf{I}$	Unit tensor	$[-]$
$\mathbf{I_G}$	Tensor of the moment of inertia w.r.t to center of gravity	$[\mathrm{kg}\cdot\mathrm{m}^2]$
KPP	Quadratic parasite drag coefficient	$[-]$
LCE	Longitudinal center of effort	$[\mathrm{m}]$
LCG	Longitudinal center of gravity	$[\mathrm{m}]$
LOA	Length over all	$[\mathrm{m}]$
LWL	Length of waterline	$[\mathrm{m}]$
m	Mass	$[\mathrm{kg}]$
M_x	Heeling moment around boat x-axis	$[\mathrm{N}\cdot\mathrm{m}]$

M_{xR}	Righting moment around boat x-axis	[N·m]
M_y	Pitch moment around boat y-axis	[N·m]
M_y	Pitch moment around boat y-axis	[N·m]
M_z	Yaw moment around boat z-axis	[N·m]
$\mathbf{n}$	Surface normal vector	[−]
p	Pressure	$[\mathrm{N/m^2}]$
P	Precision component of uncertainty U	[−]
P_k	Order of accuracy	[−]
q	Dynamic pressure	$[\mathrm{N/m^2}]$
r_k	Refinement ratio of parameter k	[−]
R_k	Convergence ratio	[−]
Rn	Reynolds number	[−]
R_H	Added resistance due to heel	[N]
R_I	Induced resistance	[N]
R_{PP}	Parasitic profile drag	[N]
R_U	Upright resistance	[N]
R_{tot}	Total hydrodynamic resistance	[N]
s	Wing span	[m]
S	Simulation result	[−]
S_C	Simulation result corrected	[−]
$\mathbf{S}_f$	Cell surface vector	$[\mathrm{m^2}]$
SF	Side force, component of the heeling force parallel to the water surface	[N]
T	Truth	[−]
T	Draft	[m]
$\mathbf{T}$	Transformation matrix, viscous stress tensor	[−, Pa·s]
TCG	Transverse center of gravity	[m]
T_E	Effective draft	[m]
TWA	True wind angle	[°, rad]
$\mathbf{u}_B$	Boat velocity vector	[m/s]
U_B	Boat velocity	[m/s]
U_P	Parameter uncertainty (e.g. iteration number I grid size G and time step T)	[−]
$U_{S_C N}$	Corrected numerical uncertainty	[−]
U_{SN}	Numerical uncertainty	[−]
U_V	Validation uncertainty	[−]
$\mathbf{v}$	Velocity vector	[m/s]
$\mathbf{v}_A$	Apparent wind vector	[m/s]
$\mathbf{v}_b$	Grid velocity vector	[m/s]
$\mathbf{v}_f$	Velocity vector at cell face	[m/s]

$\mathbf{v_G}$	Linear velocity of center of mass	[m/s]
$\dot{\mathbf{v}}_\mathbf{G}$	Linear acceleration of center of mass	$[\mathrm{m/s^2}]$
$\mathbf{v}_T$	True wind vector	[m/s]
V_A,AWA	Apparent wind angle	[°, rad]
VCG	Vertical center of gravity	[m]
VCE	Hydrodynamic vertical center of effort	[m]
V_f	Cell volume associated with cell face	$[\mathrm{m^3}]$
VMG	Velocity made good, velocity component directly into the wind, respective away from the wind	[m/s]
V_T,TWS	True wind speed	[m/s]
$\mathbf{x_G}$	Position of center of gravity	[m]
y^+	Dimensionless wallscale	[−]
z_{ref}	True wind reference height	[m]
z_0	Equivalent grain roughness	[m]
ZCE	Aerodynamic vertical center of effort	[m]

GREEK LETTERS

α	Flow angle of incidence	[°]
α_i	Volume fraction of VOF model	[−]
β	Leeway or drift angle	[°, rad]
β_A	Apparent wind angle	[°, rad]
β_T	True wind angle	[°, rad]
δ	Rudder angle	[°, rad]
$\delta_k^\star$	Error estimate with sign and magnitude of k^{th} parameter	[−]
δ_P	Parameter error (e.g. iteration number I grid size G and time step T)	[−]
δ_S	Simulation error	[−]
δ_{S_C}	Simulation error corrected	[−]
δ_{SM}	Simulation modeling error	[−]
δ_{SN}	Simulation numerical error	[−]
ϵ_{ijk}	Solution change	[−]
ϵ	Change between two solutions	[−]
λ	Scale factor	[−]
μ	Dynamic viscosity	[Pa·s]
μ_T	Turbulent viscosity	[Pa·s]
μ_{eff}	Effective dynamic viscosity	[Pa·s]
$\omega_\mathbf{G}$	Angular velocity around center of mass	[rad/s]
ϕ	Heeling angle, rotation around yacht's x-axis or distance function	[°, rad]
ϕ_C	Central node value of the NVD	[−]
$\tilde{\phi}_f$	Normalized face value of the NVD	[−]
ψ	Yaw angle, rotation around yacht's z-axis	[°, rad]
ρ	Density	$[\mathrm{kg/m^3}]$

τ	Shear stress, tab angle	$[\mathrm{N/m^2}, ^\circ]$
θ	Free surface interface angle or pitch angle, rotation around yacht's y-axis	$[^\circ, \mathrm{rad}]$
ζ	Wave height	[m]
ΔTA	Time allowance delta, time difference between two boats when sailing one nautical mile at a specific true wind angle	[s]
Δx_k	Increment in k^{th} input parameter (e.g. iteration number I grid size G and time step T)	[−]

SUBSCRIPTS

f	Cell face
C	Corrected error or uncertainty
BS	Body-fixed coordinate system
GS	Global, space fixed newtonian coordinate system

ACRONYMS

ABL	Atmospheric boundary layer
ACCV5	America's Cup class version 5
CBC	Convection boundness criterion
CFD	Computational fluid dynamics
CSYS	Coordinate system
DSKS	Delft systematic keel series
DSYHS	Delft systematic yacht hull series
EFD	Experimental fluid data
ESG	Equilibrium state guess for conventional VPP
FSBC	Free surface boundary condition
FSI	Fluid-structure-interaction
FVM	Finite volume method
HRIC	High resolution interface capturing scheme
IMS	International measurement system
ITTC	International towing tank conference
MPI	Message passing interface
NVD	Normalized value diagram
ORC	Offshore racing congress
PVM	Parallel virtual machine
RANSE	Reynolds-averaged-Navier-Stokes-equations
SIMPLE	Semi-implicit method for pressure linked equations
TG	Turbulence generator
TWFT	Twisted flow wind tunnel
UD	Upwind differencing scheme
VOF	Volume-of-fluid

VPP Velocity prediction program

CONTENTS

1

INTRODUCTION

1.1. PROBLEM DEFINITION AND OBJECTIVES

The goal of this thesis is the development of a procedure to directly derive performance information for sailing yachts from Reynolds-Averaged-Navier-Stokes-Equations (RANSE) free surface simulations. To achieve this, the flow field around the yacht as well as the orientation of the yacht itself in the flow field have to be updated according to input from a velocity performance prediction program (VPP). Therefore a VPP code has to be embedded in the global iteration of the RANSE code using direct two-way coupling.

The motivation to develop such a method is a shortcoming of the current procedure where discrete points of a test matrix of approximately 120 runs have to be tested, respectively simulated. Afterward, the hydrodynamic coefficients of a yacht are derived using linear wing theory with empirical corrections for non-linearities. Since these effects should be mainly of second order, this procedure is quite sufficient for normal optimisation tasks. However, for high-level optimisation as conducted for Volvo Ocean Race or Americas Cup campaigns these effects should be included. This thesis investigates if this could be achieved by exchanging the hydrodynamic module of the VPP with the direct input from the flow simulation were all non-linear effects are inherently included.

Furthermore, it will be investigated if such a new method is able to reduce total investigation time. The rational behind this idea is that a polar plot can now be determined by a much smaller series of runs which depend on the number of true wind speeds and true wind angle to be tested.

1.2. OVERVIEW OF THIS THESIS

In order to be able to formulate research objectives and requirements, recent and current developments in the investigation of aerodynamics and hydrodynamics of sailing yachts and the consecutive VPP analysis are reviewed in Chapter 2. The current state of the art as well as possible development directions are discussed.

Chapter 3 reviews hydrodynamic free surface modeling as well as aerodynamic sail force modeling concepts. With these theoretical reviews the necessary background is established to make the decisions regarding the backbone of the new VPP. After assessing the requirements on a flow solver to be useable in the new VPP approach, it was decided to choose the commercial RANSE solver *STAR-CCM+* from *CD-adapco*. Chapter 4 then describes a conventional approach to VPP modeling. With this pre-knowledge a conceptual design and a mathematical model of the new RANSE-VPP is developed in the second part of that chapter. Afterward, Chapter 5 outlines the theory behind the viscous flow solver and rigid body motion solver necessary for Fluid-Body-Interaction. Chapter 6 shows the implications of the RANSE-VPPs requirements on the numerical grid. Various grid motion techniques will be presented, investigated and discussed.

A formal verification & validation against experimental data is presented for the hydrodynamic model in Chapter 7. In the following, a conventional VPP procedure is conducted based on high-quality towing tank data and numerical data gained by resembling towing tank procedures. Chapter 8 shows the generation of the data necessary for the conventional VPP analysis as well as the following VPP calculation. Hydrodynamic as well as VPP results of experimental and numerical investigations are compared and discussed.

In Chapter 9, the new RANSE-VPP system is applied to the same geometry as used in the previous chapter. Velocity and performance information is generated and compared with the data gained by the conventional VPP with experimental and numerical database. Finally, Chapter 10 concludes the findings of this work and gives recommendations for further research on this topic.

2

BACKGROUND OF VELOCITY PREDICTION FOR SAILING YACHTS

2.1. PREFACE

A sailing yacht may be considered as a physical system which is located in the interface of two fluids and solely relies on fluid forces for its propulsion. In this connection, the sails, which are located in the incident air flow, may be considered as set of aerodynamic foils, which by means of the forces acting on them, ultimately produce propulsion. The sailing boat also does carry hydrodynamic foils which are located under the boat and submerged in the water. The most prominent of such submerged foils are the keel and the rudder. These foils counteract the aerodynamic forces, producing on the one hand resistance but on the other hand act against the leeway induced by the sail forces and as such operate as control surfaces. The hull, which is directly located in the interface between air and water, produces resistance and provides the necessary buoyancy as well as the structural platform for rig and appendages. In conjunction with the keel it also counteracts the heeling moment resulting from the aerodynamic forces. As one can see, a sailing boat is a complex physical system which is characterized by a strong two-way coupling of hydro- and aerodynamic fluid forces. Due to the unsteady nature of the wind, an wave forces acting on the system yacht means that the boat movement is also unsteady. This significantly increases the complexity of the performance prediction and therefore has been neglected as far as possible to date. Instead, for the prediction of boat velocity one usually limits oneself to *steady state* or, more precisely, *laboratory* conditions. From a general point of view the prediction of sailing boat performance has three major components:

1. A model for the hydrodynamic characteristics of the boat
2. A model describing the aerodynamic characteristics of the rig
3. Formulations to balance these characteristics with respect to optimum speed

To judge the benefits and drawbacks of different ways for predicting sail boat performance correctly, one should not only look at the velocity prediction procedure itself, but also on the way it acquires the data necessary for its aero- and hydrodynamic model. Therefore at first a brief sketch of the history of velocity prediction programs (VPPs) and the developments in aerodynamic and hydrodynamics of sailing yachts will be given. With this pre-knowledge one will be enabled to judge the different methods of sailing boat performance prediction which currently exist and therefore allow us to derive a hypothesis in which direction further development is meaningful.

2.2. HISTORY OF VPP

Predicting the performance of sailing vessels has been a topic for naval architects and fluid scientists for a long time, but the interest on a substantive prediction has been strongly fired by the emergence of yacht sport and an according regatta scene around 1900. Due to the complex nature of sailing yacht propulsion the development and refinement of the prediction methods has been a constant topic of research ever since. Research in this area has been traditionally dictated by the hypothesis, that the aerodynamic and the hydrodynamic forces may be investigated separately, see Figure 2.1. On the hydrodynamic part of the investigations, the first obstacle was to find a procedure which mimics the conditions a yacht experiences in reality within the possibilities of experimental facilities, namely towing tanks. Since this procedure differs significantly in terms of complexity and effort from testing of conventional vessels, it was not until the 1930's that the problem was first solved by Ken Davidson at the Stevens Institute of Technology. In his report he described a method to use a combination of full scale and model scale tests to evaluate sailing performance [1]. The method was based on measurements of boat velocity and heel angle at full scale. Afterwards the corresponding values were simulated on a towing tank model, making it possible to measure resistance and side force. These values were scaled to full scale which made it possible to determine the sail forces.

In the early 1970s researchers from Massachusetts Institute of Technology (MIT) while working on the *H. IRVING PRATT Ocean Race Handicapping Project* developed a method to predict the sailing performance of yachts for different sail states and wind conditions.

This method, which was presented by Kerwin in 1978 [2, 3, 4], contained a model with hydrodynamic forces based on towing tank tests, while the aerodynamic model relied on coefficients which were a function of the apparent wind angle. Furthermore, the method contained an optimization routine to calculate the maximum boat velocity for force equilibrium as a combination of apparent wind speed and angle which are a function of two sail trim factors, *flat* and *reef*. Therefore this method, which is known as the KERWIN MODEL, is the first real velocity prediction program (VPP) for sailing yachts. Since then, the individual components of the method have been subsequently improved. Nonetheless the fundamental principles, which form the nucleus of the method, are still used today.[1]

[1] A more elaborated insight into the principles underlying VPPs will be given in section 2.5.

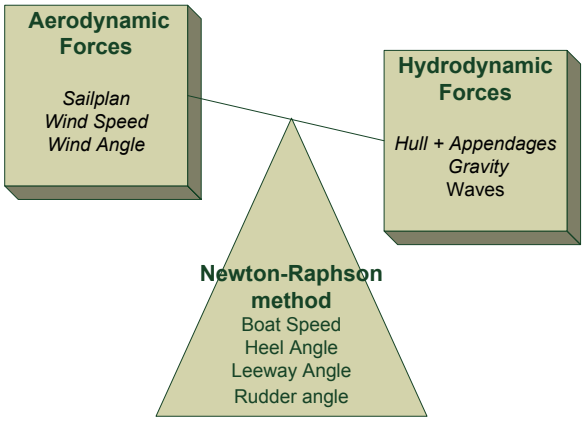

Figure 2.1: Equilibrium of Aero- and Hydrodynamic Forces

2.3. INVESTIGATION METHODS FOR AERODYNAMICS OF SAILS

Quantifying the sail forces has proven to be a difficult task for a long time. Among the first attempts to determine rig forces was the already mentioned work conducted by Davidson [1]. From this work the so called GIMCRACK-coefficients, christened after the yacht from which they were obtained, were derived. The method incorporates an inverse determination of sail forces by correlating full-scale measurement of boat speed as function of wind speed, wind angle, heel and rudder angle with towing tank data. From today's point of view the method can be considered as very basic. The first breakthrough in the field of sail aerodynamics was achieved by investigating the dedicated influence of the aerodynamic forces acting on a sail by experimental means in wind tunnels. Here the work conducted by Marchaj [5] in the 1970s in the wind tunnel of the University of Southampton has to be mentioned. A further refinement of this investigation method was achieved by the construction of so called Twisted-Flow Wind Tunnels. These kind of wind tunnels are especially designed to enable change in wind speed over height due to wind-gradient as well as the change in apparent wind speed and incident angle over height due to the movement of the yacht. This procedure therefore resembles the aerodynamic flow a yacht experiences in reality. The first of these tunnels has been erected at the University of Auckland in order to conduct investigations for the challenge of Team New Zealand for the 29th America's Cup in 1995. Since then similar facilities have been erected at the Politecnico di Milano [6] and the University of Applied Sciences Kiel [7]. Illustrations of the twisted flow wind tunnel of the Yacht Research Unit Kiel are given in Figure 2.2.

Besides wind tunnel testing, significant research effort has been put into full-scale testing. Therefore, so called sailing dynamometers have been developed. These apparatus mainly consist of sailing yachts equipped with extensive measurement devices to determine the sail forces under real sailing conditions. The first dynamometer was constructed at MIT in the late 1980s. The yacht used was 35ft scale down of a 83ft Maxi Sloop, for which towing tank data exist. Inside the yacht a frame was suspended in the hull by means of flexure rods connected to load cells to prevent cross-talk during measurement.

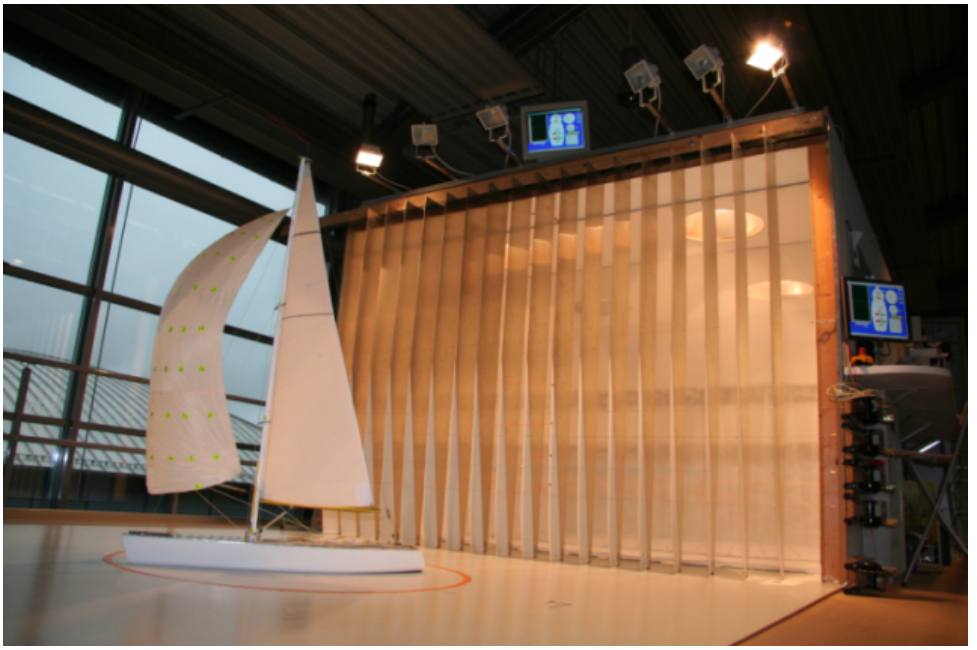

(a) IMS Spinnaker testing with Photogrammetry

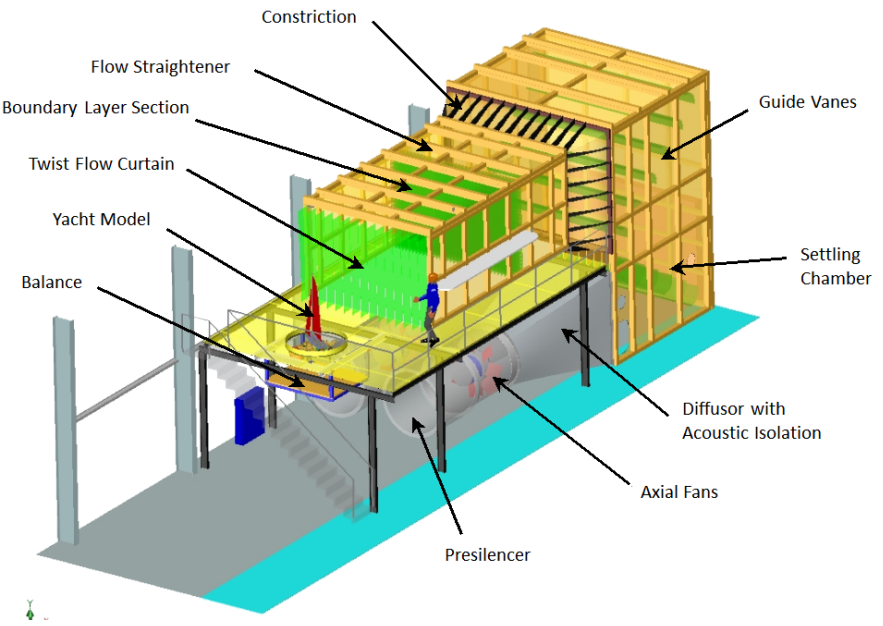

(b) Overview of the wind tunnel features

Figure 2.2: Twisted Flow Wind Tunnel of the Yacht Research Unit Kiel

Figure 2.3: The Berlin Sail-Force Dynamometer DYNA while acquiring full-scale data under sails

With this arrangement it was possible to measure the forces acting on shrouds, stays and others as well as sail shapes. The measured sail shapes were used for inviscid flow calculations to derive sail forces for a VPP. A comparison of measured and computed boat velocities showed good agreement with differences of about 2%. The results of the measurements and computations which were summarised by Milgram (1993) [8, 9]. Further sail-force dynamometers were built by Masuyama et al. (1997) [10] and by Hochkirch (2000) [11, 12]. The latter one was the so called DYNA, see Figure 2.3, built into a Dehler 33 Cruiser/Racer. It had a slightly different focus than the other dynamometers, which focused more on the hydrodynamics of the keel and the rudder. Recently, a new sailing dynamometer based on the COMET 35 hull lines has been build at the Politecnico di Milano Lecco within the *Innovation Hub Sailing Yacht Lab project*. The construction and launching of the vessel have been reported by Fossati et al. [13]. However, full-scale measurements have not been published by the time of this publication.

Besides the use of sailing dynamometers, other kinds of full-scale testing have recently seen an increased interest. Viola and Flay [14] presented measurements of pressure distributions on upwind and downwind sails and compared them with both CFD and wind tunnel results. A good agreement was reported for upwind sails, modeled with a Vortex Lattice code, as well as downwind sails, modeled using RANSE CFD. For the latter, lift and drag differed by smaller 0.5% from full-scale investigations. Agreement with wind tunnel results was similar. A comparison between full scale upwind sail shape measurements and CFD results was published by Augier et al. [15]. The comparison shows that the sail and shroud forces are well predicted in steady state and are in the right range for unsteady cases. Predicted and measured flying shape fit very well for all cases. Mausolf et al. [16] presented a comparison of full-scale and wind tunnel flying

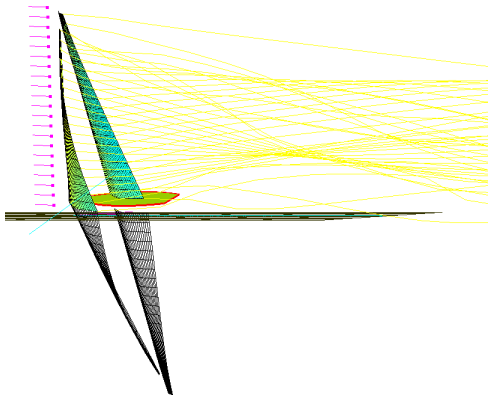

Figure 2.4: inviscid flow around sails using vortex-lattice methods

shapes of downwind sail captured by means of photogrammetry. They showed that it is possible to achieve the same relative error in flying shape resolution (about 3% leech length) for model as well as full scale testing. With the steadily growing availability of computational resources, the last years have seen an increase of CFD research and application for sails. For sails where mainly attached flow is to be expected, as is the case for close-hauled upwind sails, potential flow methods are widely used today. Since sail investigation is a aero-elastic problem, the flow code has to be coupled to an adequate structural solver to produce meaningful results. The structural solvers most common for sails today are based on membrane theory. For upwind sails these solvers are often coupled with vortex-lattice methods (Figure 2.4), as for example in Caponnetto et al. [17]. When separated flow is to be expected over large portions of the sails, viscous flow simulation has to be used to achieve meaningful results. This is the case for downwind sails which turn out to yield some challenging problems. Firstly, viscous flow codes are much more demanding in terms of computational resources compared to the inviscid ones. Secondly, the large displacements as well as the many degrees of freedom incorporated by a downwind sail, led to the need to deform the computational grid around the sail to a degree which tends to render the calculation unstable. Therefore, one can say that the simulation of downwind sail is currently a topic of intensive research activity. Important contributions include the work of Richter et al. (2003) [18] and Renzsch and Graf [19, 20, 21]. An example of an RANSE-FSI simulation is shown in Figure 2.5. One major field of research is the correct structural modeling of the sails (Renzsch and Graf [21], Trichmarchi et al. [23], Durand et al. [24]). However, one of the main obstacles is to find the optimal trim within CFD simulations. Downwind sails like spinnakers have various trim possibilities which allow for many different shapes, making optimized trimming especially difficult. Recently, Durand et al. [25] presented an interesting approach. This approach is based on an automatic trim procedure which tries to trim the gennaker such that the pressure at the leading edge is only slightly above zero. At this point, the gennaker is on the verge to collapse at the leech. Sailing and measurement experience dictates that this most often is the point of optimum downwind sail trim.

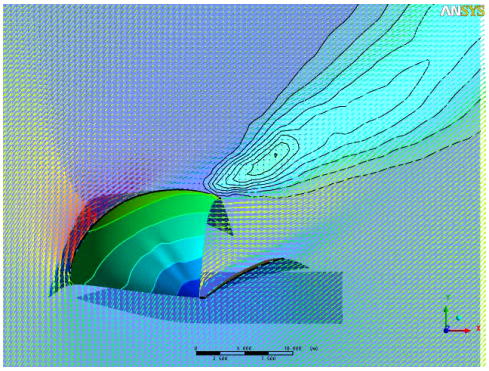

Figure 2.5: Viscous Flow around Gennaker (Source: Graf et al. [22])

These CFD-based developments are very interesting and allow new insights into the flow around sails. However, due to turnaround time and ease of use, to date twisted flow wind tunnels are still the tool to use for sail optimization. As for the wind tunnel, it seems that due to the advancements in CFD methods, there is an increasing interest in verification and validations of experimental results. For example, see Campbell [26].

2.4. INVESTIGATION METHODS FOR HYDRODYNAMICS OF YACHT HULL AND APPENDAGES

The first complete description of the mechanism underlying the development of waves by a hull moving through the water originates from William Froude and dates back to 1868. He was the first to describe the two main wave systems which are caused by a body moving at the water surface. This ship wave pattern consists of two so called Kelvin wave systems. One system is located at the bow and the other one at the stern, and in combination they are responsible for the so called wave-making resistance of a boat. Froude's investigations made it possible to conduct towing tank tests, which are comparable to full-scale by taking into account similarity of gravity forces.

Initially, these tests were not utilised for yachts but for merchant vessels and warships. The first documented experiments in a towing tank to improve the performance of racing yachts dates back to 1901. Back then George L. Watson tested eleven models for the America's Cup Challenge of Sir Thomas Lipton, though without great success. Nonetheless, it then already became clear that the America's Cup is a technology driver for sailing sport. To date, this statement has lost nothing of its validity, as can be seen from the current, 34th, edition of the America's Cup which features hydrofoiling, wingsail equipped 72 foot catamarans. The first successful tank tests for yachts date back to 1936. It was then, that K. Davidson [1] managed to approximately determine the resistance of a yacht rudimentarily correct by taking into account the influence of the sail forces on dynamic trim and sinkage. Davidson's work forms the basis for modern towing tank tests on yachts and has subsequently been further developed and refined since then.

In 1974 researchers at TU Delft started to systematically investigate the influence of hull form parameters on wave-making resistance. To this end new hulls were developed on the basis of a parent hull form by changing only certain parameters. These hulls were then investigated in upright position by towing tank tests. From the results of these tests, the influence of the form parameters on upright resistance was derived. This finally led to a regression formula allowing to empirically estimate the wave resistance of a yacht as a function of its form parameters. This so-called *Delft Systematic Yacht Hull Series* (DSYHS) is still being extended to date and has passed several iterations since its beginnings, e.g. to include the influence of modern yacht lines. The method is well documented and subject of numerous publications namely by Keuning and Gerritsma, see [27, 28, 29, 30, 31]. The whole data of the DSYHS has been recently made publicy available and can be accessed through the website `http://dsyhs.tudelft.nl`.

Besides formulations for the determination of a hull's upright resistance, other formula exist for added resistance due to heel as well as methods to approximate the influence of the appendages (*Delft Systematic Keel Series*, DSKS)[32, 33, 34, 35]. The DSYHS is one of the most significant contributions in the field of yacht hydrodynamics and since its creation it is widely applied because of its reliability, flexibility and ease of use, especially in the pre-design and early design phase. However, it has to be mentioned that inherent to the underlying system, the formula can only function properly in its investigated parameter range. Especially, local design features are often not captured properly and therefore need to be investigated in detail by means of numerical or experimental investigations.

At the beginning of systematic yacht research, one relied on towing tank tests for the investigation of hydrodynamic properties of yachts, eventually supported by wind tunnel tests for the keel. It was not until the early 1980 that *Computational Fluid Dynamics* (CFD) began to gain importance in yacht investigations.

The upside-down keel equipped with winglets by *Australia II* in its successful challenge for the 1983 America's Cup, see Figure 2.6, is reckoned to be one of the first keels to whose development CFD methods have significantly contributed.

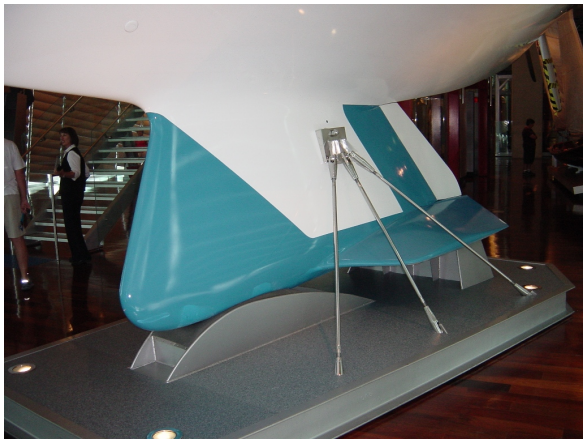

Figure 2.6: Australia II's Upside-Down Keel with winglets as seen in the WA Maritime Museum

The CFD methods used were potential flow solvers treating the fluid as inviscid, incompressible and non-rotational. The reason for these assumptions is that the problem can be formulated as a panel method, where only the boundary of the physical domain needs to be discretized. These models are linear, in contrast to the full governing flow equations, which are non-linear. This leads to an enormous reduction of computational costs, making CFD applicable in large scale at that time. Potential flow solvers were first applied mainly to develop appendages like keel and rudder, later the methods were extended to also include hulls. The calculation of flat water resistance with these methods proves to be difficult. Especially the prediction of flow separation, which occurs at the stern of yachts at higher Froude numbers, is only rudimentary possible by employing special boundary layer models which are notoriously error-prone. However, due to their low computational costs potential flow solvers still form the backbone of many flow investigations.

An example for the growing influence of CFD is the American challenge for the America's Cup 1987. Here CFD methods, most of them based on (linear) potential flow were applied in the design of the 12-metre yacht 'Stars & Stripes '87', see Boppe et al. [36]. The application of CFD for yachts steadily increased as can be seen in Caponnetto [37], Rosen et al. [38] and Tinoco[39]. The flow investigations in the fore front of the 31th America's Cup (2003) marks the upcoming of the use of computational techniques to model viscous flow. The effort needed to employ those methods is by powers higher than for programs based on potential flow. This is because contrary to potential flow methods, one has to discretize the flow field around the body with a volume grid. In the context of viscous flow methods, to date only Reynolds-Averaged-Navier-Stokes-Equations (RANSE) based methods are employed in an industrial environment since they constitute a compromise between accuracy and feasibility. For the already mentioned 31th America's Cup hydrodynamic investigations using RANSE codes have mainly been carried out for appendages. Examples include Graf [40] (2001) and Cowles et al. [41] (2003).

In the early 21st century, the successful calculation of hull resistance was still in its infancy and could only be fully realized some years later. The main problem for RANSE methods is the enormous complexity of the problem. It requires the use of multi-phase flow as well as grid movements due to dynamic trim and sinkage of the hull as a result of the sail forces. This makes the flow problem unsteady and thus introduces a time dependency of the result. In this context the work of Azecueta [42] (2001) had a significant influence, since it was the first to present a functional solution to these problems. The 32nd America's Cup (2007) now was marked by the massive use of viscous CFD methods. Besides the previously mentioned appendage studies, hull studies were also conducted to a great extent by means of RANSE methods. Here the CFD investigations only resembled the test methods known from tank tests. To date, correct capturing of wave resistance is still one of the challenging problems in viscous CFD. Although viscous CFD is gaining in maturity, formal verification and validation for sailing yacht applications is rarely seen. One of the first, if not the first, attempt to do so has been performed in the course of this work (see chapter 7) and published by Böhm and Graf [43].

2.5. CURRENT CONTRIBUTIONS TO VPP

Over the years, VPPs have become an important, reliable and versatile tool for yacht designers, flow analysts and researchers alike. Being the only means to predict the performance of sailing yachts, VPPs have been a constant topic of research to increase accuracy and reliablity of the prediction. When looking at the various methods available today, one has to distinguish between *conventional* and *dynamic* VPPs. *Conventional* VPPs, which form the overwhelming majority of the VPPs currently available, differ from *dynamic* VPPs by only seeking a valid solution for the steady state case.

2.5.1. APPROACH USING CONVENTIONAL VPPS

Conventional VPPs usually rely on a pre-calculated database of aerodynamic and hydrodynamic characteristics of a yacht. Using input values of true wind speed V_T and true wind angle β_T, the force components are then balanced by setting up and solving the resulting non-linear system of equations. In order to maximize the velocity of the yacht, an optimizer is used to simulate the trimming of the sails.

The aerodynamic database usually consists of coefficients of drag and lift, c_D and c_L, as functions of the apparent wind angle β_A. These coefficients are stored for various single sails or sail sets and are generated by means of wind tunnel testing or numerical investigation.

The hydrodynamic part of the database can be generated in two ways. The first approach uses empirical regressions derived from results of towing tank tests on systematically varied hull forms (e.g. *Delft Systematic Yacht Hull Series*). This approach is rather often used for custom build yachts with a limited budget, but due to its generic approach it obviously lacks the accuracy of dedicated investigations of the individual hull form. The second approach is to investigate the individual hull by means of towing tank test, be it numerical or physical. Here the different components that make up total resistance and total lift of a sailing yacht have to be considered. The total resistance may be considered as the sum of upright resistance at non-lifting condition, added resistance due to heel, induced resistance due to production of lift, parasitic profile drag of blade and rudder profile and added resistance due to sea state. The last contribution is often neglected since its unsteady nature makes it hard to generalize. Total lift $\mathbf{F_H}$ generated by the sailing yacht may be decomposed in lift generated due to leeway, lift due to rudder angle and lift generated by a trim tab, if applicable.

To capture the influence of differing sailing states, the yacht is tested at permutations of speed, heel angle, leeway angle and rudder angle. This leads to a large number of test runs, normally ranging between 80 to 200 runs. To a certain degree, the matrix can be curtailed by making it dense at special points of interest and sparse at points which are a at the extremes of the design conditions. After performing the investigations, hydrodynamic coefficients are derived from the resulting forces and moments. These coefficients allow quantification of the characteristics of a sailing yacht at every possible state by means of interpolation. The database of hydrodynamic coefficients is fed into the VPP program. In conjunction with the aerodynamic coefficients, the VPP calculates polar plots of optimal boat speed as function of β_T and V_T.

While much effort has been put into improving the gathering of hydrodynamic and

aerodynamic data necessary for VPP prediction, most performance prediction methods used today can still trace their lineage back to the first modern VPP which evolved in 1978 from the Pratt Project conducted by Kerwin et al. [2, 3, 4]. Over the years, the method has undergone subsequent improvements by many contributors in various parts of the method. One of its the most important successors is the IMS VPP. It is based on the *International Measurement System* (IMS) of the *Offshore Racing Congress* (ORC).

In 1993 Schlageter and Teeters [44] presented a VPP especially tailored for IACC boats including improvements in the upwind sail force model and a model for added resistance in waves.

A key paper on developments of the IMS VPP was published in 1999 by Claughton [45] from the Wolfson Unit of the University of Southampton. One of the major contributions of the paper is, that while much research had been performed in the field of sail aerodynamics, the relevant VPP formulations had not really changed for 20 years. In 2001, Jackson of the Yacht Research Unit of the University of Auckland, introduced a change in the aerodynamic model to model the effect of $twist$ [46]. The twist of a sail may be described as means to lower the vertical center of efficiency of a sail and therefore its heeling moment. In contrast to the $reef$ parameter, sail area is not reduced, but c_D is increased due to an increase in induced resistance originating from a non-optimal lift distribution. Changes in the aerodynamic coefficients of the IMS VPP regarding the efficiency of spinnaker and mainsail were presented by Teeters et al. in 2003 [47]. In 2005 Graf and Böhm [48] introduced a VPP with special focus on post-processing of towing tank data. The method allowed to derive the necessary coefficients from a limited number of towing tank tests by employing a so called *estimated state guess*. In 2008 the IMS handicap rule was replaced by the new ORC rule which also had an effect on the underlying VPP. The new ORC VPP tries to overcome some drawbacks of the old IMS VPP but still relies on the fundamentals of this formulation. The main differences of the new ORC VPP with respect to the IMS VPP, as reported by Claugthon et al. [49], are changes in the sail force model by replacing the reef model with a more realistic formulation, changes in stability assessment due to a new $twist$ function and new aerodynamic coefficients gained by experimental investigations at the Twisted Flow Wind Tunnel of the Politecnico di Milano.

2.5.2. APPROACH USING DYNAMIC VPP

In the last few years a trend can be recognized to evaluate sailing yacht performance not only in steady state conditions but also dynamically by solving the yachts equation of motion in a time series. This kind of VPP is either called *PPP* (Performance Prediction Programs) or *DVPP* (Dynamic VPP). Dynamic VPP may be divided into two main classes:

1. Classical, coefficient based VPP extended to maneuvering by employing measured data.

2. Approaches which directly calculate all time dependent hydrodynamic and / or aerodynamic data.

The goal behind the first approach is to simulate velocity losses due to tacking and gybing, leading to optimization of these maneuvers. This problem has been approached

by various contributors from different point of views. Selected contributions include the tacking model developed by Keuning et al. [50] which was presented in 2005. This model relies on pre-calculated, mainly empirical coefficients for prediction of maneuvering behavior. An different approach to predict maneuvering was taken by Masayuama et al. who presented a model based on data measured during sailing combined with a Artificial Neural Network in 1995 [51]. An extension of this method are complete pre-start simulation procedures as presented for example by Nielsen in 2006 [52] or Binns et al. in 2008 [53].

The second approach serves a different goal. By directly calculating the actual fluid dynamic properties of the yacht in a time-series, one attempts to enhance the accuracy of the performance prediction. Nonetheless, these kind of predictions are still evaluated by means of a velocity polar plot or a chart of the time difference to cover a nautical mile in varying conditions, so-called *time allowance deltas*. An advantage of this method is that it allows to rather easily implement unsteady effects, like e.g. seakeeping, into the prediction.

In 2002 Roux et al. [54] presented a numerical VPP. The implementation was aimed towards a 3-DOF VPP with the boat free to free to surge, sway and roll. It included aero- and hydrodynamics based on potential flow. The influence of fluid-structure-interaction (FSI) on sail aerodynamics was not taken into account. The method was extended by Jaquin et al. in 2005 [55] to employ a viscous flow method for the hull. In a further step, which was presented in 2008 (Roux et al. [56]) the method was extended to 5-DOF (free to move and rotate with exception of yaw motion) with the hydrodynamic forces calculated by a RANSE solver taking into account the free surface deformation by means of a Volume-of-Fluid (VOF) model. The aerodynamic solution also takes into account the effect of fluid structure interaction of the sails, but is still based on a potential flow code. This makes this approach only valid for cases for which flow separation cannot occur. Therefore this method is only applicable for conditions were the sailing yacht is sailing upwind if one is willing to neglect the influence of the separation bubble occurring on the mast and possible trailing edge separations on the sail. The method is not suitable for downwind or reaching conditions. Additionally, the cost to couple the aerodynamic and hydrodynamic solver is high. At every time-step of the hydrodynamic calculation, an aerodynamic solution has to be obtained. Keeping in mind the drawbacks of applying potential flow models to the fluid dynamics of sails, this approach seems to be unfavourable since it is rather costly in terms of computational resources and does not promise stable and accurate solutions.

A method to predict sailing yacht performance entirely based on RANSE investigation was proposed by Korpus in 2007 [57]. It included the massive use of auto-gridding in combination with overset grid techniques to automate generation of results. The calculation is performed without employing rigid body motion, instead the optimum is bracketed by calculating results for different states of the appended hull and of the sails on different meshes. The optimum itself is then found by interpolating results to a constant side force or speed.

An approach which depends entirely on the use of inviscid flow methods was presented by Maskew in 2009 [58]. The method incorporated an aero-elastic model for sails with the structural part based on membrane theory. Aero- and hydrodynamic flow is

solved simultaneously using a Boundary Element Method. Whilst showing interesting first results, the approach lacked a 6-DOF motion solver at that time, thus disallowing to generate VPP results.

An interesting experimental approach was implemented by Hansen (2006) [59] by coupling sail force measurements in a Twisted Flow Wind Tunnel with VPP calculations to achieve a so called *Real-Time VPP*. During sail testing a VPP with coefficient based hydrodynamic data was coupled with the measured aerodynamic forces. This allows one to calculate the heel angle resulting from the aerodynamic forces acting on the boat directly whilst trimming the sails. The wind tunnel model is then dynamically heeled to the correct angle during testing, allowing to take into account the effects of heel on sail efficiency and sailing performance.

2.6. OBJECTIVE OF THE RESEARCH

This thesis aims to enhance the accuracy in performance prediction of sailing yachts, with a special emphasis on the hydrodynamics. Additionally, a way to reduce turnaround times compared with conventional testing procedures is investigated.

As explained in the previous sections, a conventional velocity prediction program for sailing yachts relies on a set of aero- as well as hydrodynamic coefficients, describing the respective conditions of the yacht for a given set of state variables, in particular velocity u_B, heeling angle ϕ, leeway angle β and rudder angle δ. These coefficients are usually provided as tabulated values. The generation of hydrodynamic coefficients, even if obtained from a CFD code, resembles procedures from towing tank testing: Within a predefined test matrix, flow forces for a range of boat speeds, heel, leeway and rudder angles are analyzed. This usually causes a large number of computational runs to be carried out, including many off-equilibrium states, necessary for interpolations purposes, however rarely encountered by the sailing yacht. This results in large computational overhead.

A remedy to the drawbacks of the method described above is to include the aerodynamic forces directly into the evaluation of the hydrodynamic forces, thus creating a performance prediction. To judge which methods seems to be the most suitable to use for such an approach, the various methods to investigate aero- and hydrodynamics have to be assessed with respect to accuracy, turnaround times and the possibility to couple aero- and hydrodynamic forces. Table 2.1 shows the author's assessment of possible hydrodynamic methods taking into account Experimental Fluid Dyanmics (EFD), inviscid and viscid CFD. Table 2.2 does the same for aerodynamics. The symbols show how good the particular method is suited for the respective task.

⊕ = method is well suited for the task

⊙ = it is possible to fulfill the task with this method

⊖ = method is not suited for the task

− = method cannot be used for this task

For the hydrodynamics, one can see that in terms of accuracy viscous CFD methods and towing tank methods are on a even level, whilst potential flow method certainly

cannot reach the same quality here. However, potential methods excel the two other approaches in terms of turnaround times. The most important factor to consider is whether a method is capable of being coupled with some kind of aerodynamic input, be it direct or coefficient based. Here one must certainly say that conventional towing tank has to be neglected since such a coupling is impossible. The use of inviscid flow methods, also being attractive due to the fast turnaround times, is also being neglected since one of the goals of this thesis is to develop a method which improves the accuracy of the VPP solution compared to conventional approaches. This leaves the viscous flow method as the most appropriate choice. In particular a RANSE method is chosen for the calculation of the hydrodynamics of the yacht, since in the field of viscous flow these kind of methods resemble the current state of the art. The computational cost would be to high for methods which allow for better resolution of viscous flow phenomena, like Detached-Eddy-Simulation (DES), Large-Eddy-Simulation (LES) or even Direct-Numerical-Simulation (DNS) is so high, that they cannot be applied to this problem.

Table 2.1: Assessment of methods for Hydrodynamics of Appended Hull

Fluid dynamics technique	EFD.	Inviscid CFD	Viscous CFD
Froude similitude	⊕	⊕	⊕
Reynolds similitude	−	⊙	⊕
Viscosity	⊕	⊙	⊕
Detect Separation	⊕	⊙	⊕
Turbulence Scale	⊕	⊖	⊙
Sail Trimming Moment	⊕	⊙	⊙
Sinkage Force	⊕	⊙	⊙
Turnaround time	⊖	⊕	⊖
Coupling hydro ⇒ aero possible	⊖	⊕	⊕

To solve for the sailing equilibrium within the hydrodynamic RANSE solution one has to find a way to implement the actual sail forces. Since by today a direct calculation of both hydrodynamics and aerodynamics is out of reach in terms of computational power available, the most appropriate way seems to implement the sum of all aerodynamic forces acting on the yacht as a resultant sail force vector. This sail force vector is implemented to act on the rigid body *yacht* during the calculation of the hydrodynamics.

To calculate the necessary sail force vector, two approaches are feasible. Either, one can calculate the sail forces with a CFD model and employ a direct coupling between aero- and hydrodynamics. Since sails are flexible under wind loads, the determination of the correct flying shape is a very important factor in sail force analysis. This in turn requires the investigation technique to correctly predict effects like the separation bubble on the mast and trailing or leading edge separation on the sails. As tabulated in table 2.2, this is hard to achieve with a inviscid flow code. A viscous flow solver, however, does not have the necessary turnaround times. This drawback is made even more severe by the large number of possible states a sail can achieve, making sail trimming for optimum boat speed a highly non-linear optimization problem.

Table 2.2: Assessment of methods for Aerodynamics of Sails

Fluid dynamics technique	EFD	Inviscid CFD	Viscous CFD
Reynolds similitude	⊙	⊙	⊕
Viscosity	⊕	⊙	⊕
Detect Separation	⊕	⊙	⊕
Turbulence Scale	⊕	⊖	⊕
structural properties	⊕	⊕	⊕
Flying Shape	⊕	⊕	⊕
wrinkling	⊕	⊕	⊕
Panel Layout	⊙	⊕	⊕
Sail Trim	⊕	⊖	⊖
Turnaround time	⊕	⊕	⊖

On the other hand, it is possible to create the sail force vector by employing a sail coefficient based method. This approach has the advantage, that the coefficients may come from any source, be it numerical or experimental. Additionally, optimum sail trim is already existent for these coefficients. Since this approach fulfills all requirements in terms of accuracy, turnaround times and optimal sail trim, it is chosen for this thesis.

3

BASIC DECISIONS ON THE FORMULATION OF THE RANSE-VPP

In this chapter available methods for modeling aero- and hydrodynamics are reviewed. Critical areas are investigated and suitable solutions are assessed. Based on the findings of this chapter, decisions regarding the basic underlying modeling techniques of the new VPP are made. The goal is to find a combination of models which allows coupling aero- and hydrodynamics in a reliable and accurate manner within reasonable turnaround time.

3.1. OVERVIEW OF PRESENT METHODS IN HYDRODYNAMICS

In ship hydrodynamics, the free surface describes the phase interface between air and water. A ship moving through undisturbed water generates a wave pattern which disturbs the formerly flat interface. The energy necessary for the deformation of this interface is in direct relation with the so called *wave resistance*, an important component of the ship resistance. It is therefore mandatory for a numerical simulation of ship resistance to get a high resolution of the free surface pattern generated by the ship. In numerical simulation the position of the phase interface is only known at the initial point of the simulation. Later on it has to be computed as part of the solution. The interface and the deformation of the interface has to be modeled. Since this is not a trivial task, development and improvement of free surface modeling techniques has become an branch of its own in the development of CFD techniques. The following sections will give an overview of various techniques to model free surface flows. It starts with a description of the problem and continues with a classification of the different modeling techniques. Then the theory behind these techniques is described and details of selected methods are highlighted. This sections ends with an overview of existing codes and a discussion of the advantages and disadvantages of the various methods.

3.1.1. YACHT FLOW PROBLEMS

Before dealing with the different theoretical approaches to handle free surface flows, this section first gives an overview of the physical phenomena which have to be accounted for when computing flows around yachts. Flows with free surfaces can be encountered in many industrial applications. For yachts flow conditions normally consist of an air and an water phase with the water surface as the interface between the two phases. Consequently, free surface and water surface will be used as synonyms throughout this text.

A yacht traveling in seaways is subject to hydrodynamic forces acting on its hull and appendages. These forces may be decomposed into different physical aspects, which allows separate investigation and different models to be used to assess the performance of the yacht in question. In *conventional shipbuilding* a common decomposition is to distinguish:

- *Resistance*: the drag force acting on a ship moving without drift straight forward at constant speed through calm water;
- *Propulsion*: The required thrust force produced by the propeller, including necessary engine power, propeller dimensions and cavitation;
- *Seakeeping*: the movement of a ship due to incoming waves;
- *Maneuvering*: the ability of the ship to keep its course and to perform turns.

Sailing yachts incorporate a special method of propulsion, which shows a strong link between *resistance* and *propulsion*. Therefore, the above decomposition is of limited use when assessing the performance of sailing yachts. Sailing boats, as the name implies, are propulsed by the wind acting on sails, which may be described as *lifting surfaces subject to unsteady aerodynamic forces*. This implies that their propulsion force not only consists of a thrust force parallel to the yachts longitudinal axis, but also a perpendicular acting heeling force. Consequently, a sailing boat needs to counteract the aerodynamic forces acting on the sails with hydrodynamic counterparts.The heeling moment has to be balanced by a righting moment, consisting of ballast weight and form stability from the yacht hull. The heeling force has to be countered by an equal hydrodynamic force, which is mainly delivered by the appendages of the yacht, keel and rudder. Assuming symmetric foils on the yachts, these will have to be subject to an angle of incidence greater than zero to generate lift, implying that the yacht will drift to leeway. It is therefore mandatory that the investigation is not restricted to resistance test (non-lifting conditions) only, but also takes into account the interaction of hydrodynamic lift and drag. An ample decomposition of investigation method for sailing yachts might therefore be:

- *Resistance* in upright condition with dynamic trim and sinkage;
- *Lifting conditions*, as a permutation of
  - Boat speed,
  - leeway,
  - heeling and

  - rudder angle;

- *Seakeeping*;
- *Maneuvering*;

Performance prediction of sailing yachts is normally evaluated by looking at calm water conditions only. While motion of the yacht due to seastate has an important impact on the overall performance of the yacht, the problem is simply to complex to be investigated with sufficient accuracy using reasonable resources. The same holds true for maneuvering. Experimental evaluation of main performance parameters is based on model tests. For this purpose models of the boats are built and subsequently tested in towing basins. The length of the model varies from 1.5 to 8.5 m corresponding to model scales of 3 - 25. Due to the fact that models are smaller than full scale, the testing is subject to scale effects. In particular the Reynolds number is several orders of magnitude too small, effecting all flow properties associated with viscosity. In order to correct results of model testing to full scale values, it is a common to separate flow phenomena associated with pressure and viscosity and to neglect their interaction. The pressure component is associated with the pressure variations originating from the wave pattern generated by the yacht moving through the water. The viscous component originates from boundary layer effects on the hull surface and from the wake. These components are associated with different flow parameters and different length scales. Viscosity related errors in model testing are traditionally corrected by applying semi-empirical corrections. This practice has also been used for a long time in CFD by using inviscid flow methods and approximating the viscous components via wetted surfaces and friction lines or via boundary layer equations which are a simplified form of the Navier-Stokes equations.

It has to be noted, that these approaches neglect interaction between viscosity and pressure related flow aspects, while in reality this interaction exists. Viscous simulation of yachts at full scale has the potential to overcome the drawbacks stated above. Although viscous CFD has reached a high degree of maturity over the last decade, full scale multiphase flows are still one of the most demanding tasks. For ship hydrodynamics these demands include the correct resolution of the viscosity related flow parameters at high Reynolds numbers and for thick boundary layers. For prediction of wave resistance correct resolution of waves generated by the motion of the ship are essential. This includes the ability of the flow code to account for breaking waves. Breaking waves occur as *spilling breakers* or as *plunging breakers*, see Sarpkaya and Isaacson [60]. In the context of ship waves, Wilson et al. [61] and Wackers et al. [62] describe that spilling breakers are associated with the transverse transom wave system and can also be observed at very full bows with a small intersection angle to the water surface. Plunging breakers are normally observed at the bow wave system. Normally, it is easier to account for spilling breakers in a flow code, since these are smoother and therefore more easy to handle. Having a flow code which is able to account for plunging breakers is especially important for sailing yachts, since they operate at significantly higher relative speeds then most conventional vessels. Froude numbers of 0.4 are the norm, while boats acting at Froude numbers of 1 or slightly above are by no means uncommon. Higher boat

speeds lead to a more violent breaking of waves, so a stable method to account for the free surface shape of the plunging breakers is mandatory for sailing yachts. At these high speeds, spray also starts to become an issue. It might not be necessary to have a flow method which allows to account for formations of spray, but it would be desirable. An essential feature of a flow code, which is not directly related to free surface modeling techniques is the ability to account for motion of the floating body. While this might not be necessary for ship hydrodynamics, for yachts it is. This is because sailing yachts are subject to significant dynamic trim and sinkage forces due to aerodynamic forces from the sails. It is therefore essential to account for this force components whilst simulating flow around sailing yachts.

3.1.2. CLASSIFICATION OF FREE SURFACE MODELS

For simulation of viscous free surface flow, several different theoretical models exist. Since large differences in the treatment of the water surface exist, a classification of these models is necessary to give a overview of the pro and cons of the individual methods. The classification of these models as found in literature is not only inconsistent, but to a certain degree also ambiguous. A popular classification for viscous free surface modeling methods is given in [63] and [64]:

- *Surface Methods* also called *Interface-Tracking Methods*, where a sharp air-water interface is defined by initial and boundary conditions on the surface. The development of the interface is then tracked and the grid is deformed accordingly.
- *Volume Methods* or *Interface-Capturing Methods*. These methods do no track a sharp boundary. Instead the fraction of partly filled cells near the interface is transported through the fluid domain. The free surface shape is computed from these fractions

This classification is not unambiguous, since several methods exist which have features of both definitions. To overcome this ambiguity, [65] and [62] give a classification which divides the models into the following three categories:

- *Fitting Methods*, for which the grid is deformed to fit the water surface. The interface forms a boundary surface on which free surface boundary conditions are applied.
- *Capturing Methods with Reconstruction*. Within these methods, the grid is not deformed, but the water surface is still explicitly defined. Values defining the surface as a cut through the mesh are convected through the fluid domain. These values can either be marker particles or convected continuous functions like in the Level-Set-Method.
- *Capturing Methods without Reconstruction*. These methods employ a fixed mesh. Two fluids are treated as a multifluid with varying physical properties. The degree of mixture within a cell of these fluids is convected through the flow field as volume fractions. The water surface is only implicitly known as a numerical discontinuity and no attempt is made to reconstruct it.

In the author's opinion it is that this classification is the most descriptive and logical. It is therefore used throughout this work.

3.1.3. FREE SURFACE MODELING METHODS

FITTING METHODS

Fitting methods which are sometimes also called *Moving Mesh* or *Lagrangian Methods* represent the free surface as a sharp boundary of the flow domain. To form the wave pattern, free surface boundary conditions (FSBC) have to be applied onto this boundary and it has to deform under the influence of flow. Therefore the method requires means to either remesh or deform the volume grid. For grid deformation a variety of methods exist, for instance being based on torsional spring analogies or Lagrange interpolation of free surface changes. A overview of the principle behind surface fitting is illustrated in Figure 3.1.

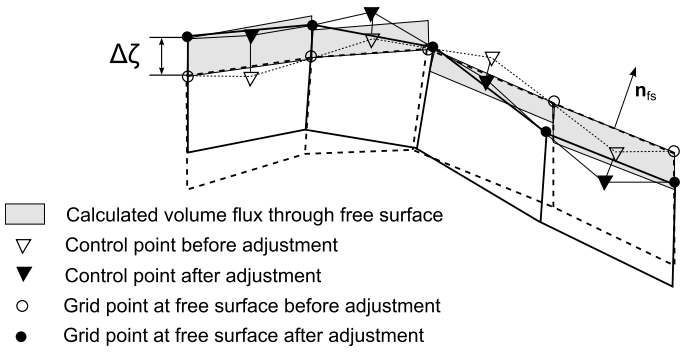

Figure 3.1: Methodology for free surface fitting (Source: Ferziger and Peric [63])

The influence of the aerodynamics on ship hull resistance is neglected in this method, allowing for single phase simulation. From the point of computational resources, this is advantageous since it limits the number of control volumes necessary and removes time-step restrictions implied by most multiphase methods. From a numerical point of view it is also advantageous that the need to discretize over a density jump of 800 is omitted. Free surface fitting methods are well known in ship hydrodynamics, being among of the first implementations to capture wave resistance in viscous flow codes. They were the preferred choice around 1995 when viscous free surface calculations for ship hydrodynamics became popular. An early implementation of this method may be found in Coleman and Haussling [66]. A larger number of examples from different sources may be found in literature [67, 68, 69, 70] and a number of known flow codes use this approach, for instance ICARE [71, 72, 73], Neptune [74], U^{2}NCLE [75, 76], PARNASSOS [77, 78, 79, 80, 81].

Governing Equations To give a valid representation of the free surface interface around the ship, the morphing boundary has to fulfill the following free surface boundary conditions:

- A Kinematic Boundary Condition which states that the free surface is a sharp interface without flux. This implies that the velocity component of the fluid normal to the free surface is equal to the velocity with which the free surface moves in this direction.

- A Dynamic Boundary Condition which demands that momentum at the free surface is conserved. Therefore forces acting on the fluid at the phase interface have to balance. This implies that normal forces at the free surface are of same magnitude but opposite sign ($\Delta p = 0$), whilst tangential forces are of equal magnitude and sign (no shear stress is exerted at the water surface, surface tension is neglected).

The kinematic condition may be written as:

$$\zeta_t + u\zeta_x + v\zeta_y - w = 0 \quad at \quad z = \zeta \tag{3.1}$$

where ζ is the wave height, u, v and w are the velocity components in cartesian coordinate x, y and z. The wave height ζ is unknown, which implies that the FSBC is nonlinear. To obtain ζ, one can integrate 3.1 in time, resulting in an unsteady calculation. If a solution for a steady wave system is searched for, e. g. resistance at constant speed, an unsteady approach is not favorable since it takes substantial time to establish a steady wave system. This is due to the fact, that in deep water wave energy travels with half the wave velocity. It would therefore be advantageous in terms of computational efficiency to reformulate the FSBC to an steady formulation. In this context, the free surface fitting method implemented in the code PARNASSOS [62] from MARIN is interesting. In this approach the FSBC are reformulated into a time-independent form to allow for steady simulations.

By applying the normal dynamic condition, pressure $p = 0$ at $z = \zeta$, on the nondimensional hydrostatic pressure p

$$p = \frac{p^* + \rho g z}{\rho U^2} \tag{3.2}$$

where p^* is the atmospheric pressure (p^*=0), ρ the water density and U the ship speed, the normal component of the dynamic condition becomes

$$Fn^2 p - \zeta = 0 \tag{3.3}$$

where Froude number $Fn = U/\sqrt{gL}$ is calculated using ship speed U and a reference length L.

Equations (3.3) and (3.1) have to be combined to introduce wave dynamics. The combined form of kinematic and dynamic normal free surface boundary condition then

evolves from substituting wave elevation from the dynamic into the kinematic condition. This yields:

$$Fn^2\left(up_x + vp_y + wpz\right) - w = 0 \quad at \quad z = \zeta \tag{3.4}$$

Together with the tangential dynamic boundary condition

$$\mathbf{t} \cdot \tau \cdot \mathbf{n} = 0, \tag{3.5}$$

one obtains the combined, time-independent formulation of the FSBC. The following iterative solution procedure is then carried out to calculate the wave field around the ship:

1. The RANS equation is solved according to the combined condition (3.4) and the tangential dynamic condition (3.5) imposed at the free surface.

2. Wave surface and computational grid are updated using normal dynamic condition. Since pressure p is known from the previous RANSE step, ζ is an explicit expression.

Summary The use of free surface fitting methods for ship hydrodynamics comes with several amenities: The free surface interface forms a boundary of the flow domain and is therefore well defined and sharp. Vertical refinement in the vicinity of the free surface is unnecessary, allowing for a relatively coarse computational grid. There is no need to discretize over a large density jump at the water surface, improving stability of the solution. The method is single phase which saves computational grid cells, removes severe time-step size restrictions and improves accuracy. Unlike an unsteady formulation, it does not resolve the temporal sequence of interface development, this way saving the otherwise necessary iterations per time step. This makes the steady state formulation at least 2 to 4 times faster than an unsteady one.

However, the method also has several disadvantages: It has problems with large topology changes which reduce grid quality. This especially holds true for breaking waves, plunging breakers and formation of spray which are impossible to simulate with this method. The method is also vulnerable to extreme wave shapes which can occur near to the hull, especially for fast ships with drift. Dynamic trim and sinkage may be included, but produce additional challenges to the computational grid, which has to be deformed to remain grid topology.

Although free surface fitting methods have some very interesting properties, especially for evaluation of resistance of ships at low Froude number, the limitations of the method are serious. This holds especially true for hydrodynamics of sailing yachts, which operate at high Froude numbers and are subject to large body motions.

CAPTURING METHODS WITH RECONSTRUCTION

Unlike Fitting methods, Capturing Methods with Reconstruction have no need to deform the computational grid. Instead the shape of the free surface is transported through

the grid by appropriate means. The interface surface between air and water is given as a cut through the fixed computational grid. An advantage that these kind of methods share with surface-fitting methods is that the approach implies that the interface is sharp.

One example for this kind of methods is the *Marker-and-Cell* scheme (MAC) as introduced by Harlow and Welch [82]. This method uses massless marker-particles at the free surface. The motion of these particles through the fluid domain is tracked and allows to reconstruct the surface of the air-water interface. This solution to the free surface flow problem is elegant, since it features a sharp interface whilst allowing to treat complex flow phenomena like breaking waves. However, it is rarely used since it requires a large number of marker particles, which in complex three-dimensional flows leads to an enormous computational effort.

Level-Set Method One of the latest developments in these kind of methods is the application of the Level-Set Method (LSM) to ship flow problems. Within this method, the water surface is implicitly given a the root of a signed distant function ϕ. Since the interface is captured between grid points, the method has the advantage that it can deal with large deformations of the free surface, e.g. overturning or breaking waves. In contrast to surface fitting methods, there is no need to remesh the grid, but this computational advantage is lost due to the need to have a refined volume in the vicinity were the interface is located. Due to its capturing nature, the method has no grid points at the exact interface to satisfy free surface boundary conditions, which implicitly reduces numerical accuracy. The Level-Set function is linearly varying making it easy to handle the convection of its properties through the domain. Difficulties arise with the conservation properties of the method since its formulation implies that it cannot guarantee that fluid volumes are preserved near the interface. This can lead to an overflow or leak of volume within a cell. Since this behavior has to be avoided, a special treatment is necessary to fulfill conservation of mass. Generally there are two main categories of Level-Set Methods for ship flow problems.

The first is a two-phase fluid approach in which both air and water phases are accounted for by a multiphase flow solver. This is the original level-set method formulation developed by Sussman et al. [83]. The formulation has been implemented into various flow codes and a large number of applications exists. Vogt and Larsson [84] used this approach to simulate a 2D submerged hydrofoil. An implementation in code version 6 of *CFDSHIP-IOWA* exists [85]. Cura Hochbaum and Schumann [86] presented an application on Series 60 Hull computed with *Neptun*, a multi-block structured grid based RANSE solver. Another implementation using the unique interface capturing method (CLSVOF) was presented by Dommermuth [87]. The hybrid method couples VOF and LSM methods to simulate flow around ships.

The second category employs a single-phase approach and calculates only the flow properties of the water phase. To get a physical correct interface, flow variables at the gas phase side of the interface are extrapolated by employing free surface boundary conditions. Neglecting the influence of air reduces the computational effort to a certain degree and gives the advantages that the solution is single-phase. This should lead to more sta-

bility and a better convergence of the solution compared to multiphase flows since the large density jump between air and water phase is avoided. Because of this advantages, the method has become rather popular over the last years. Known applications include the latest Version of *CFDSHIP-IOWA* from the Applied Fluid Dynamics Group at the University of Iowa [88, 89, 90, 91] and the Navier-Stokes solver *SURF* from NMRI [92]. The method is also implemented in $\chi shi p$ from INSEAN [93].

Governing Equations As already stated above, within the Level Set Method the water surface is usually given as the root of a signed distance function ϕ

$$\phi\left(x, y, z; t\right) = 0. \tag{3.6}$$

To simplify the numerical tracking of the root, the signed distance function fulfills the condition

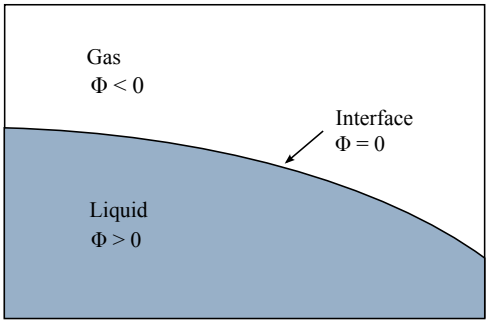

Figure 3.2: Within the Level-Set method, the isosurface defining the free surface is given at an explicit value of the distant function. Values varying from this explicit value indicate pure gas or water phase. Therefore, simulations using the Level-Set method always have a sharp free surface interface.

$$\left|\nabla\phi\right| = 1. \tag{3.7}$$

With the signed distance reading as:

$$\phi = \begin{cases} > 0 & \text{in water,} \\ = 0 & \text{at the interface,} \\ < 0 & \text{in air.} \end{cases} \tag{3.8}$$

So by convecting the level set function ϕ through the fluid domain, the water surface is transported by:

$$\frac{\partial}{\partial t} + \nabla\left(\mathbf{v}\phi\right) = 0, \tag{3.9}$$

where t is time and $\mathbf{v}$ is flow velocity. During iterations the level set function deforms due to numerical dissipation whilst convecting the distant function. The distant function therefore is not valid anymore and leaks mass. This makes it crucial to regularly

reinitialize the distant function. In principle, the reinitialization has nothing to do with the flow itself. It is simplify the replacement of the ϕ distribution by another distribution $\hat{\phi}$ which is not leaking mass. This is allowed, since the distance to the interface is zero in all points while doing so. Therefore, the interface itself does not change. A common approach to conduct the reinitialization is to determine $\hat{\phi}$ as the steady steady state solution of the following equation:

$$\frac{\partial \hat{\phi}}{\partial \tau} + S\left(\phi_0\right)\left(\left|\nabla \hat{\phi}\right| - 1\right) = 0, \tag{3.10}$$

with the artificial pseudo time step τ and the initial condition $\hat{\phi}(\mathbf{x},0) = \phi(\mathbf{x},t)$. S is a smoothed sign function

$$S\left(\hat{\phi}_0\right) = \frac{\hat{\phi}_0}{\sqrt{\hat{\phi}_0^2 + \epsilon^2}}, \tag{3.11}$$

with $\hat{\phi}_0(\mathbf{x}) = \hat{\phi}(\mathbf{x},0)$ and typical grid spacing ϵ. When steady state is achieved, the term $\partial\hat{\phi}/\partial\tau$ in (3.10) vanishes. Therefore $\left|\nabla\hat{\phi}\right| = 1$, which is the constraint which has to be fulfilled by $\hat{\phi}(\mathbf{x},\tau)$ to become a distant function. Since it has the same zero level as $\phi(\mathbf{x},t)$, one can let ϕ take the values of $\hat{\phi}$. Thus the level set function is reinitialized.

Summary An advantage of the LSM is that the free surface is given by a smooth function which is linearly varying. This makes it easy to handle the convection of its properties through the domain allowing a well defined representation of the interface. Additionally, the method allows for large deformations of the water surface, even for overturning waves.

A disadvantage is that conservation of mass is critical. The LSM leaks mass, which makes it necessary to reinitialize the function from time-to-time to restore mass conservation. Compared to fitting methods, the method has a larger computational cost since proper transport of the distance function implies that a refined volume grid is necessary in the vicinity of the interface. Finally, theoretically the method also allows for overturning waves, but the appearance of these kind of waves without formations of spray is an unphysical representation of the phenomena involved.

CAPTURING METHODS WITHOUT RECONSTRUCTION

Interface Capturing Methods without reconstruction do not treat the free surface as a sharp boundary. Instead the calculation is performed one a fixed grid, and free surface interface orientation and shape is calculated as function of the volume part of the respective fluid within a control volume (CV). The most popular of these methods is the Volume-of-Fluid method which was introduced by Hirts and Nicols (1981) [94].

Volume-of-Fluid method The Volume-of-Fluid method (VOF) employs the concept of an equivalent fluid. This approach assumes that the (two) fluid phases share the same velocity and pressure fields thereby allowing them to be solved with the same set of governing equations describing momentum and mass transport as in a single phase flow.

The volume fraction α_i of the i-th phase describes to which level the cell is filled with the respective fluid.

$$\alpha_i = \frac{V_i}{V}. \tag{3.12}$$

The free surface is then defined as the isosurface at which the volume fractions take the value of 0.5, see Figure 3.3. It is important to note, that this location is not at the control volume center but rather interpolated to the geometrical value. To simulate wave dynamics, one has solve an equation for the filled fraction of each Control Volume (CV) in addition to the equations for conservation of mass and momentum. Assuming incompressible flow, the transport equation of volume fractions α_i is described by the following conservation equation:

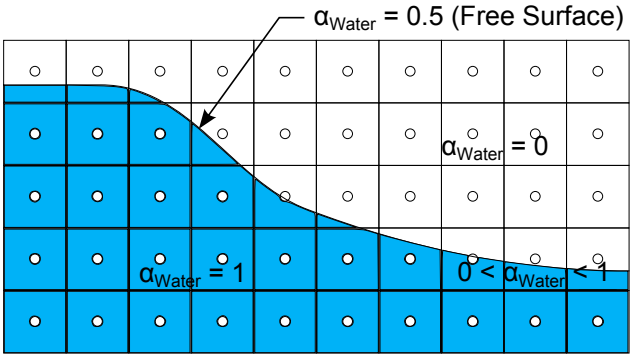

Figure 3.3: The VOF model uses the concept of volume fractions. Every control volume is always completely filled. It may be completely filled with water (volume fraction of water $\alpha_{water} = 1$) or air ($\alpha_{water} = 0$) or a fraction of both phases (for example: $\alpha_{water} = 0.7$ and $\alpha_{water} = 0.3$). Mass conservation dictates that the volume fractions α_i always sum up to 1.

$$\frac{\partial}{\partial t}\int_V \alpha_i \mathrm{d}V + \int_S \alpha_i (\mathbf{v} - \mathbf{v}_b)\cdot \mathbf{n}\mathrm{d}S = 0 \tag{3.13}$$

The physical properties of the equivalent fluid within a control volume are then calculated as functions of the physical properties of the phases and their volume fractions.

$$\rho = \sum_i \rho_i \alpha_i, \tag{3.14}$$

$$\mu = \sum_i \mu_i \alpha_i, \tag{3.15}$$

$$1 = \sum_i \alpha_i. \tag{3.16}$$

Strict conservation of mass is crucial, but this is easily obtained within this method as long as it is guaranteed that equation (3.16) is fulfilled. The critical issue for this kind of methods is the discretization of the convective term. Low-order terms like for instance 1^{st} order upwind are known to smear the interface and introduce artificial mixing of the

two fluids. Therefore higher order schemes are preferred. The goal is to derive schemes which are able to keep the interface sharp and produce a monotone profile over the interface. Development of differencing schemes for hyperbolic convection equations has been the pinnacle of research in the fields VOF methods for many years. Consequently a large number of schemes is available and have been successfully used in different codes. The vast majority of these schemes is based on the Normalized Variable Diagram (NVD) and the Convection Boundedness Criterion (CBC) introduced by Leonard in 1979 [95].

Normalized Variable Diagram The NVD provides a framework for the development of convective schemes which in combination with the CBC guarantees boundedness of the solution. Boundedness is the restriction of a mathematical function to a certain range. In context of the NVD, boundedness allows to create convection schemes which are both stable and accurate. The elementary schemes all have certain advantages and disadvantages. Pure upwind schemes are stable but diffusive. The central differencing scheme is more accurate but introduces propagating dispersion why may lead to unphysical oscillations in large regions of the solution. Therefore, practical schemes are often designed as a blending of upwind, downwind and central differencing schemes to obtain the desired properties. The advantage of the NVD is its simplicity. New schemes designs can be easily controlled regarding stability and boundedness. It also allows conclusion regarding accuracy of the scheme, this will be addressed later. The NVD takes the following form: For a 1D case, it allows to plot the locally normalized convected control-volume face variable $\tilde{\phi}_f$ with respect to the normalized adjacent upstream node variable $\tilde{\phi}_U$, see Figure 3.4. The position of the nodal value relatives to each other is defined as:

ϕ_D = Downwind

ϕ_C = Central

ϕ_U = Upwind

The normalized variable $\tilde{\phi}$ for each cell face is defined as:

$$\tilde{\phi} = \frac{\phi - \phi_U}{\phi_D - \phi_U}. \tag{3.17}$$

It has to be noted that this results in $\tilde{\phi}_U = 0$ and $\tilde{\phi}_D = 1$. With this definition any differencing scheme using only nodal values at point U, C and D to evaluate ϕ_f may be written as

$$\tilde{\phi}_f = f\left(\tilde{\phi}_C\right). \tag{3.18}$$

To avoid that the solution oscillates unphysical, $\tilde{\phi}_C$ has to be locally bounded between $\tilde{\phi}_U$ and $\tilde{\phi}_D$.

$$0 = \tilde{\phi}_U \leq \tilde{\phi}_C \leq \tilde{\phi}_D = 1. \tag{3.19}$$

If this criterion is satisfied for every point in the solution domain, then no unphysical oscillations will occur. According to the Convection Boundedness Criterion (CBC), a numerical approximation of $\tilde{\phi}_f$ is bounded, if: $\tilde{\phi}$ is bounded below in the range $0 \leq \tilde{\phi}_C \leq 1$ by the function $\tilde{\phi}_f = \tilde{\phi}_C$, bounded above by 1 and passes through (0,0) and (1,1). This corresponds to the shaded area in 3.5.

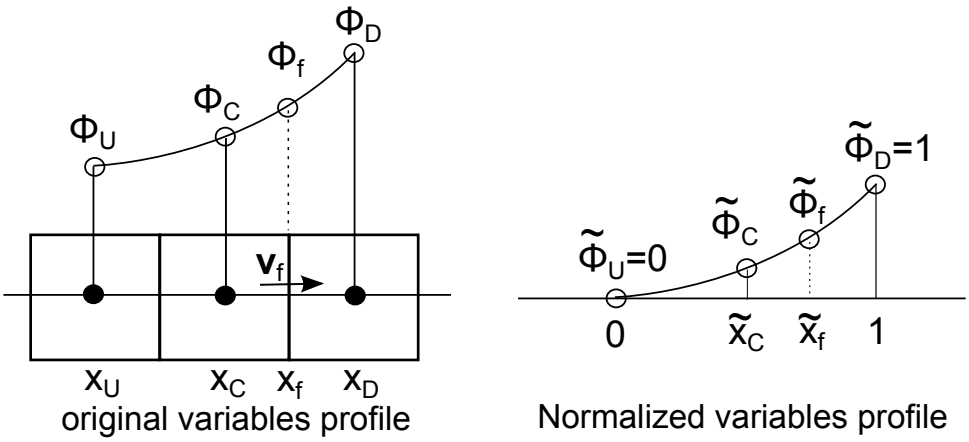

Figure 3.4: Node variables adjacent to the cell face of interest. Original variables are shown on the left while the right side displays values normalized using Equation (3.17)

Figure 3.6 gives an overview of a several of popular linear schemes. The point $Q = (0.5/0.75)$ is of special importance when judging accuracy of a convection scheme. Leonard [95] showed by making a Taylor series expansion around the CV face, that for any scheme

- passing through Q is necessary and sufficient for second-order accuracy.
- passing through Q with a slope of 0.75 is is necessary and sufficient for second-order accuracy.

However, this only holds true for a uniform grid. One can see that apart from the UD, which passes well below Q, all schemes are passing through Q. It also has to be noted that with exception of UD none of these schemes fulfill the boundedness criterion. So it can the concluded that the linear schemes either lack stability or accuracy. The need for boundedness, stability and accuracy consequently led to the desire to combine the advantages of the different linear schemes. This led to the development of nonlinear schemes.

Some of these schemes have been developed in the last decade and further development is still the topic of ongoing research. Some popular and successful schemes are shown in Figure 3.7. In particular we have the CICSAM scheme (Compressive Interface Capturing Scheme for Arbitrary Meshes) developed by Ubbink [64], the IGDS (Interface Gamma Discretization Scheme) from Jasak et al [96], BRICS (Blended Reconstructed Interface Capturing Scheme) from Wackers [65] and the HRIC (High Resolution Interface Capturing Scheme) of Muzaferija and Peric [97]. The CICSAM scheme starts with a linear blend between upwind and downwind differencing on slope of 3.08 until $\tilde{\phi}_C = 0.285$. Afterwards the blend continues with a slope of 0.175 until $\tilde{\phi}_C = 1.0$ is reached. Pure downwind differencing is never reached, but the scheme has a sufficiently compressive character allowing it to maintain a sharp interface. The IGDS (Figure 3.7c)) is an extension of the Gamma Differencing Scheme (GDS) with an emphasis on compressive scheme character to build a sharp interface. The scheme establish a smooth blending

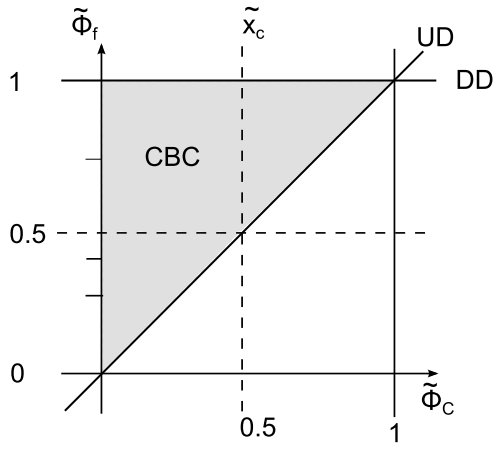

Figure 3.5: This the basic form of the Normalized Variable Diagram (NVD). The shaded area shows the zone for which the CBC is valid. It is bounded by the upwind differencing scheme (UD) and the downwind differencing scheme (DD). Blended schemes which are bounded by this area are stable and the solution is free of unphysical oscillations.

between upwind and downwind differencing. It finally switches to downwind differencing at $\tilde{\phi}_C = 0.5$. The main disadvantage of the IGDS is its limitation to a Courant number < 0.3. The Courant number CFL is a measure of through how many cells a flow particle is transported per time step and is defined as:

$$CFL = \frac{\mathbf{v}_f \mathbf{S_f} \mathrm{d}t}{V_f}, \tag{3.20}$$

where $\mathbf{S_f}$ is the surface vector of the cell face with the volume V_f, $\mathrm{d}t$ is the time step size and $\mathbf{v}_f$ is the flow velocity through the cell face.

The BRICS scheme tries to avoid the Courant number limitation of the IGDS. It starts with a blending between the GDS an the IGDS scheme. Therefore, the blending to downwind differencing is not as pronounced as for the IGDS, but it is more robust. In contrast to the IGDS, the HRIC scheme blends linear between upwind and downwind differencing. The point were pure downwind differencing is used is also at $\tilde{\phi}_C = 0.5$. In contrast to the IGDS, the HRIC should be less compressive but more robust in the range $0 \leq \tilde{\phi}_C \leq 0.5$. These kind of overviews are very common to compare different schemes, but they are not complete. They only show the base configuration of the schemes which is valid only for a Courant number lower or equal 0.3 and a flow direction with an angle of 90° (straight through the face f). For other Courant numbers and/or angles these schemes are blended towards upwind differencing to enhance stability of the solution. In the following this blending strategy is exemplified by a detailed description of the HRIC scheme.

HRIC Scheme The HRIC scheme is one of the most popular advection schemes and widely used in many CFD codes. It has been developed by Muzaferija and Peric [98, 99,

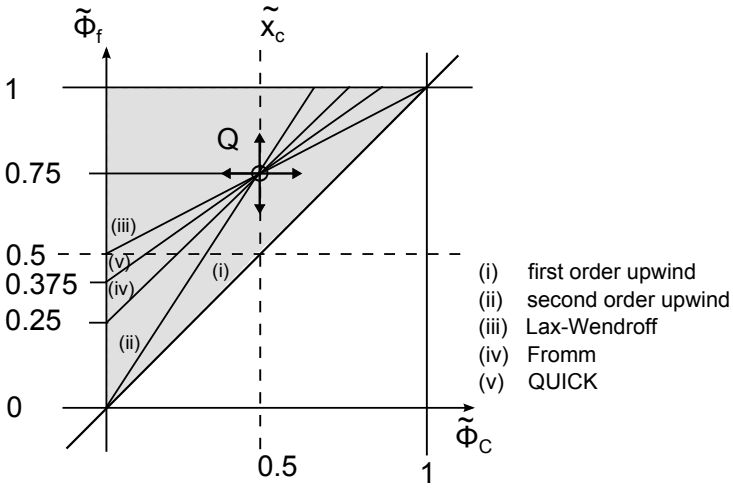

Figure 3.6: First-order upwinding, second-order upwinding, third-order upwinding (QUICK), Lax-Wendroff and Fromm schemes plotted in the Normalized Variable Diagram

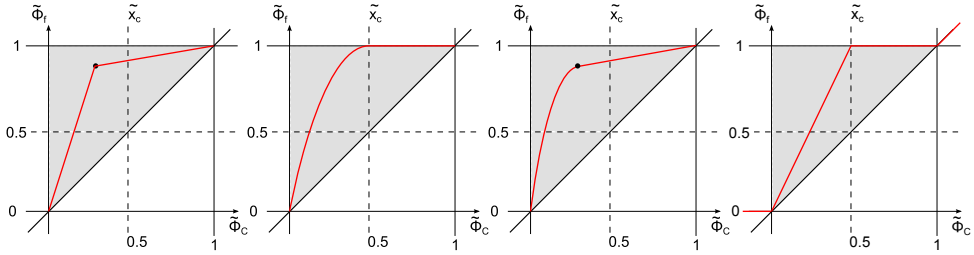

(a) CICSAM scheme (b) BRICS scheme (c) IGDS scheme (d) HRIC scheme

Figure 3.7: Overview of Interface Capturing Schemes

97]. Like most others schemes, it is based on an blending of bounded Upwind and Downwind schemes. The aim is to combine the compressive properties off the Downwind differencing scheme with the stability of the Upwind scheme. The bounded downwind scheme is formulated as:

$$\tilde{\phi}_f = \begin{cases} \tilde{\phi}_C & \text{if } \tilde{\phi}_C < 0 \\ 2\tilde{\phi}_C & \text{if } 0 \leq \tilde{\phi}_C \leq 0.5 \\ 1 & \text{if } 0.5 \leq \tilde{\phi}_C \leq 1 \\ \tilde{\phi}_C & \text{if } 1 \leq \tilde{\phi}_C \end{cases} \tag{3.21}$$

Since the amount of one fluid convected through a cell face shall be less or equal than amount available in the donor cell, the calculated value of $\tilde{\phi}_f$ is corrected with respect to the local Courant number. The correction takes the form of (3.22) and effectively controls the blending between HRIC and UD scheme with two limiting Courant numbers CFL_L

and CFL_U which normally takes values of 0.5 and 1.0 respective 0.3 and 0.7.

$$\tilde{\phi}_f^* = \begin{cases} \tilde{\phi}_f & \text{if } CFL < CFL_L \\ \tilde{\phi}_C + \left(\tilde{\phi}_f - \tilde{\phi}_C\right) \frac{CFL_U - CFL}{CFL_U - C_L} & \text{if } CFL_L \leq CFL < CFL_U. \\ \tilde{\phi}_C & \text{if } CFL_U \leq CFL \end{cases} \tag{3.22}$$

Effectively, this correction implies that the HRIC scheme is used for a CFL smaller than the lower CFL limiter and UD scheme for CFL equal or greater than the upper CFL limiter. Between those values a blending of both schemes is used. This correction is applied to improve robustness and stability when large time variation of the free surface shape is present and the time step is too big to resolve it. After this correction $\tilde{\phi}_f^*$ experiences a final modification based on the interface angle, which is the angle θ between the normal of the free surface interface $\mathbf{n}$ and the cell surface vector $\mathbf{S}_f$, see Figure 3.8. This final modification reads:

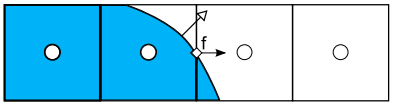

Figure 3.8: interface angle between two fluids

$$\tilde{\phi}_f^{**} = \tilde{\phi}_f^* (\cos\theta)^{C_\theta} + \tilde{\phi}_C (1 - \cos\theta)^{C_\theta}. \tag{3.23}$$

Here C_θ represents an angle factor. Its default value according to [97] is 0.05. The ratio behind (3.23) is that for different interface angles different differencing schemes are favorable. In case that the interface is perpendicular to cell face, the front sharpening effect of the downwind differencing scheme is needed. If the interface is parallel to the cell face, the downwind differencing scheme tends to wrinkle the interface. Therefore the upwind differencing is used in this case. For interface angles between these two extrema, the HRIC scheme is blended according to (3.23). The final cell face value is calculated as:

$$\phi_f^{HRIC} = \tilde{\phi}_f^{**} \left(\phi_D - \phi_U\right) + \phi_U. \tag{3.24}$$

As a consequence of these modifications due to interface angle and local Courant number, the NVD can take different forms. For the three different blending states depending on local CFL, Figure 3.9 illustrates the possible forms of the HRIC scheme with respect to the interface angle θ. The areas shaded in red represent the possible forms the scheme can take depending on the angle factor for the respective local Courant number. This kind of blending strategy is more or less the same for all interface capturing schemes, so care has to be taken when modeling free surface flows to avoid unwanted switching to a lower resolution which is often accompanied with interface smearing.

Summary Free surface modeling based on VOF methods clearly holds some advantages. The approach is very general and allows for complex shapes of the free surface. It is currently the only reasonably applicable method which can take into account violent wave breaking and even formation of spray. This is possible because instead of the exact

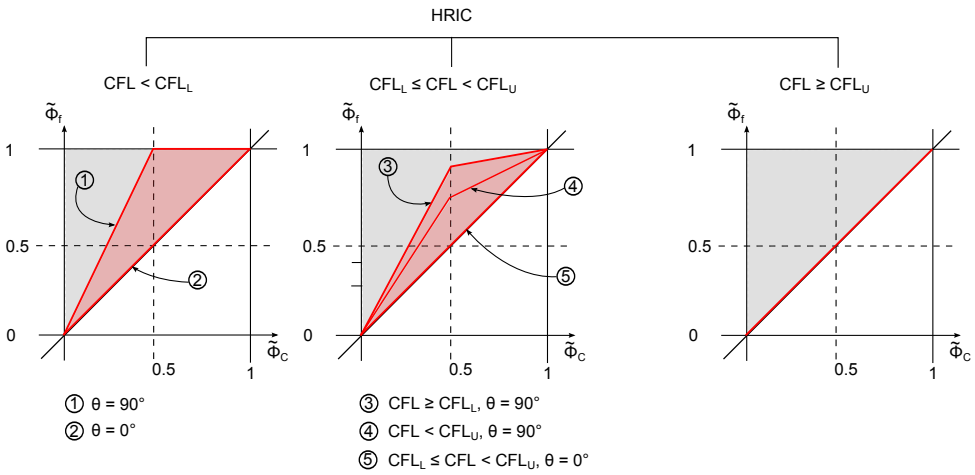

Figure 3.9: Depending on Courant number CFL and interface angle θ, the NVD of the High Resolution Capturing Scheme (HRIC) takes different forms. The left plot shows the scheme for CFL below the lower limiter CFL_L and for interface angles of 0° and 90°. The middle plot shows the scheme for CFL values between upper and lower limiter and again interface angles of 0° and 90°. The right plot visualizes the situation for CFL above the upper limiter. Here the HRIC scheme is reduced to a pure upwind differencing scheme, regardless of the interface angle.

shape of the wave a fraction of the volume in a cell is transported. The computational grid remains fixed, thus avoiding problems inherent to mesh deformation algorithms, for instance the possibility to produce negative Jacobians of the control volume which would be fatal for the simulation. Important topics for yacht hydrodynamics, as for instance motion of the boat and strong motions in seaways, can be implemented with reasonable effort. The conservative formulation of the method inherently guarantees mass conservation.

The biggest advantage of the method, the possibility to simulate complex and also non-sharp interfaces also holds some disadvantages. Since the shape of the surface is not sharply defined and transported, the interface is usually smeared out over 1 - 3 cells. This implies that the free surface shape cannot be absolutely exact and that the grid should be locally refined in the expected area of the free surface. Another problem is interface smearing. As shown above several approaches have been developed to overcome this problem. Also interface smearing should normally not occur when the necessary care has been taken during model set-up, it is intrinsic to the method that a sharp interface can never be completely guaranteed.

3.1.4. OVERVIEW OF EXISTING CODES

This section will give an overview of the development of free surface modeling techniques used in viscous flow codes, both commercially and academic, over the last decade. An practical method to do so is to review the participants at relevant conferences. Here the so called *CFD Workshop on Ship Hydrodynamics* is especially interesting. It focuses

on benchmarking of a variety of codes and validation and verification of simulation results against experimental data. The ship hulls used are three modern ship forms, the KRISO Tanker (KVLCC2), the KRISO Containership and the US Navy Combatant DTMB 5415. For all hulls Experimental Fluid Data (EFD) and geometries are publicly available. Since 1990 this workshop is held roughly every five years, alternating between Gothenburg and Tokyo as conference places. The Gothenburg 2000 workshop [100] was the second which saw a large number of codes which tried to derive the free surface wave pattern around the ship hull. A total of 17 codes were used for the simulations, with only one being of potential flow type. Several different methods were used to account for the free surface. The largest group used free surface fitting methods (7 codes, 41%). The second largest group (5, 29%) had no means to capture a dynamic free surface at all. The remaining participants used free surface modeling methods of Level-Set or Volume-of-Fluid type (2 each, 12%). So it can be easily concluded that at this time free-surface fitting methods were the most popular choice to model free surface interfaces. By the time of

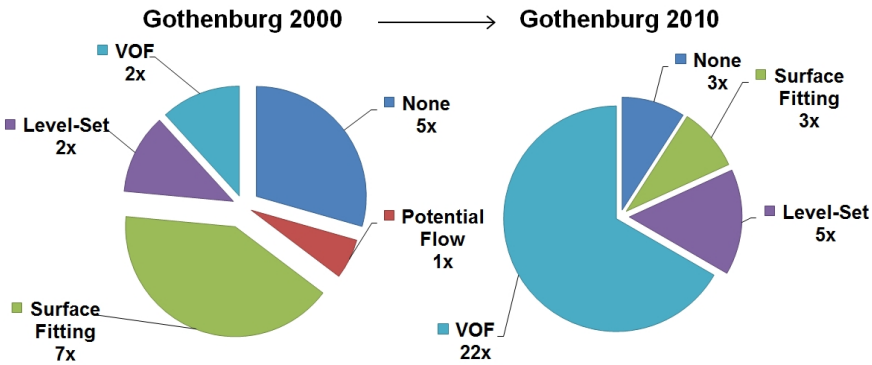

Figure 3.10: Development of Free Surface Modeling techniques used at the *Workshops on CFD in Ship Hydrodynamics*

the Gothenburg 2010 workshop [101, 102], this had changed dramatically. A comparison between those two workshops is illustrated in Figure 3.10. By now, the use of potential flow based free surface methods completely disappeared. Only 3 of 33 participants still used free-surface fitting methods (9%). Level-Set became slightly more popular and formed the second largest group (5 codes, 15%). The Volume-of-Fluid method became by far most popular choice. It was used by 22 participants thus representing the largest group (67%).

Table 3.1 gives an overview of the codes used in the workshop. In the author's opinion this list is also representative for the codes used in maritime CFD. It can be clearly seen that all major CFD codes use the VOF method. This is probably due to its general approach, easy implementation and robustness. Some smaller, specialized codes, often of non-industrial type, still use other methods, which can be sensible for special problems. In any case it can be concluded that the Volume-of-Fluid is currently the most popular surface modeling technique for ship hydrodynamics.

Although popularity and quality of a method are not the same, this is still an interesting result. Since the participants of the workshops represent some of the worlds's leading

Table 3.1: Overview of RANSE/FS codes

Organization	Code	Free Surface
IHI/Univ. Tokyo	WISDAM-UTokyo	Density function
MARIN	PARNASSOS	Free-surface fitting
IIHR	CFDShip-Iowa	Level set
MOERI	WAVIS	Level set
NMRI	SURF	Level set
ECN/HOE	ICARE	Nonlin. track
VTT	FINFLO	Nonlin. track
Kyushu University	RIAM-CMEN	THINC
ANSYS	FLUENT12.1	VOF
ANSYS	ANSYS CFX12.1	VOF
CD-Adapco	STAR-CCM+	VOF
CD-Adapco	COMET	VOF
ECN/CNRS	ISIS CFD	VOF
FLOWTECH	SHIPFLOW-VOF-4.3	VOF
HSVA	FreSCo+	VOF
NavyFOAM (NSWC/P S ARL)	NavyFOAM	VOF
SGI	OpenFOAM	VOF
NUMECA	FineMarine	VOF
MARIN	ReFreSCo	VOF

testing facilities, research institutes and CFD software developers one can assume that their choice of the VOF method has some authority. Nonetheless, it is not unlikely that the VOF method will also disappear in a few years, being replaced by a better methods.

3.1.5. CONCLUSIONS

In this section the theoretical aspects of the three most popular viscous free surface techniques have been reviewed. In the context of the successful application of this techniques to resolve yacht flow problems (see also Section 3.1.1), several criteria need to be fulfilled:

Generally, the technique must allow for correct resolution of waves resulting from the movement of the yacht through calm water. This includes allowance for modeling of breaking waves. In terms of marine hydrodynamics sailing yachts can be considered as *high speed vessels* since they are operating at Froude numbers between 0.4 to 1.0 and above. It is therefore necessary for free surface modeling techniques used in yacht hydrodynamics to account for plunging breaker (overturning waves) which occurs at these high speeds. It would also be advantageous to have the ability to account for formations of spray, which also occur at these high speeds. However, the latter does not seem to be mandatory. A further requirement is that the free surface modeling techniques does not form an insurmountable obstacle for the implementation of the motion of the yacht. Due to the propulsion by sail power, yacht hydrodynamics is highly dynamic, making it

necessary to account for dynamic trim and sinkage thus altering the position of the yacht in water surface fixed coordinate system.

At first glance *free surface fitting methods* seem to form an elegant solution to the problem of free surface simulation for yacht flows. The method has several big advantages, which include a sharp free surface interface, no vertical refinement in the expected area of the free surface, relatively coarse grids, the possibility to treat the problem as single phase flow, no time step size restrictions and the possibility to formulate the problem as steady state, making the method very fast. A deeper investigation of the pro and cons of free surface fitting methods reveals severe disadvantages. Intrinsic to its implementation is an inability of the method to deal with overturning waves (plunging breakers) and large topology changes which can occur near hull due to drift. It is also impossible to account for formation of spray. It is possible but challenging to include dynamic trim and sinkage. It is unknown to the author if the same holds true for larger changes like for instance heeling. The method is generally not recommended for large motions of the ship [62].

It is therefore clear, that although the advantages of free surface fitting methods are appealing, the disadvantages are too serious to consider them for the evaluation of yacht hydrodynamics.

Capturing methods with reconstruction, with their most prominent representative, the Level-Set-Method give a well defined representation of the free surface. In contrast to the free surface fitting method a refinement of the grid in the expected vicinity of the water surface is necessary, thus coming with a greater computational cost. It is possible to formulate these kind of methods as single phase flow, thus increasing stability of the solution. Contrary to free surface fitting methods, Level-Set-Methods allow for large deformations of the free surface, although overturning waves might be critical. A numerical disadvantage of the method is the need to reinitialize the function from time-to-time to retrieve mass conservation. On the other hand, the convection of the free surface as the iso-surface of a linearly varying function is easy to handle. Little can be found in literature about the implementation of ship motion, but even large motions should theoretically be possible although there might be some challenges related to mass conservation issues. The only topic of the criteria for yacht flow problems as stated above which the method cannot fulfill is the simulation of formations of spray. In the authors opinion this leads to an unphysical representation of overturning waves since these are normally accompanied by spray. However, this error might be of acceptable magnitude.

The third category, *capturing methods without reconstruction* is also represented by its most popular representative, the Volume-of-Fluid method. The Volume-of-Fluid method excels with its very general approach, easily allowing for large topology changes, overturning waves and, intrinsically, even for formations of spray. Motion of the yacht, be they small or large, are easily implemented and the conservative formulation of the method inherently guarantees mass conservation.

The general approach of the method also holds some disadvantages. The exact shape of the interface is not sharply defined and usually smeared over 1 - 3 cells. Therefore the grid has to be refined in the expected area of the free surface. This results in greater grid

sizes and smaller cells which lead to smaller time steps. Both effects raise the computational cost of the simulation. Convection of the volume fraction scalar defining the free surface interface is much harder to handle then for the Level-Set Method and if not correctly applied tends to smear the interface. However, although care has to be taken during modeling, the VOF method is the only one which fulfills all requirements to resolve the yacht flow problem.

In this section, three different techniques have been reviewed regarding their ability to resolve the free surface around yacht hulls. Of these three, *free surface fitting methods* have to be disregarded as unfit for this task. The remaining two methods, Volume-of-Fluid and Level-Set-Method, both seem to be adequate. However the Volume-of-Fluid Method gives the additional possibility to resolve formations of spray. Taking into account the findings of Section 3.1.4 which clearly showed that the VOF method can be considered as the currently most popular, the VOF method is chosen as the free surface modeling technique used in the remainder of this thesis.

3.2. OVERVIEW OF PRESENT METHODS IN AERODYNAMICS

The purpose of this section is to give an overview of the aerodynamics of sails and its impact on sail force modeling for a VPP. The first section will describe the peculiarities of sail aerodynamics in contrast to airplane aerodynamics while in Section 3.2.2 the non-uniform onset flow, which a sail experiences, will be described. Afterward Section 3.2.3 discusses different methods to determine sail force. The chapter ends with an review of sail force modeling for VPP and an overview of existing sail force models.

3.2.1. AERODYNAMICS OF SAILS

The flow around sails poses an interesting aerodynamic problem which is a subject of ongoing research. However, the general principles have been described in numerous publications including for example the works of Marchaj [5], Fossati [103, 104, 6] and Hansen [59]. In principle, the aerodynamics of flow around sails can be described by the thin airfoil theory as published by Abbott and Doenhoff [105] or Hoerner [106, 107]. Sails can thus be described as lifting bodies which create lift from fluid flow. A typical pressure distribution around an airfoil is shown in Figure 3.11. Any fluid force acting on 2D airfoil or a wing, which is a airfoil with finite length, can be expressed as non-dimensional force coefficient as follows:

$$C_F = \frac{F}{0.5\rho V^2 A_{ref}}, \tag{3.25}$$

with the relations between the constant 0.5, density ρ and flow speed V often expressed in terms of the dynamic pressure q yielding

$$q = 0.5\rho V^2. \tag{3.26}$$

The reference area A_{ref} can be chosen at will as long as it is used consistently. In aerodynamics it has become kind of a standard to use wing planform area at least for lift and induced drag. The wing planform is defined as $A_{ref} = c \cdot L$, with chord length c and wing span L. For frictional and viscous pressure drag it is would be appropriate to use the

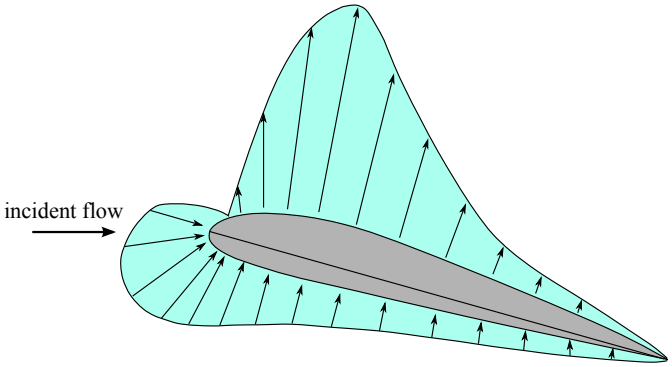

Figure 3.11: Pressure Distribution around airfoil. At the bottom surface of the airfoil, the pressure is higher than the freestream static pressure. For the top surface, the opposite holds true. Here the pressure is below the static freestream pressure. The pressure difference causes a force component perpendicular to the incident flow which is called lift

surface area as A_{ref}, however using planform area is also quite usual.
Moment coefficients C_M are obtained from any moment M in a way similar to force coefficients, but with additionally considering the chord length c.

$$C_M = \frac{M}{qA_{ref}c}. \tag{3.27}$$

Commonly forces acting on an airfoil are decomposed into lift and drag. There respective coefficients are mainly functions of the angle of the incident flow α. Here drag is acting in direction of the incident flow while lift is perpendicular to it. Measuring α for sails is difficult. Usually there are several sails on a boat which all have their individual α. Another problem is the deformation of the sails under load, especially the sail luff. Stay tension and variable mast bending also influences the measurement. Additionally, α will change over sail height due to twist of the sail. Therefore, instead of α, the apparent wind angle of a boat is commonly used. For details on apparent wind angle see Section 3.2.2.

Drag can be decomposed into several drag components. Skin friction and viscous pressure drag are usually combined into the drag at zero lift C_{D0}, commonly referred to as parasitic profile drag.

Added drag due to lift may be divided into induced drag Di and flow separation drag Ds. The separation drag coefficient C_{Ds} is defined as a function of C_L^2 and the c_s separation drag constant.

$$C_{Ds} = c_s C_L^2. \tag{3.28}$$

Literature [3] gives values of 0.016 - 0.019 for separation drag constant c_s. However, since it is hard to separate D_s and D_i both drag components are often combined in the induced drag. Induced drag is caused by pressure difference between suction and pressure side of a lifting three-dimensional wing. Due to this pressure difference, there has to be a flow around the wingtip from high pressure side to the low pressure side. This spanwise flow affects the flow all along the trailing edge as the flow leaves the high pressure

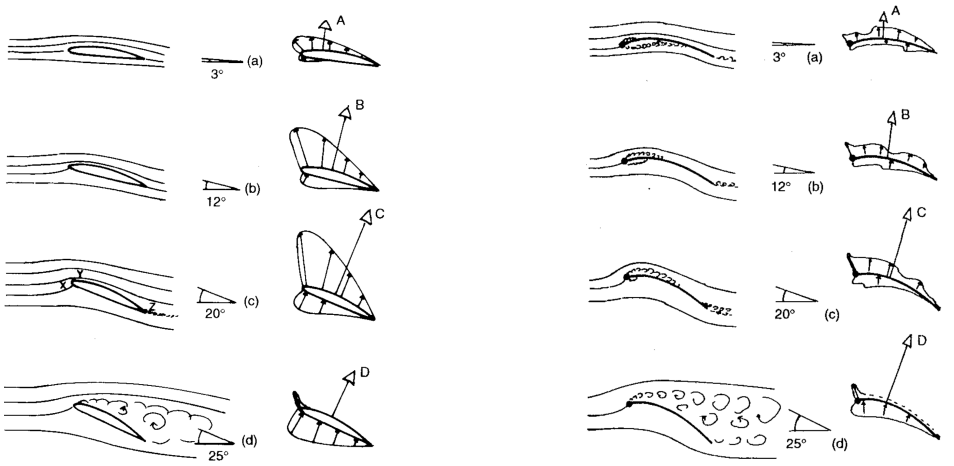

(a) wing profile (b) sail profile

Figure 3.12: Comparison of airflow and pressure distribution at different angles of attack (Source: Bethwaite [108]). The left side shows a modern airfoil, while the right side shows sail profile attached to a mast section. Due to the thinness of the sail profile, the difference in curvature of these profiles, especially at the high pressure side, is large. While modern aircraft mainly operate at operational angles where separation does not occur, this is not true for the sails. Here occurrence of separation cannot be avoided. Standard operational angles for sails are larger, normally around 12°.

side moving outward and the low pressure side moving inward. When these opposing flows reach the trailing edge, they result in a swirling motion which concentrates itself into a tip vortex. For a wing with two wing tips (two free edges), like on a airplane, two counter-rotating tip vortices can be observed. Obviously, the creation of tip vortices requires energy, which has to be transferred from the wing to the air. This energy transfer is called induced drag.

$$C_{Di} = \frac{C_L^2}{e\pi AR}, \tag{3.29}$$

with efficiency coefficient e and wing aspect ratio AR. AR is defined as the squared mast span divided by planform area A_{Sails}.

$$AR = \frac{s^2}{A_{Sails}}. \tag{3.30}$$

Combing the drag components yields the total drag coefficient C_D

$$C_D = C_{D0} + C_{Ds} + C_{Di} \tag{3.31}$$

Compared to the pressure distribution illustrated in Figure 3.11 there are several specific features to sail aerodynamics which significantly differ it from common airfoil aerodynamics. This includes the onset flow in which a sail operates, as well as the the properties of the sail itself which is almost infinite thin and so flexible that it is deformed by the surrounding flow. According to Bethwaite [108], sails are low speed wing sections like in

early planes and thus do not behave like modern airplane wings. The main differences are greater operational angles of attack and a larger curvature which combined with almost zero thickness lead to separated regions and stepped or reversed flow which would be unusual for an modern airfoil in operational state. Figure 3.12 illustrates the different airflows around a wing section and a sail profile which is attached to a mast section. It is noticeable that the flow around the wing section keeps completely attached up to angle of incidence of 20° (Figure 3.12(a)). Here first separation tendencies can be observed which start to move forward from the trailing edge. This is typical for high speed adverse pressure gradient separation on air- or hydrofoils. For an angle of attack α of 25° the wing profile is completely subject to adverse pressure gradient speration, commonly called stall. In contrast to that, the profile section in Figure (3.12(b)) is already showing a leading edge separation bubble at both pressure and suction side for $\alpha = 3°$. What one can see here is the occurrence of a *long separation bubble* separation which is classical associated with low-speed profiles and of totally different nature as the adverse pressure gradient separation observed in Figure 3.12(a). The presence of the (round) mast section in contrary to that the long separation bubble Figure 3.12(b) severely promotes the occurrence of the separation bubble which causes a redistribution of pressure outside the bubble. Due to this redistribution the sail profile has no forwardly directed suction. The miss of this suction is the reason why the maximum lift from the sail profile is smaller than for the airfoil on the left side. Apart from the separation at the suction side there is also separation occurring at the pressure side. Again, the presence of the mast is a major contributor to this separation bubble which reduces pressure. A third separation may occur at the free shear layer of the trailing edge. With increasing α the influence of the pressure side is more and more reduced, whilst the separation bubble on the suction side increases. For high α values the pressure side separation bubble finally vanishes whilst the suction side is completely separated and thus stalled. A detailed sketch of the flow properties around a conventional sail-mast combination is given in Figure 3.13.

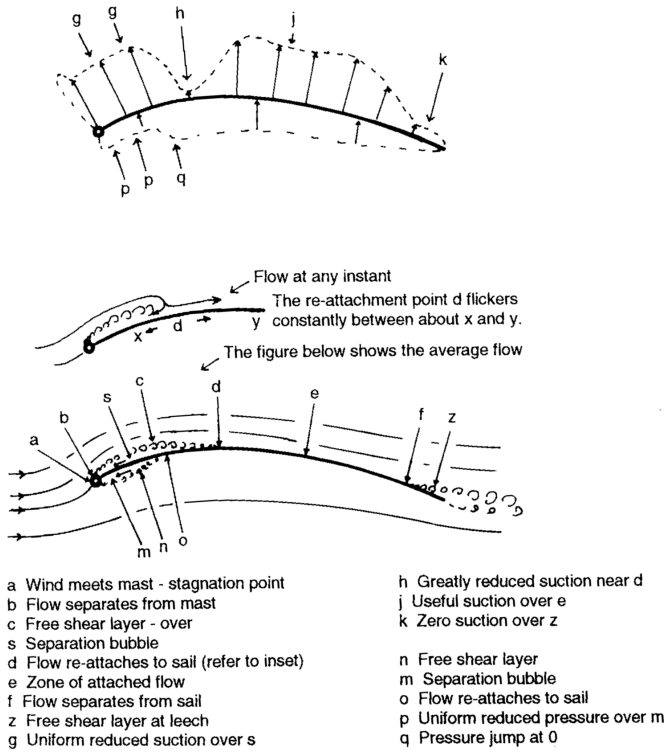

Figure 3.13: Flow and pressure distribution around conventional sail-mast combination (Source: Bethwaite [108]). The figure illustrates the separation zones typical occurring on a standard main sail and their influence on pressure. It shows that the mast section has a big influence on the occurrence of two separation bubbles, which significantly decrease the effectiveness of the sail. To a certain degree, these separations could be avoided by the use of a rotating wing mast.

3.2.2. STRUCTURE OF THE APPARENT WIND

In this section the structure of the apparent wind a boat experiences while sailing will be discussed. For a sailing boat, several physical phenomena influence the onset flow which it experiences. For wings, we assume that the air is at rest and incoming velocity is due to the speed of the aircraft. For sails, this is different. There must be wind and we have the movement and rotation of the boat.

ATMOSPHERIC BOUNDARY LAYER

The flow a sail encounters in a natural environment is not uniform. Instead it is subject to a vertical speed gradient which is called the Atmospheric Boundary Layer (ABL) as illustrated in Figure 3.14. The ABL arises from the friction between the water and the air blowing over it. In principle, it is a classical boundary layer with zero wind speed at the water surface and a increase in wind speed until it reaches the undisturbed speed at the height of the free atmosphere. For yacht sails only the lowest portion of the boundary layer is of interest and effects like Coriolis Force and centrifugal forces can be neglected, the latter ones only being of interest for meteorological purposes or very large structures. According to Bethwaite [108], the ABL at low wind speeds is of laminar type with heights varying from 10 m to maximum of 100 m, while for turbulent breezes the height ranges from 500 m up to 300 m in strong winds. For comparison, the boundary layer on a sail varies from approximately 5 mm at the leading edge to 25 mm at the trailing edge.

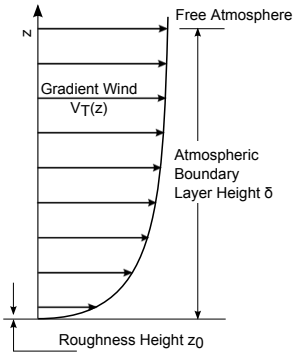

Figure 3.14: Atmospheric Boundary Layer (APL), where z_0 is the roughness height, z denotes the height above water and $V(z)$ is true wind speed as a function of z. The roughness height z_0 is a constant which describes the roughness of the surface over which the wind blows, see Table 3.15.

In order to determine the vertical gradient of the true wind for yacht sails, it is sufficient to use empirical velocity profiles, for example the logarithmic wind law as shown in (3.32). Here V_T denotes the true wind speed which is normally known at a reference height z_{ref} as an input parameter for the purpose of determining variation of V_T with height for yacht sails.

$$V_T(z) = V_T\left(z_{ref}\right) \frac{ln\left(z/z_0\right)}{ln\left(z_{ref}/z_0\right)}. \tag{3.32}$$

According to (3.32), $V_T(z)$ not only depends on the reference heigth z_{ref}, but also on the so called Equivalent Grain Roughness z_0. The coefficient z_0 accounts for the roughness

of the surface over which the wind blows. Common values for z_0 are given in Table 3.15 which shows that the roughness parameters varies by several orders of magnitude between urban areas and water. The effect of these different parameters on the vertical speed gradient of the ABL is shown in Figure 3.16. $V_T(z)$ has been calculated exemplary for all roughness coefficient in table 3.15 for a wind speed of 5 m/s at a reference height of 10 m. This reference height is the one commonly used for weather reports. It can be seen from Figure 3.16 that due to the higher surface roughness, friction is much larger on urban areas thus causing a slower increase in speed and larger boundary layer height. Over a water surface, however, the speed increase with height is much faster resulting in a smaller overall boundary layer height and smaller vertical speed differences after the first few meters. Nonetheless, the speed gradient is still of such an order that it has to be taken into account whilst looking at airflow around sails.

Surface Area	z_0 [m]
Land	5.0×10^{-2}
Cities & Urban Areas	5.5×10^{-1}
Wood	5.5×10^{-1}
Water	1.0×10^{-4}

Figure 3.15: Characteristic surface roughness parameters for typical land and sea surfaces.

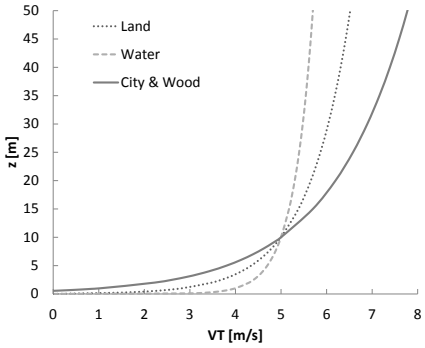

Figure 3.16: Vertical speed gradient for wind blowing over surfaces with different levels of roughness. Due to the relative smoothness of the water, the vertical speed distribution for wind flowing over it converges fastest towards the undisturbed wind speed.

APPARENT WIND TRIANGLE

A second important influence on the onset flow a sail experiences is the speed of the boat itself. As the boat moves trough the water it experiences an additional vector component of the wind with magnitude of its velocity. Figure 3.17(a) illustrates how the vectors true wind speed V_T and boat velocity V_S add up to form the so called apparent wind speed V_A. Angles β_T and β_A represent true and apparent wind angles with respect to the movement direction of the boat whilst γ_s and α show the leeway angle of the yacht and the angle of incidence of the sail chord. Figure 3.17(a) yields that a yacht beating to windward experiences an apparent wind which is of larger magnitude than the true wind speed and of smaller wind angle. For a boat on a broad reach or running downwind the opposite holds true. Figure 3.17(b) shows that with decreasing mast height the true wind speed also decrease due to the ABL thus increasing the impact of boat speed on apparent wind speed. This leads to an decrease of apparent wind speed magnitude and a smaller apparent wind angle β_T which becomes more afore. This overall variation of

the onset flow a yacht experiences due to the presence of ABL and boat speed is called *twist* or *twisted flow*. The effects illustrated in Figure 3.17(a) and (b) combined with simple trigonometry lead to equations (3.33) and (3.34) for apparent wind speed $V_A(z)$ and apparent wind angle $\beta_A(z)$.

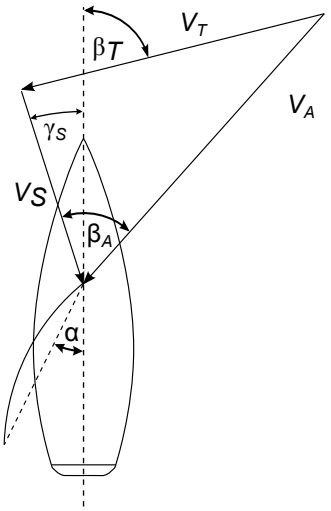

(a) The Apparant Wind Triangle, where V_T and V_A denote true and apparent wind speed and β_T and β_A their respective angles. The boat speed is given by V_S, whilst its leeway angle is γ_S. Angle of incidence of the sail chord is denoted α.

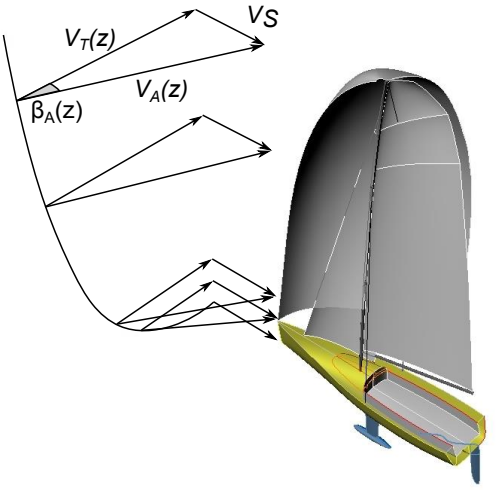

(b) Twisted onset flow on Sailing Yacht. The boat speed V_S, in combination with the height depended true wind speed $V_T(z)$, causes a twist in the apparent wind speed $V_A(z)$ and wind angle $\beta_A(z)$ the boat experiences, which is therefore also a function of height z

Figure 3.17: Effects of ABL and Boat Speed on Apparent Wind

$$V_A(z) = \sqrt{\left(V_T(z)\cos\beta_T + V_S\right)^2 + \left(V_T(z)\sin\beta_T\right)^2}, \tag{3.33}$$

$$\beta_A(z) = \arctan\frac{V_T(z)\sin\beta_T}{V_T(z)\cos\beta_T + V_S}. \tag{3.34}$$

It has to be mentioned that these equations include the simplification that leeway angles are very small and their influence on apparent wind can be neglected. A further simplification is that at the current stage these equations only describe an upright boat without heel. Effects of heel will be discussed in Section 3.2.2.

The differences in apparent wind speed and twist profiles are illustrated in Figure 3.18 for characteristic upwind and downwind β_T of 40° respective 160°. Vertical speed and twist profile have both been normalized with mast height. It can be seen that the differences for the various boat types are quite pronounced. Generally, speed and twist variations are more pronounced on slower boats like the ACCV5 than on faster ones (e.g.

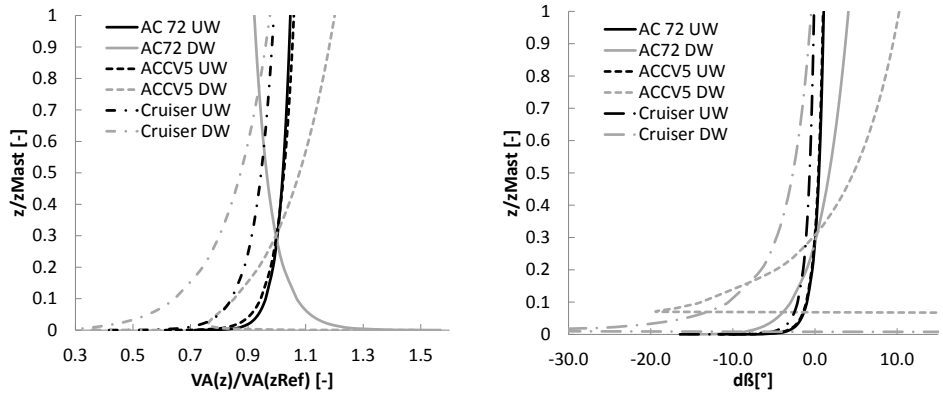

(a) Speed gradient

(b) Twist profile

Figure 3.18: Figure a) and b) show the comparison of speed gradient and twist of onset flow for various boat types in upwind and downwind conditions. The compared boat types are two monohulls, a standard cruiser, a America's Cup Class V5 boat, and a mulithull of America's Cup 72 class.

AC72) and occurs stronger in downwind than in upwind conditions. Furthermore, the effects are greater on boats with smaller masts like the common cruiser than they are on boats with taller ones.

EFFECTIVE ANGLE THEORY

Section 3.2.2 and 3.2.2 showed the influence of ABL and boat speed on the structure of the apparent wind for an *upright* sailing boat without heel and pitch. However, it is fact that sail boats, especially monohulls, heel significantly while using sails as propulsion methods. The effect of heel on onset flow thus has to be considered to get the *effective apparent wind* a yacht experiences. Effects of pitch are also present, but are of much smaller scale and therefore can be neglected if simplification is sought. However, Fossati [109, 110, 111] and Gerhardt [112, 113] showed that the effect of pitch becomes important when using unsteady sail force models, e.g. for dynamic velocity predictions including seakeeping. Regarding the effect of heel, Kerwin [3] stated the *Effective Angle Theory* assuming that the sails can be considered insensitive to the component of the incident flow direct up the mast and thus only the flow component perpendicular to span contributes to lift and drag forces. Kerwins theory has been derived from aircraft wing theory and as will be explicated later in this section, there is strong evidence that it also holds true for flexible sails. Since the effective angle theory implies that only the portion on the incident flow in the plane perpendicular to mast span is of interest, one is able to derive an effective apparent wind speed v_{AE} and and effective apparent wind angle β_{AE} (Figure 3.19). This has the advantage that sail lift and drag coefficient are now not functions of heel.

In the following, the transformation from *upright* apparent wind $\boldsymbol{v_A}$ to *effective* apparent wind $\boldsymbol{v_{AE}}$ is written in vector form. The apparent wind vector $\boldsymbol{v_A}$ in the world

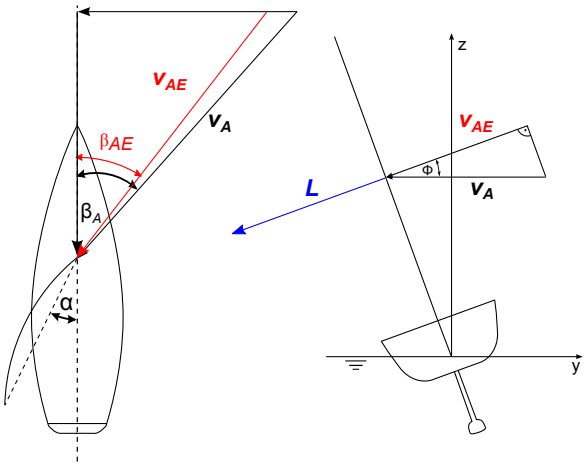

Figure 3.19: Effect of heel on a apparent wind $\mathbf{V_A}$ according to the Effective Angle Theory

coordinate system is given as:

$$\boldsymbol{v_A} = v_A \begin{bmatrix} -\cos\beta_A \\ \sin\beta_A \\ 0 \end{bmatrix}. \tag{3.35}$$

The rotational transformation matrix $\boldsymbol{T}$ for the transformation from upright (world) to heeled (yacht) coordinate system (CSYS) yields

$$\boldsymbol{T} = \begin{bmatrix} 1 & 0 & 0 \\ 0 & \cos\phi & -\sin\phi \\ 0 & \sin\phi & \cos\phi \end{bmatrix}, \tag{3.36}$$

with ϕ being the heel angle of the yacht. The *effective* apparent wind vector $\boldsymbol{v_{AE}}$ is then given by:

$$\boldsymbol{v_{AE}} = \boldsymbol{T}^{-1}\boldsymbol{v_A}. \tag{3.37}$$

Effective apparent wind speed v_{AE} and angle β_{AE} are then easily derived from (3.37) as:

$$v_{AE} = \sqrt{v_{AEx}^2 + v_{AEy}^2}, \tag{3.38}$$

$$\beta_{AE} = \arctan\frac{v_{AEy}}{-v_{AEx}}. \tag{3.39}$$

Expanding v_{AEx} and v_{AEy} with the components from rotational matrix as well as true wind angle β_T and height depended true wind speed $v_T(z)$ yields (3.40) for effective apparent wind speed and (3.41) for effective apparent wind angle.

$$v_{AE}(z) = \sqrt{\left(v_T(z)\cos\beta_T + v_S\right)^2 + \left(v_T(z)\sin\beta_T\cos\phi\right)^2}, \tag{3.40}$$

$$\beta_{AE}(z) = \arctan \frac{V_T(z)\sin\beta_T \cos\phi}{V_T(z)\cos\beta_T + V_S}. \tag{3.41}$$

Kerwins effective angle theory, which states that in terms of lift and drag sails are only sensitive to incident flow in the plane perpendicular to mast span, has been topic of scientific research. Marchaj [114] conducted tests on a Dragon rig. The tests were conducted at fixed trim and several angles of heel. Results were processed into lift coefficients and divided by the cosine of the heel. Marchajs results are shown in Figure 3.20. The wind tunnel tests conducted by Marchaj and subsequent analysis by Jackson [115, 46] showed that the assumption of the effective angle theory are sufficiently accurate to resemble effects of heel on onset flow of the sails and thus aerodynamic lift and drag. Further analysis by Hansen [59] revealed some secondary effects not captured by the effective angle theory, however these were of magnitudes such that they reduced boat speed V_s by less than 1% and thus are generally neglected.

It is a general convention that the terms apparent wind speed V_A and angle β_A are used to describe the *effective* apparent wind speed and angle. This convention is followed in this thesis and the subscript E is omitted from here on.

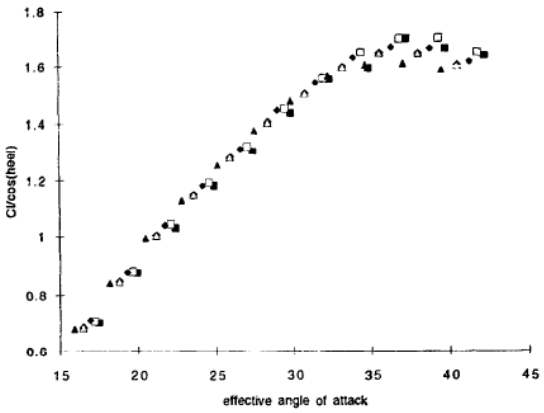

Figure 3.20: Variation of Lift with effective angle at fixed trim and several heel angles (Marchaj [114]).

3.2.3. AERODYNAMIC FORCE MODELS

The purpose of an aerodynamic force model is to create the possibility to link the aerodynamic forces and moments originating from the individual sail characteristics to the hydrodynamic model of a VPP. Therefore, any suitable sail force models must account for sail forces with respect to boat speed, heel angle and environmental wind conditions as well sail characteristics like sail area, sail planform, sail shape and also interaction of sails. The principles of fluid dynamics require every force coefficient to take the following form:

$$C_{Force} = \frac{Force}{qA} = C_{Force}\left(\beta_a, \phi, sailplan, shape\right) \tag{3.42}$$

Equation (3.42) yields that every sail force coefficient has to be described not only by several variables regarding the incident flow (dynamic pressure q, Apparent wind angle β_A and heel angle ϕ) but also by several parameters describing the shape of the sail itself. These shape parameters are:

- *sailplan*, which is a set of ratios which is fixed for a given set of sails, e.g. sail area, girth dimensions, etc.
- *shape*, an additional set to represent changes of the flying shape due to the action of the trimmers.

Jackson [46] pointed out that several additional parameters exist, e.g. sail tissue weight, sail stretch and viscosity. Since these are commonly regarded as 2nd order effects, they are usually neglected. In general there a two possibilities to model aerodynamic force models for VPPs. The first is to find force coefficients for explicit sail *shapes*. This means that a test matrix covering all possible shapes of the sails need to be examined and the VPP then finds the optimal shape for the actual combination of environmental wind and boat state. This approach has the advantage that force coefficients of individual sails can be precisely described and effects like depowering due to trim can be included. This approach implies that the sails are kept rigid and a loop is performed over all possible shapes *one thinks* the sail could have. This brings an enormous simplification for the CFD simulation but gives the problem that sail shapes cannot be related to trim settings. Even more problematic is that since pressure distribution for a given shape has to be in equilibrium with membrane stress distribution one has no guarantee that the tested sail shapes can be reproduced in reality by a sail cut. Generally speaking, the main problem for a sail force model using explicit sail shape description is the sheer number of possible shape permutations necessary to find force coefficients for relative positions of sails and vertical distribution of chord, draft and camber of the individual sails. Therefore the use of explicit sail shapes to define a sail force model is usually restricted to the better funded yacht programs like America's Cup and Volvo Ocean Race campaigns or big maxi racers. Examples of this method can be found in Day [116], Euerle and Greeley [117] and Korpus [57]. Given the problems outlined above, ways are sought to describe sail shapes with fewer variables. Therefore description is changed from sail *shape* to sail *trim*. One is now able to directly describe explicit sail shapes by including common trim parameters known from yacht racing like sheet length, traveler angle, etc. These parameters could well be used to describe a sail trim in a wind tunnel. Unfortunately the same does not hold true for CFD simulations since the trim parameters do not give the necessary input to describe the shape of the sail which would be needed as geometry for the calculation. To overcome this problem, one can account for the flexibility of real sails by performing an FSI simulation. Besides the challenging structural part, the CFD method must be able to cope with deformations of the computational grid due to displacement of the sail. Depending on the CFD method used, trim states acquired almost instantaneous in the wind tunnel will take from several minutes up to hours of computational time. However, this sail force model described by explicit sail trims still needs a large number of variables to cover the full range of aerodynamic states a sail could take. To reduce the number of variables involved, one can change to an implicit description of sail trims. This means, only one optimal sail trim has to be found and sail trim actions which

derive from this sail trim, like twisting (depowering), are accounted for by a penalty. This way the number of investigations are greatly reduced, making this approach more fit for engineering practice. The fundamental difference of this approach is that no attempt is made to link the aerodynamics of sails to their actual shape. This way of modeling aerodynamic forces has first been developed by Kerwin [3, 4] during the Pratt Project. Most of the modern quasi-steady sail force model can trace their origin back to the Kerwin model, so the model and its derivatives are still widely used today.

Regardless which of the approaches described above is chosen, a suitable aerodynamic force model should:

- give aerodynamic lift, drag and resulting heel moment for any combination of apparent wind and trim;
- be based on a sound aerodynamic theory;
- use the least possible number of parameters to describe effects of sail trim;
- use only parameters which are applicable in full scale, wind tunnel testing and CFD;
- permit to derive the best sail from performance optimization.

In the author's view currently the only feasible approach to associate parameters describing sail shapes with their actual aerodynamic performance is to use implicit measures of sail trim, for example extensions of the *Kerwin* model. In the following, this model is described in detail.

3.2.4. KERWIN / HAZEN / IMS MODEL

The first modern aerodynamic sail force model which could be used in a VPP has been derived by Kerwin. It incorporates two parameters, *flat* and *reef*, to account for deviations from optimal trim in order to reduce the heeling moment. The model has been widely used and extended to include improvements of the description of the underlying physics. A major contributions has been made by Hazen [118] whose model forms the base of the International Measurement System model (IMS). Descriptions of the model may be found in Poor and Sironi [119] and van Oossanen [120]. Changes in the IMS-VPP until 1999 are summarized by Claughton [45]. Rule changes regarding Spinnaker rating are found in Teeters [47] while more recent progress is reported in Claughton [49] and the ORC VPP documentation [121].

In 1980, Hazen [118] reanalyzed the Bay Bea sail measurement data, named after the yacht from which they were obtained, and managed to isolate coefficients for five sails including main, jib, mizzen and mizzen stay sail as functions of apparent wind angle β_A. These coefficients could now be used to integrate sails of varying sizes and geometry into a velocity prediction program making it a semi-empirical model. The underlying assumption to this approach is that the sails interact in a way that an increase in force on one sail is counterbalanced by a decrease on another. As Hazen points out, this is not exactly what happens in reality, but the simplification gained is worth the small incorrectness in physics.

By applying aerodynamic theory of finite wings Hazen separated the total drag into three components, namely viscous profile drag C_{Dp}, induced drag C_{Di} and windage C_{D0}.

$$C_D = C_{Dp} + C_{Di} + C_{D0} \tag{3.43}$$

The general form of the governing equations of the sail force model is shown below.

$$C_L = flat\ reef^2\ C_{Lmax}(\beta_A), \tag{3.44}$$

$$C_D = C_{Dp}(\beta_A)\ reef^2 + CE\ flat^2\ C^2_{Lmax}(\beta_A)\ reef^2, \tag{3.45}$$

$$CE = KPP + \frac{1}{\pi\ AR_{eff}}, \tag{3.46}$$

$$C_M = reef\ ZCE\ C_S. \tag{3.47}$$

with moment coefficient C_M as function of vertical center of effort ZCE of the sail forces times side force coefficient C_S which is derived from lift and drag coefficients C_L and C_D, respectively. The induced drag is assumed to be proportional to lift squared and inversely proportional to the rig aspect ratio. Trim parameters *flat* and *reef* may take values between 0 and 1. Their impact on the overall results will be discussed later in this section.

In order to take into account the contribution of the individual sails to the total sail force, one has to calculate a set of *aggregate sail coefficients*. The reference sail area A_{ref} for this aggregate sail coefficients is calculated as the sum of the individual sail areas A_i.

$$A_{ref} = \sum_{i=1} A_i. \tag{3.48}$$

The aggregate sail coefficients can than be calculated with the contributions of the individual sails as follows:

$$C_L = \sum_{i=1} \frac{C_{Li} B_i A_i}{A_{ref}}, \tag{3.49}$$

$$C_{Dp} = \sum_{i=1} \frac{C_{Dpi} B_i A_i}{A_{ref}}, \tag{3.50}$$

where B_i is a blanketing factor which is usually assumed to be $B_i = 1$ for all i. For the vertical center of effort of the sail set this yields

$$ZCE = \sum_{i=1} \frac{ZCE_i \sqrt{C^2_{Li} + C^2_{Dpi}} B_i A_i}{A_{ref} \sqrt{C^2_L + C^2_{Dp}}}, \tag{3.51}$$

with ZCE_i as the vertical distance of the geometrical center of area of the individual sail from the waterline of the boat.

The quadratic parasite drag coefficient KPP for the compound sail set is calculated as follows

$$KPP = \sum_{i=1} \frac{KPP_i C^2_{Li} B_i A_i}{A_{Ref} C^2_L}, \tag{3.52}$$

to complete the equations for lift and drag coefficients one has to calculate the efficiency coefficient CE according to equation (3.46). To calculate this function one needs to know the effective rig aspect ratio AR_{eff} which is calculated as follows

$$AR_{eff} = \begin{cases} \frac{(1.1H_{eff})^2}{A_{ref}} & \text{if } \beta_A \leq 90° \\ \\ \frac{(Heff)^2}{A_{ref}} & \text{else where} \end{cases} \tag{3.53}$$

with a constant of 1.1 accounting for mirroring span while sailing close hauled. The effective height H_{eff} in (3.53) is merely an effective geometric height from the waterline to the suspension point of the (highest) sail. The sail force model is now able to describe lift and drag and thus heeling moment with respect to apparent wind. Lift and drag can be transformed into force components acting in the yacht fixed coordinate system yielding

$$\boldsymbol{F_S} = 0.5\rho A_{Ref} \boldsymbol{v_A^2} \begin{bmatrix} -\cos\beta_A \sin\beta_A \\ \sin\beta_A \cos\beta_A \end{bmatrix} \begin{bmatrix} C_D \\ C_L \end{bmatrix}, \tag{3.54}$$

for the sail force vector $\boldsymbol{F_S}$. Optimization to maximize yacht performance within the VPP is driven by the trim parameters $flat$ and $reef$ which theoretically may adopt values between 0 - 1. A reduction of $flat$ yields an linear reduction of lift and a quadratic reduction of drag. The reduction of lift is responsible for the reduction of heeling moment whilst the quadratic reduction of drag contains the drag penalty for deviation from optimum span-wise loading of the sail set. As Figure 3.21 illustrates, $flat$ allows force coefficient variations only along the C_D vs. C_L^2 curve. Effects of trimming to move the sail center of effort are not considered, which is not necessarily the same as in reality. $reef$, however can be considered more as an geometric than an aerodynamic factor. The main criticism on its formulation is that it changes all sail dimensions by scaling them equally whilst in reality one would expect discrete steps here, e.g. a smaller Jib with the same main. In contrast to $flat$, $reef$ lowers ZCE thus reducing heeling moment by reducing ZCE and side force C_S simultaneously. As Figure 3.22 demonstrates, $reef$ equally reduces C_D and C_L without adding a drag penalty for derivation from optimum sail trim which is also not correctly modeled. Despite this criticism, the model is still successfully used today. Reports about attempts to improve the model can be constantly found in literature, for example, the addition of a twist function to add variation of ZCE within the flat parameter in the 2012 Edition of the IMS VPP. Some derivatives of the model which imply larger changes are described in the Appendix A.

Despite its deficiencies, the *Kerwin* model has shown its capability of modeling sail forces to be used for performance prediction of sailing boats. The main objective of this thesis is to develop a VPP with a hydrodynamic model directly coupled to a flow solver. Therefore, the absolute accuracy of the aerodynamic force model is of minor importance, as long as it allows comparison of the RANSE-VPP with conventional VPPs. With this in mind, a *Kerwin* based sail force model is chosen for the modeling of the RANSE-VPP.

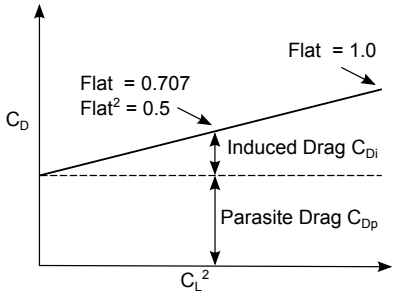

Figure 3.21: Influence of $flat$ parameter on drag and lift coefficient.

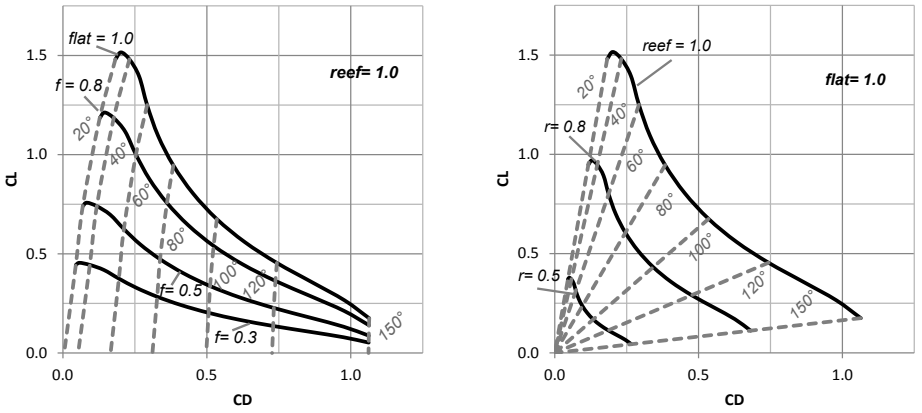

(a) Polar Plot with flattening

(b) reefing Effects on $C_D - C_L$

Figure 3.22: Effects of flat and reef parameters on C_L and C_D

4

MATHEMATICAL MODEL

4.1. STANDARD MATHEMATICAL MODELS FOR CONVENTIONAL VPPS

Velocity Prediction Programs calculate the equilibrium of aero- and hydrodynamic forces for certain wind conditions and then optimize for boat speed. Conventional monohull VPPs allow from 2-Degree-of-Freedom (DOF) to 4-DOF. Here VPPs of 2-DOF type usually only take into account resistance force F_x and heeling moment M_x, whilst 4-DOF types additionally account for side force F_y and yawing moment M_z. Vertical sail force F_z and resulting pitching moment M_y are usually accounted for during evaluation of hydrodynamic data and can thus be neglected in the VPP. Various theoretical models exist. The theory described here shows a approach based on the example of *AVPP* (Graf and Böhm [48]), an in-house development of the *Yacht Research Unit Kiel*.

4.1.1. COORDINATE SYSTEM

The coordinate system for this VPP approach is shown in Figure 4.1. Two right-hand coordinate systems are used to describe a yacht.

One is a yacht attached, geometric reference system (GRS) defined by x,y,z. Its x-axis corresponds to the yacht centreline, pointing astern, y-axis is pointing to starboard and z-axis upward in direction the mast. All modeling is done in this reference system.

The second system is a state reference system (SRS), defined by X,Y,Z, which corresponds to flow direction and hydrostatic forces. Its X-axis points into the direction of the

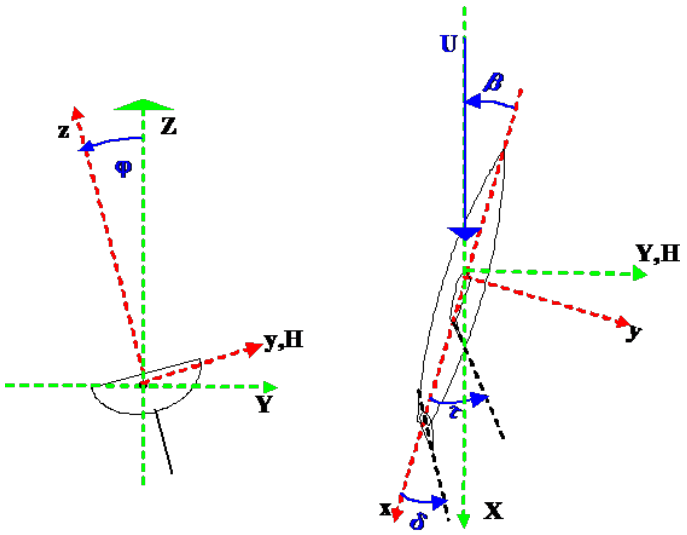

Figure 4.1: Coordinate system used for the VPP approach. State reference system (SRS) XYZ is described by the green lines, while the Geometric reference system (GRS) xyz is shown as red lines. U denotes the hydrodynamic flow with the leeway angle β to the yacht. Rudder and tab angle are denote by δ and τ, respective.

hydrodynamic flow and its Y-axis is parallel to the undisturbed water surface. Z-axis is pointing upwards.

As an additional coordinate, H is perpendicular to X and the span of mast and hull appendages, thus pointing in the direction of lift.

4.1.2. HYDRODYNAMIC MODEL

The hydrodynamic model describes the method to calculate forces and moments for the given degrees of freedom for any combination of values of the state variables, including *off-equilibrium* states of the yacht. This is necessary to allow proper interpolation within the solution algorithm. The hydrodynamic model is based on dimensionless hydrodynamic coefficients, which can be derived from towing tank tests or any other suitable source. To reduce the effort of generating hydrodynamic data without compromising accuracy, it is desirable to have a test matrix which is more dense in the region of to sailable states and less dense for off-equilibrium ones. Within the VPP procedure described here, this is addressed by using an *equilibrium state guess* around which all towing tank-tests are centered. The equilibrium state guess (ESG) defines rudder angle δ_0 and tab angle τ_0 depending on heeling angle:

$$\delta_0 = f(\phi), \tau_0 = f(\phi). \tag{4.1}$$

ESG is defined as a table and approximated with a spline function during calculations. The total hydrodynamic force in X-direction is the resistance: $F_X = R_{Tot}$. It is calculated

using:

$$R_{Tot} = R_U + R_H + R_I + \sum R_{PP}. \tag{4.2}$$

Here R_{Tot} is total resistance, R_U upright resistance at non-lifting condition, R_H added resistance due to heel, R_I induced resistance due to production of lift and $\sum R_{PP}$ parasitic profile drag of blade and rudder profile.

R_U is defined as a table $R_U = f(U)$ derived from towing tank results. R_H is defined as a table $r_H = R_H/R_U = f(U,\phi)$ as a fraction of R_U. Induced resistance R_I is calculated from base induced resistance $R_{I\beta}$ at rudder angle $\delta = \delta_0$ and tab angle $\tau = \tau_0$ and additional induced resistance components for deviations of rudder and tab angle from ESG-values:

$$R_I = R_{I\beta} + R_{I\delta} + R_{I\tau}. \tag{4.3}$$

Simple superposition is sufficient here since $R_{I\delta}$ and $R_{I\tau}$ can be assumed to be small for proper ESG. $R_{I\beta}$ is calculated using effective draft $T_{E\beta}$ of yacht's canoe body and appendages arranged under the canoe body:

$$R_{I\beta} = \frac{F_{H\beta}^2}{T_{E\beta}^2 0.5\rho U^2 \pi}, \tag{4.4}$$

where $F_{H\beta}$ is the heeling force acting in H-direction (lift perpendicular on flow direction and span). ρ is fluid density and $T_{E\beta}$ is the effective draft. The base effective draft $T_{E\beta}$ is derived from towing tank test results as approximation of $\partial F_x/\partial F_H^2$, see Figure 4.3. It is defined as functions $t_{E\beta} = T_{E\beta}/T = f(U,\phi)$, where T is the geometric draft of the yacht. Heeling force $F_{H\beta}$ is calculated from:

$$F_{H\beta} = \left(f_{H0} + \frac{\partial f_H}{\partial \beta}\beta\right) 0.5\rho U^2 \nabla_{CB}^{2/3}, \tag{4.5}$$

where ∇_{CB} is canoe body's buoyancy and f_H is the heeling force coefficient. f_{H0} is the heeling force coefficient at zero leeway, $\frac{\partial f_H}{\partial \beta}$ its gradient with respect to β, both at base rudder and tab angle δ_0 and τ_0. A table generated from towing tank data supplies $f_{H0}(U,\phi)$ and $\frac{\partial f_H}{\partial \beta}(U,\phi)$. For small deviations of rudder and tab angle from ESG-values some heeling force corrections are calculated as follows:

$$F_{H\delta} = \frac{\partial f_H}{\partial \delta}(\delta - \delta_0) \text{ and } F_{H\tau} = \frac{\partial f_H}{\partial \tau}(\tau - \tau_0). \tag{4.6}$$

Derivatives $\frac{\partial f_H}{\partial \delta}$ and $\frac{\partial f_H}{\partial \tau}$ are derived from towing tank test results as function of heeling angle ϕ only. Total heeling force F_H is calculated from:

$$F_H = F_{H\beta} + F_{H\delta} + F_{H\tau}. \tag{4.7}$$

For deviations of rudder and tab angles from ESG-values additional induced resistance is calculated as follows:

$$R_{I\delta} = \frac{F_{H\delta}^2}{T_{E\delta}^2 0.5\rho U^2 \pi}, \tag{4.8}$$

$$R_{I\tau} = \frac{F_{H\tau}^2}{T_{E\tau}^2 0.5\rho U^2 \pi}, \tag{4.9}$$

$t_{E\delta} = T_{E\delta}(\phi)/T$ and $t_{E\tau} = T_{E\tau}(\phi)/T$ are given tabulated data, derived from towing tank data or, alternately, calculated using empirical formulations. The decomposition of induced resistance as applied here neglects some non-linearity. In addition, a situation where total side force F_H is lower than base side force $F_{H\beta}$ induced resistance of rudder and tab are modeled incorrectly. However this can be avoided with proper ESG-values. Moments are calculated around x- and Z-axis as follows:

$$M_z = \left(F_{H\beta} LCE_\beta + F_{H\delta} LCE_\delta + F_{H\tau} LCE_\tau\right) \cos\phi. \tag{4.10}$$

LCE_β / L_{Ref} and respective values for δ and τ are tabulated functions of ϕ to be derived from towing tank test data.

$$M_x = F_y VCE = F_H VCE / \cos\beta. \tag{4.11}$$

Here the transformation $F_y = F_H / \cos\beta$ assumes small leeway angles and resistance to be smaller than side forces. It is also assumed that a wing only generates resistance in flow direction and lift perpendicular to flow force direction and span (no flow forces are generated in the direction of span). The vertical centre of efficiency VCE is assumed to depend on ϕ only, being independent of distribution of side forces on keel, rudder and tab. It is given as a tabulated function. For total moment around X-axis, the hydrostatic moment $M_{xRighting}$ has to be added:

$$\begin{aligned} M_{xR} = &- \left(h\left(|\phi|\right) \nabla_{CB}\, g\, \rho \right. \\ &+ m_{crew}\, g\, h_{crew} \cos(\phi) \min\left(1, \frac{|\phi|}{6}\right) \\ &\left. + M_{RDyn}\right) sgn(\phi) \end{aligned} \tag{4.12}$$

Here ϕ is the heeling angle in degree, h is hydrostatic righting arm, m_{crew} and h_{crew} are crew mass and crew arm respectively. It is assumed that crew righting moment applies fractionally only for heeling angles less than 6°.

4.1.3. DERIVATION OF HYDRODYNAMIC COEFFICIENTS FROM TOWING TANK TEST RESULTS

The set of hydrodynamic coefficients is summarized in the following list:

- $R_U = f(U)$ Upright Resistance
- $r_H = f(U, \phi)$ Heeled Resistance Coeff.
- $t_{E\beta}, t_{E\delta}, t_{E\tau} = f(U, \phi)$ Effective Draft Coefficients

- $f_{H0} = f(U, \phi)$ Side Force Coefficient at zero leeway
- $\frac{\partial f_h}{\partial \beta} = f(U, \phi)$ Side Force Gradients
- $\frac{\partial f_h}{\partial \delta}, \frac{\partial f_h}{\partial \tau} = f(U)$ Side Force Gradients
- $LCE_{\beta,\delta,\tau} / LR = f(\phi)$ Centre of Efficiency Coefficients
- $VCE = f(\phi)$ Vertical Centre of Efficiency Coefficient

The coefficient listed above are generally independent of each other and may thus be derived from any suitable source, be it towing tank testing, CFD, regression methods or a combination of those. In the following the procedure will be shown for towing tank tests. However, the method is also applicable to any other data source. To derive a complete set of hydrodynamic coefficients care has to be taken to develop a test matrix which allows to detect any non-linearity. A suitable test matrix might consist of:

- non-lifting resistance tests in upright conditions
  - 7 - 20 boat speeds
- leeway angle tests tested at ESG-values for rudder angle
  - 3 - 4 heel angles
  - 4 - 6 leeway angles
  - 2 - 5 boat speeds
- rudder angle tests
  - 2 - 3 heel angles
  - 3 - 5 rudder angles
  - 2 - 3 boat speeds

The numbers given above do not reflect any strict dependencies. However, the test matrix must be chosen such, that it allows to derive coefficients which allow to reflect the boat characteristics by means of interpolation. The importance of the various parameters on boat performance should be reflected in the test matrix. Therefore, one might want to put more emphasis on leeway tests then on rudder angle tests.

The test matrix as listed above consists of 43 to 185 runs. In case yawing balance is not of interest the matrix can be curtailed to 31 to 140 runs. The procedures of a towing tank test itself will not be described here. A description of common procedures and implications may be found in Claughton et al. [122].

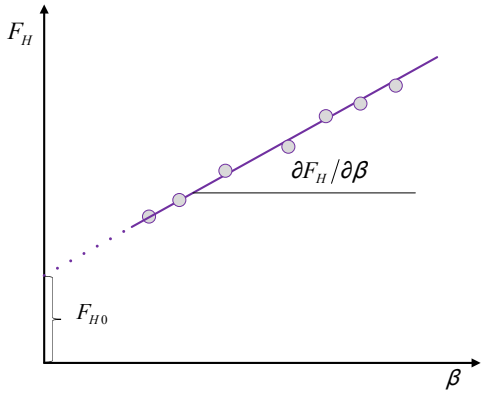

Figure 4.2: Example of results from leeway tests plotted as F_H over β. The results are used to approximate the change of heeling force F_H due to leeway β as the slope $\partial F_H/\partial\beta$. Side force at zero leeway, F_{H0}, is the ordinate of F_H over β.

Model test results are transformed to full scale by applying a slightly modified version of the ITTC'78 Performance Prediction Method [123]. For the method presented here only upright resistance tests have to be transferred to full scale. All other data is transformed into dimensionless hydrodynamic coefficients.

In the following diagrams of the hydrodynamic flow forces or moments will be plotted. Hydrodynamic coefficients are then derived by approximating these values by linear functions. This is done for any combination of boat velocity and heeling angle. Plotting heeling force $F_H = F_Y/\cos\phi$ over leeway angle β allows us to derive $\partial F_H/\partial\beta$ and F_{H0}, see Figure 4.2. With canoe body buoyancy ∇_{CB}, density of fluid ρ and velocity U the following coefficients can be calculated:

$$\partial f_H/\partial\beta = \frac{\partial F_H/\partial\beta}{0.5\rho U^2\nabla_{CB}^{2/3}}, \tag{4.13}$$

$$f_{H0} = \frac{F_{H0}}{0.5\rho U^2\nabla_{CB}^{2/3}}. \tag{4.14}$$

To derive effective draft ratio $t_{E\beta} = T_E/T$ and added resistance due to heel, the results from the leeway tests at base rudder and tab angle, longitudinal flow forces F_X are plotted over F_H squared. The sum of upright resistance and added resistance due to heel $R_H + R_U$ can be derived from an extrapolation of a linear approximation of $F_X = f\left(F_H^2\right)$, while effective draft can be derived from slope of linear approximation, see Figure 4.3.

$$r_H = \frac{R_H}{R_U} = \frac{F_X\left(\phi, F_H = 0\right) - F_X\left(\phi = 0, F_H = 0\right)}{F_X\left(\phi = 0, F_H = 0\right)} \tag{4.15}$$

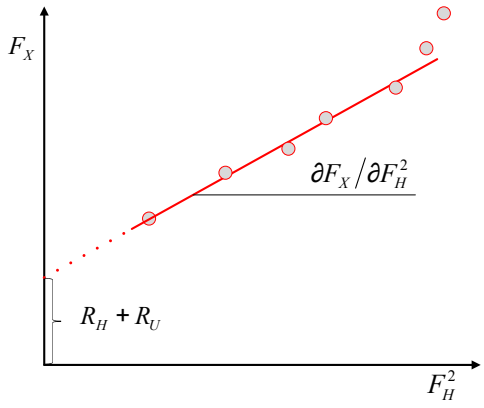

Figure 4.3: Plotting test results as F_X over F_H^2 visualizes the derivation of effective draft and added resistance due to heel. Effective draft T_{Eff} is based on a linear approximation of $\partial F_X/\partial\left(F_H^2\right)$. Added resistance due to heel R_H is the ordinate of $\partial F_X/\partial\left(F_H^2\right)$ slope minus the upright resistance R_U.

$$t_{E\beta} = \frac{1}{T\sqrt{\partial F_X/\partial\left(F_H^2\right)0.5\rho U^2\pi}} \tag{4.16}$$

Plotting yawing moment M_Z and side force F_Y over leeway angle β allows deriving side force and yawing moment slope, see Figure 4.4. Longitudinal centre of efficiency can then be calculated by:

$$LCE_\beta = \frac{\partial M_Z/\partial\beta}{\partial F_Y/\partial\beta}. \tag{4.17}$$

LCE_β has to be corrected by the distance of longitudinal position of measurement dynamometer from origin. Equation (4.17) assumes that $M_Z = 0$ at $F_H = 0$. This is only correct for upright conditions $(\phi = 0)$. Since the error introduced is assumed to be small, a more detailed approach is neglected to avoid complication of data acquisition.

For vertical center of efficiency, it is assumed that it does not vary with velocity. For VCE_β, $M_X - M_{XHS}$ is plotted over leeway angle β (Figure 4.5). Assuming $F_Y = F_H/\cos\beta$, VCE will be derived from:

$$VCE = \frac{\partial\left(M_X - M_{XHS}\right)/\partial\beta}{\partial F_Y/\partial\beta}. \tag{4.18}$$

Here M_{XHS} is the hydrostatic righting moment of model, which can be derived from an additional heeling test at $U = 0$. It has to be subtracted to separate the hydrodynamic from the hydrostatic heeling moment. VCE is calculated for ESG-values of rudder and

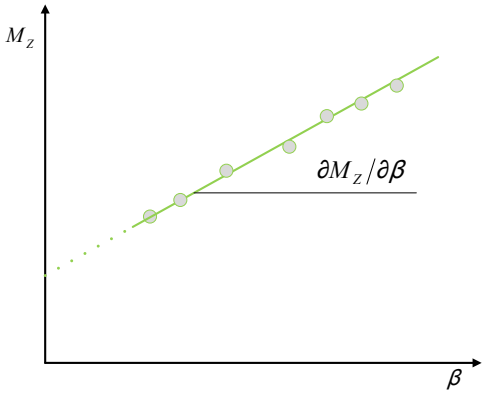

Figure 4.4: Derivation of yawing moment slope $\partial M_Z/\partial\beta$ visualized by plotting results for M_Z over β. In conjunction with $\partial F_Y/\partial\beta$, the slope $\partial M_Z/\partial\beta$ is used to calculate the longitudinal center of efficiency, LCE_β

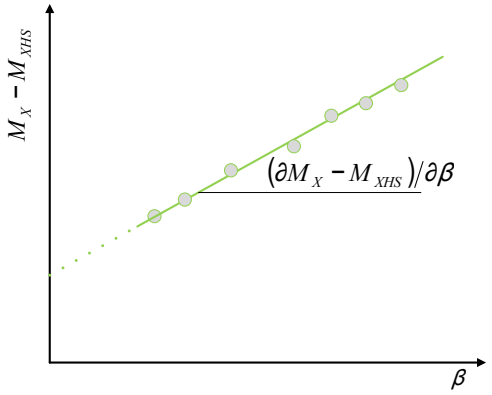

Figure 4.5: Heeling moment M_X minus hydrostatic heeling moment M_{XHS} plotted over leeway angle β. The hydrodynamic heeling moment slope $(\partial M_X - M_{XHS})/\partial\beta$ is used to compute vertical center of efficiency VCE_β.

tab angles. It is assumed that VCE does not change if side forces change due to non-ESG-values of rudder and tab angles. VCE has to be corrected by the distance of the dynamometer centre of heeling rotation to origin. Rudder and tab side force coefficients, effective span and longitudinal centre of efficiency are derived similarly. To derive rudder and tab side force coefficients, plots of side forces $F_{H\delta}$ respective $F_{H\tau}$ against rudder angle δ (tab angle τ) at leeway angle $\beta = \beta_0$ are used:

$$\partial f_H/\partial\delta = \frac{\partial F_H/\partial\delta}{0.5\rho U^2 \nabla_{CB}^{2/3}}, \tag{4.19}$$

$$\partial f_H/\partial\tau = \frac{\partial F_H/\partial\tau}{0.5\rho U^2 \nabla_{CB}^{2/3}}. \tag{4.20}$$

For effective span, heeling force $F_{H\delta}$ ($F_{H\tau}$) squared are plotted against F_X. Effective span coefficients for rudder and tab can then be calculated using:

$$t_{E\delta} = \frac{1}{T\sqrt{\partial F_X/\partial F_{H\delta}^2 0.5\rho U^2\pi}}, \tag{4.21}$$

$$t_{E\tau} = \frac{1}{T\sqrt{\partial F_X/\partial F_{H\tau}^2 0.5\rho U^2\pi}}. \tag{4.22}$$

For longitudinal centre of efficiency of rudder and tab the following equations are used:

$$LCE_\delta = \frac{\partial M_Z/\partial\beta}{\partial F_{Y\delta}/\partial\beta}, \tag{4.23}$$

$$LCE_\tau = \frac{\partial M_Z/\partial\beta}{\partial F_{Y\tau}/\partial\beta}. \tag{4.24}$$

All coefficients derived so far are dimensionless and can be transferred to full scale without further corrections, as long as geometric values of reference length L_{Ref} and draft T are used corresponding to model scale. Additionally a table of righting arms $h = f(\phi)$ has to be supplied by the user in order to define righting moments as in equation (4.12).

4.1.4. AERODYNAMIC MODEL

The aerodynamic model is responsible for the calculation of aerodynamic forces. As described in Section 2.5, the most common method is the IMS sail force model. It is based on individual sail force coefficients for mainsails, jibs and spinnakers, derived from wind tunnel coefficients. A detailed description of the aerodynamic model used in the present VPP is given in Section 3.2.4

A full description of all forces and moments acting on a sail yacht has to include the wind resistance of so called windage elements. The term describes any part of the yacht generating aerodynamic resistance that is not taken into account by the sail forces model. In the present VPP model this done by adding a table of drag areas of windage elements.

4.1.5. SOLUTION ALGORITHM

The general solution algorithm calculates equilibrium of aerodynamic and hydrodynamic forces by applying root-finding based on Newton-Raphson method. For estimated values of the velocity $\hat{U}$, heeling angle $\hat{\phi}$, leeway angle $\hat{\beta}$ and rudder angle $\hat{\delta}$ the aerodynamic and hydrodynamic forces and moments are calculated. A correction of estimated state variables is then calculated solving:

$$\begin{bmatrix} \partial F_X/\partial U & \partial F_X/\partial \beta & \partial F_X/\partial \phi & \partial F_X/\partial \delta \\ \partial F_H/\partial U & \partial F_H/\partial \beta & \partial F_H/\partial \phi & \partial F_H/\partial \delta \\ \partial M_X/\partial U & \partial M_X/\partial \beta & \partial M_X/\partial \phi & \partial M_X/\partial \delta \\ \partial M_Z/\partial U & \partial M_Z/\partial \beta & \partial M_Z/\partial \phi & \partial M_Z/\partial \delta \end{bmatrix} \begin{pmatrix} \Delta U \\ \Delta \beta \\ \Delta \phi \\ \Delta \delta \end{pmatrix} = - \begin{bmatrix} F_X^A(\hat{U},\hat{\phi},\hat{\beta},\hat{\delta}) + F_X^H(\hat{U},\hat{\phi},\hat{\beta},\hat{\delta}) \\ F_Y^A(\hat{U},\hat{\phi},\hat{\beta},\hat{\delta}) + F_Y^H(\hat{U},\hat{\phi},\hat{\beta},\hat{\delta}) \\ M_X^A(\hat{U},\hat{\phi},\hat{\beta},\hat{\delta}) + M_X^H(\hat{U},\hat{\phi},\hat{\beta},\hat{\delta}) \\ M_Z^A(\hat{U},\hat{\phi},\hat{\beta},\hat{\delta}) + M_Z^H(\hat{U},\hat{\phi},\hat{\beta},\hat{\delta}) \end{bmatrix}. \tag{4.25}$$

Derivatives $\partial F_x/\partial U$... can be developed from wing theory or calculated as finite differences. Boat speed is optimised by applying a multi-step minimization search method to the trim parameters $flat$ and $reef$. The minimization is performed using Brent's Method as described by Press et al. [124].

4.2. MATHEMATICAL MODEL FOR RANSE COUPLED VPP

The general idea behind the RANSE-VPP is to directly implement the calculation of sailing equilibrium into a RANSE Solver. Sail forces for a given true wind condition have to be calculated and coupled to the hydrodynamic forces from the RANSE simulation. A rigid body motion solver is used to couple the two systems. Figure 4.6 shows the principle interaction between these three modules. In principle, evaluation of aerodynamic forces could be directly integrated in the flow solver. As explained in Chapter 2, this would require an additional trim optimization loop for the sails at every time step. Together with additional problems like the necessity to account for the flexibility of the sails, this would lead to an enormous increase of complexity and computational effort of the RANSE-VPP. Therefore, a decoupled approach is chosen were the sail forces are

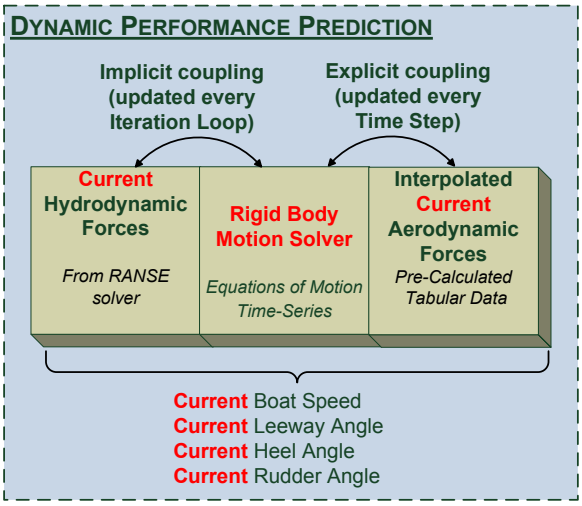

Figure 4.6: General overview of the approach used for the dynamic VPP. Aerodynamic and hydrodynamic forces are coupled via a rigid body motion solver. Forces acting on the rigid body are updated every time step (aerodynamic forces) or iteration (hydrodynamic forces).

calculated from external data and act as external forces on the rigid body. This changes the state of the rigid body, which in turn has an influence on hydrodynamic flow conditions. The RANSE solver will calculate hydrodynamic flow forces at these conditions, thus updating forces acting on the rigid body, which in turn has influence on aerodynamic forces. This loop continues until equilibrium between aerodynamic and hydrodynamic forces is reached.

In contrast to a conventional VPP, this approach does not only give *final* values of boat speed, heel angle and so on, but also *current* values. Given correct frame conditions like a suitable sail force model and a appropriate time resolution, one is able to get correct solutions during the complete simulation time. These solutions would of course include accelerations. This offers future possibilities regarding maneuvering and seakeeping.

The coupling procedure illustrated in Figure 4.6 shows that coupling of forces with the rigid body motion solver differs between aerodynamics and hydrodynamics. Aerodynamic forces on the rigid body are updated at every time step when the unsteady RANSE solution advances in time. Interaction of hydrodynamic forces and rigid body motion are implicitly coupled and thus updated at every outer iteration loop of the RANSE solver.

In order to create a system as described above, one has to solve the RANS equations and the fully integrated equations of motion of the sailing yacht, which is considered to be a rigid body. Theoretical aspects of RANSE procedure and approaches to solve rigid body motion with focus on fluid body interaction is given in Chapter 5.

4.2.1. COUPLING OF RANSE SIMULATION AND VPP

The general course of the RANSE-VPP is illustrated in the flow chart in Figure 4.7. In principle, the RANSE-VPP is written as a management routine which, besides calculating the current value of the aerodynamic forces, steers the procedure calls of the RANSE simulation and the rigid body motion solver. The management routine is coded in JAVA and employs *STAR-CCM+* to solve viscous flow and rigid body interaction. A typical simulation is conducted as follows:

1. The VPP starts with a set of true wind conditions as input data.
2. First, the management routine is called before the time step.
   (a) Retrieve current boat state (forces, moments, orientation, velocity,..) from simulation.
   (b) Calculate apparent wind and sail forces using current boat state as input.
   (c) Check convergence. If simulation has not converged move to 3. Else continue.
   (d) Run Optimizer. If optimum is reached save results and continue with new V_T and β_T at 6. Else set new flat value and continue at 2(b).
3. Write Sail forces as external Forces on Rigid Body.
4. Solve RANS Equation and Rigid Body motion until stop criterion of outer iterations is reached.
5. Advance in time and loop to 2.
6. Proceed to 1. and select next combination of V_T and β_T.

Besides the main functions as listed above, the JAVA routine includes numerous auxiliary functions. One example of these functions is the *adaptive time step* which keeps the Courant number between certain limits. Another example is a limiter for allowed heeling moment. Based on the righting moment of the boat, this limiter decreases the heeling moment by changing $flat$ such that a maximum heel angle is not exceeded. These auxiliary functions will not be treated here in detail. Instead the main functions of the program will be described in the following sections.

4.2.2. FORMULATION OF AERODYNAMIC FORCES

To account for the aerodynamic forces imposed by the sails, an additional, external force is modeled which is acting on the sailing yacht which is treated as a rigid body. Since this external sailing force vector $\mathbf{F}_{\mathbf{Aero}}$ is of unsteady nature, modeling of this vector implicitly requires that its calculation routine is directly coupled with the rigid body motion solver.

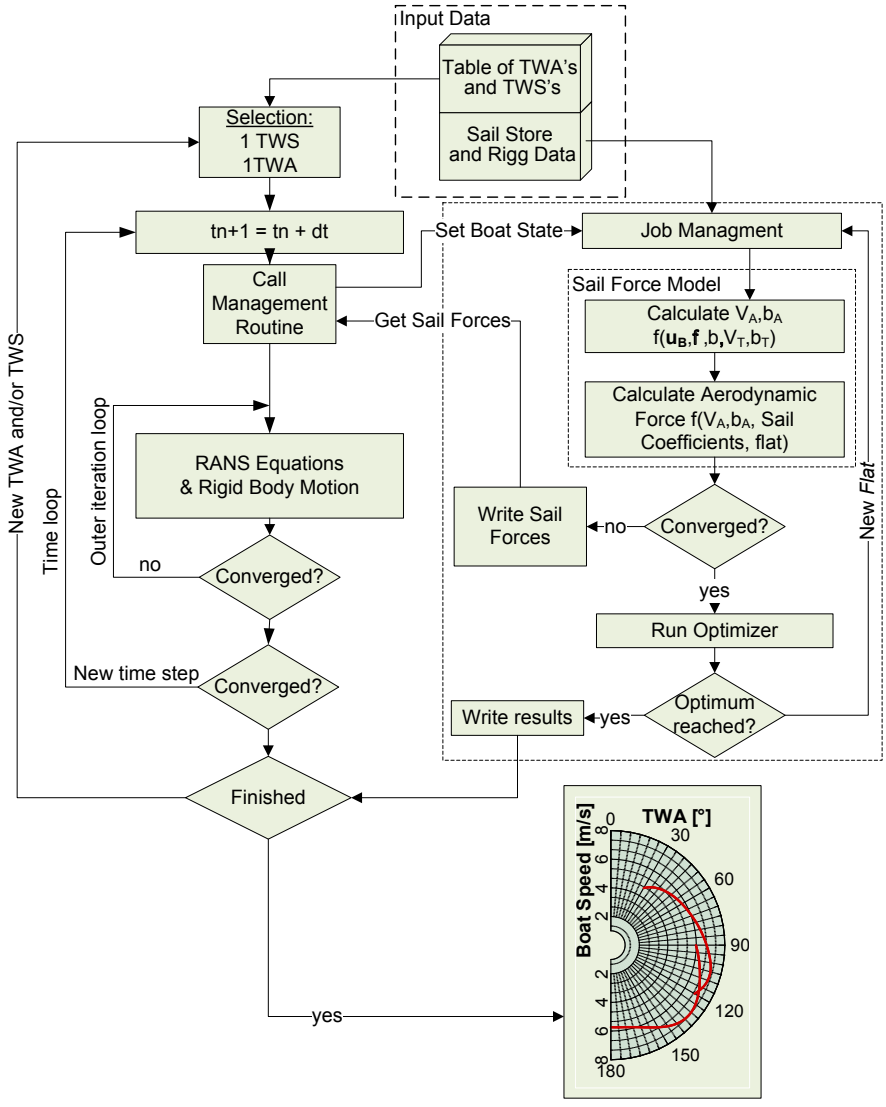

Figure 4.7: Principle flow of RVPP

Along with gravity force and hydrodynamic forces acting on the yacht, this sailing force vector is used to solve the equations of motion.

The sailing force vector itself is calculated using a semi-empirical sail force model as explained in Section 3.2.4. This approach willfully keeps up the paradigm of separation of aerodynamic and hydrodynamic investigation for several reasons: It allows taking into account sailing force data from virtually any source and in conjunction with depowering algorithms, resembling the trimming of the sail carried out by sailors. It simplifies the analysis of cause and effect of changes in aerodynamic or hydrodynamic parts of a yacht. Finally it allows to take into account advanced techniques for the prediction of aerodynamic forces, e.g. fluid structure interaction methods. As an initial input before the beginning of the calculation procedure, the user has to provide tables with permutations of true wind angle β_T and true wind speed V_T as well as data about the sail plan of the yacht and aerodynamic data of the individual sails in form of lift C_L and drag coefficients C_D as functions of the apparent wind angle β_A.

During the simulation, the flow code is called by the sail force calculation routine at the beginning of every time-step and receives the yachts current linear and angular velocity components as well as its orientation in space as input data. From these the sail force vector $\mathbf{F_{Aero}}$ is calculated in the following manner:

First, the apparent wind vector $\mathbf{v_A}$ is calculated as a function of true wind conditions, boat speed and heel angle.

$$\mathbf{v_A} = \begin{bmatrix} V_T \cos\beta_T + u_x + u_{rot,x} \\ V_T \sin\beta_T \cos\phi + u_y + u_{rot,y} \\ 0 \end{bmatrix}. \tag{4.26}$$

The standard procedure is modified to take into account additional force components originating from unsteady motion and orientation of the boat, allowing calculating their influence on boat movement as a time series. Here, the vector $\mathbf{u_{rot}}$ has been added in the equation to account for changes in $\mathbf{v_A}$ due to rotating motions of the boat, namely pitch and roll. Thus, $\mathbf{u_{rot}}$ is defined as the angular velocity of the boat $\omega_\mathbf{B}$ times the vertical center of effort of the sails, zce_{Aero}, see 4.27.

$$\mathbf{u_{rot}} = \mathbf{zce_{Aero}} \times \omega_\mathbf{B}, \tag{4.27}$$

Using $\mathbf{v_A}$ as calculated above, one can easily derive β_A 4.28 and V_A 4.29 by applying basic vector calculus.

$$\beta_A = \arctan\frac{v_{A,y}}{v_{A,x}}, \tag{4.28}$$

$$V_A = \sqrt{v_{A,x}^2 + v_{A,y}^2}. \tag{4.29}$$

The RANSE-VPP uses a modification of the sail force calculation method that has been implemented in the IMS velocity prediction program, for details see Section 3.2.4. Whilst the individual sail force data for RVPP may come from any source, the procedure has been adapted because of its versatile usable approach.

From the individual sail coefficients aggregate lift and drag coefficients $C_{L_{total}}$ and $C_{D_{total}}$ for a sail set are calculated from:

$$C_{D_{total}} = C_D \, reef^2 + CE \, C_L^2 \, flat^2 \, reef^2, \tag{4.30}$$

$$C_{L_{total}} = flat \, reef^2 \, C_L. \tag{4.31}$$

Here C_D and C_L are weighted sums of the drag and lift coefficient of all sails in the sail set while CE is an efficiency coefficient, taking into account the quadratic parasite profile drag and the effective span of the sail set. $reef$ and $flat$ are trimming parameters for the sail to obtain maximum boat velocity via depowering the sail or reducing sail area. $flat$ is a linear reduction of lift and a squared reduction of induced and parasitic drag at constant span, corresponding to a sail chord or traveller angle trimming action of the sailors. $reef$ is a factor taking into account a reduction of sail luff length as the name implies, with corresponding impact on lift, drag and effective span. Whilst theoretically available, the factor $reef$ is omitted in the current version of RANSE-VPP. This mainly due to the fact that the development of RANSE-VPP aims towards racing yacht for which reefing most often is not an option. For details of the IMS method see Claughton [125] or the IMS documentation from the Offshore Racing Council [121].

By using the aggregate sail coefficients as calculated in (4.30) and (4.31) one can calculate the sail force $\mathbf{F_S}$ as shown in (4.32):

$$\mathbf{F_S} = \frac{1}{2} \rho_{Air} A_{Sails} V_A^2 \begin{bmatrix} C_{L_{total}} \sin\beta_A - C_{D_{total}} \cos\beta_A \\ C_{L_{total}} \cos\beta_A - C_{D_{total}} \sin\beta_A \\ 0 \end{bmatrix}. \tag{4.32}$$

Experience gained from seakeeping investigations showed that the added air mass of sails contributes significantly to the moment of inertia of a sailing yacht, especially around the longitudinal axis. For details see Graf et al. [126]. Therefore an additional added mass force $\mathbf{F_{SA}}$ due to the movement of the sails in the surrounding air is taken into account:

$$\mathbf{F_{SA}} = -C_M \frac{\pi}{4} \rho_{Air} \, c \, A_{Sails} \, \dot{\omega}_{\mathbf{B}} \, zce_{Aero}, \tag{4.33}$$

with added mass coefficient C_M, density of air ρ_{Air}, mean sail chord c and combined sail area A_{Sails} accounting for the added mass of the sails. The acceleration of the boat is given by its angular acceleration $\dot{\omega}_{\mathbf{B}}$ acting at the vertical center of effort of the sail forces zce_{Aero}. This leads to the final definition of the sail force vector as shown below.

$$\mathbf{F_{Aero}} = \mathbf{F_S} + \mathbf{F_{SA}} \tag{4.34}$$

After transformation from the coordinate system planar to the water surface to a boat-fixed coordinate system, the sail force vector $\mathbf{F_{Aero}}$ is applied to the boat at the position

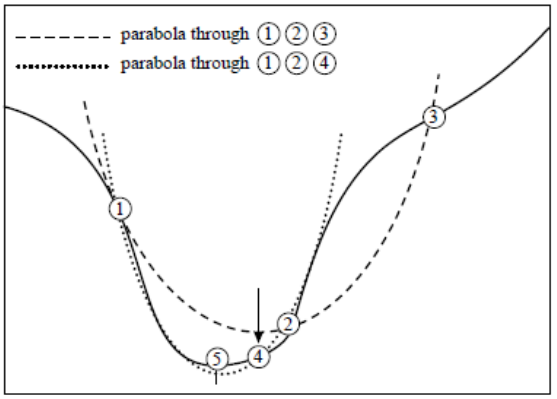

Figure 4.8: Brent's Method: Inverse parabolic search to converge towards a minimum (Source: Pratt et al.[124])

of aerodynamic longitudinal and vertical center of efficiency. The center of efficiency CE_{Aero} is approximated to be at the geometrical center of the sails.

4.2.3. OPTIMIZATION OF BOAT SPEED

To reflect the efforts of the sailors to trim the sails for optimum boat speed $\mathbf{u}$ an optimizer has to be applied on the trim parameter $flat$.

$$\frac{\partial \mathbf{u}}{\partial flat} = 0 \tag{4.35}$$

Evaluation of different $flat$ states is time consuming, since it requires the RANSE-VPP to converge toward an equilibrium with sail forces for the new $flat$ value. It is therefore crucial to find an optimizer which only evaluates $flat$ as few times as reasonably possible.

The optimizer applied here is a custom modification of Brent's Method described by Press et al. [124], combining a bracket search with a parabolic search algorithm. The principle is illustrated in Figure 4.8 with the formula yielding

$$x = b - \frac{1}{2}\frac{(b-a)^2\left[f(b)-f(c)\right]-(b-c)^2\left[f(b)-f(a)\right]}{(b-a)\left[f(b)-f(c)\right]-(b-c)\left[f(b)-f(a)\right]} \tag{4.36}$$

with abscissa x as the minimum of a parabola through the three point $f(a)$,$f(b)$ and $f(c)$.

Optimizing boat speed is based on the principle of "depowering" the sail; $flat$ reduces total lift coefficient and total drag coefficient, (4.30) and (4.31). Linear reduction of lift generates quadratic reduction of drag. This implies a derivation from optimum trim

settings accompanied with an increase of induced drag. However, the heeling moment and consequently the heel angle is reduced which might result in a favorable reduction of hydrodynamic resistance.

4.2.4. INTEGRATION OF RUDDER FORCES

The main task of the rudder in context of a VPP is to counter M_z and thus provide yaw balance. Therefore, the sum of M_z shall be zero (4.37).

$$\sum M_z = M_{z,Boat} + M_{z,Sails} + M_{z,Rudder} = 0. \tag{4.37}$$

To achieve this, rudder forces have to be altered during simulation. To do this with an moving rudder is not an easy task since it would require a method to move a part of the computational grid relative to the moving main grid without comprising grid integrity. Furthermore, an adaptive rudder controller, for example a PID (proportional-integral-derivative) controller would have to be implemented. Since the gain does not seem to justify the increased computational effort, a simpler method has been used.

The rudder itself is integrated as a non-movable part of the geometry. This way parasitic drag at zero lift is implicitly taken into account and changes of lift are only accompanied by induced drag. The change in sideforce ΔF_{Ry} at the current time step n necessary to achieve yaw equilibrium may be derived as sum of yawing moments (4.37) from the last timestep $n-1$ divided by the longitudinal center of effort of the rudder, $LCE_{x,Rudder}$.

$$\Delta F_{Ry,n} = \frac{\sum M_{z,n-1}}{LCE_{x,Rudder}}. \tag{4.38}$$

This yields

$$F_{Ry,n} = F_{Ry,n-1} + \Delta F_{Ry,n}, \tag{4.39}$$

for the current added lift $F_{Ry,n}$ generated by the rudder. To determine the drag component in ship x-axis resulting from such a sideforce, one has to calculate the generated lift $L_{R,n}$.

$$L_{R,n} = \frac{F_{Ry,n}}{\cos\beta} \tag{4.40}$$

The induced drag $D_{Ri,n}$ can than be calculated from

$$D_{Ri,n} = \frac{L_n^2}{T_{Eff}^2 0.5\rho u_B^2 \pi} \tag{4.41}$$

yielding

$$F_{Rx,n} = -D_{Ri,n}\cos\beta \tag{4.42}$$

for the drag component in ship x-axis, $F_{Rx,n}$. The rudder model as described above includes some simplifications and linearisation. It assumes that it is permissible to take rudder forces into account by applying wing theory. It can be only accurate for rudder

angles up to approximately 12° since it does not take into account effects of flow separation. Since the model assumes that a fixed, non-moving rudder is present in the CFD model, drag is accounted for by changing the induced resistance only. As the yacht is not allowed to truly rotate around the z-axis, the RANSE-VPP is virtually of 5+1 DOF type.

4.2.5. CONVERGENCE CRITERION

The definition of convergence for unsteady RANS simulations is often problematic. Residuals as the standard measure for convergence only have a limited value here. Therefore, a convergence criterion has been defined which focuses on force equilibrium. The three vector components of the hydrodynamic forces $\mathbf{F_{Boat}}$ are compared with the respective vector components of combined hydro- and aerodynamic forces $\mathbf{F_{Total}}$ as per equation (4.43).

$$\frac{\sum_n \mathbf{F_{Boat}}}{\sum_n \mathbf{F_{Total}}} < p \tag{4.43}$$

If the differences of all three vector components are all smaller than a chosen precision p, the simulation is assumed to have converged. To assure that this not a random occurrence but a steady equilibrium, forces are summed up over a interval of n time steps.

4.2.6. SUMMARY

In contrast to the conventional VPP approach, the procedure described above has no need for a database of hydrodynamic coefficients. The hydrodynamic data of the yacht is directly calculated via the RANSE solver. This has a direct impact on the number of runs necessary to predict boat velocity. As mentioned before, the method is used for hydrodynamic assessment of yacht performance. Therefore, interpolation errors of the empirical aerodynamic force prediction are accepted, as long as the method is used for the comparison of different yacht hulls with identical sails. If the focus of the investigation changes to aerodynamics, the method can be inverted. Aerodynamic forces would then be calculated accurately without any interpolation from the RANSE simulation, while hydrodynamic properties would be predicted using empirical methods.

Results of a VPP analysis are usually displayed in a polar plot depicting boat speed for a given true wind speed over true wind angle. On average such a plot will show 3-5 polar lines for upwind and for downwind courses.

- 3 - 5 true wind speeds
- 30° - 120° β_T Upwind
- 90° - 180° β_T Downwind

This gives about 60 to 100 simulation runs, which is far fewer than the numbers needed for a conventional VPP if high accuracy is demanded. Additionally, it is possible to investigate only the areas most interesting for a specific boat type, for example maximum VMG (velocity made good) upwind and downwind, which further reduces the number of necessary runs dramatically to about 24 to 40. Since any interpolation is avoided, full accuracy of the prediction of hydrodynamic properties is inherently maintained. This includes the righting moment, which takes the real deformed water surface into account.

The current implementation of RANSE-VPP aims towards a steady state solution. The reason for this is that the RANSE-VPP, as a new developed method, needs validation. This is done against conventional VPP results, which are of steady nature. However, hydrodynamics and rigid body motion are already solved in the time domain. Therefore, RANSE-VPP is ready for further development towards a tool to evaluate unsteady problems like maneuvering. Evaluation of unsteady problems would require development, validation and verification of an unsteady sail force model which is beyond the scope of this thesis. The sail force model as detailed in Section 4.2.2 is in principle steady, but contains some unsteady features. These features are not intended to make the model suitable for unsteady simulations like maneuvering. Instead they are used to accelerate the search for a steady solution by introducing sail damping effects sails.

This section detailed the modeling of the RANSE-VPP. Details on the viscous flow solver and rigid body motion and the coupling of both methods are given in Chapter 5. A comparison of RANSE-VPP and conventional VPP will be given in Chapter 9.

5

NUMERICAL METHOD

In this chapter theoretical aspects of viscous fluid flow simulation with Fluid-Body Interaction will be treated. Viscous flow simulations using RANSE methods have risen to a certain maturity over the last decade. Descriptions of the RANSE based methods are readily available and widely spread. Therefore, this part will only be briefly outlined here. For a more detailed description see for example Ferziger and Peric [63] for a good and detailed overview of the whole topic. After the outline of the flow solver, aspects of the rigid body motion solver and the coupling with the flow simulation will be treated in more detail.

5.1. OUTLINE OF THE RANSE SOLVER

5.1.1. GOVERNING EQUATIONS

The numerical method used to solve the viscous flow problem is of Finite-Volume type. It is assumed that the flow is governed by Reynolds-Average-Navier-Stokes-Equations which evolve from time averaging mass and momentum conservation for a continuous flow. The conservation equations in integral form yield

$$\frac{\mathrm{d}}{\mathrm{d}t}\int_V \rho \,\mathrm{d}V + \int \rho\,(\mathbf{v}-\mathbf{v_B})\,\mathbf{n}\,\mathrm{d}S = 0, \tag{5.1}$$

for mass conservation and

$$\frac{\mathrm{d}}{\mathrm{d}t}\int_V \rho\mathbf{v}\,\mathrm{d}V + \int_S \rho\mathbf{v}(\mathbf{v}-\mathbf{v_B})\,\mathbf{n}\,\mathrm{d}S = \int_S \big(\mathbf{T}-p\mathbf{I}\big)\,\mathbf{n}\,\mathrm{d}S + \int_V \rho\mathbf{b}\,\mathrm{d}V, \tag{5.2}$$

for momentum conservation. Here V denotes a Control Volume (CV) bounded by a closed surface S with unit vector $\mathbf{n}$ pointing outwards. Body forces per unit mass are denoted by $\mathbf{b}$ and fluid density is ρ, $\mathbf{v}$ is the fluid velocity vector and $\mathbf{v_B}$ is the velocity with which the control volume surface moves. $\mathbf{T}$ represents the viscous stress tensor expressing the viscous and Reynolds stresses in terms of velocity gradients and eddy viscosity. $\mathbf{I}$ is the unit tensor and p represents pressure.

$$\mathbf{T} = \mu_{eff}\left[\nabla\mathbf{v} + (\nabla\mathbf{v})^T\right]. \tag{5.3}$$

The effective dynamic viscosity of the fluid μ_{eff} is calculated as sum of the dynamic viscosity μ and the turbulent viscosity μ_T

$$\mu_{eff} = \mu + \mu_T. \tag{5.4}$$

The Reynolds stresses evolving from time averaging are modeled using the eddy viscosity hypothesis and two-equation turbulence models. In this case Menters Shear Stress Transport (SST) turbulence model is used. It calculates the turbulent viscosity μ_T from the turbulent kinetic energy k and the specific turbulent dissipation ω:

$$\mu_T = \frac{a_1 k}{max(a_1\omega, \Omega F_2)}. \tag{5.5}$$

with the closure coefficient a_1, the invariant measure of strain rate Ω and the function for the blending from $k-\omega$ to $k-\epsilon$ formulation F_2. The scalar quantities k and ω of the model have to be transported. The transport equation for generic scalar quantities reads

$$\frac{\mathrm{d}}{\mathrm{d}t}\int_V \rho\phi\,\mathrm{d}V + \int_S \rho\phi\,(\mathbf{v}-\mathbf{v_B})\,\mathbf{n}\,\mathrm{d}S = \int_S \Gamma\nabla\phi\,\mathbf{n}\,\mathrm{d}S + \int_V \rho b_\phi\,\mathrm{d}V, \tag{5.6}$$

with ϕ as the scalar variable (k or ω), Γ being the diffusivity coefficient and b_ϕ representing sources or sinks of ϕ.

In case of a arbitrarily moving CV the *space conservation-law* has to be satisfied to guarantee the conservation of mass and other conserved quantities. It describes the conservation of volume when CVs change shape or position with time due to moving walls.

$$\frac{\mathrm{d}}{\mathrm{d}t}\int_V \mathrm{d}V - \int_S \mathbf{v_B}\,\mathbf{n}\,\mathrm{d}S = 0, \tag{5.7}$$

with $\mathbf{v_B}$ being the velocity with which the CV moves. It guarantees that the sum of all volume fluxes is equal to the rate of volume change.

In order to account for the free surface between two fluid phases in a multiphase simulation one has to solve an additional transport equation to transport the quantity defining the free surface through the computational domain. For example, the quantity in question for the *Volume-of-Fluid method* is its volume fraction α. Free Surface methods were treated in more detail in Chapter 3.1.

5.1.2. DISCRETIZATION

So far, three equations for continuity, one for mass, two for turbulence and one for free surface properties have to be solved. To make these equation system solvable by means of computer systems, the conservation equation in integral form with initial and boundary condition are transformed into an algebraic equation system. These can then be solved by means of discrete approximations. To do so, the spatial domain is first divided into a finite number of control volumes. These CVs may be polyhedral of any shape. However, if the general flow direction is known it is sometimes more economic and accurate to use hexahedral shapes.

The conservation equations are discretized by means of a Finite-Volume-Method (FVM) on each CV. For every CV, one algebraic equation is then obtained. Each of these equations includes unknowns from their CV center as well as from all CVs with which they shares faces.

The equations are non-linear and thus have to be linearized. To obtain the algebraic equations, all integrals (surface, volume, time) are approximated by midpoint rule. The value of the function to be integrated is first evaluated at the the center of the integration domain. For surface integrand this is the CV face center, for volume integrands CV center and for time integrands the time level. It is then multiplied by the respective integration range (face area, cell volume or time step size). Since all values are calculated at the CV center, values at CV face centers have to be interpolated. This is mainly done by linear interpolation, but sometimes blended with linear upwind differencing for stability reasons. Gradients are needed to compute diffusive fluxes at cell faces and some turbulence quantities require gradients at the CV center. In general, all the approximations mentioned above are of 2^{nd} order regardless integration domain (polyhedral, hexahedral, and so on).

5.1.3. SOLUTION PROCEDURE

The resulting approximations are solved in a coupled but segregated iterative method (e.g. SIMPLE-algorithm). Here SIMPLE stands for *Semi-implicit Method for Pressure Linked Equations*. The principle steps of solving the discrete equations by using the SIMPLE-algorithm are listed below. Details are widely available in literature (e.g. Ferziger and Peric [63])

1. Set initial values of pressure and mass fluxes trough cell faces at every cell.
2. Solve linearized momentum component equations by using current pressure and mass fluxes through cell faces (inner iterations).
3. Determine a pressure-correction (pressure-correction equation derived from continuity equation). Correct pressure and mass flux components.

4. Solve equations for volume fraction and turbulence.
5. Go to 2) and repeat sequence until all non-linear and coupled equations are within a prescribed stop criterion (outer iterations).
6. Proceed to next time level.

There are several other, newer algorithms which allow to solve such equations systems. However, the SIMPLE algorithm is still widely used due to its robustness. However, this robustness is achieved by raising computational cost. The major drawback of the SIMPLE algorithm is that the intermediate velocities u^* are neglected when correcting pressure. Therefore, the pressure corrections often become too large, causing divergence of the solution. This problem is solved by under-relaxing. Under-relaxation in this context is a method to build a weighted average of the result of a current iteration step with the previous. This leads to increased stability but also slows the solution procedure significantly. It is therefore desirable to avoid under-relaxation, for example by using SIMPLEC (*SIMPLE Corrected*) or PISO (*Pressure Implicit with Splitting Operator*), or to keep the under-relaxation close to 1.

Computation of this large and non-linear equation system requires a lot of computational power and memory, especially if the simulation is of unsteady nature. It is therefore crucial to decompose the problem in space and time and solve it by using parallel computing. The most popular message passing libraries which enable parallel computing are PVM (parallel virtual machine) and MPI (Message Passing Interface).

5.2. RIGID BODY DYNAMICS

In order to correctly determine fluid dynamics of floating bodies, one has to introduce rigid body dynamics in 6-degree-of-freedom (DOF) into the flow simulation to identify the correct running attitude of the body. Depending on the size of the investigated body, resulting variations in orientation and translation of the body can be relatively large. The effect is more pronounced for smaller boats like sailing yachts, than for large merchant vessels. Nonetheless, it should be included in both cases to increase accuracy of results. Several approaches to resolve the resulting motion in the flow domain exist. These will be dealt with in Chapter 6. The equations for rigid body dynamics presented in this section are valid for all these approaches. The section starts with the used *frames of reference* in which rigid body dynamics are defined. Afterwards, governing equations of the rigid body dynamics and their discretization into an algebraic equation system are introduced. Finally, the coupling of fluid flow and rigid body motion will be treated.

5.2.1. FRAMES OF REFERENCE

The following two reference systems (Figure 5.1) are used to describe rigid motion:

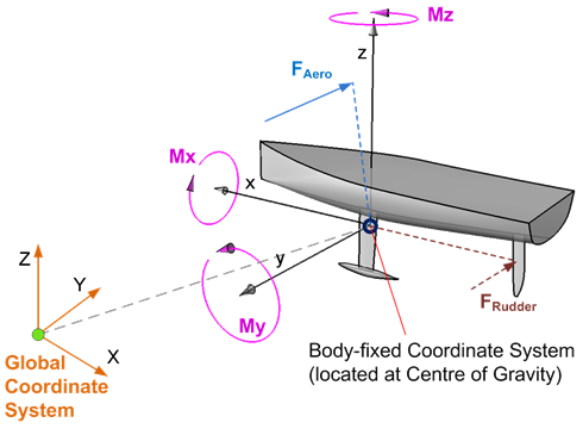

Figure 5.1: Definition of the reference systems used. The global coordinate system (orange) is a space fixed, non-moving coordinate system. Its X-axis is aligned with the principle flow direction, X- and Y-axis are parallel to the undisturbed free surface and and Z-axis is pointing upward. The body reference system is a moving reference system which is fixed to the boat. It is located at the center of mass of the boat, with x-axis point forward, y-axis to port and z-axis upward.

- a global, space-fixed, non-moving, non-accelerating Newtonian coordinate system (GS). It is defined with XY-plane parallel to the undisturbed free surface. For convenience, X-axis points in principle flow direction and Z-axis points upwards. The global coordinate system is used to describe the RANSE equations and position and orientation of the rigid body at any point in space and time.
- a body-fixed coordinate system (BS) which has its origin at the center of mass. The xy-plane is parallel to the design water plane and x-axis is pointing forward in the boats longitudinal axis. y-Axis and z-Axis are pointing to port respective upward. The BS system maintains the orientation of the boat and is helpful to identify rigid body orientation and to realize its motion.

5.2.2. EQUATIONS OF MOTION OF THE RIGID BODY

Since the equation describing the fluid flow are expressed in the GS reference system, the variables velocity and pressure are also expressed in this system. Therefore fluid forces (shear and pressure forces) acting on the rigid body are calculated in the GS. Translation and rotation of the rigid body in 6 Degree-of-Freedom (DOF) is determined by integrating the equation of linear and angular momentum. The equation of variation of linear momentum with respect to the center of gravity reads:

$$\frac{\mathrm{d}(m\mathbf{v_G})}{\mathrm{d}t} = \mathbf{F}. \tag{5.8}$$

Here m stands for the mass of the investigated body, $\mathbf{v}$ is the linear velocity of the center of mass and $\mathbf{F}$ is the resultant force acting on the body at the center of mass. Assuming the mass to be constant, equation (5.8) may be written as:

$$m\dot{\mathbf{v}}_\mathbf{G} = \mathbf{F}, \tag{5.9}$$

with $\dot{\mathbf{v}}_\mathbf{G}$ as the total linear acceleration of center of gravity $\mathbf{G}$ in GS reference frame. The equation of the angular momentum with respect to center of gravity (BS) yields

$$\frac{\mathrm{d}\left(\mathbf{I}_\mathbf{G}\omega_\mathbf{G}\right)}{\mathrm{d}t} = \mathbf{M}_\mathbf{G} \tag{5.10}$$

with $\omega_\mathbf{G}$ representing the angular velocity of the rigid body and $\mathbf{M}_\mathbf{G}$ the resultant moment acting on the body, all with respect to $\mathbf{G}$. $\mathbf{I}_\mathbf{G}$ is the tensor of the moment of inertia of the investigated body with respect to the body fixed coordinate system.

$$\mathbf{I}_\mathbf{G} = \begin{bmatrix} I_{xxG} & -I_{xyG} & -I_{xzG} \\ -I_{yxG} & I_{yyG} & I_{yzG} \\ -I_{zxG} & -I_{zyG} & -I_{zzG} \end{bmatrix} \quad . \tag{5.11}$$

For example principal moments of inertia of the body along the diagonal, the roll moment of inertia around its x-axis yields

$$I_{xxG} = \int \left(y^2 + z^2\right) \mathrm{d}m. \tag{5.12}$$

the remaining principal moments of inertia for pitch, I_{yyG}, and yaw, I_{zzG}, are calculated in the same manner. Off-diagonal moments of inertia I_{xyG}, I_{xzG} and I_{yzG} are calculated as

$$I_{xyG} = \int x\, y \,\mathrm{d}m, \tag{5.13}$$

Since the tensor $\mathbf{I}_\mathbf{G}$ is symmetric, $I_{xyG} = I_{yxG}$, $I_{xzG} = I_{zxG}$ and $I_{yzG} = I_{zyG}$.

Assuming again that the mass m of the rigid body is constant and that its moments of inertia $\mathbf{I}_\mathbf{G}$ stay constant with respect to BS, equation (5.10) may be rewritten as

$$\mathbf{I}_\mathbf{G}\frac{\mathrm{d}\omega_\mathbf{G}}{\mathrm{d}t} = \mathbf{I}_\mathbf{G}\dot{\omega_\mathbf{G}} + \omega_\mathbf{G} \times \mathbf{I}_\mathbf{G}\omega_\mathbf{G} = \mathbf{M}_\mathbf{G}. \tag{5.14}$$

When expressing the tensor of the moments of inertia with respect to center of mass expressed in the GS reference system, it changes with every rotation motion of the body. Therefore, ${\mathbf{I}_\mathbf{G}}^{GS}$ has to be updated at every time step. Transforming equations for linear and angular momentum ((5.9) and (5.14)) from BS to GS then yields

$$m\dot{\mathbf{v}}_\mathbf{G}^{GS} = \mathbf{F}^{GS}, \tag{5.15}$$

$$\mathbf{T_T I_G T_T^{-1}} \dot{\omega_G}^{GS} + \omega_G{}^{GS} \times \mathbf{T_T I_G T_T^{-1}} \omega_G{}^{GS} = \mathbf{M_G}{}^{GS}, \tag{5.16}$$

with $\mathbf{T_T}$ as the transformation matrix from BS to GS reference system. It implies that the tensor moment of inertia of the body with respect to the GS, $\mathbf{I_G}{}^{GS}$, is not constant. It changes with motion of the body and therefore has to be updated every time the body changes position. The columns of the matrix $\mathbf{T_T}$ are the unit vectors $\mathbf{x}$, $\mathbf{y}$, $\mathbf{z}$, expressed in the GS system, attached to the BS system.

5.2.3. EULER ANGLE

The orientation of any reference frame relative to another can be given by three angles. These *Euler angles* are consecutive rotations about the xyz-axis in a way that ensures that the rotated frame is carried into coincidence with another. Care has to be taken with the order of rotation because the rotation does not commute. Therefore the sequence of rotations needs to be fixed. This sequence is, in principal, arbitrary, a common convention is to use x-y-z-rotations. The cycle of such a rotation sequence, often also denoted as ψ-θ-ϕ- rotation, is shown in Figure 5.2:

1. The starting coordinate system is $Ox_S y_S z_S$. Rotation ψ about Oz_S carries the axis to the intermediate position $Ox_2 y_2 z_2$. ψ is called the *azimuth* or *yaw* angle.
2. From $Ox_2 y_2 z_2$, rotation θ about Oy_2 further carries the axis to $Ox_3 y_3 z_3$. θ is the *elevation* or *pitch* angle.
3. Finally, from $Ox_3 y_3 z_3$, rotation ϕ about Ox_3 carries the axis to the final position $Oxyz$. ϕ is the *bank* or *heel* angle.

In vector form, the rotations about the intermediate axis of Figure 5.2 may be defined as follows:

$$\mathbf{x_2} = \frac{\mathbf{x} - (\mathbf{x} \cdot \mathbf{z_s}) \cdot \mathbf{z}}{|\mathbf{x} - (\mathbf{x} \cdot \mathbf{z_s}) \cdot \mathbf{z}|}, \tag{5.17}$$

$$\mathbf{y_2} = \mathbf{z_s} \times \mathbf{x_2}. \tag{5.18}$$

From these relations Eulerian angles ψ, θ and ϕ are obtained by

$$\begin{aligned} \psi &= \arcsin\left[(\mathbf{x_s} \times \mathbf{x_2}) \cdot \mathbf{z_s}\right], \\ \theta &= \arcsin\left[(\mathbf{x_2} \times \mathbf{x}) \cdot \mathbf{y_2}\right], \\ \phi &= \arcsin\left[(\mathbf{y_2} \times \mathbf{y}) \cdot \mathbf{x}\right]. \end{aligned} \tag{5.19}$$

This rotation sequence can be combined in the transformation matrix $\mathbf{T_T}$ from BS to GS as series of subsequent principle rotation matrices as follows:

$$\mathbf{T_T} = \begin{pmatrix} \cos\psi & -\sin\psi & 0 \\ \sin\psi & \cos\psi & 0 \\ 0 & 0 & 1 \end{pmatrix} \cdot \begin{pmatrix} \cos\theta & 0 & \sin\theta \\ 0 & 1 & 0 \\ -\sin\theta & 0 & \cos\theta \end{pmatrix} \cdot \begin{pmatrix} 1 & 0 & 0 \\ 0 & \cos\phi & -\sin\phi \\ 0 & \sin\phi & \cos\phi \end{pmatrix} \tag{5.20}$$

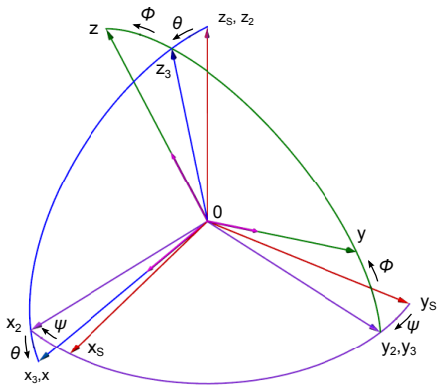

Figure 5.2: Sequence of rotations using Euler Angles. By rotation around the Oz_S-axis, the body is rotated from the starting Coordinate system $Ox_S y_S z_S$ into $Ox_2 y_2 z_2$. From there the body is rotated by a rotation around the Oy_2-axis into $Ox_3 y_3 z_3$. A rotation around $0x_3$ brings the body in its final orientation $Oxyz$. For details see Section 5.2.3

Note that to express $\mathbf{T_T}$ in terms of the Euler angles, the sequence of rotation has to be reversed. Since the product of any number of rotation matrices is itself a rotation matrix, this yields

$$\mathbf{T_T} = \begin{pmatrix} \cos\theta\cos\psi & \sin\phi\sin\theta\cos\psi - \cos\phi\sin\psi & \cos\phi\sin\theta\cos\psi + \sin\phi\sin\psi \\ \cos\theta\sin\psi & \sin\phi\sin\theta\sin\psi + \cos\phi\cos\psi & \cos\phi\sin\theta\sin\psi - \sin\phi\cos\psi \\ -\sin\theta & \sin\phi\cos\theta & \cos\phi\cos\theta \end{pmatrix} \tag{5.21}$$

The Euler angles as described above can be ambiguous, a problem which is called gimbal lock. To avoid this behavior the ranges for a ψ-θ-ϕ- rotation sequence are limited to:

$$\begin{aligned} -\pi \le \psi < \pi, \\ -\frac{\pi}{2} \le \theta \le \frac{\pi}{2}, \\ -\pi \le \phi < \pi. \end{aligned} \tag{5.22}$$

One way to solve this ambiguity would be to use quaternions, which do not suffer from gimbal locks. Quaternions are a construct which spans a 4-dimensional vector space and shows similarities to complex numbers. Since this approach is not implemented in the flow solver used it will not be described here.

5.2.4. COMPUTATION OF IMPRESSED FORCES

The contributions of external and internal forces to the resulting force **F** may be summed as follows:

$$\mathbf{F} = \mathbf{F}_{\mathbf{Hydro}} + m\mathbf{g} + \mathbf{F}_{\mathbf{Ext}} \tag{5.23}$$

where $\mathbf{g}$ denotes the gravity vector which is pointing in downward direction of the GS and $\mathbf{F}_{\mathbf{Ext}}$ may be any kind of external force applied. Typical examples for this application are the sail force and the additional rudder force vector. The flow force $\mathbf{F}_{\mathbf{Hydro}}$ is the resultant force of the flow field acting on the body. It is determined from the RANS equations by integrating viscous wall shear stresses and pressure field over the body's boundary faces.

$$\mathbf{F}_{\mathbf{Hydro}} = \int_S \left(\mathbf{T} - p\mathbf{I}\right)\mathbf{n}\,\mathrm{d}S. \tag{5.24}$$

Here p is the pressure acting on the face of a control volume whilst $\mathbf{n}$ is the normal vector of the individual control volume face. $\mathbf{T}$ is the viscous stress tensor given by (5.3) and $\mathbf{I}$ is the unit tensor whilst S is the surface of the control volume face.

The resultant moment $\mathbf{M}_{\mathbf{G}}$ acting on the center of gravity $\mathbf{G}$ of the rigid body is the sum of external and hydrodynamic moments

$$\mathbf{M}_{\mathbf{G}} = \mathbf{M}_{\mathbf{Ext}} + \mathbf{M}_{\mathbf{Hydro}}. \tag{5.25}$$

Here $\mathbf{M}_{\mathbf{Ext}}$ represent the trimming moment due to external forces which may be expressed as:

$$\mathbf{M}_{\mathbf{Ext}} = (\mathbf{x}_{\mathbf{CE}} - \mathbf{x}_{\mathbf{G}}) \times \mathbf{F}_{\mathbf{Ext}}, \tag{5.26}$$

with $\mathbf{x}_{\mathbf{CE}}$ representing the vector to the center of effort of the external force and $\mathbf{x}_{\mathbf{G}}$ the vector to the center of mass. The dynamic contribution of the flow force to the fluid flow moment $\mathbf{M}_{\mathbf{Hydro}}$ may be expressed as stated below. Here $\mathbf{x}$ denotes the vector to the control volume face center.

$$\mathbf{M}_{\mathbf{Hydro}} = \int_S (\mathbf{x} - \mathbf{x}_{\mathbf{G}}) \times \left(\mathbf{T} - p\mathbf{I}\right)\mathbf{n}\,\mathrm{d}S. \tag{5.27}$$

5.2.5. INTEGRATION OF RIGID BODY EQUATIONS

The motions of a rigid body are described by a set ordinary differential equations (ODE). In order to obtain translational and rotational motion from fluid forces, they have to be integrated. Here several possible methods exist. One could use a 1$^{\text{st}}$ order Euler method as one of the simplest approaches. However, this has the disadvantage that this method is explicit and has the tendency to become unstable if the time step is not sufficiently small. This would introduce unwanted time dependencies into the simulation process. It is therefore more appropriate to use an implicit method an therefore to implement the determination of body motion into the iteration of the flow solver. Furthermore, fluid forces acting on the body influence its orientation and translation which in turn influence the fluid flow. This also suggests that fluid flow and rigid body motion should be

solved in a coupled iterative manner. In the following a second-order predictor-corrector method is described which can be used for prediction rigid body motion. The description follows the one given by [127] and resembles the method used within *Star-CCM+*.

In order to calculate translational motion of the center of gravity **G** one has to integrate the equation of variation of linear motion in time. Therefore (5.8) has to be approximated to acceleration yielding

$$\frac{\mathrm{d}\mathbf{v_G}}{\mathrm{d}t} = \frac{\mathbf{F}}{m}. \tag{5.28}$$

First, velocity of the body at the new time step $n+1$ is predicted using forces and velocities from the previous time step n. This *predictor* step is of explicit Euler type. Next, this predictor is corrected for later iterations i. The *corrector* steps employs trapezoidal rule to compute the derivative.

$$\begin{aligned} \mathbf{v_G}_{n+1}^{i+1} &= \mathbf{v_G}_n + \frac{\mathbf{F}_n + \mathbf{F}_{n+1}^{i+1}}{2m}\Delta t \\ &= \underbrace{\mathbf{v_G}_n + \frac{\mathbf{F}_n}{m}\Delta t}_{predictor} + \underbrace{\frac{\mathbf{F}_{n+1}^{i+1} - \mathbf{F}_n}{2m}\Delta t}_{corrector}. \end{aligned} \tag{5.29}$$

With the new estimated velocities known, the new position of the center of gravity $\mathbf{x_G}_{n+1}^{i+1}$ can then be determined in a similar manner as the velocities, again employing a predictor corrector scheme.

$$\begin{aligned} \mathbf{x_G}_{n+1}^{i+1} &= \mathbf{x_G}_n + \frac{\mathbf{v}_n + \mathbf{v}_{n+1}^{i+1}}{2}\Delta t \\ &= \underbrace{\mathbf{x_G}_n + \mathbf{v}_n\Delta t}_{predictor} + \underbrace{\frac{\mathbf{v}_{n+1}^{i+1} - \mathbf{v}_n}{2}\Delta t}_{corrector}. \end{aligned} \tag{5.30}$$

The necessary incremental displacements to move the rigid body from its position at previous iteration i to new iteration $i+1$ are computed as the delta between these values

$$\Delta\mathbf{x}_{n+1}^{i+1} = \mathbf{x}_{n+1}^{i+1} - \mathbf{x}_{n+1}^{i}. \tag{5.31}$$

In principal, the procedure for rotational motion of the body follows the one of the translational motion above. To find the new orientation of the rigid body at time step $n+1$ one first has to compute the angular velocities $\omega_\mathbf{G}$. Therefore, equation (5.14) is

discretized as follows

$$
\begin{aligned}
&\mathbf{I}_{\mathbf{G}}{}^{i}_{n+1}\omega_{\mathbf{G}}{}^{i}_{n+1} \\
&= \mathbf{I}_{\mathbf{G}n}\omega_{\mathbf{G}n} + \left(\mathbf{M}_{\mathbf{G}n} + \mathbf{M}_{\mathbf{G}}{}^{i+1}_{n+1}\right)\frac{\Delta t}{2} \\
&\quad - \left(\omega_{\mathbf{G}n} \times \mathbf{I}_{\mathbf{G}n}\omega_{\mathbf{G}n} + \omega_{\mathbf{G}}{}^{i}_{n+1} \times \mathbf{I}_{\mathbf{G}}{}^{i}_{n+1}\omega_{\mathbf{G}}{}^{i}_{n+1}\right)\frac{\Delta t}{2} \\
&= \underbrace{\mathbf{I}_{\mathbf{G}n}\omega_{\mathbf{G}n} + \left(\mathbf{M}_{\mathbf{G}n} - \omega_{\mathbf{G}n} \times \mathbf{I}_{\mathbf{G}n}\omega_{\mathbf{G}n}\right)\Delta t}_{predictor} \\
&\quad \underbrace{+ \left(\mathbf{M}_{\mathbf{G}}{}^{i+1}_{n+1} - \mathbf{M}_{\mathbf{G}n}\right)\frac{\Delta t}{2} - \left(\omega_{\mathbf{G}}{}^{i}_{n+1} \times \mathbf{I}_{\mathbf{G}}{}^{i}_{n+1}\omega_{\mathbf{G}}{}^{i}_{n+1} - \omega_{\mathbf{G}n} \times \mathbf{I}_{\mathbf{G}n}\omega_{\mathbf{G}n}\right)\frac{\Delta t}{2}}_{corrector}.
\end{aligned}
\tag{5.32}
$$

The new tensor of the mass moment of inertia $\mathbf{I}_{\mathbf{G}}{}^{i}_{n+1}$ in the GS reference frame is calculated using the transformation matrix $\mathbf{T}_{\mathbf{T}}{}^{i}_{n+1}$ yielding

$$
\mathbf{I}_{\mathbf{G}}{}^{i}_{n+1} = \mathbf{T}_{\mathbf{T}}{}^{i}_{n+1}\mathbf{I}_{\mathbf{G}}\left(\mathbf{T}_{\mathbf{T}}{}^{i}_{n+1}\right)^{-1}. \tag{5.33}
$$

5

Instead of further integrating $\omega_{\mathbf{G}}{}^{i}_{n+1}$, the orientation of the body can be determined by integrating the unit vector $\mathbf{x}$, $\mathbf{y}$ and $\mathbf{z}$ of the body-fixed BS which are attached to the transformation matrix $\mathbf{T}_{\mathbf{T}}$. Here only two of the unit vectors need to be integrated. The discretized equation for $\mathbf{x}^{i}_{n+1}$ yields

$$
\mathbf{x}^{i}_{n+1} = \mathbf{x}_{n} + \frac{\Delta t}{2}\left(\omega_{\mathbf{G}n} + \omega_{\mathbf{G}}{}^{i}_{n+1}\right) \times \mathbf{x}_{n}, \tag{5.34}
$$

for the second unit vector $\mathbf{y}$ the procedure to obtain $\mathbf{y}^{i}_{n+1}$ is the same. The third unit vector $\mathbf{y}^{i}_{n+1}$ can than be calculated as the cross product of the two others

$$
\mathbf{z}^{i}_{n+1} = \mathbf{y}^{i}_{n+1} \times \mathbf{x}^{i}_{n+1}, \tag{5.35}
$$

with the new unit vectors $\mathbf{x}^{i}_{n+1}$, $\mathbf{y}^{i}_{n+1}$ and $\mathbf{z}^{i}_{n+1}$ known, the new Euler angles ψ^{i}_{n+1}, θ^{i}_{n+1} and ϕ^{i}_{n+1} are calculated using (5.19).

5.2.6. COUPLING OF FLUID FLOW AND RIGID BODY DYNAMICS

In order to remove unwanted time-dependencies, fluid flow and rigid body motion solvers are coupled in an implicit manner. Figure 5.3 shows the schematic procedure of the iterative, coupled simulation of flow and flow-induced motion of floating bodies. The rigid body motion is implicitly coupled to the flow solver by updates within outer iteration loops using the following procedure:

1. Advance in time $t_{n+1} = t_n + \Delta t$

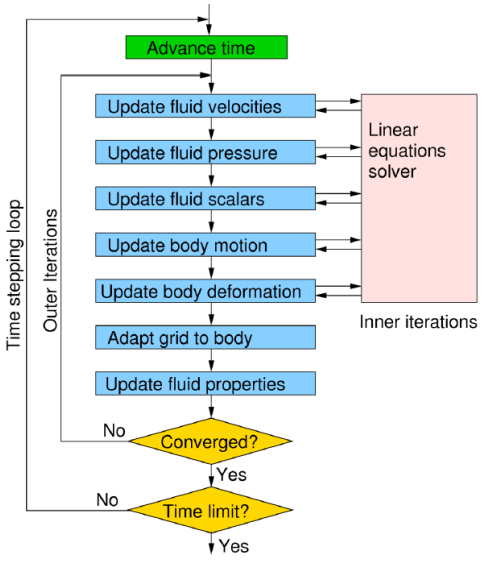

Figure 5.3: Integration of Rigid Body Motion into Flow Solver (Source: Peric and Schreck [128])

(a) Advance outer iteration i = i +1;

(b) solve for fluid velocities and pressure using inner iterations until convergence of linear solver is achieved;

(c) solve body motions using linear equations solver;

i. integrate pressure and shear forces on the rigid body;

ii. solve the discretized equation for rigid body linear velocity $\mathbf{v}_{\mathbf{G}}{}_{n+1}^{i+1}$ and angular linear velocity $\omega_{\mathbf{G}}{}_{n+1}^{i+1}$;

iii. compute changes in orientation $\mathbf{T}_{\mathbf{T}}{}_{n+1}^{i+1}$ and position $\mathbf{x}_{\mathbf{G}}{}_{n+1}^{i+1}$ of the rigid body.

iv. repeat (c) until stop criterion is reached;

(d) goto (a) and repeat steps until stop criterion for outer iterations is reached

2. goto 1. and repeat all steps until maximum simulation time is reached.

The procedure allows to take into account changes in fluid body interaction within the outer iterations of the flow solver instead of only within a time step. It usually takes 5-20 outer iterations per time steps for a solution to converge, depending on the required accuracy in terms of waves and orientation and motion of the ship.

6

NUMERICAL GRIDS

Since the approach is based on a Finite-Volume-Method, the volume of the fluid domain has to be discretized using a finite number of control volumes which constitute the computational grid. In general, two major approaches to form a computational volume grid can be distinguished. These two approaches are one based on a *structured* grid or the use of an *unstructured* one. Structured grids have the advantage that the locations of neighboring cells are known a priori, which allows to solve the equation system more efficiently. If aligned with the flow, they are also more accurate then unstructured grids, due to a decrease in numerical diffusion. However, if misaligned, the contrary holds true. In this case some unstructured grids, in particular polyhedral ones, have the advantage that they always introduce approximately the same diffusion error for every flow direction. The disadvantage of structured grids is, that they are often more difficult to generate and therefore often require much manual work. This makes the grid generation more time consuming. Therefore, nowadays mainly unstructured grids are used. These lend themselves more easily to automation but have to store information about their neighboring cells, which increases computational effort.

After the main choice between structured and unstructured grids, many different grid types exist which handle the distinctive shape of the used control volumes. The following types of grids are commonly used:

- Hexahedral Grid (unstructured and structured):
    - ⊕ Less numerical diffusion if aligned with flow, if structured, less computational costs since neighboring cells are known, use of higher order convection schemes possible.

  - ⊖ Manual effort to generate mesh is very high. Often more computational cells necessary than for all other grid types, due to propagation of cell numbers.

- Tetrahedral / Polygonal Grid with Prism Layers for Boundary Layer (BL) resolution (unstructured only):
  - ⊕ Easy to generate, approximation of every shape possible. Good control over cell density in areas of special interest. Error caused by numerical diffusion approximately the same for all flow directions.
  - ⊖ Increased numerical diffusion. To balance the error introduced by numerical diffusion, higher grid cell numbers are necessary to achieve same accuracy as grids aligned to the flow.
- Trimmed Cartesian Grid with anisotropic refinement and Prism Layers for BL resolution (unstructured):
  - ⊕ Easy to generate, approximation of every shape possible. Very good control over cell density in areas of special interest. Alignment with flow direction possible.
  - ⊖ Can introduce large cell size steps, leading to jumps in the solution which decease accuracy and stability. Compromise between hexahedral and tetrahedral approaches in terms of numerical diffusion.

6.1. GRID MOTION TECHNIQUES

During conventional steady or unsteady RANSE CFD investigations, the computational grid is usually kept rigid and fixed. To resolve the effects of flow forces acting on a rigid body on the body's orientation and translation, the rigid body must be allowed to move. There a several techniques available to resolve the movement of the body, which all have their benefits and drawbacks. Within this work the following methods have been evaluated:

- Grid Motion (6.1.1);
- Mesh Morphing (6.1.2);
- Sliding Interfaces (6.1.3);
- Overset Grids (6.1.4);

6.1.1. GRID MOTION

Within this method, the entire grid is moved according to the motions of the rigid body. The grid itself is not altered but instead kept rigid. This approach bears several advantages. Since only the flow variables have to be corrected according to the body motion,

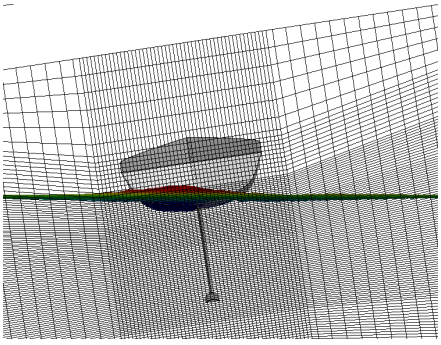

(a) Moving grid

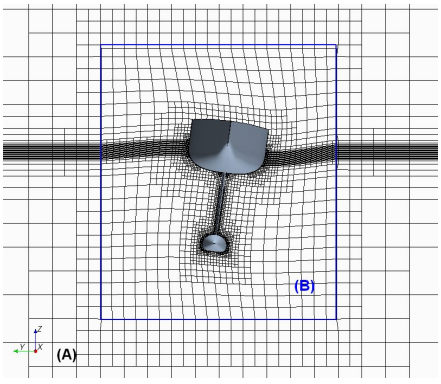

(b) Grid morphing

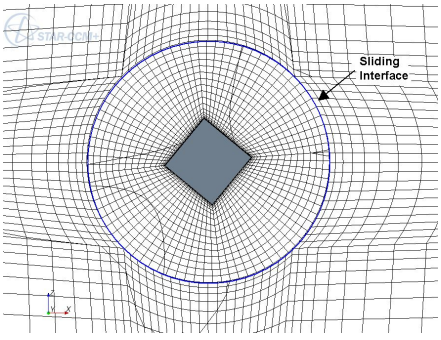

(c) Sliding interface

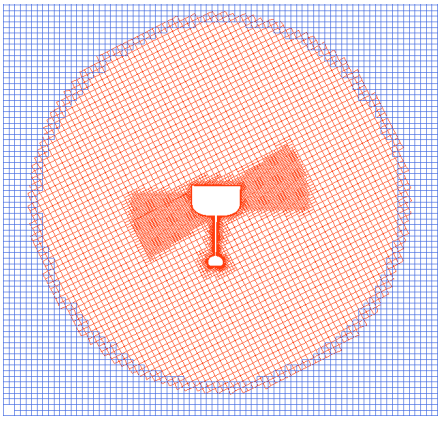

(d) Overset Grid

Figure 6.1: Overview of Grid moving Strategies

the method is very robust and the computational overhead is small. On the other side, the method is only applicable for the motion of one rigid body. Simulation of the interaction of multiple bodies is not possible. The major drawback is the care which has to be taken to smoothly resolve the free surface interface. Figure 6.1a shows an x-normal plane of a grid with the free water surface included. One can see that the grid pattern on the port side almost follows the free surface contour, while on starboard side the grid cells are intersected in an inappropriate angle.

This leads to interpolation errors in the free surface interface and introduce the need to produce a grid which is sufficient to resolve the free surface for heel angles of $+/-30°$ around the boat's Construction Waterline (CWL) for the moving grid strategy. This claim is not an easy one since at first glance, it restricts the possible grid types to hexahedral and requires an immense manual effort to produce such grid. Moreover, such a grid will have significantly more cells than necessary for the other approaches.

6.1.2. MESH MORPHING

Mesh Deformation, also known as mesh morphing is a technique to move the body with its surrounding grid whilst keeping the distant part of the mesh fixed. Most often this is achieved by allowing the grid to move and deform around the body within a predefined box (Figure 6.1b). The grid within the outer box (A) is fixed and not allowed to deform. The advantage of the method is that only a portion of the grid has to be highly refined while in the farfield the higher resolution is only necessary in the vicinity of the fixed free surface interface. Nonetheless, this method has several drawbacks. For instance, the method lacks reliability since for larger amplitudes of motion negative Jacobians of the CVs may be produced. Additionally, the computational overhead associated with this method is significant.

6.1.3. SLIDING INTERFACE

Another technique to incorporate rigid body motion could be to use a so called sliding interface between a part of the grid which rotates with the investigated body and the non-rotating outer part (Figure 6.1c). Linear movements are resolved by both parts of the grid. Therefore the technique allows having fewer cells in the outer grid, since one only needs to resolve the fixed free surface interface here. The computational effort increases by about 20 - 50% compared to the moving grid strategy, which seems acceptable. To allow for rotation in all 3-DOF, the body to be investigated has to be integrated into a sphere. With boats being much longer than broad, this does not allow to take advantage of having fewer cells in the outer grid since the sphere has to have a diameter bigger than maximum boat length. Therefore one has the disadvantage of higher cell numbers necessary to resolve the free surface which is associated with the moving grid approach plus the additional computational overhead for interpolating the solution over the sliding interface. The method therefore is more computational costly than the grid motion

approach and bears no advantage in terms of accuracy.

6.1.4. OVERSET GRID

Another strategy could be to use overset grids. Within this technique, a fixed background grid is employed in combination with a second grid around the rigid body. This second grid overlaps the background grid and is allowed to move freely within it (Figure 6.1d). Overlapped regions in the background grids are set inactive and transfer cells (donor / acceptor cells) between background and overset grid are computed as the rigid body moves through the domain. Flow variables from donor cells are interpolated on the acceptor control volumes using linear or distance-weighted interpolation algorithms. In the author's opinion, this approach has the potential to become the most flexible and elegant.

However, the technique is relatively new and still lacks some reliability. It also comes with some disadvantages inherent to the method. The most obvious disadvantage is a Courant number restriction. Flow through donor cells shall not exceed CFL=0.5, respective 0.3 for a second-order time-integration scheme, in order to correctly model the flux of transport variable between the two grids. Furthermore, one has to be cautious that grid motions relative to each other do not cover more than half a cell per time step in order to avoid numerical instabilities. The idea behind this is, that a cell has to be a acceptor cell for at least one time step (two for second-order time integration) in order to hold a solution history which enables it to act as a donor cell. A further problem is that due to the interaction of fluxes on the two grids, mass conservation is not guaranteed. Furthermore, the necessary determination of donor and receiver cells and the interpolation between them adds a significant amount of computational effort to the simulation.

Despite this restriction, simulations have been carried out using a suitable combination of background and overset grid on a yacht hull geometry. Care was taken that the difference in volume of grids in the overset region did not exceed factor 2 in order to fulfill interpolation requirements. In a first attempt (Testcase 1) to emulate large motions, the boat was rotated to a heeling angle of 27.5° degree. It was then allowed to heel, pitch, heave and sway. After setting the body free, the boat successfully returned to its upright position see Figure 6.2a) within a few oscillations. Details of the free surface interface are illustrated by Figure 6.2b), showing that the interface is normally captured within three cells.

In a second test, Testcase 2, heel and sway have been fixed and the simulation was run for a simulation time of 20 s at a time step size of $\Delta t = 0.005$ s. In initial conditions, the free surface interface was captured over approximately 3 cells. However, this slowly changed as illustrated by Figure 6.3a). As one can see from the detail view in Figure 6.3b), the free surface interface is not sharply captured over 1-3 cells, but instead the interface is thick and covers almost 20 cells.

As mentioned earlier, due to the interaction of fluxes on the two grids, mass conservation is not guaranteed within the overset grid approach. It therefore seems most likely that the encountered problem in steady conditions results from an interpolation error at the intersection between the two grids. This seems to introduce a self-energizing error in transport of VOF scalars which degrades the solution. It is noticeable that the problem has not been encountered within simulations in which significant motions occur. Therefore, despite its great potential, the method was abandoned as not suitable for the time being.

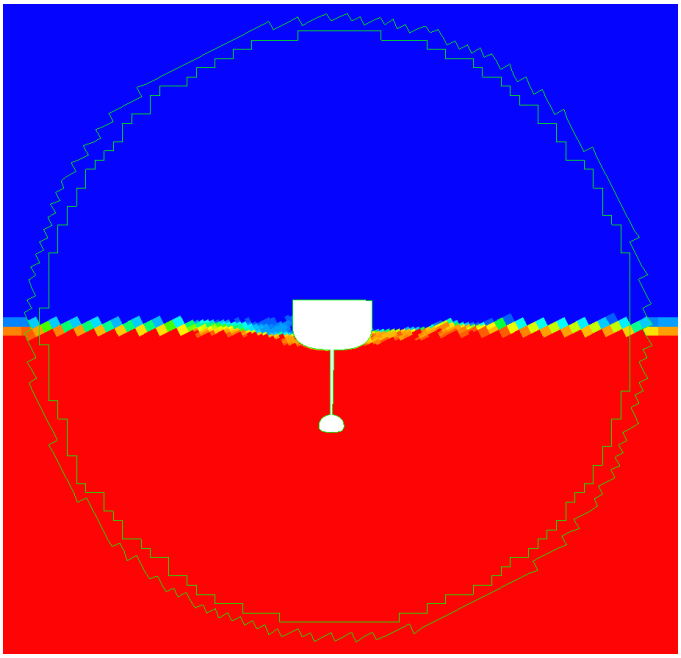

(a) Boat in upright position after righting from 27.5° heel.

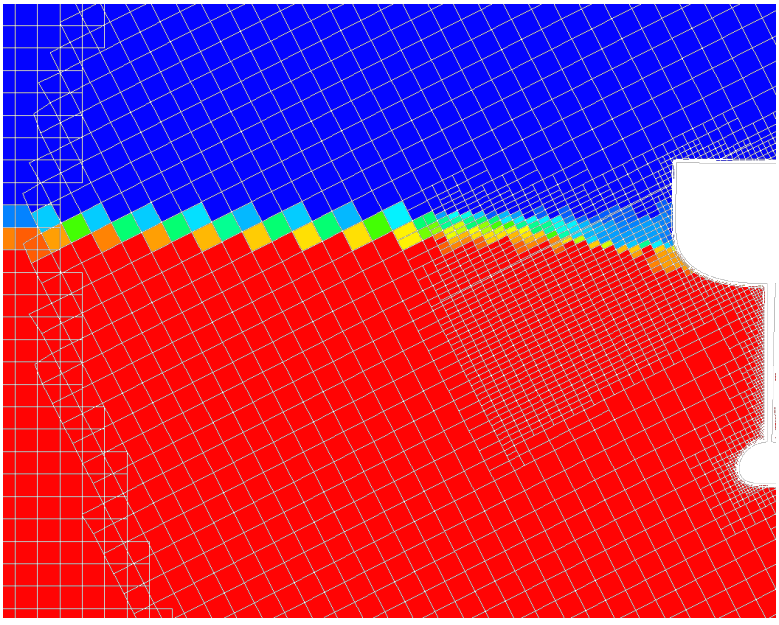

(b) Detail of free surface around boat in upright position

Figure 6.2: Testcase 1: Test of relative grid motion using overset grids by self-righting of a boat from heeled condition.

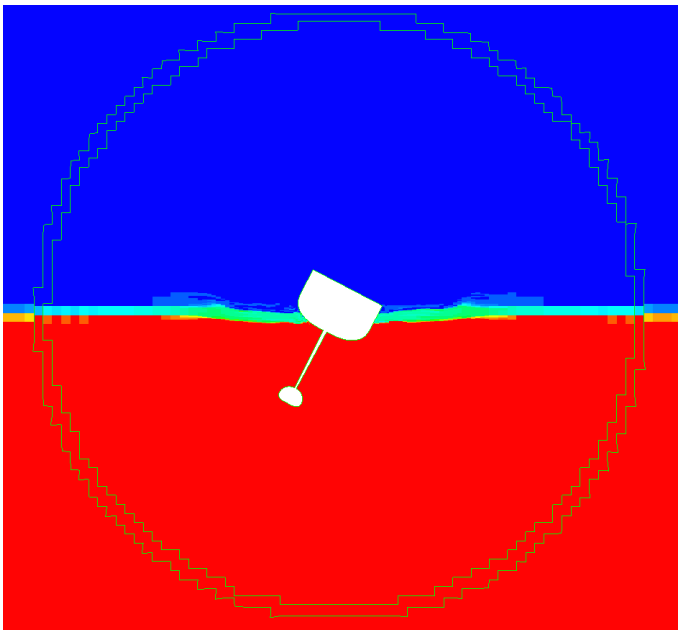

(a) Free surface representation in fixed conditions, after $t = 20$ s of simulation time.

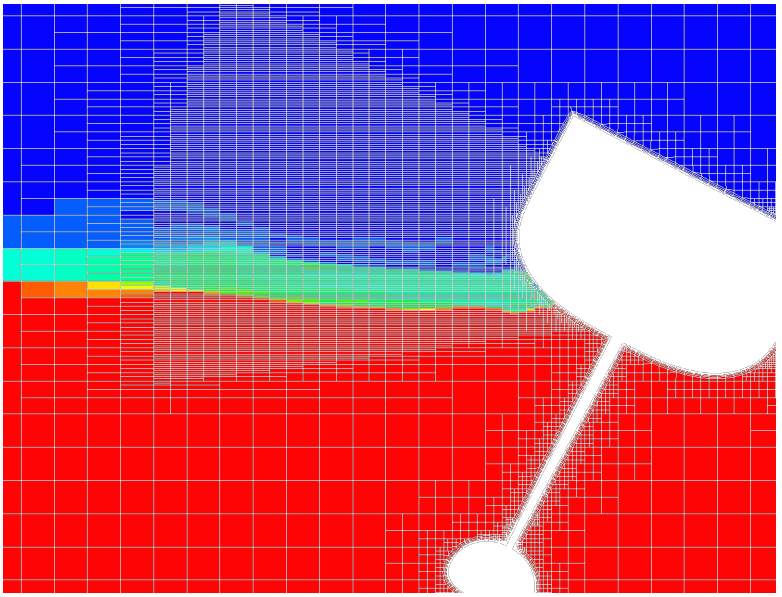

(b) Detail of free surface representation after $t = 20$ s.

Figure 6.3: Testcase 2: Test of free surface capturing in steady conditions (no rotations and translations) using overset grid approach.

6.2. GRID MOTION APPROACH FOR RANSE-VPP

From the review of grid motion techniques in Section 6.1, the moving grid strategy emerged as the most efficient and robust solution. However, the free surface interface is not smoothly resolved when grid cells are cut in an inappropriate angle. This makes it difficult to cover large heel angle variations.

The solution used throughout this work is to allow only a limited amount of rotation per simulation of yacht state for a given combination of true wind speed V_T and true wind angle β_T. Therefore, the approximate amount of heeling moment to be expected has to be estimated in advance.

In order to allow for fine resolution of the free surface interface, the initial refinement zone in this region as depicted in Figure 6.4a) is extended by introducing a vertical refinement zone (Figure 6.4b). Care has to be taken regarding suitable aspect ratio of cells in order to allow geometric reconstruction of the free surface interface. The strategy as described above approximately doubles the total grid cell number and allows for rotation angle of +/- 7°. Free Surface resolution with and without vertical refinement is illustrated in Figures 6.4 c) and d). It can be seen that while the free surface in Figure 6.4c) shows wrinkles, the same in Figure 6.4d) is smooth. While larger rotation angles would have been desirable, the approach proved to be sufficient as will be shown in Section 9.

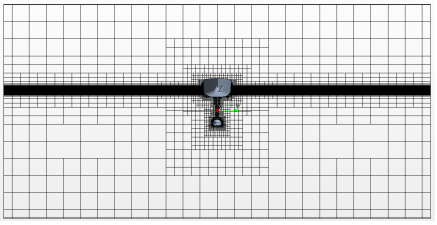

(a) Initial moving grid

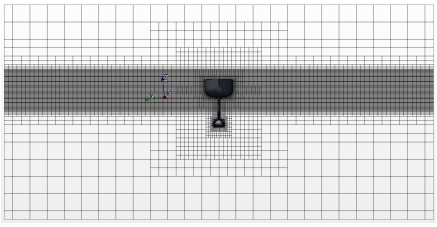

(b) Moving grid with vertical refinement zone

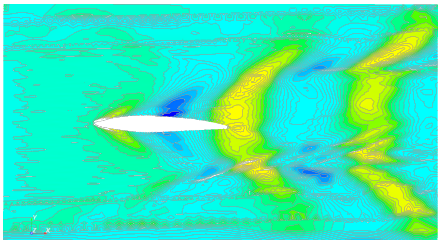

(c) Free Surface Resolution with Initial moving grid

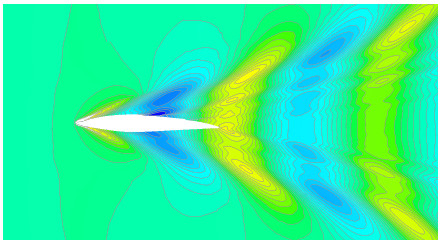

(d) Free Surface Resolution with vertical refinement zone

Figure 6.4: Grid motion approach with vertical refinement zone

7

VERIFICATION AND VALIDATION OF PREREQUISITES FOR RANSE-VPP

7.1. INTRODUCTION

This following chapter describes the verification and validation for the hydrodynamic model of the RANSE-VPP. It starts with problems encountered and presents a solution approach derived from the free surface theory review in Chapter 3.1. This solution approach is then proved by means of an academical test case. Afterward, a formal verification and validation of the hydrodynamic model is shown, based on ITTC procedures regarding *Uncertainty Analysis in CFD* [129].

7.1.1. PROBLEM OVERVIEW

In a first attempt to validate free surface simulations of an ACCV5 yacht with experimental towing tank data, significant differences in resistance values have been found. The RANSE CFD simulations showed a lower resistance than the experimental data. Figure 7.1 shows the resistance curve for both EFD and CFD. The difference between both resistance curves is approximately 8%.

Single phase RANSE simulations normally tend to over-predict drag values if grid resolution is insufficient. This behavior is not absolutely transferable to free surface ship flows, were an insufficient resolution of the wave pattern might also lead to a under-prediction of drag. Nonetheless, under-prediction of drag hints to look at modeling errors. Figure 7.2 illustrates the *volume fraction of water* values on the hull. Normally one

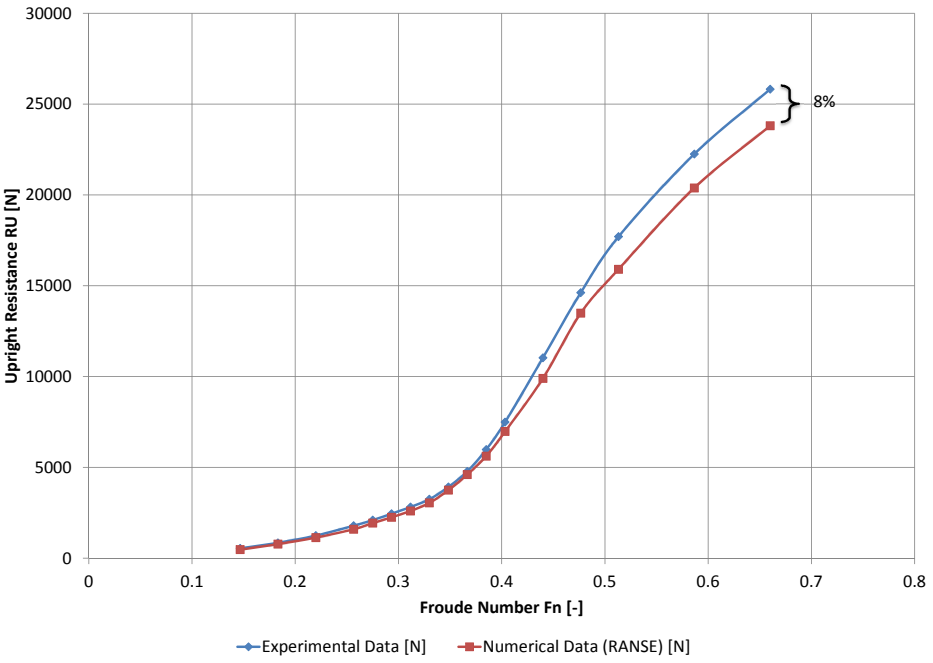

Figure 7.1: Comparison of experimental and numerical resistance data

would expect that the values are zero in the air region, one in the submerged area of the hull and between zero and one in a small region around the free surface interface. In the vicinity of a sharp interface, this region should not significantly extend over more than three cells. Figure 7.2 clearly shows that this not the case here. Instead volume fractions are smeared over the complete hull, except around the appendages and in their wake. This clearly indicates a smeared free surface interface. Due to the nature of the treatment of physical properties of flow phase within the VOF model, this will lead to smaller resistance values. For a detailed description of the VOF model see Chapter 3.1.3. It has to be noted that the interface smearing as described above has only been encountered for specific floating bodies. These bodies have in common that they share a rather blunt bow which forms a small, acute entrance angle with the waterline. For conventional vessel which normally have sharp bow with a right angle at the dead water line (DWL), this problem does not occur. It is therefore kind of yacht-specific.

7.1.2. THEORETICAL TEST CASE

The convection scheme used in the context of this work to transport volume fraction values through the domain is the HRIC scheme. The HRIC scheme is the currently most successful advection schemes and widely used in many CFD codes. It has been devel-

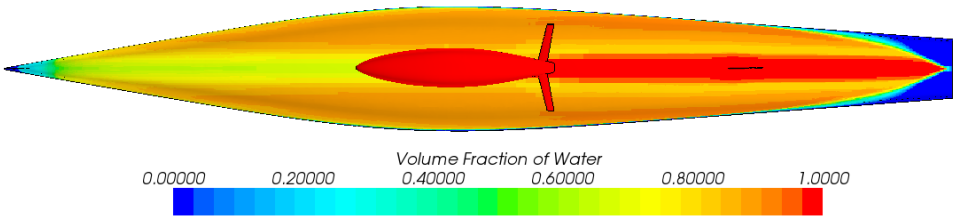

Figure 7.2: Volume Fractions under an ACCV5 yacht. The plot illustrates problems encountered with interface smearing

oped by Muzaferija and Peric [98, 99, 97]. Like most others schemes, is based on an blending of bounded Upwind and Downwind differencing schemes. Its aim is to combine the compressive properties of the Downwind differencing scheme with the stability of the Upwind scheme. A detailed review of the model is presented in Chapter 3.1.3. As described in Chapter 3.1.3, the HRIC scheme is modified depending on local Courant number. This modification blends between the HRIC scheme and a UD scheme depending on an upper and an lower Courant number. Below the lower limiting number CFL_L, the HRIC scheme is used. Between CFL_L and the upper limiting number CFL_U HRIC and UD scheme are linearly blended. Above CFL_U pure 1st order UD scheme is used.

Since various authors have found that the UD scheme smears the free surface interface (for example see Ferziger and Peric [63] or Andrillion and Alessandrini[130]), this could well be the main source for the problems reported in the previous section. From a theoretical point of view, the sole purpose of the correction of the HRIC scheme for local CFL is to improve robustness. If unsteady phenomena like slamming and or seakeeping are of interest, local Courant Number should be inherently lower than 0.5 anyway. If robustness is not problematic then this switch should be of no interest for calculations which seek a steady state solution. Since simulations mimicking towing tank procedures seek such a steady state solution, the HRIC scheme is modified such that the switch is effectively removed.

From theory review in Chapter 3.1.3 the conclusion was drawn that it is possible to conduct free surface simulation without smeared interface at Courant number greater than the switch level under the assumption that the simulation only searches a final or steady solution. Here the idea is to suppress the switching to pure Upwind Differencing Scheme. To control the validity of this assumption a test case has been constructed. Aim of the test case is to produce a worst case scenario which makes it possible to judge if the modified differencing scheme can cope with this situation. From a theoretical point of view, the case which would produce the highest amount of numerical diffusion and thus the highest amount of interface smearing is a flow through a quadratic grid cell at an angle of 45°. Therefore a 2D Cartesian grid has been build which consists of 128 x 128 grid cells. The grid spacing was chosen to be 1/128 of the domain edge length. Due to this very fine grid spacing, a refinement study has been omitted. Initial volume fraction

distribution is such that the lighter fluid (air) occupies the upper left triangle of the domain (blue) whilst the heavier fluid (water) is found in the lower right side (red). Inflow conditions for volume fraction have been set such that this state should remain within the simulation. Outlet has been set to Neumann conditions. A sketch of the setup is depicted in Figure 7.3. The initial distribution of the field variables at simulation start gives a interface which is smeared over three cells. Depending on the local Courant number, the HRIC scheme switches between:

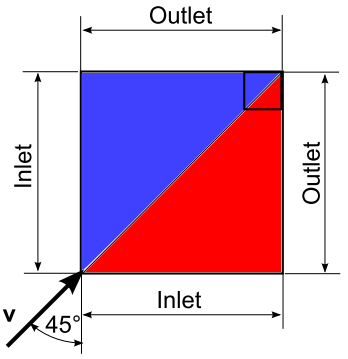

Figure 7.3: Sketch of test case setup

1. A pure HRIC scheme if CFL < 0.5
2. A linear interpolation between HRIC and UD scheme if 0.5 ≤ CFL ≤ 1.0
3. A pure UD scheme if CFL > 1.0

The influence of these different states on the sharpness of the interface is tested by varying flow speed and time step size such that the relevant criteria is fulfilled. First, CFL is set to 0.2823 resulting in a pure HRIC scheme (Figure 7.4 a)). Even though the flow direction with respect to cell faces is unfavorable, the HRIC scheme is able to resolve the sharpest interface possible within the VOF method (1 cell). Next the CFL is increased to 0.75, resulting in 50% blend between HRIC and UD (Figure 7.4 b). This blend is also still sufficient to retain the sharp interface and therefore gives a valid solution. An explanation for this behavior can be found in the blending strategy depending on interface angle. As depicted in Figure 3.9, the difference between the pure HRIC and the blended HRIC is reasonably small for a cell flow angle of 45° which explains the similar results. Finally, flow speed and time step size of the unsteady simulation are set to values such that the Courant Number in the entire domain is 2.823. This leads to switching to a pure Upwind Differencing Scheme within the HRIC scheme. As a result the interface between air and water becomes severely smeared and is forming a cone-like shape starting from inlet towards outlet (Figure 7.4 c). Now the HRIC scheme is modified by removing the CFL dependency. The Courant number is kept at 2.823 and the simulation repeated. Figure 7.4 d) illustrates the result which clearly shows that this modification allows using higher CFL numbers whilst a sharp interface is retained.

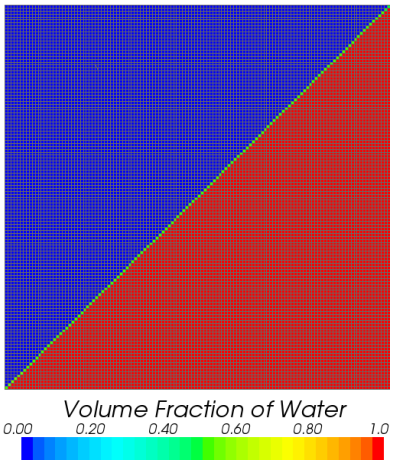

(a) HRIC, CFL = 0.2823

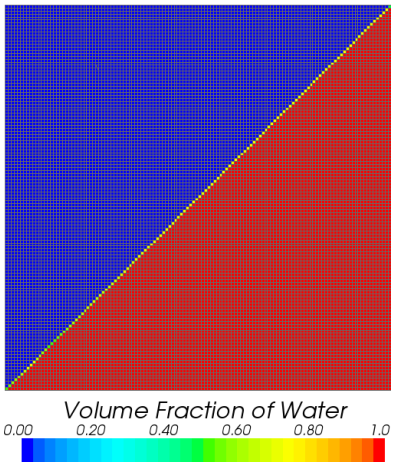

(b) 50% Blend HRIC/UD

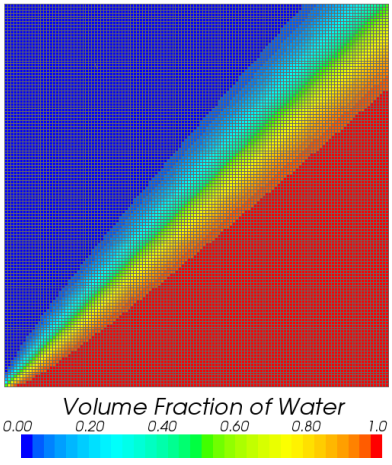

(c) Upwind Convection Scheme, CFL= 2.823

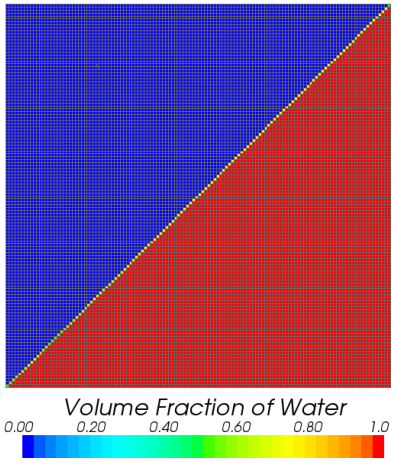

(d) Modified HRIC, CFL = 2.823

Figure 7.4: Overview of test case

To see if the results achieved for the 2D test case are also valid for the 3D, fully non-linear case of a free surface calculation around a boat free to move, simulations have been conducted with and without the described modification to the HRIC scheme. Also the results will be discussed in more detail in Section 7.2.3, Figure 7.5 gives a first impression of the impact of the modification on numerical ventilation on the boat surface. The upper plots show volume fraction of water for the standard approach with Courant number dependency, while the lower plots do the same for the modified approach. It can be clearly seen that the new approach gives a much sharper interface. For example, the bow wave is captured in more detail in Figure 7.5c) then in Figure 7.5a). However, it also has to be noted, that the interface is still not perfectly sharp and some smearing remains. This is especially good visible in Figure 7.5d). Also this remaing smearing is not satisfying, one can see large improvement between Figure 7.5b) and Figure 7.5d). The range of volume fraction for the old approach was between 0.4 and 1.0, while for the new approach the range is between 0.85 and 1.0. The impact on wave resolution will discussed in Section 7.2.3 and is shown in Figure 7.9. Summarizing the above, it can be concluded that the modification of the HRIC scheme seems well suited to simulate free surface flows at higher Courant numbers, allowing to converge faster towards a steady state solution. The applicability of the modification will be further investigated in Section 7.2.3.

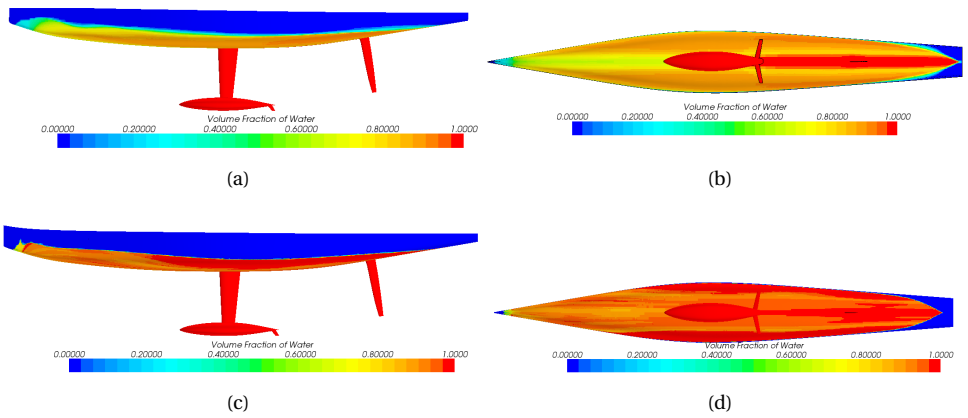

Figure 7.5: Comparison of Numerical Ventilation with Courant Number dependency (old approach (a) and (b)) and without (new approach (c) and (d))

7.2. VALIDATION AND VERIFICATION OF FREE SURFACE FLOW AROUND AN ACCV5 YACHT AGAINST TOWING TANK DATA

Verification and validation procedures are carried out against experimental data of an America's Cup V5 boat. Since the model scale $\lambda = 3$, which is rather close to the original compared with towing tank testing of conventional vessels, it was decided that it is possible to do the validation in full scale. Therefore, experimental data have been transformed

to full scale by employing a modified version of the ITTC procedures. The modification applied mainly consists of individual treatment of the various surfaces of yacht hull and appendages with respect to friction and $(1+k)$ values. As stated in Section 7.1.1, the initial comparison between numerical results and experimental data showed a resistance difference of about 8%. Besides the numerical error introduced by the smeared interface, it was found that pitch angles differed significantly between simulation and experiment. Since this error most probably results from different application of sail trimming moments, it was decided to remove this error source from the validation and verification procedures. Therefore the simulation model was pre-trimmed to the pitch angle stated in the experimental data and kept fixed. The boat is thus only allowed to heave dynamically.

First a short definition of the terms verification and validation is necessary:

Verification includes the assessment of numerical uncertainty, magnitude and sign of numerical error (if possible) and uncertainty in error estimation.

Validation is the assessment of uncertainty of the simulation model by means of experimental data plus the assessment of the modeling error itself.

The verification and validation procedure will be carried out in accordance with recommendations of the ITTC regarding *Uncertainty Analysis in CFD* [129]. For a detailed description see also Stern et al. [131, 132]. The simulation error δ_S is defined as the difference between simulation result S and reality or truth T. It consists of the modeling error $\delta_{SM}$and the numerical error δ_{SN}. Unfortunately S can never be determined exactly since instead of T only experimental results are available which also contain a certain level of uncertainty.

$$\delta_S = S - T = \delta_{SM} + \delta_{SN}. \tag{7.1}$$

For some cases magnitude and sign of the numerical error can be estimated, leading to corrected numerical uncertainty $U_{S_C N}$. For the uncorrected case only the numerical uncertainty U_{SN} is assessed. Therefore the numerical error δ_{SN} is decomposed into contributions from iteration number δ_I, grid size δ_G, time step δ_T and other parameters δ_P. With U_P as described above this gives the following expression:

$$U_{SN}^2 = U_I^2 + U_G^2 + U_T^2 + U_P^2. \tag{7.2}$$

For validation purpose the comparison error E between the benchmark experimental data D and the simulation result S is determined in order to asses modeling uncertainty U_{SM}.

$$E = D - S = \delta_D - (\delta_{SM} + \delta_{SN})\,. \tag{7.3}$$

To determine if validation of a value has been achieved, comparison error E is compared with the validation uncertainty U_V.

$$U_V^2 = U_D^2 + U_{SN}^2. \tag{7.4}$$

If $|E| < U_V$, than the combination of all errors in both simulation and experimental data is smaller than the validation uncertainty. Then validation has been achieved for this validation uncertainty level. In the case that $U_V << |E|$, the modeling error δ_{SM} can be used to achieve modeling improvements.

7.2.1. VERIFICATION PROCEDURE

In the course of the verification process a grid convergence study on m solutions has to be conducted. In order to do this it is necessary to use a minimum of three grids ($m = 3$) which have been uniformly refined with an increment Δx_k such that constant refinement ratio r_k exits.

$$r_k = \frac{\Delta x_{k_2}}{\Delta x_{k_1}} = \frac{\Delta x_{k_3}}{\Delta x_{k_2}} = \frac{\Delta x_{k_m}}{\Delta x_{k_{m-1}}}. \tag{7.5}$$

ITTC Guidelines recommend refinement ratio r_k between $\sqrt{2}$ and 2. Throughout this work a ratio of 2 has been chosen. Next a convergence ratio R_k is defined to give information about convergence respective divergence of a solution. This is done by considering the solution changes ϵ_{ijk} for the input parameter k between three solutions ranging from fine S_{k_1} to medium S_{k_2} and coarse S_{k_3}.

$$\begin{aligned} \epsilon_{21_k} &= \hat{S}_{k_2} - \hat{S}_{k_1} \\ \epsilon_{32_k} &= \hat{S}_{k_3} - \hat{S}_{k_2}, \\ R_k &= \epsilon_{21_k} / \epsilon_{32_k} \end{aligned} \tag{7.6}$$

According to the ITTC guidelines [129], three different cases may occur:

$$\begin{aligned} &(i) \text{ Monotonic convergence: } 0 < R_k < 1 \\ &(ii) \text{ Oscillatory convergence: } R_k < 0^i \\ &(iii) \text{ Divergence: } R_k > 1 \end{aligned} \tag{7.7}$$

In the case of (i) the Generalized Richardson Extrapolation (RE) is used to assess the uncertainty U_k or the error estimate $\delta_k^\star$ and the corrected uncertainty U_{k_C}. For oscillatory convergence (case (ii)) the uncertainty U_k is estimated by determining the error between minimum and maximum of the oscillation. Equation (7.7) is only valid if we are in the asymptotic regime. This is only the case for simplified test cases but not for complex 3-dimensional flows around ship hulls. However, Stern et al. [132, 133] demonstrated, that it is feasible to apply the procedure to free surface simulations of ships. The procedure is recommended by the ITTC and good practice in maritime CFD by today. Nonetheless, one has to be careful with the results of this verification and validation procedure. It has to be pointed out that even with a successful verification and validation one still has to look closely at the results and judge them with expert knowledge. This is especially true for yacht hydrodynamics, for which, to the author's knowledge, this procedure has been used for the first time.

$$U_k = \frac{1}{2}(S_U - S_L) \tag{7.8}$$

Oscillatory convergence might be erroneously recognized as case (i) or (iii). Therefore it is often necessary to investigate more than three solutions to get a sensible assessment of the error $\delta_k^\star$. In the case of divergence (iii) it is not possible to estimate errors or uncertainties.

GENERALIZED RICHARDSON EXTRAPOLATION

As stated above, in case of monotonic convergence generalized RE is used to determine the error $\delta_k^\star$ with respect to refinement ratio r_k and order-of-accuracy P_k [129]. Here, order-of-accuracy P_k denotes a quantification of the rate of convergence. Usually $\delta_k^\star$ is estimated for the finest solution of the input parameter $m = 1$ only. With number of available solutions $m = 3$ only the leading-order term of the error may be evaluated. This gives the following equations for $\delta_k^\star$ and p_k:

$$\delta_{k_1}^\star = \delta_{RE_{k_1}}^\star = \frac{\epsilon_{21_k}}{r_k^{p_k} - 1}, \tag{7.9}$$

$$p_k = \frac{ln\left(\epsilon_{32_k}/\epsilon_{21_k}\right)}{ln\left(r_k\right)}. \tag{7.10}$$

In the range of monotonic convergence, p_k as formulated in (7.10) gives a quantification, with respect to refinement ratio r_k, of how good the solution S_{k1} on the fine grid is converged towards a grid independent solution. Values of $p_k > 1$ here describe a state near to grid independence. The error $\delta^\star_{k_1}$ is then evaluated by using RE as formulated in (7.9). The formulation has been generated from an analytical derivation of the simulation error equation which is given in detail by Stern et al. [133]. The extrapolation implies that small solution changes from medium to fine grid in combination with a high rate of convergence give a small error $\delta^\star_{k_1}$. Unless the solution is in the asymptotic range, (7.10) only gives a poor estimation of the rate of convergence. Therefore a correction factor C_k is used to include the effect of higher-order terms neglected earlier. C_k is defined as follows:

$$C_k = \frac{r_k^{p_k} - 1}{r_k^{p_{k_{est}}} - 1}, \tag{7.11}$$

with $p_{k_{est}}$ as an estimation of the theoretical rate of convergence. The correction factor C_k mainly divides the denominator of (7.9) by $p_{k_{est}}$, thus replacing r^{p_k} with $r^{p_{k_{est}}}$. The corrected error $\delta^\star_{k_1}$ is defined by combining equations (7.9) and (7.11)

$$\delta^\star_{k_1} = C_k \delta^\star_{RE_{k_1}} = C_k \left(\frac{\epsilon_{21_k}}{r_k^{p_k} - 1} \right). \tag{7.12}$$

The correction C_k makes (7.12) a single term estimate which roughly accounts for higher order terms. Depending how close the corrected error $\delta^\star_{k_1}$ is to the asymptotic range (how close C_k is to 1) the expression to assess the uncertainties takes different forms. If C_k is sufficiently greater than one and there are reasons to doubt simulation results, for example due to local oscillations, only U_k is estimated by the following formula:

$$U_k = \left| C_k \delta^\star_{RE_{k_1}} \right| + \left| (1 - C_k)\, \delta^\star_{RE_{k_1}} \right|. \tag{7.13}$$

The above assumes, that the uncertainty $U_k = \delta^\star_{RE_{k_1}}$ in the range of $0 \leq C_k \leq 1$. For C_k being sufficiently smaller than one the ITTC recommends to use expression (7.14) to assess U_k.

$$U_k = \left| \delta^\star_{RE_{k_1}} \right| + 2 \left| (1 - C_k)\, \delta^\star_{RE_{k_1}} \right| \tag{7.14}$$

This results in a larger uncertainty for $C_k < 1$ which slowly converges towards the original formulation in (7.13) for $C_k = 1$. The reason for this modification is that Wilson and Stern [134] showed that the estimate for uncertainty U_k of (7.13) was not conservative enough. If C_k is sufficiently close to 1, the error $\delta^\star_k$ can be estimated. This allows to determine a corrected solution S_C and a thus a corrected uncertainty U_{k_C}.

$$U_{k_C} = \left| (1 - C_k)\, \delta^\star_{RE_{k_1}} \right| \tag{7.15}$$

7.2.2. VALIDATION PROCEDURE

As stated in Section 7.2, validation is defined as a process to model the uncertainty U_{SM} and, if possible, sign and magnitude of the modeling error δ_{SM} itself. This is done by using experimental data to compare the simulation results with. Therefore, the error in the experimental data has to be considered. This implies, that if the experimental is error is large, a validation of simulations is easier achieved than for small experimental errors, but obviously the quality of such a validation suffers. It must thus be stressed that the quality and the level of validation is strongly depended on the quality of the comparison data. To judge the quality of a validation, one should always take into account the quality of the data which were used as reference. The validation procedure is based on the relation between validation uncertainty U_V, predefined programmatic validation requirement U_{reqd} and comparison error $|E|$. These three variables may form the following six combinations:

$$\begin{aligned} &|E| < U_V < U_{reqd} \\ &|E| < U_{reqd} < U_V \\ &U_{reqd} < |E| < U_V \\ &U_V < |E| < U_{reqd} \\ &U_V < U_{reqd} < |E| \\ &U_{reqd} < U_V < |E| \end{aligned} \tag{7.16}$$

In cases 1 - 3 of (7.16) the results are validated. Validation is achieved at the level of validation uncertainty U_V. This means that the comparison error is below the noise level resulting in an impossibility to estimate error due to modeling assumption δ_{SMA}. In the case of 1, the validation level is also below U_{reqd} which makes the validation successful from a programmatic point of view. For case 4 - 6 the comparison error is above the noise level. Sign and magnitude of E can be used to estimate δ_{SMA}. In the fourth case the validation is achieved at $|E|$ level with respect to the used software.

7.2.3. GRID CONVERGENCE STUDIES ON ACCV5 BOAT FOR NON-LIFTING CASES

Verification and validation is performed on the geometry of Americas Cup Class Version 5 (ACCV5) boat for which experimental towing tank data is available. These boats have a rather complex geometry which besides hull, keel fin and rudder also includes a trim tab for the keel and a ballast bulb with wings (Figure 7.6). Principal dimensions of the yachts and the fluid properties used are illustrated in Table 7.1. The conditions of the calculations are a Froude number Fn of 0.403 and normalized Reynolds number Re of 4.75×10^6. The boat is allowed to sink dynamically, but not to pitch. The pitch angle is prescribed at $\psi = 0.46°$ bow down trim. The commercial flow solver *STAR-CCM* is

used to solve the Reynolds-Average-Navier-Stokes equations for the flow field around the yacht. The simulation is conducted at fully turbulent conditions and the $k-\omega$ based *Shear Stress Transport (SST)* model has been used to model turbulence.

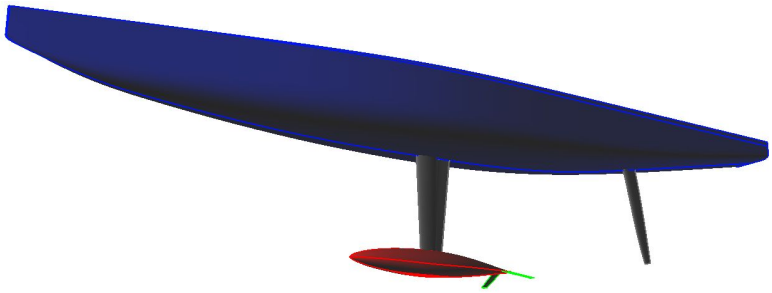

Figure 7.6: ACCV5 geometry

Table 7.1: Geometry and flow dimensions

Principle Dimensions		
LOA:	[m]	25.250
BMAX:	[m]	3.217
Draft:	[m]	4.178
LWL:	[m]	20.015
Sailing Displ:	[t]	26.405
LCG:	[m]	-0.942
TCG:	[m]	0.000
VCG:	[m]	-2.361
Fluid Properties		
Density ρ:	$[\mathrm{kg\,m^{-3}}]$	1025.00
Dynamic Viscosity μ:	[Pa s]	1.22×10^{-3}
Froude Number Fn:	[−]	0.403
norm. Reynolds Nr. Rn:	[−]	4.75×10^{6}
y^+:	[−]	50
Datum Point is intersection of DWL, Centreplane and Hull Station 5. X is positive forward, Y is positive to Port, Z is positive up.		

COMPUTATIONAL GRIDS

Grid Convergence studies have been conducted using 3 different combinations of refinement parameters to study their impact on grid densities and computational results. The computational grid has been modeled such that it depends on one *base number*. The *base number* is a absolute dimension which is considered typical for the resolution of the flow field. All other grid parameters, like surface minimum and maximum sizes,

free surface refinement and so on, are given as percentage of the *base number*. This way it can be ensured that a constant grid refinement ratio r_k is used. Two exceptions from this modeling paradigm exist. First the prism layer used to resolve the boundary layer around hull and appendages is excluded from refinement because this would lead to large changes in Y^+ values. In turn, this most likely would lead to changes in near-wall treatment like using a low-Reynolds approach for one simulations and wall functions for the other. This would render the simulations incomparable. Therefore the total thickness of the prism layer, the thickness of the wall nearest node and the number of prism layers are kept constant throughout this verification and validation. The second exception concerns the resolution of the free surface. Since free surface resolution is very important for correct resolution of ship drag, it has been given its own base number. This way it is possible to evaluate the influence of different refinement ways on grid sizes and simulation results. The refinement ways investigated within this work are:

1. *Global refinement*; were only the global grid base number is refined.
2. *Free Surface refinement*; were only free surface parameters are refined by their base number. Free surface refinements consists of a vertical refinement in the whole domain at the expected level of the wave pattern and a second refinement in both longitudinal and traversal direction in the vicinity of the Kelvin pattern.
3. *Overall refinement*; were both global and free surface base number are modified as a function of the refinement ratio r_k.

For all three cases four grids with constant refinement ratio $r_k = 2$ have been constructed. The three cases along with the changes in free surface parameters and resultant grid size are illustrated in Table 7.2. It is interesting to note that the influence on total grid size is very different for the particular parameters. This happens because the grids are not uniformly refined. Instead the grids are refined by changing the relevant base number(s). The refinement is therefore based on changes to cell numbers on surface and in control volumes defined as refinement zones. These refinements are aimed at areas where large flow gradients occur. There are several reasons behind this approach:

1. The grid approach is of trimmed cartesian type. In contrast to a hexahedral grid, this approach does not lend itself naturally to uniform refinement.
2. If a uniform refinement would have been chosen, the cell numbers necessary to achieve high accuracy would have led to very high computational costs. This would not have been manageable by the available computational resources.
3. The chosen approach allows new insights regarding necessary refinement areas and volumes which can be used for future simulations of yacht drag.

Figure 7.7 shows that free surface refinement has the biggest influence on grid size, whilst the influence of the global base size is minor. It has to be kept in mind that re-

finement in the volume grid, like in the case of free surface refinement, is also projected on adjacent surfaces thus creating a fine surface grid within the refinement area.

Table 7.2: Overview of Grid Parameter Variations

General Base Size [m]	Free Surface Refinement Factor (-)	Interface dz [mm]	Interface Spacing [m]	Grid Size [–]
Global refinement				
1	1	30	0.25	10.39×10^6
2	1	30	0.25	8.94×10^6
4	1	30	0.25	8.18×10^6
8	1	30	0.25	7.80×10^6
Free Surface refinement				
1	1	30	0.25	10.39×10^6
1	2	60	0.5	4.38×10^6
1	4	120	1	3.47×10^6
1	8	240	2	3.30×10^6
Overall refinement				
1	1	30	0.25	10.39×10^6
2	2	60	0.5	2.97×10^6
4	4	120	1	1.36×10^6
8	8	240	2	0.81×10^6

VERIFICATION AND VALIDATION OF RESISTANCE

The verification of resistance has been performed with respect to grid convergence. Iterative convergence has been taken into account, but since it was in the order of 0.05% C_T it was considered negligible. Grid convergence studies have been performed for three different meshing approaches at 4 grids each. The results of these studies have been summarized in Tables 7.3 and 7.4. Table 7.3 illustrates the C_T values for the different grids as well as the solution change ϵ from a coarser to a finer solution between adjacent grids. Here ϵ is defined as:

$$\epsilon = \frac{(S_i - S_{i+1})}{S_{i+1}}. \tag{7.17}$$

The solution change ϵ gives a clue about the influence of further grid refinements and the convergence of the solution towards grid independence. The results show that the changes of C_T between the different solutions are largest in the case were free surface parameters variations are involved. Keeping in mind that the free surface grid parameters also created large differences in grid size (see Figure 7.7) this is not surprising. Verification results are illustrated in Table 7.4. Here convergence ratio R_G indicates monotonic

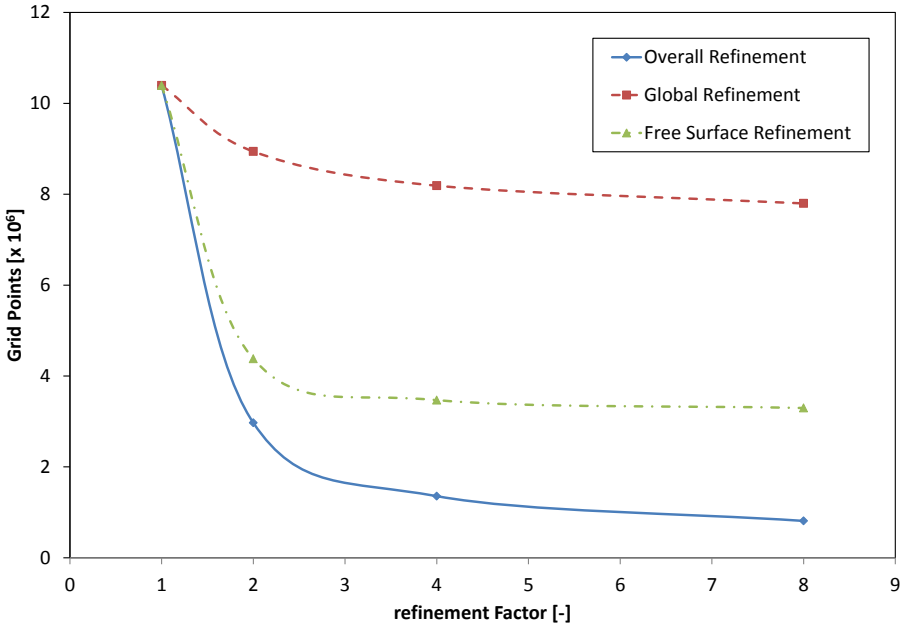

Figure 7.7: Number of grid points plotted over refinement factor r_k for the three refinement strategies used. One can see, that the global refinement strategy has a relative minor influence on grid cell numbers, while the influence of the free surface refinement is more distinctive. This is due to the fact, that free surface refinement create refined volumes while the global refinement is more biased towards the resolution of yacht hull and appendages. Combining both strategies (*Overall Refinement*) obviously has the biggest impact on cell numbers.

grid convergence of solutions for grids 1-3 for all three case ($R_G < 1$). For the coarser grid sequence (grids 2-4) only case 1 (Global refinement) shows monotonic convergence. This confirms the observation gained from the review of grid size (Figure 7.7) and grid convergence (Table 7.3), that the impact of global refinement parameters is not as large as the influence of free surface parameters. For the coarser grid sequence of the free surface refinement study (case 2) R_G indicates divergence while for the same grid sequence of the global refinement study (case 3) the solution appears to be of oscillatory nature. However, this last indicator seems to be misleading, so results for case 3.b are also treated as divergent. Section 7.2.1 showed that it is necessary to have at least oscillatory convergence to estimate the uncertainty and monotonic convergence is required to estimate the error. Therefore, it is not possible to estimate error or uncertainty for case 2.b and 3.b. Where appropriate Generalized Richardson Extrapolation is used to estimate the grid error. Order of accuracy p_G and the correction factor C_G are calculated according to equation (7.10) respective (7.11). C_G is deemed to be sufficiently close to 1 for all cases, thus allowing to estimate sign and magnitude of the error $\delta_G^\star$ and a corrected uncertainty U_{G_C} as well as a corrected solution S_C (equations (7.9) - (7.15)). The thus gained corrected solution can be compared to the solution S_G. This gives an esti-

Table 7.3: Grid convergence study for total resistance $C_T\,(\times 10^{-3})$ for ACCV5.

Case	*Var*	*Grid 4*	*Grid 3*	*Grid 2*	*Grid 1*	*EF Data*
1)	C_T	6.46	6.33	6.29	6.28	6.32
	ϵ		-2.0%	-0.6%	-0.2%	
2)	C_T	5.87	6.02	6.19	6.28	6.32
	ϵ		2.6%	2.7%	1.5%	
3)	C_T	6.06	6.05	6.24	6.28	6.32
	ϵ		-0.1%	3.1%	0.6%	

$\%S_G$

Table 7.4: Verification of total resistance $C_T\,(\times 10^{-3})$ for ACCV5. The table lists convergence ratio R_G, order of accuracy p_G, correction factor C_G, grid uncertainty U_G, error $\delta_G^\star$, corrected uncertainty U_{G_C} and corrected solution S_C.

Case		R_G	p_G	C_G	U_G	$\delta_G^\star$	U_{G_C}	S_C
1)	*(grids 1-3)*	0.34	1.54	0.64	0.11%	0.07%	0.04%	6.28
	(grids 2-4)	0.30	1.75	0.79	0.26%	0.20%	0.05%	6.28
2)	*(grids 1-3)*	0.58	0.79	0.24	2.06%	-0.50%	1.56%	6.31
	(grids 2-4)	1.08	-	-	-	-	-	-
3)	*(grids 1-3)*	0.20	2.32	1.33	0.25%	-0.20%	0.05%	6.29
	(grids 2-4)	-40.39	-	-	-	-	-	-

$\%S_G$

mate of the level of uncertainty of the simulation. Cases 1.a and 1.b result in corrected solutions of $-0.07\%S_G$ respective $0.01\%S_G$ whilst Case 2.a yields $0.50\%S_G$. The difference of the corrected solution to the fine grid solution for Case 3.a is $0.20\%S_G$. In all cases where an estimate of the numerical uncertainties was possible, the corrected solution does not differ much from the originally calculated. It can thus be concluded that in all those cases the level of verification is rather good and the results can be considered verified.

Validation of the simulation results is performed with respect to the results of the towing tank tests. Therefore the error is calculated according to equation (7.3) taking into account the simulation result S and the experimental data D. In order to conduct the validation as defined in (7.16), the validation uncertainty U_V has to be calculated (7.4). If applicable, a programmatic validation requirement U_{reqd} may be defined. Since this is not mandatory it was waived in this investigation. Validation is conducted for the uncorrected solution S and the corrected solution S_C. The corrected comparison error E_C is defined as in (7.3) but using S_C instead of S. Table 7.5 summarizes comparison error E, validation uncertainty U_V, experimental uncertainty U_D and simulation uncer-

Table 7.5: Validation of total resistance $C_T\,(\times 10^{-3})$ for ACCV5. For comparison error E and corrected comparison error E_C, the table shows comparison error E% itself, validation uncertainty U_V%, experimental uncertainty U_D%, simulation uncertainty U_{SN}%, all as percentage of experimental data D.

Case			E%	U_V%	U_D%	U_{SN}%
1)	*(grids 1-3)*	E	0.6	2.0	2.0	0.11
		E_C	0.7	3.2	2.0	0.04
	(grids 2-4)	E	0.4	2.0	2.0	0.26
		E_C	0.6	3.2	2.0	0.05
2)	*(grids 1-3)*	E	0.6	2.9	2.0	2.04
		E_C	0.1	4.1	2.0	1.55
	(grids 2-4)	E	2.1	-	2.0	-
		E_C	-	-	2.0	-
3)	*(grids 1-3)*	E	0.6	2.0	2.0	0.25
		E_C	0.4	3.2	2.0	0.05
	(grids 2-4)	E	1.2	-	2.0	-
		E_C	-	-	2.0	-

%D

tainty U_{SN} as percentage of D for both corrected and uncorrected approaches. It has to be noted that data uncertainty U_D has not been specified in the experimental towing tank data. Details regarding experimental uncertainties of large towing tank facilities are rarely found in literature. Longo and Stern [135] give values between 0.6% - 1.5% for a investigation of the surface combatant DTMB 5415 model while Yan et al. [136] give values of 2.8% for the same ship. Similar data for yacht investigation are not available. The only source for uncertainties of yacht investigation has been found in a presentation given by DeBord at Stevens Institute [137]. The data given in this presentation show the long term repeatability of towing tank tests to be approximately 3%. Also this overview of towing tank uncertainties is by no means complete, it can be concluded that the data uncertainty normally should not exceed 3%. However, a lower uncertainty level increases the quality of a validation. Under the assumption that the quality of the used measurement data is high, it was therefore decided that it is feasible to take into account a experimental uncertainty U_D of 2% for validation purpose. By comparing E% and U_V% in Table 7.5 one can easily see that for all cases in which the comparison error could be calculated, $E < U_V$ is true. Therefore results have been validated for all cases except case b (grids 2- 4) in case both free surface and overall refinement are applied. This coincides with the findings of the verification study and allows the conclusion that both verification and validation have been achieved for all refinement studies except the two cases stated above.

The formal validation and verification procedure as conducted above only allows to

draw conclusion regarding the finest grids in the study, in this case grid 1 and grid 2 respectively. While not giving the same level of certainty, a plot of resistance coefficient ΔC_T versus grid cells, as illustrated in Figure 7.8, is a feasible approach to judge the sensitivity of the solution to grid changes. It is interesting to note that with ongoing refinement, cases including free surface grid parameters show an increasing drag while for the general refinement case the opposite holds true. The latter one coincides with the commonly observed, that with ongoing refinement a RANSE solution gives smaller forces until grid invariance of results is reached. These investigations suggest that while this certainly holds for single phase investigation of deeply submerged bodies, it is not applicable to free surface flows around floating bodies. The reason for this behavior is that probably a too coarse resolution of free surface leads to increased wave damping thus altering the pressure fluctuations on the hull such that a lower wave resistance is predicted. However, to be sure this hypothesis would have to be proofed. The distribution of results also illustrates the high impact of free surface refinement parameters on overall grid density and resulting accuracy. It can be concluded that special attention has to be paid to these parameters in order to achieve reliable results.

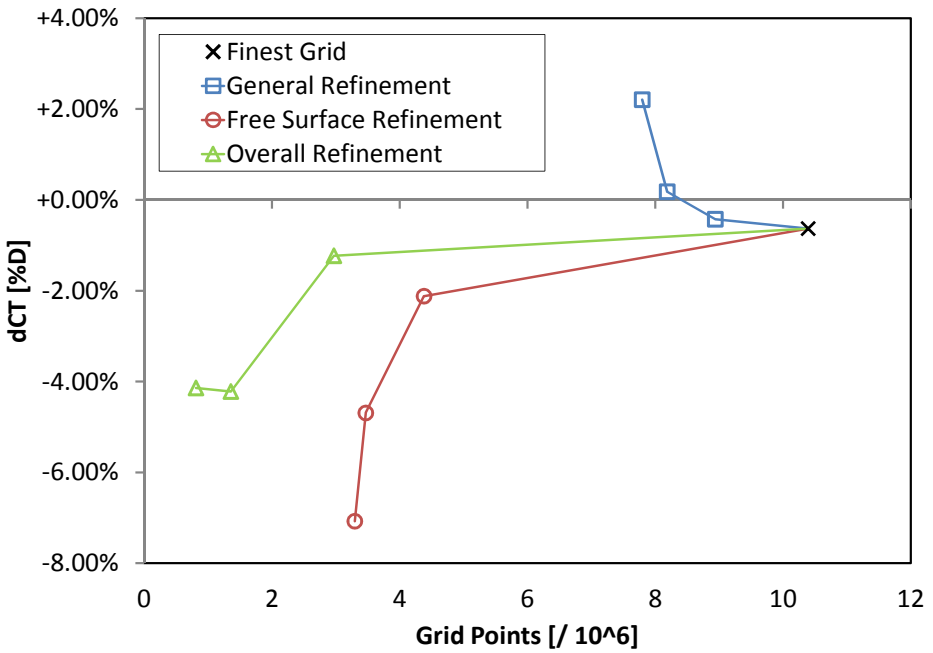

Figure 7.8: ΔC_T over Grip Points w.r.t to Experimental Data

Since the correct determination of wave resistance is crucial for reliable results on total resistance of ships, a refinement study for free surface flows has to take into account also its influence on generated wave patterns. Therefore wave patterns resulting from the simulations will be reviewed. Figure 7.9 compares wave resolution from ini-

tial studies (top) with results obtained with the modified HRIC scheme. The top picture shows that the computational domain is too short and the wave patterns diffuse and is damped. Especially this damping suggests an insufficient resolution of the free surface. The bottom of Figure 7.9 shows the finest grid in the investigation with 10.4×10^6 grid cells. Obviously there are large differences between the two simulations. The wave pattern obtained on the fine grid shows a sharp resolution of primary and secondary wave trains. Here wave damping is significantly reduced.

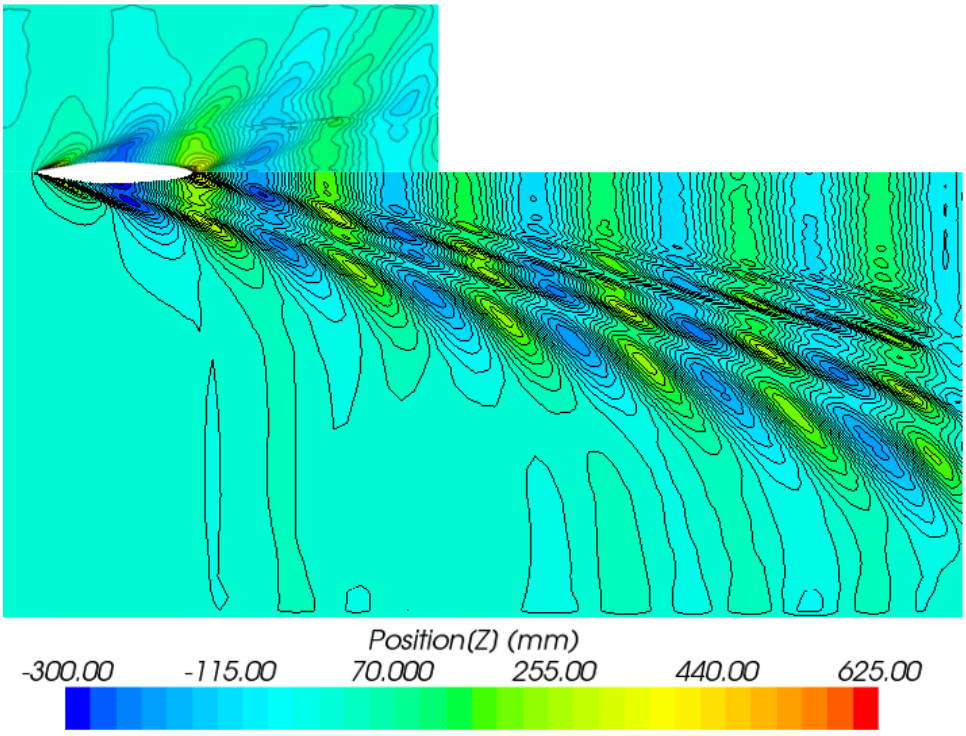

Figure 7.9: wave contours from *initial studies* (top) and from *Grid Convergence* studies (grid 1 - finest grid)

In the following the impact of the various grid refinement strategies on wave resolution will be discussed. The results of the general refinement show almost no differences in wave patterns. Keeping in mind that this part of the study did not explicitly alter free surface grid parameters, this is not very surprising. This observation also agrees with the findings from Figure 7.8 that increasing refinements lead to smaller forces holds true.

The situation for free surface refinement and overall refinement study is quite different. Since both studies show the same trend, only the wave contours of the overall refinement study are depicted in Figure 7.10.

First differences in wave field resolution can already be observed at the fine grid (grid 2) although it is still very close to the finest grid (grid 1, Figure 7.9, bottom). The medium

grid (grid 3) still shows the overall characteristics of the wave pattern but misses the sharpness of the finer grids. This indicates a damping of the ship waves caused by the coarser resolution of the free surface volume. This impact of the free surface resolution is further continued for the coarsest grid, grid 4. Here resolution is so low, that the characteristics of the wave pattern are completely damped away. Transverse and divergent wave trains are smeared together and cannot be distinguished resulting in an underestimation of wave resistance.

To analyze if numerical errors are present, wave heights resulting from the simulations on the various grids are compared. Figure 7.11 shows the wave height behind the yacht for all grids. The display plane is the symmetry plane of the hull. All values are normalized by the water line of the yacht, LWL. One can see, that the first wave crest behind the hull ($x \approx 0$) is captured similarly by all grids. The first amplitude at $x/LWL = 1$ is also captured similarly. However, first differences become visible. One can see that the finer the grid, the faster the wave, indicating a small dispersion error. Furthermore, wave height gained from coarser grids is higher than from finer grids. Physically, one has to expect a decrease in wave height with increasing distance from wave source. However, this not true here, indicating a problem with boundary conditions blocking energy exit at the outflow. This problem is more emphasized for coarser than for finer grids. To estimate if the decrease in wave height is captured correctly at least for fine and very fine grid, the wake angle has been measured. It was found that within measuring accuracy the angle is a constant of 19.47° for all grids. This wake angle corresponds with theory. Assuming wave energy to be constant, the decrease in wave height has been approximated for all grids. The decrease is plotted in Figure 7.11 as envelope of the wave amplitudes. One can see, that the decrease in wave height matches reasonably well at the very fine grid for the first 3-4 amplitudes. The fine mesh only represents amplitudes 1 and 2 well and for all the other grids only the first amplitude is captured correctly. For further work, the error on the outlet should therefore be investigated and solved. A possible solution might be a larger coarsening area at the outlet or a damping function. Comparison with procedures from towing tank testing and CFD simulations performed by Pegel [138] suggest that an area of 2 ship length behind the ship are normally enough to correctly determine wave resistance. Since wave height in this area is captured reasonably well for fine and very fine grids, the error seems to be negligible and is therefore accepted for the current work.

It has to be noted that also the resolution of grid 4 is way below that of the other grids, it is still better than the result of the initial study (Figure 7.9 a) and b)). This is especially notable since the initial study had a finer grid resolution on the yacht surface as well as at the free surface. The grid size of the initial study was 3.5×10^6 cells while grid 4 only incorporates 0.8×10^6 cells. Therefore the finer free surface resolution of grid 4 must be related to the modification in the HRIC scheme which successfully reduces numerical smearing of the interface.

This further confirms the findings from the review of the total resistance C_T that it is more important to pay attention to the resolution of the water surface than to excessive refinements on the yacht surface in order to obtain the correct total resistance.

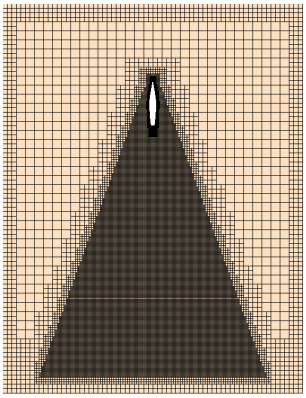

(a)

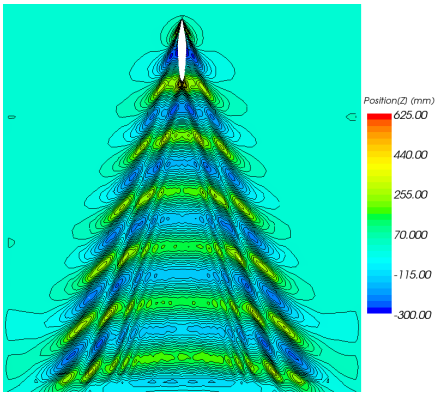

(b)

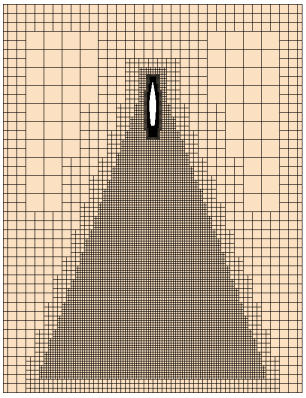

(c)

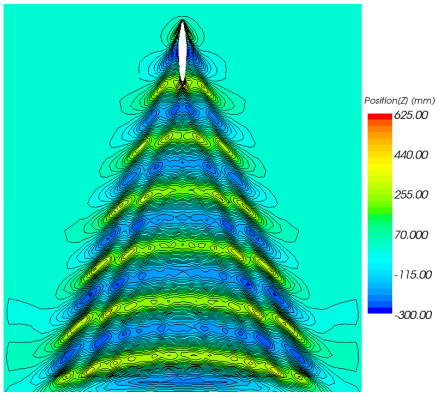

(d)

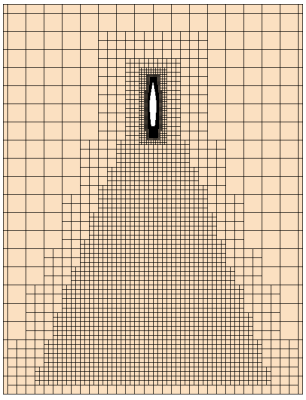

(e)

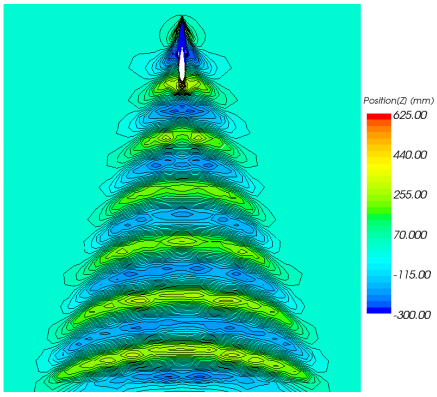

(f)

Figure 7.10: Grids and wave contours from *Overall Refinement* studies: (a) & (b) grid 2 - fine grid, (c) & (d) grid 3, (e) & (f) grid 4 - coarsest grid

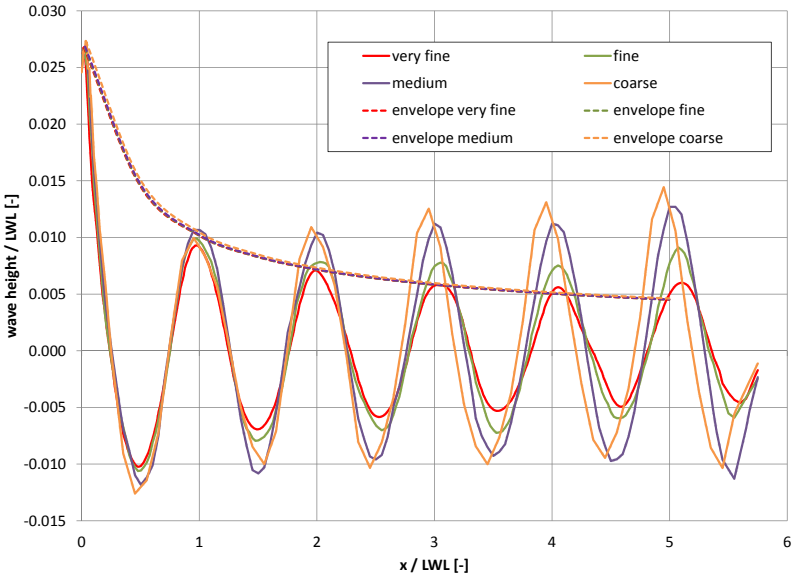

Figure 7.11: Wave height behind yacht for all grids, displayed at the symmetry plane of the hull. Wave height and length x are normalized by the length of the waterline. The envelope of the amplitudes is approximated assuming wave energy to be constant.

One of the goals of this investigation was to reduce numerical ventilation caused by the smearing of the free surface interface. Figure 7.12 shows the volume fractions of water at the yacht surface for the old approach with Courant number dependency (Figure 7.12 a) and b)) and for the new approach without (Figure 7.12 c) and d)). Comparing the two cases one can clearly see from the profile view (left column) that the new approach gives a much sharper interface between air (blue) and water (red). The differences are most pronounced at the bow wave which takes an entirely different shape. The bow wave of the old approach 7.12a) has a large region over which the interface is smeared and this smearing is transported significantly downstream. For the new approach 7.12 c) the bow wave is much more distinctive and the free surface interface is usually captured over 3-4 cells. This clearly shows an advantage of the modified approach over the old. However, plan view (right column) reveals that the volume fraction achieved with the new approach still is not perfect. While the improvements between old approach Figure 7.12 b) and new approach 7.12 d) are obvious, sub-figure 7.12 d) still reveals some remaining interface smearing. The improvement, however, is large since the volume fraction for the old approach ranges between 0.4 and 1.0, while in the new approach the range is between 0.85 and 1.0. It seems that within the VOF method achieving perfect results without smeared interfaces for this rather blunt bows is still very hard if not impossible. Nonetheless, from an engineering point of view the simulation is absolutely applicable since with respect to the verification and validation results the error in total resistance is small.

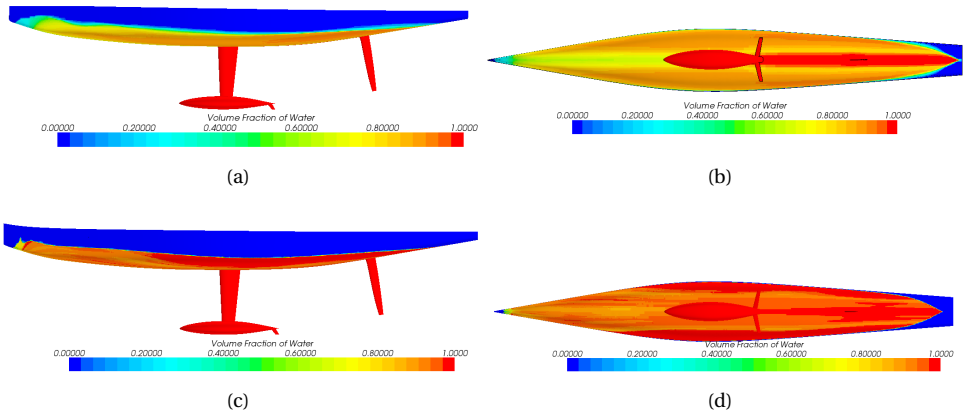

Figure 7.12: Comparison of Numerical Ventilation with Courant Number dependency (old approach (a) and (b)) and without (new approach (c) and (d))

7.2.4. GRID CONVERGENCE STUDIES INCLUDING LIFT

After the successful verification and validation for the variable C_T for the sailing yacht in upright conditions reported in Section 7.2.3, a further study has been conducted in order to demonstrate the feasibility of the approach for heeled conditions of the yacht. Heeled conditions include the generation of hydrodynamic lift by the yacht and its appendages. Therefore a validation and verification for these conditions cannot be restricted to the evaluation of total resistance C_T. Instead, it has to include the lifting component to consider the complete state of the yacht. Lifting surfaces are commonly described in terms of their lift and drag properties. Since this is more meaningful then expressing force values in a yacht geometry fixed coordinate system this approach is also used for this convergence study. Therefore the two point values total drag coefficient C_D and total lift coefficient C_L are evaluated together. The correct evaluation of these forces within towing tank experiments or CFD simulations requires the modeling of aerodynamic forces which a sailing yacht encounters. Decomposition of forces shows that aerodynamic thrust and hydrodynamic drag are collinear vectors of equal length and different sign. In order to correctly simulate the influence of the aerodynamic force generated by the sails, one has to introduce an additional dynamic sail trimming moment around the y-axis of the yacht which is equal to hydrodynamic drag D times the vertical center of efforts of the sails VCE_{aero}. The aerodynamic center of effort may be approximated from the geometrical center of the sails [103] or derived from wind tunnel data. For towing tank testing a rough approximation of the VCE_{aero} being 0.44 times mast height above the deck is usually sufficient.

$$M_{Y_{dyn}} = D \cdot VCE_{aero} \tag{7.18}$$

Additionally, the generation of lift by the yacht hull and appendages introduces a vertical force pointing up. Similar to the trimming moment explained above, this force has to be counter balanced by a collinear aerodynamic vector of equal length and different sign. This sail force has to be modeled during testing as a additional dynamic sink force $F_{Z_{dyn}}$.

It is modeled as heeling force F_H times the sine of the heeling angle ϕ.

$$F_{Z_{dyn}} = F_H sin\phi \tag{7.19}$$

The relationship between these forces is illustrated in Figure 7.13.

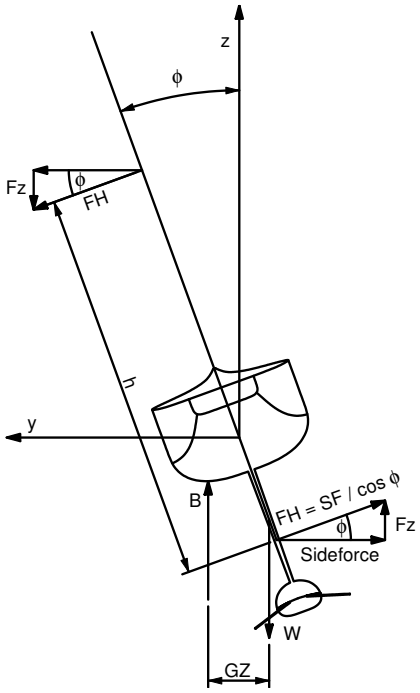

Figure 7.13: Sail forces introduce a heeling force F_H which heels the yacht to an angle ϕ. At ϕ, the righting moment of the boat, boat weight W times righting arm GZ to the center of buoyancy B, is such that it counter balances the heeling moment introduced by heeling force times heeling lever $F_H \cdot h$. The heeling force F_H has to be counter balanced by hydrodynamic sideforce $SF = F_H \cos\phi$ and vertical force $F_z = F_H \sin\phi$.

INFLUENCE OF INPUT PARAMETERS ON SOLUTION

Contrary to the upright resistance tests, the heeled tests have been conducted on model scale. This approach not only allows easier comparison between results but also makes the dependence on the various additional input parameters easier. The scale of the model is 1/3 which is a rather small difference between model and full-scale. The geometric values of the model and the fluid properties have been applied according to the towing tank test configuration sheet and are given in Table 7.6. The dimension of the towing tank itself is given in Table 7.7. Whether correction parameters have been applied to the tank data and if yes, to which extend, is unfortunately unknown. Empirical tank correction coefficient for this tank are unknown, however, available tank geometry data allow calculation of corrections for tank blockage and for additional drag due

Table 7.6: Geometry and flow dimensions

Principle Dimensions			
Length over all	LOA:	[m]	8.417
Max. breadth	$BMAX$:	[m]	1.072
Draft	T:	[m]	1.390
Length of waterline	LWL:	[m]	6.672
Sailing Displacement	Δ:	[kg]	953.19
Longitudinal center of gravity	LCG:	[m]	-0.314
Transverse center of gravity	TCG:	[m]	0.000
Vertical center of gravity	VCG:	[m]	-0.787
Vertical center of effort sail forces	VCE_{Aero}:	[m]	5.955
Fluid Properties			
Density	ρ:	$[\mathrm{kg\,m^{-3}}]$	999.0
Dynamic Viscosity	μ:	[Pa s]	1.14×10^{-3}
Dimensionless wall-scale	y^+:	[−]	50

Datum Point is intersection of dead water line, Centreplane and Hull Station 5.
X is positive forward, Y is positive to Port, Z is positive up.

to turbulence generators. While for the non-lifting test cases validated in Section 7.2.3 trim was kept fixed and only sinkage was dynamically calculated, the present case leaves both state variables free. This is a major change since it makes it necessary to account for similar trim and sinkage forces in order to compare simulation and experiment. For the towing tank experiment prescribed trim moments and vertical forces are applied as input values. These values have been used as input data for the CFD simulation instead of dynamic calculation of these values, which would also have been possible. Since a certain uncertainty about these input data exists, test calculations have been conducted to settle this issue. A test case at heel of 27.5°, yaw angle of 0° and a full-scale boat speed of 10kts corresponding to a Froude number of 0.37 was selected. The first calculations showed that drag was underestimated by about -7% while lift was overpredicted by 11%. Furthermore, the trim angle showed a bow up rather than a bow down pitch. Review of input data and comparison with theoretical values derived by means of equations (7.18) and (7.18) showed that while the input value for sail sinkage force was of the expected order of magnitude, sail trim moments were only about 1/4 of expected size. Since this difference is most probably related to different reference points for application of the trim moment, it was decided to use a precalculated value according to equation (7.18) with reference drag from EFD. Since the preliminary calculations suggested that the EFD results at hand are raw data with only minimal smoothing and correction, two corrections were applied to the experimental data. First, a blockage coefficient is calculated from the tank dimensions and used to correct the model speed. For this model, the correction is in the order of 1% u_M. The second correction is for additional drag due to turbulence generators. This correction varies with speed and reduces EFD drag by an amount of 0.6% at lowest tested speeds to 0.3% at highest Froude numbers. With these

Table 7.7: Towing Tank related Dimensions

Towing Tank of the Institute of Ocean Technology, St. John's/CAN			
Length of Channel	L_C	[m]	200
Beam of Channel	B_C	[m]	12
Height of Channel	H_C	[m]	7
Blockage Coefficient	κ	[−]	0.583
Speed Coefficient	ω	[−]	1
Parameters Turbulence Generators			
Chain Dimension TG:	l_{TG}	[m]	0.6
Height of TG:	h_{TG}	[m]	0.001
Drag Coefficient TG:	C_{TG}	[−]	0.4
Mid Ship Section Area:	A_M	[m^2]	0.740

corrections applied, the simulation was redone. Results showed a difference of -3.9% in drag and 2.1% in lift while trim angle displayed the correct order of magnitude. These results show the importance of the various input values, especially for sailing yacht testing. The level of accuracy gained is deemed sufficient to act as starting point for the grid invariance study which will be described below.

COMPUTATIONAL GRIDS

The variations of trim moments and sinkage forces reported above have been conducted to gain a higher level of confidence regarding the input parameters for the towing tank experiment. With this confidence a grid convergence study has been conducted. The grid convergence study has also been conducted according to ITTC standards as discussed in Section 7.2.3. For details on the method see the beginning of this section or [129]. The design of the grids is similar to the one used in Section 7.2.3. It includes refinement of the free surface in vertical direction and additionally in horizontal dimensions in the vicinity of the Kelvin angle around the boat. The results of the non-lifting verification and validation study clearly showed that the major factor towards a grid independent solution is the refinement of the free surface. Figure 7.8 illustrated that surface grid refinement is already sufficient. Therefore only free surface refinement has been applied for the present grid convergence study. Grid parameters have been systematically varied according to Table 7.8. In contrast to the grid convergence study for the non-lifting case in Section 7.2.3, the constant grid refinement factor has been decreased from 2 to 1.5. This has been done to get a more uniform refinement in terms of cell sizes which makes it easier to compare the different results. The differences of lift and drag coefficient to the experimental data derived from the grid convergence study are shown in Figure 7.14. This figure illustrates that the drag coefficient C_D is always underestimated, while the lift coefficient C_L is always overpredicted. However, differences to EFD are rather small for both coefficients. Generally, both coefficients converge quite satisfac-

Table 7.8: Grid Parameter for Grid Invariance Study

Free Surface Refinement Factor [−]	Interface Spacing dz [mm]	dx & dy [m]	Grid Size [−]
1.0	10.0	0.0625	1.25×10^7
1.5	15.0	0.0938	7.07×10^6
3.0	22.5	0.1406	3.57×10^6

torily, giving a first indication of a high quality solution. Table 7.9 gives the numerical

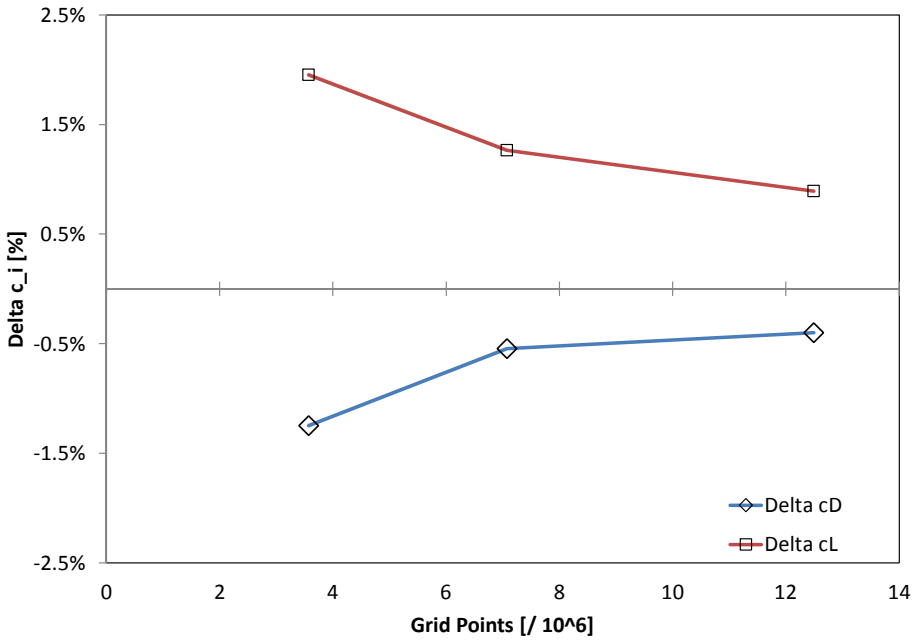

Figure 7.14: ΔC_i over Grid Points

values of the convergence of drag, lift and lift/drag-ratio. The solution changes from a coarser to a finer solution ϵ, as defined in (7.17), decreases continuously. The results of the verification procedure, Table 7.10, show that the convergence ratio $R_G < 1$ holds for all cases, allowing the conclusion that the decrease is monotonic for all values. The biggest uncertainty of the computational grid U_G is 0.52% for the lift-to-drag ratio C_L/C_D which is already very low. Since the convergence is monotonic, it is possible to use *Generalized Richardson Extrapolation* in order to apply a correction for numerical error. In particular, it is possible to calculate a correct grid uncertainty U_{G_C} and a corrected solution S_C. With a maximum deviation of 0.14%, these corrected values are even closer

Table 7.9: Grid Convergence of drag and lift for ACCV5

	Grid 3	Grid 2	Grid 1	EF Data
C_D	8.94	9.00	9.01	9.05
ϵ	-	0.7%	0.1%	
C_L	1.89	1.88	1.87	1.86
ϵ	-	-0.7%	-0.4%	
C_L/C_D	2.12	2.09	2.08	2.05
ϵ	-	-1.4%	-0.5%	

$\%S_G$

to the experimental values. It can be generally said that from a numerical point of view the results of the grid convergence study show a smooth behavior and steadily converge towards the experimental values with grid refinement. This allows the conclusion that the simulation is verified. Table 7.11 gives an overview of the values necessary for the

Table 7.10: Verification of drag and lift for ACCV5

Variable	R_G	p_G	C_G	U_G	$\delta_G^\star$	U_{G_C}	S_C
C_D	0.21	3.91	3.10	0.19%	-0.12%	0.08%	9.02
C_L	0.54	1.50	0.67	0.44%	0.30%	0.14%	1.87
C_L/C_D	0.37	2.47	1.38	0.52%	0.41%	0.11%	2.07

$\%S_G$

validation procedure. Data uncertainty U_D and numerical simulation uncertainty U_{SN} are combined to the validation uncertainty U_V. $U_V$is then compared to the comparison error E_C which is defined as data D minus simulation result S as per equation 7.3. The table lists all values both for the uncorrected solution and the solution corrected by means of Generalized Richardson Extrapolation. By definition, a simulation is validated if the comparison error is less or equal the validation uncertainty. This clearly is the case for all six comparison cases. The simulation can therefore be considered validated at validation uncertainty level.

It can be summarized that verification and validation for lifting conditions was highly successful. The results are not only considerably below validation uncertainty level but also very close to experimental data. Although this formally does not decrease the uncertainty of the results, it still increase the confidence in the applied methods. It also shows that the assumptions regarding free surface interface smearing made in the previous sections are correct.

Table 7.11: Validation of drag and lift for ACCV5

Variable		E%	U_V%	U_D%	U_{SN}%
C_D	E	0.4%	2.0%	2.0%	0.19%
	E_C	0.3%	2.0%	2.0%	0.08%
C_L	E	-0.9%	2.0%	2.0%	0.44%
	E_C	-0.6%	2.0%	2.0%	0.15%
C_L/C_D	E	-1.3%	2.1%	2.0%	0.53%
	E_C	-0.9%	2.0%	2.0%	0.11%

$\%D$

VELOCITY SWEEP

In the previous sections successful verification and validation has been performed for non-lifting and lifting conditions of the appended yacht. These results establish a solid platform to work from, however one has to be prudent to control these results for a wider range of combinations of state variables to ensure their applicability for a complete test matrix. Therefore two further investigations have been performed. The first consists of several boat velocities at constant angle of incidence, while the second probes several yaw angle at constant Froude number. Figure 7.15 illustrates the results of the velocity sweep. Here the blue lines represent the experimental data while the red lines are the CFD results. It can be seen, that the general trend is very well captured. However, small differences remain. In case of the drag coefficient, these differences increase with decreasing boat speed, the maximum drag difference being $-4.2\%C_D$. For the lift, the same is true but the maximum difference from EFD is $2.07\%C_L$ which is smaller than the drag differences. It has to be kept in mind that the grid spacing has been kept constant. Thus with changing inflow velocity, y^+ values are implicitly changed. Besides this effect, the change of wave length also has the impact, that for lower speeds the relative grid resolution at the free surface interface is coarser than for higher speeds.

A review of the average $\bar{y^+}$ values shows that $50 \leq \bar{y^+} \leq 60$ in the investigated velocity range. The difference in dimensionless wallscale is therefore regarded as too small and thus does not explain the differences in drag. A further indicator which supports this view is that the differences in lift differences are small, indicating a constant resolution of the boundary layer. It is therefore most likely that the drag differences arise from the implicit coarse grid resolution caused by the smaller wave length associated with smaller Froude numbers. However, even maximum drag differences of -4.2% can be considered as sufficiently small. Therefore the results are considered sufficiently accurate.

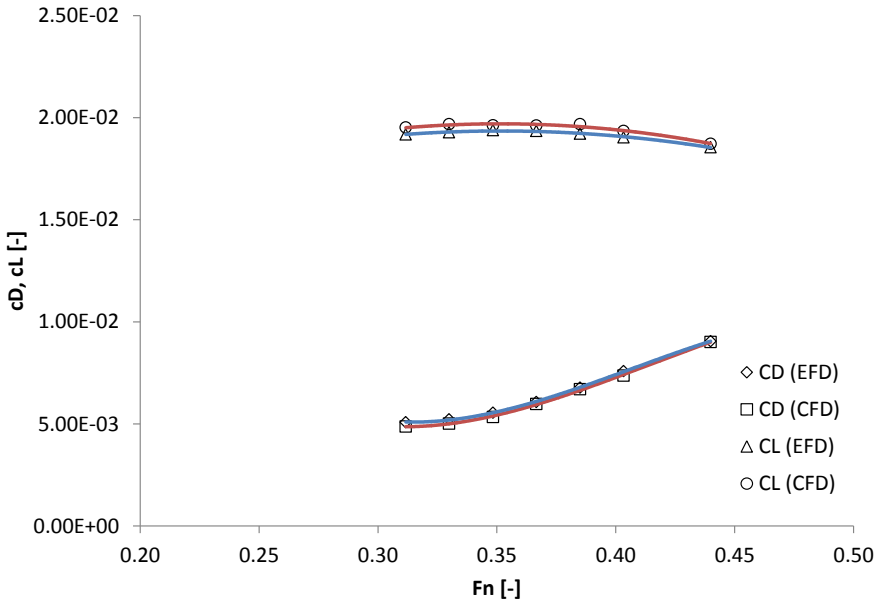

Figure 7.15: C_D over Froude Number

YAW SWEEP

As a second control of the validity of the results, two series of yaw angle sweeps at constant boat velocity have been performed. The tested yaw angles range from -1° to +1° in 0.5° steps. For the simulation, both tab and rudder angle are kept constant at 8° and 1.75° respectively. This matches the setup used during experiment with the exception of 1° yaw angle. Here the experimental rudder angle was 4°. Since the experimental test matrix has been divided in 1° steps for the yaw angle sweep, intermediate results are interpolated from experimental values. Therefore the +0.5° yaw angle result is also partially affected by the differing rudder angle at 1° leeway. The yaw sweep has been performed for Froude numbers of 0.37 and 0.44 which resemble fulls-scale speeds of 10 and 12 knots respectively. Results are shown in Figure 7.16 as drag coefficient over lift coefficient squared. This representation method is especially useful since it allows one to derive effective draft and induced drag from the curve slope. Effective draft is a measure for the effectiveness of a appendage configuration under a hull and how close this configuration resembles optimum elliptical lift distribution. It is especially descriptive since it can be compared to the geometry draft. Effective draft T_E may be derived from measured values as follows:

$$T_E = \frac{1}{\sqrt{\frac{\partial D}{\partial F_H^2} 0.5 \rho v_B^2 \pi}}, \tag{7.20}$$

with total drag D, heeling force F_H^2, water density ρ and boat velocity v_B^2. From effective draft one is able to calculate the induced resistance which is proportional to T_E. Induced drag D_I is a drag component caused by the energy losses due to the tip vortex created by lifting foils. It is calculated as follows:

$$D_I = \frac{F_H^2}{T_E^2 0.5 \rho v_B^2 \pi}. \tag{7.21}$$

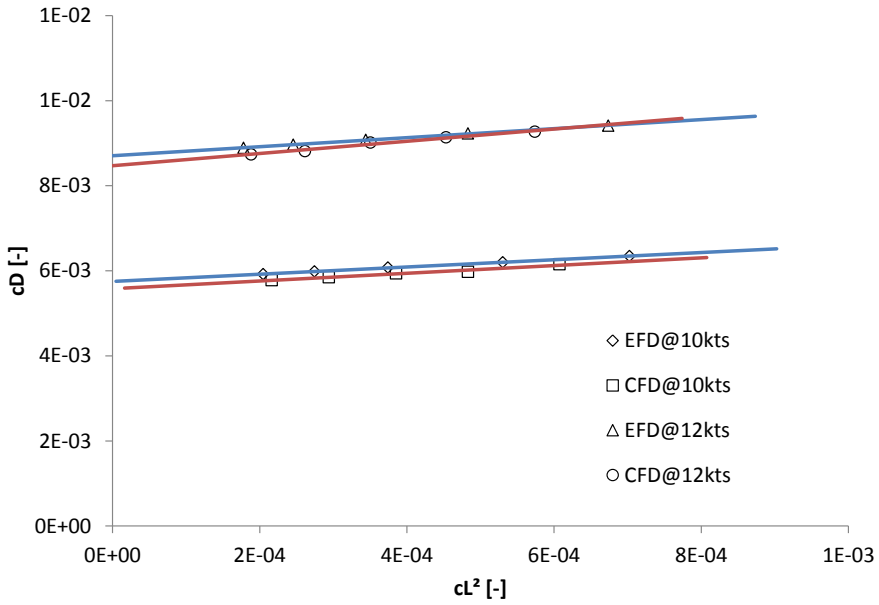

Figure 7.16: Comparison of experimental and numerical C_D over C_L^2 for yaw sweeps at 10 and 12 knots

Figure 7.16 illustrates that at both flow states experimental and computational results are matched quite well. However, there are distinctive difference between the two results. For the lower speed of 10 knots, the experimental and CFD results have an constant offset while the curve slope is almost identical. In contrast to this, the CFD results for 12 knots are at first instance closer to the EFD but show a different curve slope. This is indicated by the values of Table 7.12 which show a difference of only 3 cm or -1.9% in effective draft for 10 knots but a difference of 16.7 cm which amounts to -11.3% for 12 knots.

Table 7.12: Yaw Sweep EFD vs. CFD

	u = 12 kts			u = 10 kts		
	EFD	CFD	Δ [%]	EFD	CFD	Δ [%]
T_E [m]	1.483	1.316	-11.3	1.658	1.627	-1.9
$\partial f_H/\partial\beta$ [m/deg]	0.042	0.040	-3.9	0.041	0.040	-2.3
f_{H0} [−]	0.149	0.151	1.3	0.155	0.158	1.9
$D(\phi, F_H = 0)$ [N]	430.091	415.520	-3.4	197.187	191.586	-2.8
$D_i(\beta = 0)$ [N]	19.283	24.924	29.3	11.660	12.459	6.9

In contrast to T_E the gradient of the side force with respect to leeway angle, $\partial f_H/\partial\beta$, remains relatively constant for all cases. Side force coefficients at zero leeway f_{H0} are also represented with only small differences. Drag at zero lift is comparable to both speeds with differences of around 3% between EFD and CFD. Induced drag was calculated at zero leeway for all cases. Here differences range from 29.3% for 12 kts to 6.9% for 10 kts. However, the proportion of induced resistance on total drag is around 5.5% to 6% for both speeds. Since the contribution of induced resistance to the total drag is small and thus the investigated component is also small, it is hard to judge the source of these differences. The greatest uncertainty lies in the details of the setup of the towing tank sessions. These details are only scarcely documented but have a great impact on overall results. It is assumed that the differences arise from these uncertainties in the experiments. However, since the overall differences are small the quality of results is considered adequate.

7.3. VERIFICATION AND VALIDATION SUMMARY

The motivation for this investigation was a failed first attempt to correctly determine total resistance of free surface flow around an ACCV5 hull. A review of the first simulations led to the assumption that the problem could be traced back to the occurrence of extensive interface smearing at the yacht hull. Therefore, a thorough review of the theory behind the interface capturing model has been conducted in Chapter 3.1. This review showed that the problems encountered were most likely situated in the use of Courant numbers which can exceed 0.5, thus causing the switch to a 1st order upwind differencing scheme. Reducing the overall time step size such, that it would allow the maximum Courant number to be lower than 0.5, would lead to undesirable long simulation times. An alternative approach was sought to allow the use of higher order schemes like e.g. the HRIC scheme within acceptable time step size. It was concluded that it might be possible to modify the VOF model such that it does not switch to upwind differencing even if the local Courant number would be larger than 0.5. This approach seems feasible as long as only a steady state solution is sought. The numerical test case in Section 7.1.2 confirmed this assumption. Therefore, the modified scheme was applied to the simulation of the total resistance of the ACCV5 yacht. Verification and Validation according to

the ITTC guidelines was then conducted against experimental data.

An extensive grid study has been carried out, thus also allowing to judge the sensitivity of the results to the change of various grid parameters. The results showed a much sharper capturing of the free surface interface with the new approach. It was also shown that the initial differences in overall resistance were mainly caused by the poor free surface resolution caused by the interface smearing. This interface smearing caused a numerical damping of the waves resulting in a wave resistance which was to small. The result was, that the overall resistance obtained by the first, failed attempt to validate the simulation was too small. Since this is unusual for RANSE based CFD simulations, it can be quite misleading. The new grid convergence studies clearly demonstrated that the free surface simulations for yachts are more sensible to free surface resolution and thus to wave resistance then they are to yacht surface resolution (friction and pressure forces). Overall it can be concluded that the use of the higher order scheme, which was made possible by the modification of the existing implementation, led to large improvements and a successful verification and validation. It has to be stressed that the new approach with the modified scheme is only valid if one is interested in a steady solution. The results showed that the simulation still suffers from a small amount of interface smearing, however the overall effect on the results may be considered small. Generally, the error in verification and validation was satisfactorily small.

The study was than extended to include heeled cases were the investigated yacht produces dynamic lift. Setup for these cases proved more difficult since they raised the need for further modeling of aerodynamic forces to correctly simulate the underlying physics. This made it necessary to account not only for dynamic sinkage but also for trim, adding another degree of freedom into the motion model making it 2-DOF. Uncertainties in available data for towing tank test configuration turned out to be another obstacle. However, these uncertainties were dispelled by preliminary investigation regarding the sensitivity of results to input data. With this improved model a second verification and validation was conducted, this time with the yacht in lifting conditions. The study was again conducted according to ITTC guidelines. Results demonstrated that both drag and lift could be reproduced to a very high degree of fidelity and well below experimental validation uncertainty.

8

YACHT PERFORMANCE PREDICTION USING CONVENTIONAL VPP

8.1. EVALUATION OF EXPERIMENTAL TOWING TANK DATA

In this section, towing tank test data of an ACCV5 boat are evaluated in order to generate the coefficients necessary for subsequent velocity prediction using a conventional VPP. The towing tank tests have been conducted with models of scale factor $\lambda = 1/3$. The models are equipped with studs as turbulence stimulators, located at a small distance from the stem/leading edge of the canoe body, fin, rudder, wings and bulb. Unfortunately, the exact location of the stimulators as well as how this location was determined by the experimenter remains unknown. Assuming a correct placement of these turbulence stimulator, the flow is considered to be fully turbulent flow on the entire wetted surface. The model has been tested at a sailing trim configuration conforming to a full scale total mass of approx. 26400 kg. The following test matrix has been investigated:

- Resistance tests at non-lifting condition (no heel, no leeway, zero rudder and tab angle)
- Perturbation of heel angles of 10°, 20°, 27.5° and 35° with leeway angles of −1°, 0°, 1° and 2.5°.
- For any combination of heel and leeway angle the boat velocity has been varied between 6 kts and 12 kts full scale.

- Rudder angle has been set to predefined values being constant for any combination of heel and leeway angle. No rudder sweep at constant values for heel and leeway has been carried out.

The entire test matrix consists of 117 test runs.

Processing of test results has been carried out as described in Section 4.1. For model to full-scale transformation of resistance at non-lifting condition the ITTC-78 performance prediction method has been used. Here Reynolds number correction of viscous resistance has been done individually for the canoe body and the appendage elements fin, rudder, bulb and wings.

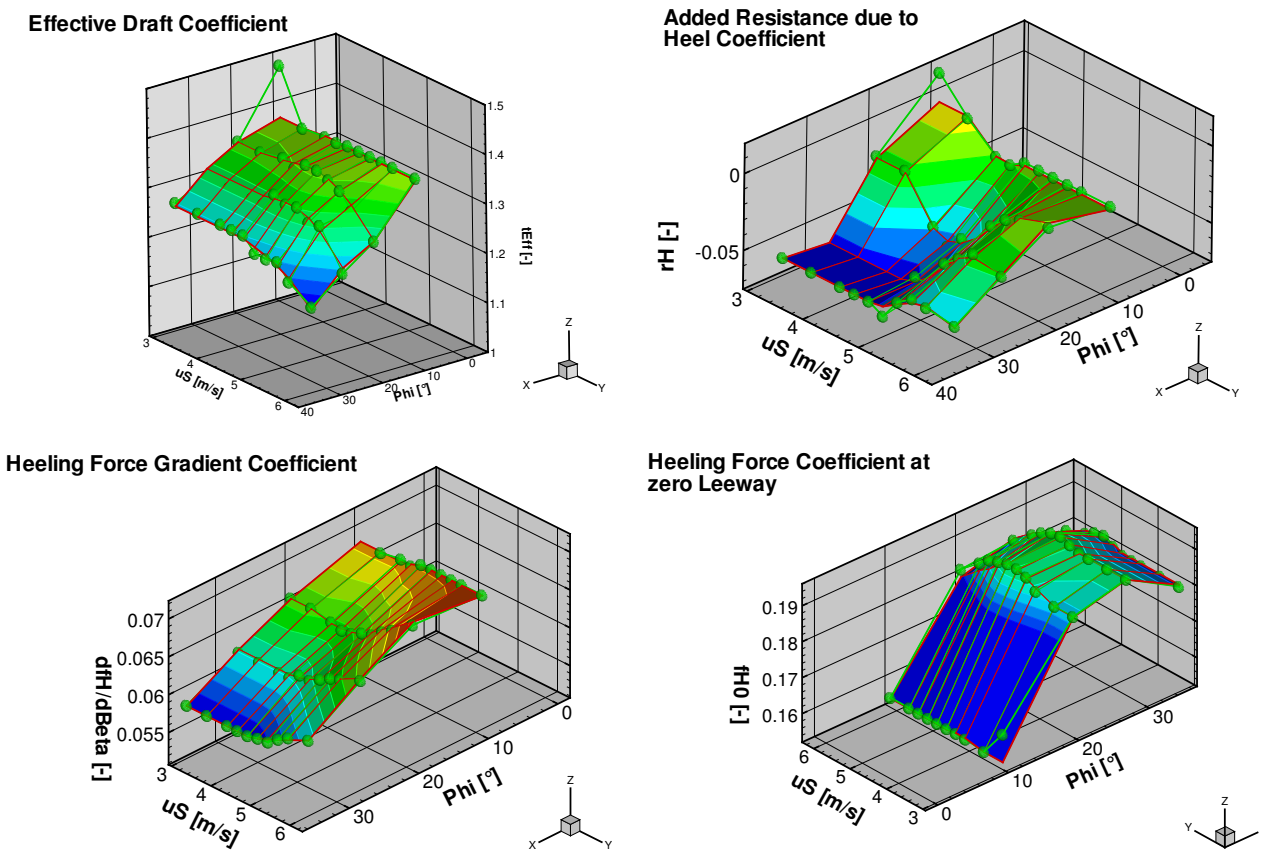

Figure 8.1: Hydrodynamic coefficients for effective draft t_{Eff}, added resistance due to heel r_H, heeling force gradient $\partial f_H/\partial\beta$ and heeling force coefficient at zero leeway f_{H0} derived from towing tank data. The surfaces describe the coefficients for lifting $\left(t_{Eff}, \partial f_H/\partial\beta, f_{H0}\right)$ and non-lifting conditions $\left(r_H\right)$ as functions of boat speed u_S and heeling angle ϕ.

For non-zero heel and leeway conditions the hydrodynamic properties of the yacht are described by the effective draft and added resistance due to heel. Heeling force is calculated from side force coefficients f_{H0} and $\partial f_H/\partial\beta$. The coefficients resulting from the analysis of the experimental data are depicted in Figure 8.1. The upright resistance curve is depicted in Section 8.3, Figure 8.2.

8.2. GENERATION OF NUMERICAL TOWING TANK DATA

In the previous section, the data set necessary to derive hydrodynamic coefficients for a subsequent VPP analysis had been created using experimental towing tank methods. Now a similar data set is created by means of RANSE CFD simulation. Geometry and simulation setup are identical to the one used in the verification and validation explicated in Chapter 7. Simulations are conducted fully turbulent using the SST model to describe turbulence. The free surface modification described in Section 7.1.2 is applied. The computational grid has the same properties as the finest grid used in Section 7.2.3 for the upright case, and Section 7.2.4 for lifting cases. Grid size in both cases is about 12.5×10^6 cells.

As described in Chapter 7, upright resistance is calculated with the ACCV5 boat geometry in full scale while lifting cases are calculated in model scale. The ratio behind this approach is that the static sail trim moments and sinkage forces used during EFD are applied. Normally, it would be more convenient to use dynamic sail forces and moments during CFD simulation, but here this approach was chosen to enhance comparability of results.

When compared with EFD, the CFD test matrix has been modified to a certain degree. This has been done to increase the suitability of the results for generation of hydrodynamic data sets for VPPs as described in Section 4.1. The following states have been tested:

- Resistance tests at non-lifting condition (no heel, no leeway, zero rudder and tab angle)
- variation of leeway angles
  - Perturbation of heel angles of 0°, 10°, 20° and 27.5° with leeway angles of −1°, 0°, 1° and 2.5°.
  - For any combination of heel and leeway angle the boat velocity has been varied between 6 kts and 12 kts full scale.
  - Rudder angle has been set to predefined values being constant for any combination of heel and leeway angle.
- variation of rudder angles

- Rudder Sweep at heel angles of 0°, 20° and 27.5° with rudder angles of 0°, 1.25°, 3.25° and 5.25°. Yaw has been set constant to 0°.
- the boat velocity has been varied between 6 kts and 12 kts full scale for any combination of heel and rudder angle .

The entire test matrix consists of 149 test runs. The calculations have been performed in parallel using 16 Cores of a Intel Xeon E5-2670 type CPU clocked at 2.6 GHz on a Linux cluster per single test matrix point. Computational run time is approximately 6 hours for a solution. The results of the calculation are discussed in the next section and being compared with EFD results.

8.3. COMPARISON OF RESULTS

The two resistance curves depicted in Figure 8.2 show resistance coefficient C_T derived from numerical and experimental towing tank tests in upright conditions. In general, there is a good agreement between the EFD and the CFD towing tank tests. Figure 8.3 shows ΔC_T between both resistance curves. On average, ΔC_T equals 0.8% whilst peaks normally do not exceed +/- 2.0%. This behavior is still in good accordance with the validation uncertainty established in Chapter 7.2. However, there are two exceptions to this good agreement of resistance coefficients. One peak is at Fn=0.37 and the other at Fn=0.66 with both peaks giving a deviation of CFD results of -4.8% with respect to EFD. A possible explanations for ΔC_T at Fn=0.37 is that this speed, which is slightly above hull speed, describes a state where unsteady phenomena occur which both hard to measure and simulate. Furthermore, it can be observed that there is a general trend that for higher Froude numbers the resistance calculated by CFD is lower than the EFD values. Nonetheless, the agreement between the two data set is satisfactory.

Figure 8.4 illustrates a comparison of hydrodynamic coefficients for lifting conditions. The coefficients derived from CFD calculations are shown as surfaces whilst the values from EFD are inserted as green dots. It has to be noted that the test matrix of the two procedures differed slightly. Whilst EFD included heel angle of 10° to 30°, CFD ranged from 0° to 27.5°. With the exception of heeling force coefficient at zero leeway, f_{H0}, the general trend of all coefficients is the same for both EFD and CFD. This can be especially good observed for added resistance due to heel, r_H. On average, the difference Δr_H between the EFD and CFD is 2.5%. Average differences for effective draft t_{Eff} and heeling force gradient $\partial f_H/\partial \beta$ are -0.2% respective -3.0%.

The difference between EFD and CFD is largest for f_{H0}. While the data sets reach an agreement of -0.5% for larger heeling angles, smaller angles differ by approximately 22%. In general, EFD values of f_{H0} show a sudden decrease at heel angle of 10°. For CFD data, this is not the case. Instead CFD values remain more or less constant over the whole heel angle range. By reviewing the data set, the difference was traced back to differences in the test matrix. The CFD simulations have been conducted with constant settings

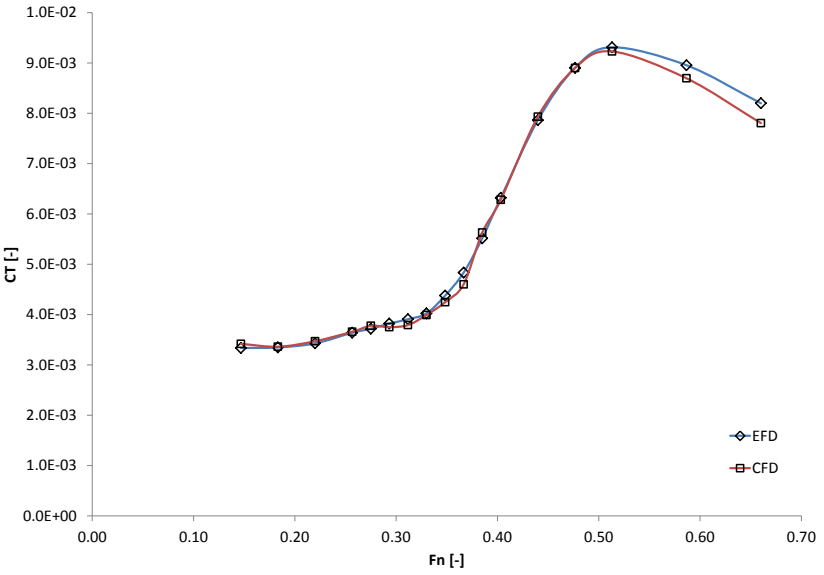

Figure 8.2: Comparison of resistance coefficient C_T of EFD (blue curve) and CFD (red curve)

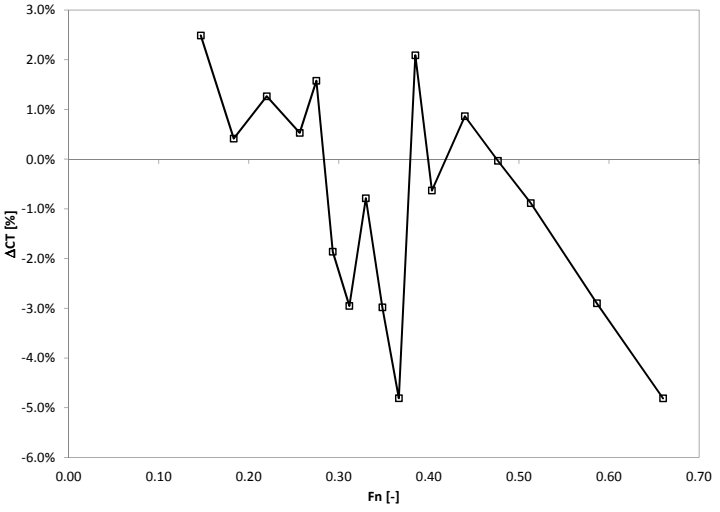

Figure 8.3: Difference between experimental and numerical resistance curve shown as ΔC_T in % over Froude number

for trim tab angle and rudder angle of 8° and 1.75° respectively. During experimental towing tank tests, rudder angle and trim tab angle were changed. For large heel angles, the same trim tab and rudder angles as in the CFD simulations were applied. For smaller heel angles, trim tab and rudder angle were steadily reduced. For the smallest heeling angle tested, $\phi = 10°$, the trim tab angle was 7° and the rudder angle 0°. This explains why the side force coefficient at zero leeway, f_{h0} of the experimental data is smaller for small heel angle than the value observed for the simulation data. It can therefore be concluded that both methods give the correct results.

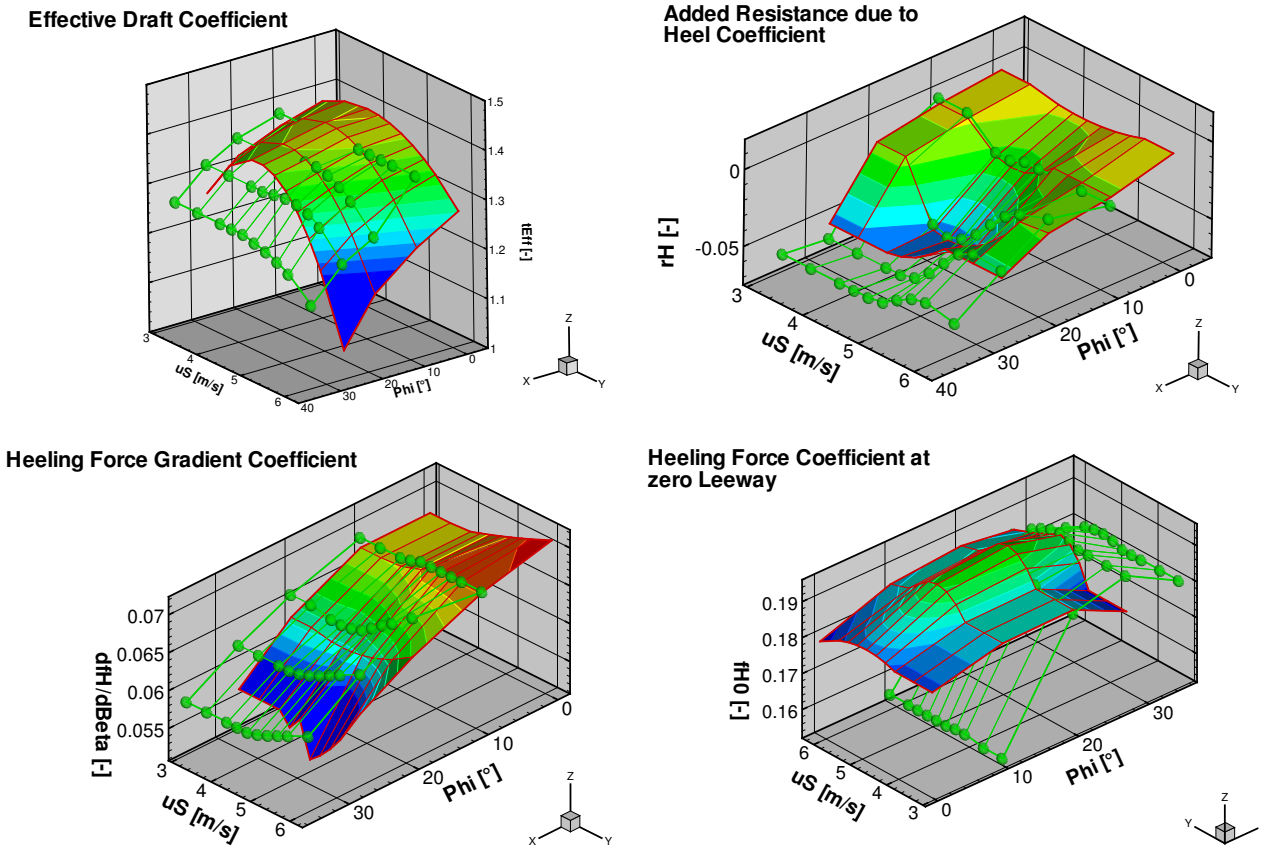

Figure 8.4: CFD generated hydrodynamic coefficients for lifting conditions versus EFD data

In general, comparison of EFD and CFD data brought up only small differences between the two methods. In the following section, resulting VPP polars will be discussed.

8.4. PERFORMANCE PREDICTION USING CONVENTIONAL VPP

After the generation of hydrodynamic coefficients as described in the previous section, conventional VPP calculations have been performed to derive velocity polars from both data sets. A semi-empirical sail force model as described in Section 4.1.4 was used to account for aerodynamic forces and a $flat$ factor was used to vary sail forces for optimum boat speed. For details on the VPP method, see Section 4.1. Calculations were performed for an upwind and an downwind sail set at the following true wind conditions.

- True wind speed $V_T = \{5.0, 7.5, 10.0\}$ [m/s]
- Upwind sail set: True wind angle $\beta_T = \{30, 40, ..., 120\}$ [°]
- Downwind sail set: $\beta_T = \{100, 110, ..., 170\}$ [°]

Table 8.1 lists the characteristics of the sails used in the sail force model. The symbols used are illustrated in the sketch below the table. Main sail area is calculated using trapezoid integration

$$A_{Main} = P/4\,(0.5E + MGL + MGM + 0.75MGU + 0.5MGT + 0.25HB) \tag{8.1}$$

whilst jib sail are is calculated from sail triangular

$$A_{Jib} = 0.5LP\sqrt{I^2 + J^2} \tag{8.2}$$

The sail area of the symmetric spinnaker is calculated using IMS formula

$$A_{SymSpi} = 0.6\,(SL\,SMW - 0.25SL(SMW - SF)) \tag{8.3}$$

Results of the calculations are illustrated in Figure 8.5 as polar plot of boat speed u_B over β_T for the various wind speeds. Results based on EFD data are colored in orange to red colors with filled symbols while CFD results are in green shades and empty symbols. Furthermore the results are displayed as *Time Allowance Deltas* ΔTA. Time allowance in this context describes the time in seconds necessary to travel a nautical mile at a certain combination of V_T and β_T,

$$TA = \frac{1\text{nm}}{u_B\left(V_T, \beta_T\right)}. \tag{8.4}$$

Consequently, ΔTA is measurement how many seconds at boat would be faster or slower than an opponent under the same environmental conditions.

$$\Delta TA = TA_{Boat_1} - TA_{Boat_2}. \tag{8.5}$$

Here, ΔTA is calculated as $TA_{EFD} - TA_{CFD}$.

Table 8.1: Optimum Upwind / Downwind VMG

Main			Jib			Spinnaker		
P	[m]	30.55	I	[m]	26.07	SF	[m]	22.13
HD	[m]	2.43	J	[m]	10.7	SMW	[m]	22.3
MGT	[m]	4.53	LP	[m]	8.31	SL	[m]	32.5
MGU	[m]	5.87				ISP	[m]	27.81
MGM	[m]	7.41						
MGL	[m]	8.36						
E	[m]	8.97						
BAD	[m]	1.97						
S	[m^2]	210.26	S	[m^2]	146.38	S	[m^2]	371.38
VCE	[m]	16.32	VCE	[m]	11.45	VCE	[m]	19.56

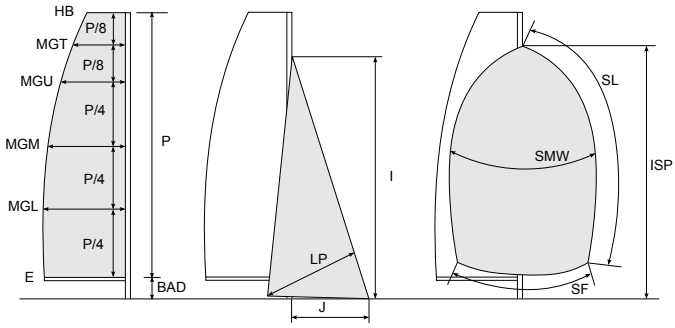

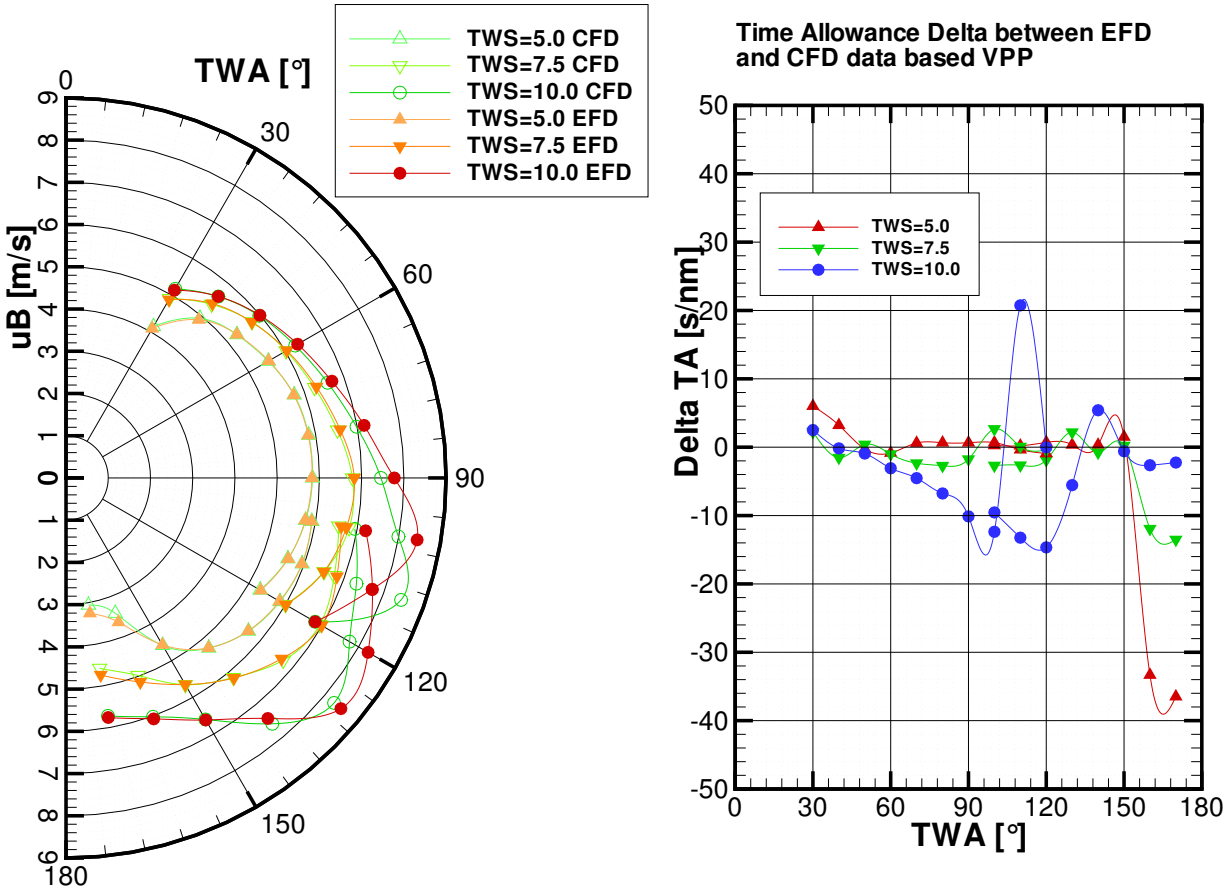

Figure 8.5: Velocity polars for EFD and CFD data and time allowance delta between the two solutions

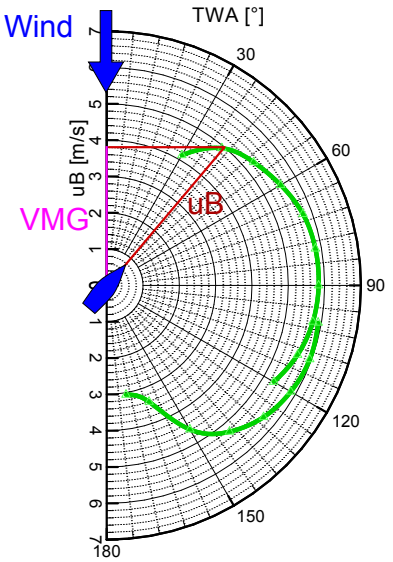

Figure 8.6: Velocity Made Good (VMG) is the component of the boat speed u_B opposite to the wind direction $\left(VMG_{upwind}\right)$, as shown here, or directly in wind direction $\left(VMG_{downwind}\right)$.

Looking at the polar plot, one can see that despite the small differences in coefficients for lifting conditions the calculated boat speeds are very similar for upwind and downwind conditions at V_T 5.0 m/s and 7.5 m/s. A look at ΔTA confirms that impression. Time allowance for both true wind speeds is around 2 seconds for all true wind angles except β_T of 160° and 170°.

For the highest true wind speed of 10.0 m/s, the picture is somewhat different. While u_B remains comparable for most β_T, there is a noticeable difference at high boat speeds. Maximum Δu_B in upwind conditions is 0.73 m/s or 9.5%u_B for β_T 110°. Downwind, the maximum Δu_B is 0.51 m/s (6.1%u_B) at 120°. These differences in boat speed correlate with the differences in upright resistance from Figure 8.2.

Another important information of the velocity polar is how fast the boat is traveling into the wind. This is described as the velocity made good (VMG) of the boat, see Figure 8.6. When looking towards maximum VMG, these differences are of minor importance for upwind conditions. However, they might be important for downwind conditions.

Table 8.2 gives an overview of the optimum upwind and downwind VMG with its accompanying true wind angle β_T for all wind speeds V_T. Differences in boat speed range under 1%, while differences in β_T are a little bit larger with up to -4.23%. However, this largest delta still resolves to only 1.23°β_T which will be hard to measure on a boat let alone to steer. Generally, the differences in both speed and true wind angle are so small

that it would be very hard to measure them in a sea trial. This allows the conclusion that the agreement between both VPP results is good.

Table 8.2: Optimum Upwind / Downwind VMG

	EFD	CFD	Δ [%]
$V_T = 5.0$ [m/s]			
$VMGmax$ [m/s]	3.74	3.77	0.98%
β_T [°]	38.24	37.83	-1.07%
$VMGmin$ [m/s]	-3.99	-3.98	-0.29%
β_T [°]	144.19	144.22	0.02%
$V_T = 7.5$ [m/s]			
$VMGmax$ [m/s]	4.22	4.23	0.15%
β_T [°]	32.77	31.38	-4.23%
$VMGmin$ [m/s]	-4.83	-4.87	0.75%
β_T [°]	154.5.25	149.55	0.81%
$V_T = 10.0$ [m/s]			
$VMGmax$ [m/s]	4.43	4.47	0.85%
β_T [°]	32.15	33.23	3.35%
$VMGmin$ [m/s]	-5.77	-5.73	-0.80%
β_T [°]	166.05	166.38	0.22%

With the exception of the highest wind speed and very deep downwind courses, it can be concluded that differences in boat speed u_B between VPP results from EFD and CFD are smaller than 1% or 0.05 knots. It is shown in Table 8.2 that this difference has no effect on optimum VMG. It can therefore be concluded that these data set form a suitable base which can be used as comparison data for the result from RANSE-VPP.

In the following, various values which characterize the boat state will be discussed. Figures 8.7 and 8.8 illustrate the resultant heeling angle from EFD and CFD based VPP calculations for the upwind and the downwind sail set. Here red lines indicate EFD based calculations while blue lines represent CFD based results.

It can be seen, that the agreement between upwind and downwind heeling angle curves is very good for V_T of 5 m/s and 7.5 m/s. On average, the difference is about 0.5°. However, for V_T = 10 m/s the picture is somewhat different. Here, heeling curves differ significantly for $60° \leq \beta_T \leq 100°$ in the upwind case and between $100° \leq \beta_T \leq 120°$ for the downwind sail set. Difference of up to 6.8° occur, with the results gained from CFD always showing the smaller heel angle. Comparison with the polar curves (Figure 8.5) shows that these differences in heel angle occur in the vicinity of the highest boat speeds.

To investigate the source of the heel differences, the various components of the total resistance components have been reviewed. Figure 8.9 shows total resistance R_T, up-

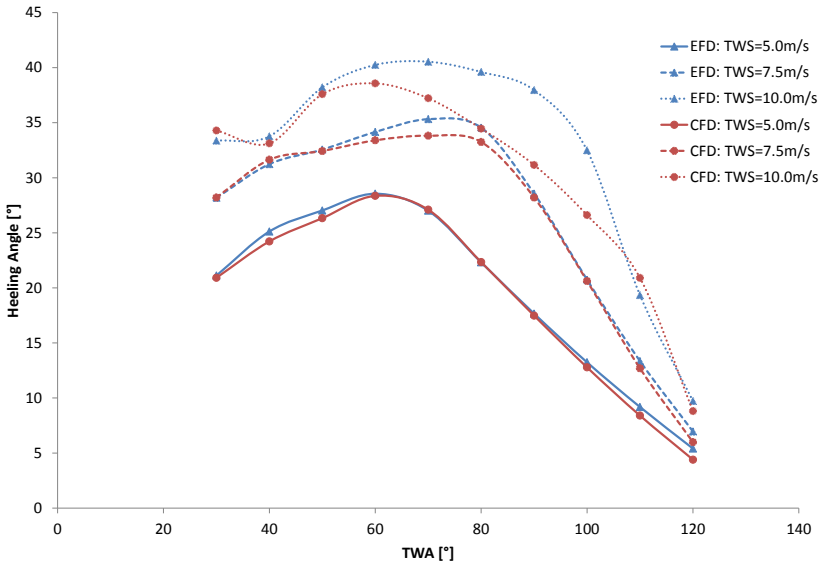

Figure 8.7: Comparison of upwind heeling angles calculated from EFD and CFD data

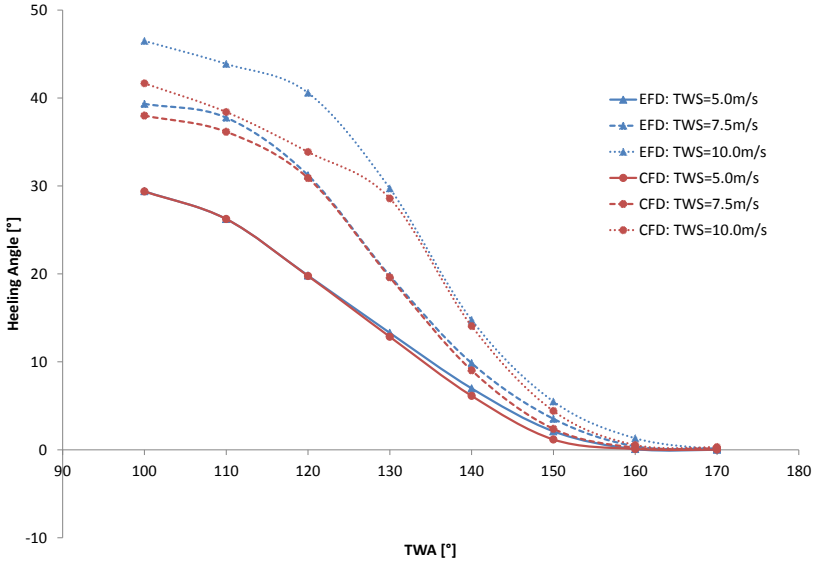

Figure 8.8: Heeling angles calculated for the downwind sail set

right resistance R_U, added resistance due to heel R_H and induced resistance R_i for EFD and CFD data sets. For both data sources, resistance components are shown at the same boat speed $u_B = 6.95$ m/s and for a heel range of $35° \leq \phi \leq 50°$. Figure 8.9 demonstrates, that the total resistance R_T (solid curves) is already 4.67% higher for CFD (red curve) than for EFD (blue curve) at $\phi = 35°$. The impact of the various resistance components on total resistance is as follows:

- Upright resistance R_U is almost identical in terms of absolute values. However, its relative contribution is very different. For CFD data, R_U contributes to R_T by 74.38% $R_{T_{CFD}}$. For EFD data the contribution is larger, being 92.89% $R_{T_{EFD}}$.
- Added resistance due to heel R_H is also almost identical, but slightly larger for EFD values. Its contribution to total resistance is limited (-1.51% $R_{T_{CFD}}$, -0.03% $R_{T_{EFD}}$);
- Induced resistance R_i turns out to be the source of difference in R_T between EFD and CFD data. R_i is much larger for CFD than for EFD. Its contribution to R_T is 27.13% $R_{T_{CFD}}$ and only 5.75% $R_{T_{EFD}}$.

The observed differences in heel and resistance can therefore be traced back to the differences in coefficient f_{h0} discussed in Section 8.3. This is the reason why for high boat speeds, the VPP finds a optimum boat speed at a more upright position for CFD than for EFD.

The next value of interest is the leeway angle. Predicted leeway angles for the upwind sail set are depicted in Figure 8.10, while the graphs for the downwind sail set are found in Figure 8.11. For most β_T, leeway angles upwind differ only by values smaller than 0.25°, which is very small. However, differences are again greatest for high values of β_T ($> 80°$). Here, leeway differences steadily increase to up to 0.7° with EFD giving smaller leeway angles. This agrees with the pattern previously observed for the heel angles and can be traced back to the differences in resistance.

Downwind, the pattern is similar. However, differences are generally a bit larger with up to 1°. Furthermore, these differences also occur at lower boat speeds. Therefore, the difference in leeway angle might also be in correlation with smaller heeling angles. Here, differences in heeling force at zero leeway f_{h0} and (smaller) differences in heeling force gradient $\partial f_H / \partial \beta$ as shown in Figure 8.4 might be the reason for leeway angle differences.

Finally, difference in $flat$ values are investigated. For the $flat$, only the upwind case is shown. This is because, as Figure 8.12 shows, the differences between EFD and CFD based $flat$ values is extremely small. The biggest difference does again occur at the highest boat speeds, were CFD based values are up to -0.1 smaller than EFD.

Overall the differences between results calculated from experimental and numerical data sets are in an order of magnitude such that it would be hard to reproduce them in sea trials. It can therefore be concluded RANSE CFD calculations allow to derive results

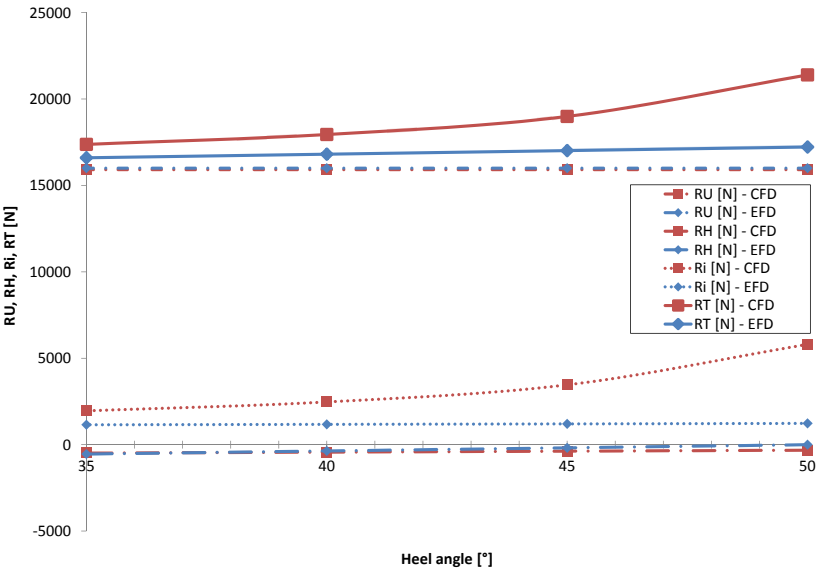

Figure 8.9: Breakdown of total resistance R_T into components upright resistance R_U, added resistance due to heel R_H and induced resistance R_i for EFD and CFD data sets. Boat speed $u_B = 6.95$ m/s for both CFD and EFD data, heel angle ϕ ranges from $35° \leq \phi \leq 50°$.

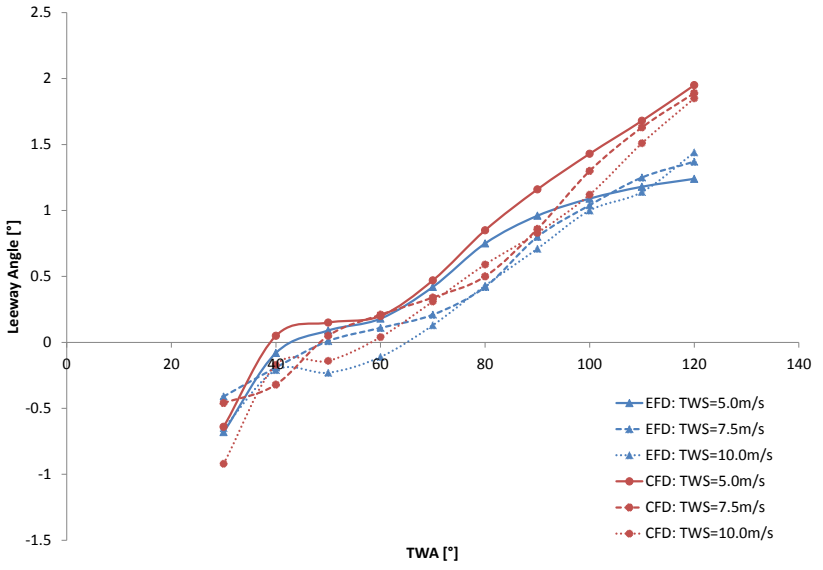

Figure 8.10: Leeway angles upwind from VPP calculation

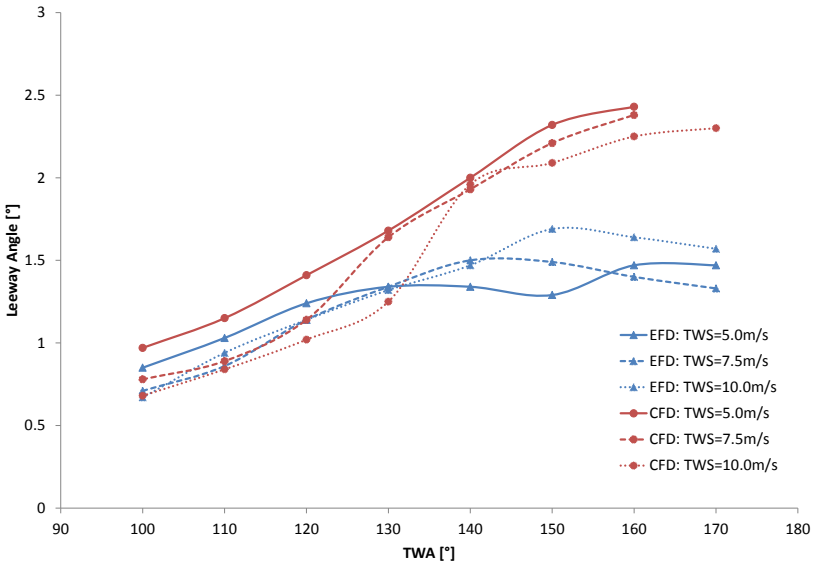

Figure 8.11: Comparison between EFD and CFD based VPP results for leeway angles on downwind courses

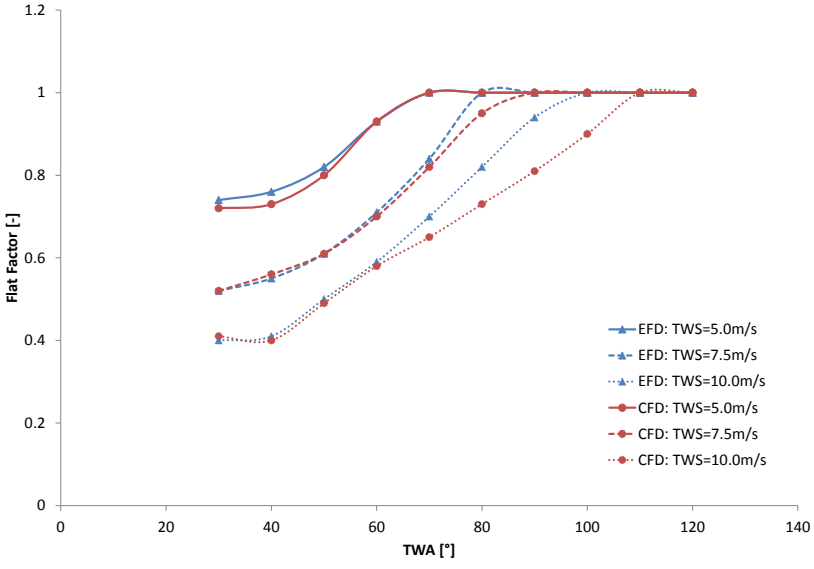

Figure 8.12: Flat factor on upwind courses for EFD and CFD based VPP results

which can match the quality of experimental towing tank data and therefore lead to a similar performance prediction. Furthermore, it can also be concluded that the data sets presented here form a suitable base which can be used as comparison data for the result from RANSE-VPP.

9

PERFORMANCE PREDICTION USING THE RANSE-VPP

In the following, VPP calculation using the RANSE-VPP will be described. The first section details the simulation setup used. Afterwards results from RANSE-VPP will be discussed and compared to the results of the conventional VPP calculations from Section 8.3

9.1. SIMULATION SETUP

The simulation setup in principle resembles that from the numerical towing tank described in the previous Chapter. The computational grid has also been created using the same meshing parameters, with exception of an additional extended vertical refinement zone to account for boat motion as described in Chapter 6. This vertical refinement zone extends 3.7 m above and below the calm water line. It implies an increase in grid cell size. For the present case this gives grid sizes of 15×10^6 cells. This is an increase of about 2.5×10^6 cells compared to the numerical towing tank.

The body motion module uses the same mass moment of inertia and center of gravity as for the numerical towing tank setup. However, the boat is allowed to move freely in 5-DOF instead of 2-DOF. The only motion which is kept fixed is the yaw rotation. Here the virtual rudder model as described in Section 4.2.4 is used to balance yawing moment M_z. Dynamic sail forces calculated by the aerodynamic model coupled to the simulation are applied to the yacht at their center of effort. For comparison reasons, the same sail force model was used as for the conventional VPP (see Section 8.3). However, in principal the choice of sail force model is arbitrary, as long as the same model is used for

the conventional VPP as for the RANSE-VPP calculations. Sail geometries and sail coefficients are identical to the conventional VPP approach. With these prerequisites, the RANSE-VPP calculation is started after an initial phase. The boat is set free and allowed to find its equilibrium. After force equilibrium for a certain wind condition is found, boat speed is further optimized using the trimming parameter $flat$.

The test matrix is identical to the conventional VPP and consists of:

- True wind speed $V_T = \{5.0, 7.5, 10.0\}$ [m/s]
- Upwind sail set: True wind angle $\beta_T = \{30, 40, ..., 120\}$ [°]
- Downwind sail set: $\beta_T = \{100, 110, ..., 180\}$ [°]

resulting in 10 wind directions upwind and downwind each at 3 wind speeds. In order to improve the free surface resolution, differences in heeling angle are restricted to +/-7.5 degrees. Therefore, a number of grids at varying heeling angles (0°, 10°, 20°, 27.5°, 30°, 35°) have been created. From an estimation of the expected heeling moment these grids are assigned to the individual wind condition. The whole investigation was then run completely automatically including automatic boat speed optimization using the $flat$ parameter.

9.2. RESULTS OF THE RANSE-VPP

Overall 155 valid boat conditions have been calculated to find the 60 optimum boat speeds for every wind condition of the test matrix. This corresponds to an average of 2.58 variations $flat$ to find the optimum boat speed.

Computational run time of the whole simulation was about 1344 hours. The simulation was run simultaneously on 4 servers reducing overall time to produce the results to 336 hours, or 2 weeks. This is roughly comparable to the time necessary for the large test matrix of the numerical towing tank simulations in Section 8.2. The amount of data produced during the simulation is about 0.87 TB.

Figure 9.1 shows a typical results of the RANSE-VPP. The boat is traveling at a boat speed of 4.99 m/s at true wind conditions of $\beta_T = 40°$ and $V_T = 5$ m/s. Resultant apparent wind speed and angle as well as forces on the boat and orientation of it are depicted on the lower left side. Red arrows mark the center of effort of rudder and sail force vectors. Free surface resolution looks as detailed and well defined as during verification and validation studies reported in Chapter 7.

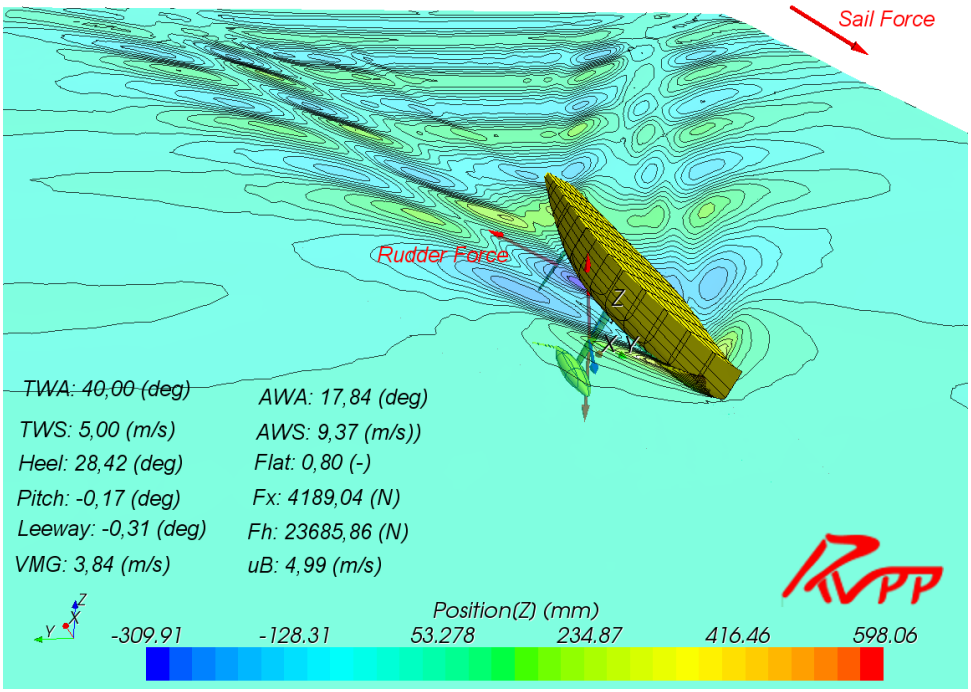

Figure 9.1: A typical results of RANSE-VPP: The boat is propelled and heeled by the sail forces, deforming the free surface around it. Essential values regarding sailing state of the boat are found on the lower left side of the plot. True wind conditions are denoted as TWS and TWA and indicate a close-hauled sailing state. The orientation of the boat is given in terms of leeway, heel and pitch. Boat velocity is displayed in terms of u_B and velocity made good VMG. For this case, the trim optimization routine has found an optimum trim for this case at $flat$=0.8. Resulting apparent wind conditions AWA and AWS as well as resistance Fx and heeling force Fh are also shown.

9.3. COMPARISON WITH CONVENTIONAL VPP

In the following, the optimum boat performance as calculated by RANSE-VPP will be compared to the conventional VPP results. To enhance clarity and comparability, results are shown for only one true wind speed V_T per diagram. Every diagram shows upwind and downwind sail set results for all three VPP variants (EFD, CFD and RANSE-VPP based). Blue lines represent EFD based VPP results, red lines stands for CFD based results whilst the green lines typify RANSE-VPP values.

In the first diagram, Figure 9.2, heeling angle variations for V_T = 5 m/s are shown. In general, the diagram shows that heeling angles curves from RANSE-VPP are not as smooth as the curves of the conventional VPP. Furthermore, the RANSE-VPP tends to predict a larger heeling angle for the upwind case than the other two data sets. On average, the difference is about 3.5° of heel, maximum being 4.4°. This offset is noticeable and relates to a difference of approximately 15% in heeling force. However, ACCV5 boats have some well known specific design criteria, for example see van Oossanen [139]. These should be kept in mind while judging the presented results. ACCV5 boats have a U-shaped hull with relatively small width and are therefore known to rely on weight stability. This boat type is designed to heel early in order to create a longer and narrower waterline. To this end, these boat have a relatively large design heels of about 27.5°. It is possible that the RANSE-VPP captures this effect better. However, since no full-scale comparison data is available, this remains an open question. For the downwind sail set, the difference in heeling angle is smaller and the three data sets compare much better.

Heeling angles for V_T = 7.5 m/s show a similar trend. The RANSE-VPP again gives larger heeling angles than the conventional VPPs. The offset is almost constant at an average of 3.6°, which is slightly larger than for V_T = 5 m/s. With 10.2° the difference is largest at β_T = 100°, where the RANSE-VPP curve shows a peak. Downwind, the difference is also slightly larger than for the lower wind speed, the average difference in heel being 2.0°.

For the largest wind speed of 10 m/s, the differences in heel angle get smaller between EFD and RANSE-VPP. Differences between RANSE-VPP and EFD on the one side and CFD on the other side increase. The difference between RANSE-VPP and EFD based VPP is almost constant with a mean difference of 2.1° upwind and 0.40° downwind. Differences for results from CFD based VPP are obviously larger in upwind case since these also deviate from EFD. It was demonstrated in Section 8.3 that the differences in heel between EFD and CFD at V_T = 10 m/s are related to differences in induced resistance, see Figure 8.9. It is interesting to note that the results of the RANSE-VPP here seem to confirm the VPP results gained from EFD and not the ones from CFD. Comparison of leeway angles is shown here exemplary for V_T = 5 m/s (Figure 9.5) since the patterns are identical for the other two wind speeds. Generally, leeway angle upwind is larger for RANSE-VPP than for EFD and CFD results. The curve slope of RANSE-VPP follows the CFD based VPP results at an average difference of 0.74° and with an almost constant offset. For the downwind sail set, the picture is somewhat different. At first, the lee-

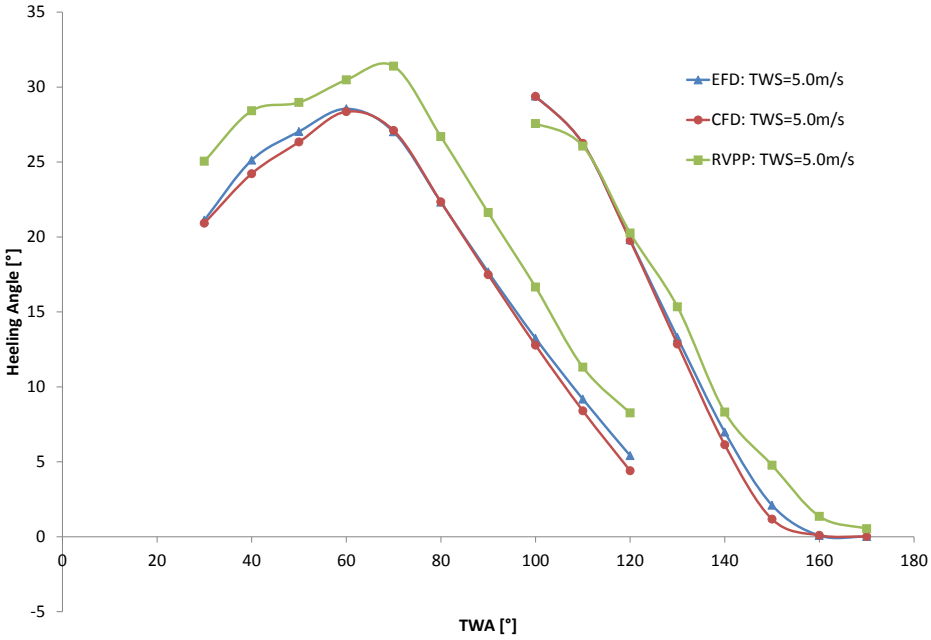

Figure 9.2: Comparison of heeling angles for $V_T = 5$ m/s

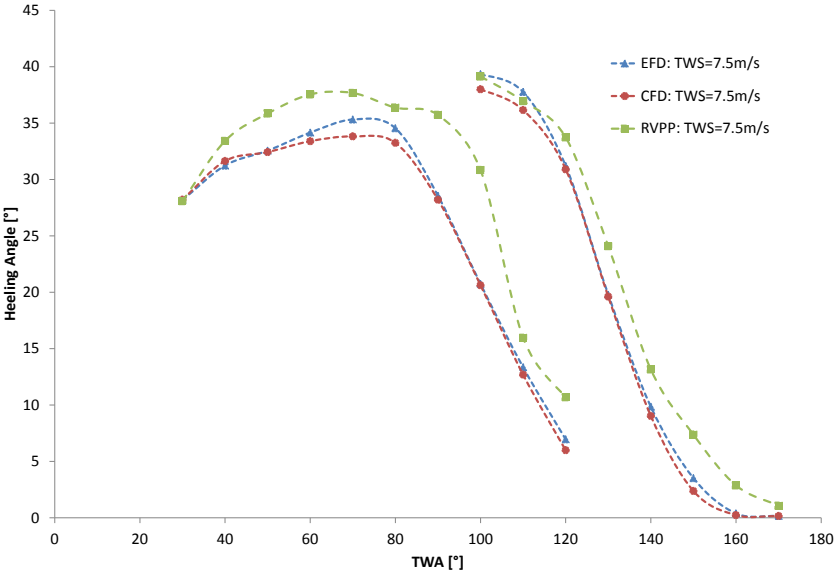

Figure 9.3: Heeling angles from EFD, CFD and RANSE-VPP based VPP results for $V_T = 7.5$ m/s

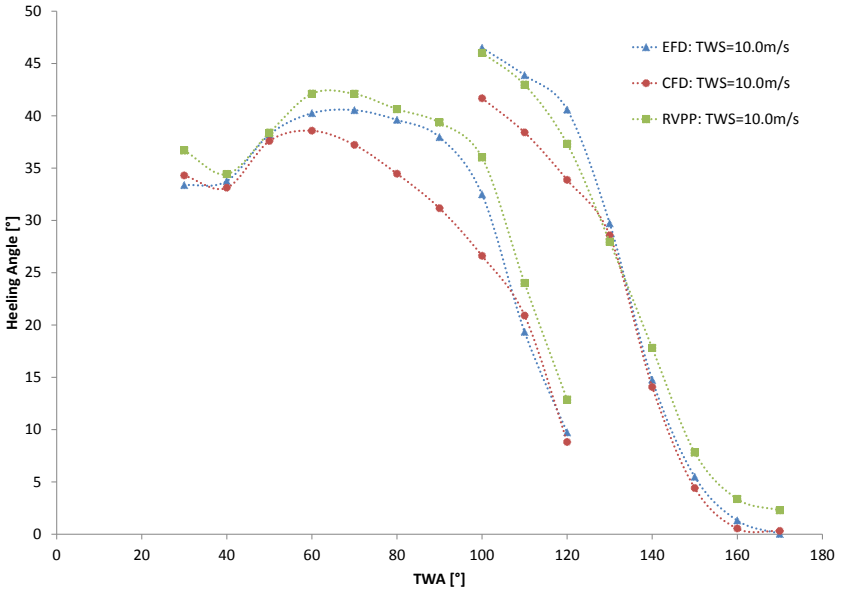

Figure 9.4: Comparison of heeling angle for $V_T = 10\,\mathrm{m/s}$

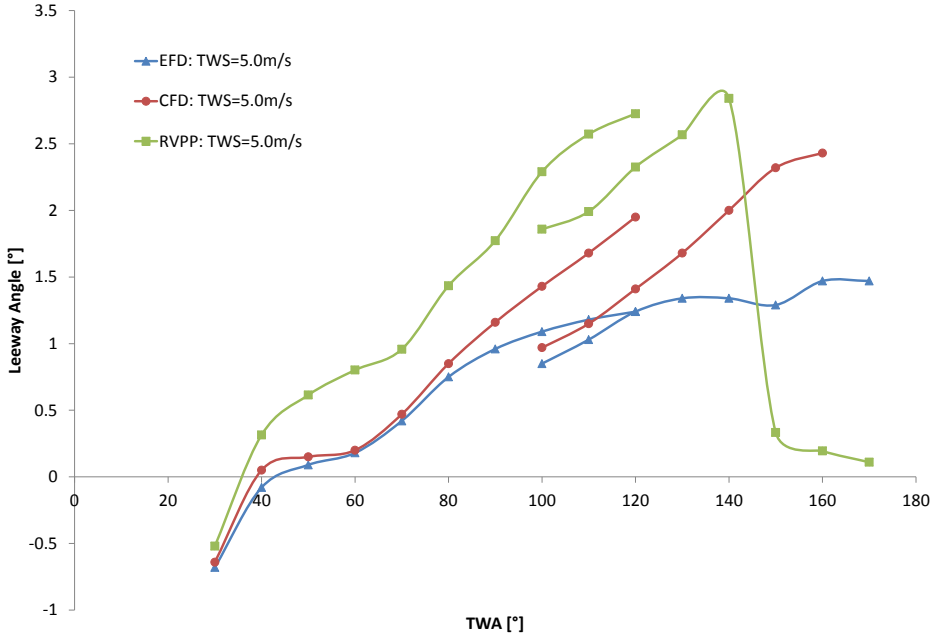

Figure 9.5: Comparison of leeway angle for $V_T = 5\,\mathrm{m/s}$

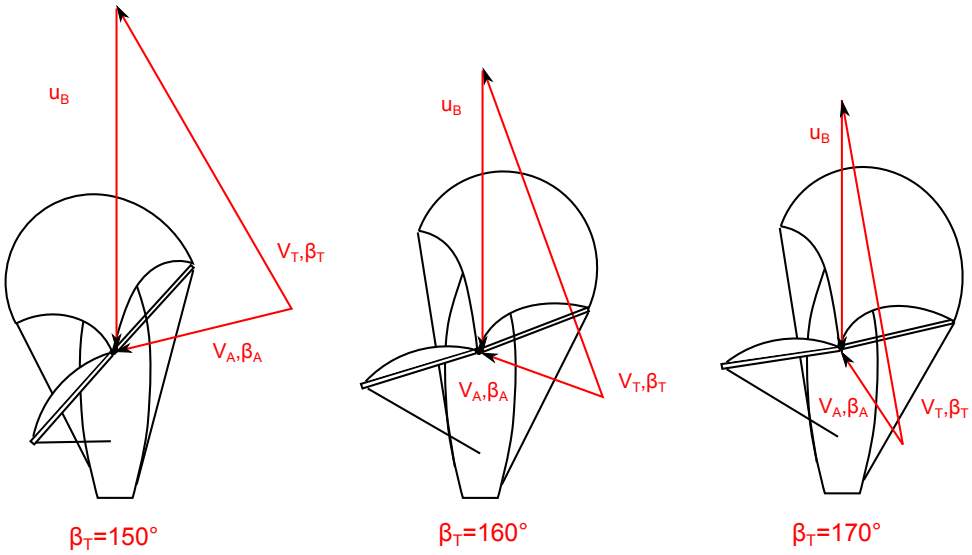

Figure 9.6: Influence of true wind angle β_T on apparent wind speed V_A and angle β_A for downwind courses. U_B denotes boat speed. For constant true wind speed V_T the apparent wind speed V_A and angle β_A change significantly with increasing β_T.

way angle curve also resembles the slope of the CFD results. When reaching $\beta_T = 150°$, the RANSE-VPP leeway angles suddenly drops to almost zero, while the other two VPP results still show an increase in leeway. The increase in leeway predicted by the conventional VPPs is rather surprising, since with increasing true wind angle, wind enters more astern. The influence on apparent wind is illustrated in Figure 9.6. At $\beta_T = 150°$, apparent wind angle $\beta_A < 90°$, resulting in close reach to beam reach conditions. Since lift is acting perpendicular to apparent wind, this conditions can induce a significant side force, which in turn implies leeway. From $\beta_T = 160°$ on, apparent wind begins to enter from astern. Apparent wind is wandering from broad reach over beam reach to running conditions at $\beta_T = 170°$. Additionally, apparent wind speed V_A decreases. These combined effects reduce sideforce and result in a decreasing leeway. Therefore, the trend predicted by the RANSE-VPP is more realistic.

The next parameter to be investigated is the $flat$ factor, which is a measure of how much the sail has to be depowered by the sailors. Similar to leeway angle, comparison of $flat$ values will also only be shown for the smallest wind speed. Again, this is because the overall pattern stays the same for the whole investigated wind range.

Figure 9.7 shows the slope of the $flat$ curves for the three methods. One can easily see that all curves are similar, enhancing confidence that the optimization algorithms as implemented in the RANSE-VPP works well. Differences are very small and mainly exist for β_T of 170° and 180°. Since the apparent wind angle for these cases is such that heeling forces are almost non-existent, the reduction of $flat$ factor, as seen in EFD and

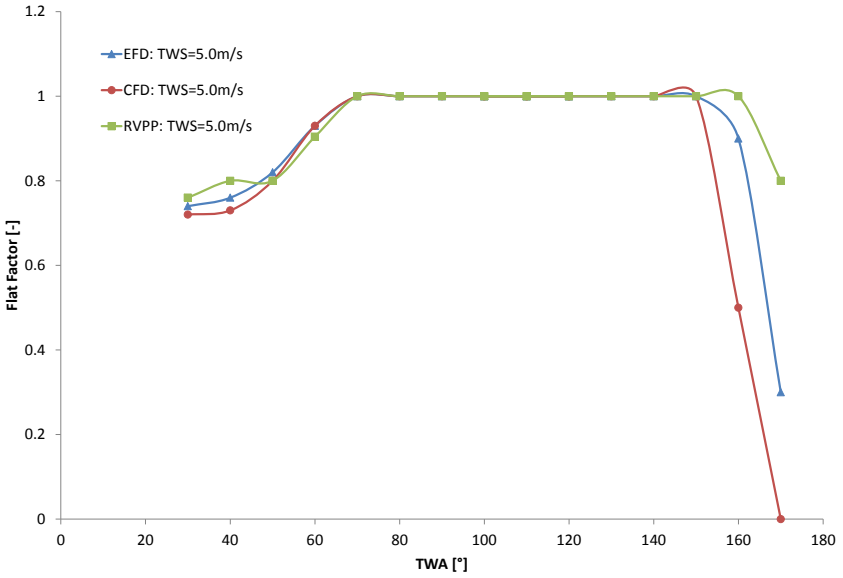

Figure 9.7: Flat factor for $V_T = 5$ m/s

CFD, should not be necessary. Here, RANSE-VPP seems to give more realistic values.

Naturally, the most important result of a VPP is the predicted boat velocity. Therefore, the velocity polars obtained with the different methods will be discussed. Again, the results will be presented for both upwind and downwind sail set, all methods used and one true wind speed per time. Figure 9.8 illustrates velocity polars and time allowance deltas for $V_T = 5$ m/s. EFD based VPP results are colored red, CFD based VPP results are represented by blue lines and the green lines show the RANSE-VPP results. Time allowance deltas, as a measure of time necessary to sail one nautical mile, are with respect to the RANSE-VPP. The velocity polar show that differences between RANSE-VPP and the conventional VPP data is very small for most of the true wind angle range. However, the biggest difference occurs in the interesting areas of maximum upwind and downwind VMG. Upwind the maximum difference is roughly 0.1 m/s ($2\% u_B$) while downwind maximum differences vary from 0.45 m/s (EFD) to 0.67 m/s (CFD) ($12-20\% u_B$). Especially the later difference is quite remarkable but coincides with the findings of the heel angle in Figure 9.2 and the leeway angle (Figure 9.5). Here the heel angle from RANSE-VPP was found to be a bit larger than the others, indicating more power on the boat. Leeway angle, on the other hand was found to be significantly smaller at this point of sailing for the RANSE-VPP. This should be accompanied by a reduced resistance compared with the conventional VPPs and could be a possible explanation for velocity polars in Figure 9.8. Time allowance deltas confirm that the difference in boat speed is generally very small. For most β_T the difference to sail one nautical mile is around 2 seconds. Again, the difference grows larger for the high upwind and low downwind courses with the most

significant difference being around 95 seconds on a downwind run.

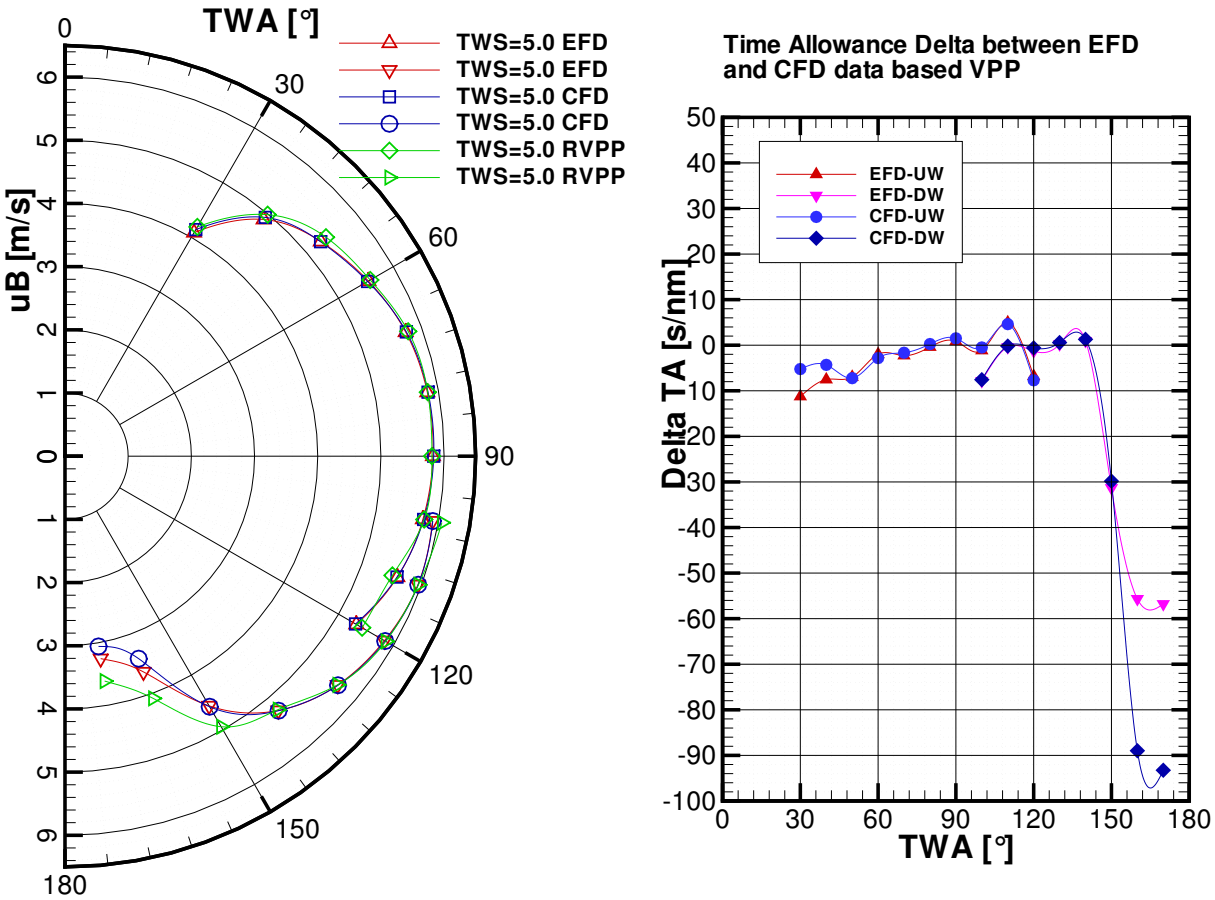

Figure 9.8: Velocity polar and time allowance deltas for $V_T = 5$ m/s

For $V_T = 7.5$ m/s the relative difference between the results stays approximately the same. However, the region in which the maximum differences occur changes. Whilst for $V_T = 5$ m/s these differences occurred at close-hauled and running points of sailing, these now occur at beam and broad reaching courses. Maximum Δu_B is 0.4 m/s upwind (6%U_B at $\beta_T = 90°$) respective 0.2 m/s downwind (3%U_B at $\beta_T = 150°$). Time allowance delta plot shows that average ΔTA has slightly increased to about 12 seconds upwind and 5 seconds downwind. However, maximum ΔTA has decreased to smaller than 19.3 s. As a general trend, RANSE-VPP gives slightly larger boat speeds. Since $V_T = 7.5$ m/s is already a considerable wind speed, this might be due to the use of dynamic righting moments from fluid body interaction instead of a righting moment curve as used in the conventional VPPs.

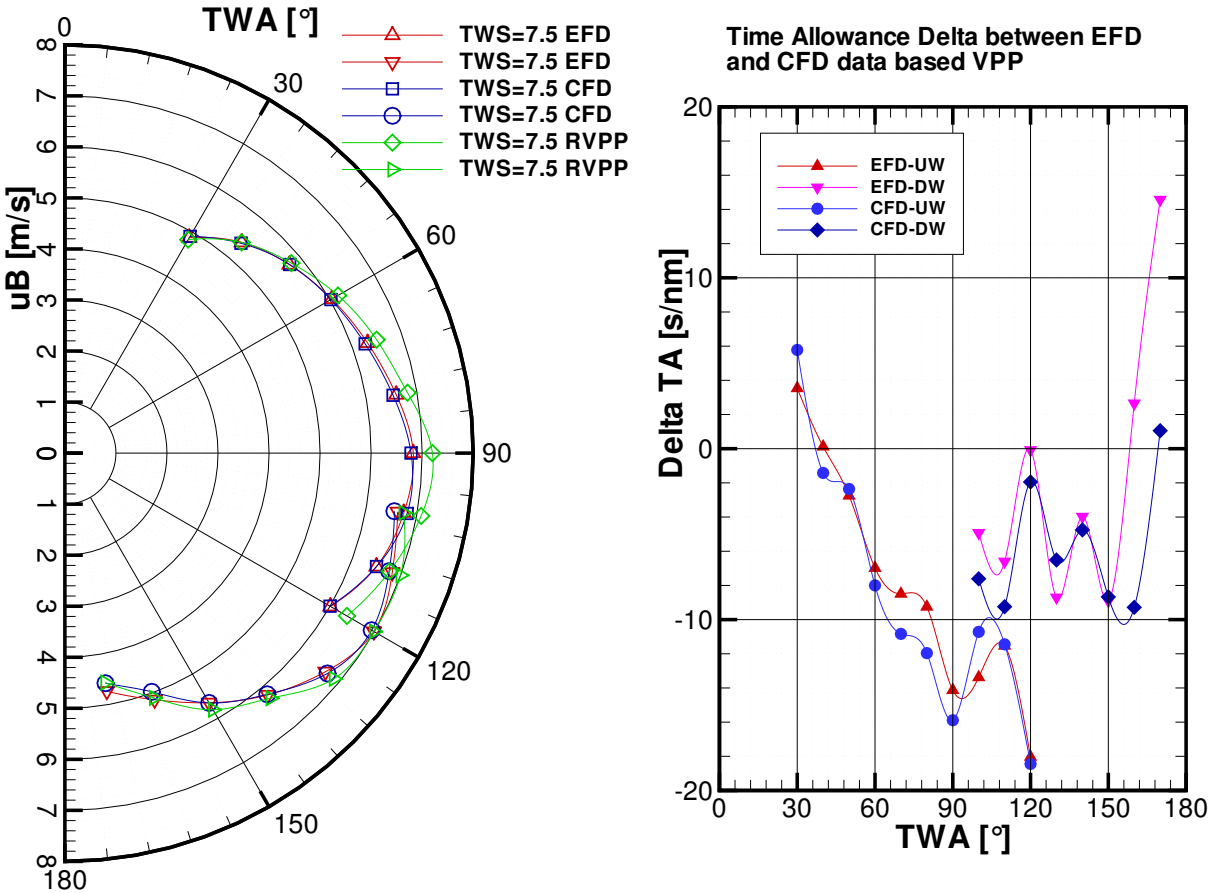

Figure 9.9: Velocity polar and time allowance deltas for $V_T = 7.5$ m/s

The last investigated true wind speed is 10 m/s. Here the trend that RANSE-VPP predicts slightly higher boat speeds as previously seen for the lower wind speeds is not valid anymore. Instead, the predicted velocity matches very good with the data from conventional VPPs and EFD. The average difference in boat speed u_B is 0.038 m/s for the upwind and 0.009 m/s for the downwind case. Maximum deviation is 0.46 m/s upwind and 0.27 m/s downwind corresponding to 7%u_B respective 3%u_B. However, the velocity polar of RANSE-VPP for V_T = 10 m/s fits smoothly between the differences of EFD and CFD based velocity information. Especially the peaks at 100° for the EFD and 110° for the CFD found in the upwind data are not depicted that sharply in the RANSE-VPP data. Time allowance deltas are similar to V_T = 7.5 m/s in terms of average and maximum differences.

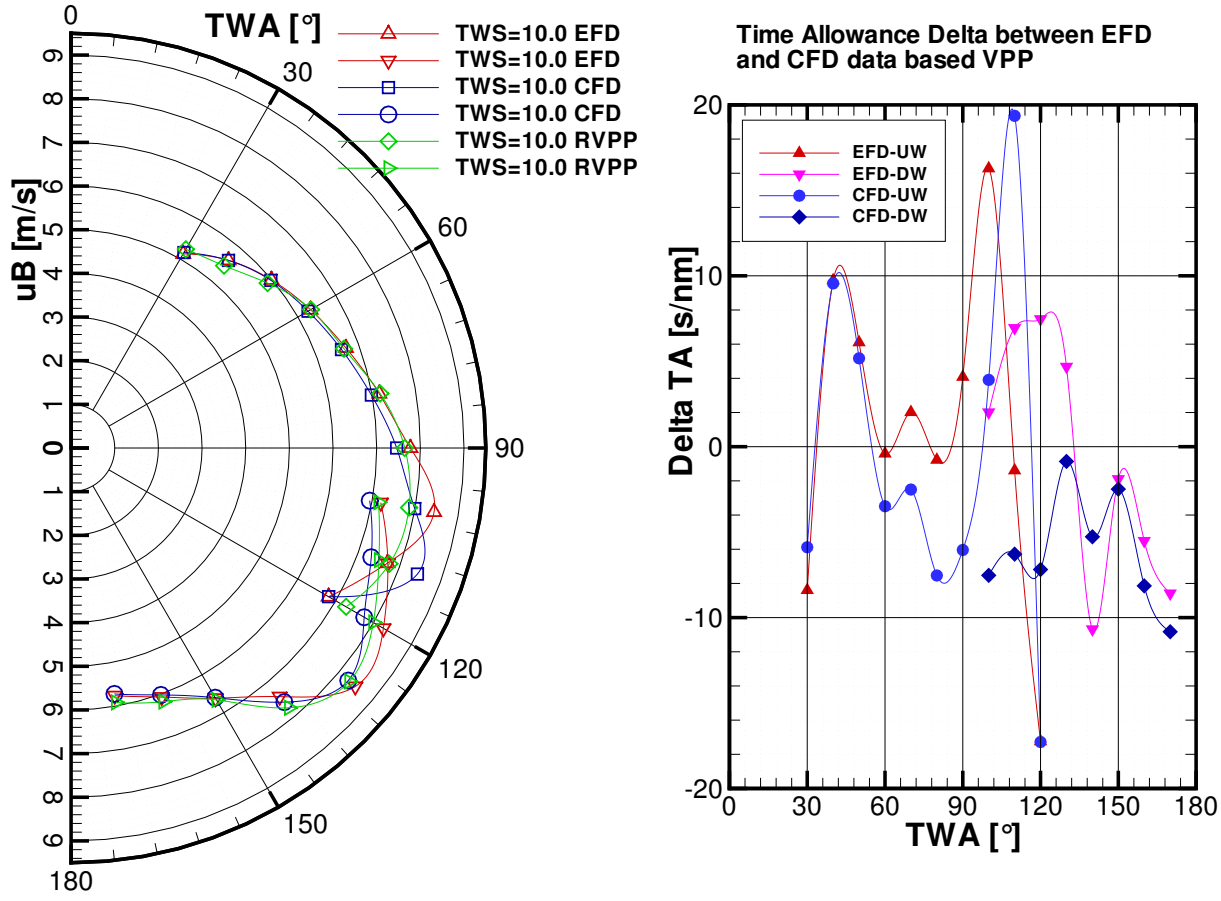

Figure 9.10: Velocity polar and time allowance deltas for $V_T = 10$ m/s

A major design information is the maximum achievable velocity made good on upwind and downwind courses. Optimum upwind and downwind VMG are listed for all three VPP approaches in Table 9.1. The relative deviation listed in the table are all with respect to RANSE-VPP. In general, upwind VMG shows only small differences in boat speed with these normally being smaller than 0.05 m/s. The maximum difference is 0.12m/s at $V_T = 10\,m/s$. Differences in optimum true wind angle β_T are a bit larger. Here the differences rank from around 0.4° to 0.8° ($V_T = 5$ m/s) over 2.77° to 1.83° ($V_T = 7.5$ m/s) to 3.23° to 2.15° ($V_T = 10$ m/s). These differences are noticeable. However, considering that sailing boat instruments are able to resolve apparent wind angle to ±2° and boat speed to the first digit, the differences are still on the verge what is measurable on a boat. Furthermore, the deltas are of only slightly higher magnitude than the those between the EFD and CFD data set using the conventional VPP approach.

Table 9.1: Optimum Upwind / Downwind VMG

	EFD	CFD	RVPP	ΔEFD [%]	ΔCFD [%]
			$V_T = 5.0$ [m/s]		
$VMGmax$ [m/s]	3.74	3.77	3.82	2.27%	1.28%
β_T [°]	38.24	37.83	38.66	1.09%	2.18%
$VMGmin$ [m/s]	-3.99	-3.98	-4.29	7.47%	7.78%
β_T [°]	144.19	144.22	151.02	4.74%	4.72%
			$V_T = 7.5$ [m/s]		
$VMGmax$ [m/s]	4.22	4.23	4.19	-0.67%	-0.81%
β_T [°]	32.77	31.38	30.00	-8.45%	-4.40%
$VMGmin$ [m/s]	-4.83	-4.87	-5.00	3.47%	2.7%
β_T [°]	153.25	154.50	151.81	-0.94%	-1.74%
			$V_T = 10.0$ [m/s]		
$VMGmax$ [m/s]	4.43	4.47	4.54	2.44%	1.58%
β_T [°]	32.15	33.23	30.00	-6.68%	-9.71%
$VMGmin$ [m/s]	-5.77	-5.73	-5.91	2.44%	3.26%
β_T [°]	166.05	166.42	166.38	0.2%	-0.03%

Downwind differences are found to be slightly larger. VMG differs around 0.3 m/s and 7° for $V_T = 5\,m/s$. This is in accordance with the assumption that leeway and heeling angle calculated by RANSE-VPP have an favorable influence on boat speed as explained above for the respective velocity polar. For $V_T = 7.5$ m/s the achieved VMG is about 0.2 m/s larger and the optimum β_T is between the values of conventional VPP, varying from -1.86° (CFD) to +1.44° (EFD). At the highest wind speed of 10 m/s, VMG is around 0.25 m/s larger, whilst optimum downwind β_T is almost identical for all 3 VPP results. It is noticeable that optimum downwind β_T experiences a significant shift of roughly 14° from $V_T = 7.5$ m/s to $V_T = 10$ m/s. This makes the optimum downwind course for such a high wind speed a running course instead of the broad reach which is normally preferred at lower wind speeds. The ratio behind this is that the stability of the yacht

is not sufficient to remain on a broad reach. Therefore the optimum course here is one with more abaft winds. Again, this well known phenomenon is captured accurately by the RANSE-VPP.

9.4. SUMMARY

This section showed performance prediction with the RANSE-VPP. The achieved results have been compared with those from conventional VPP. In general, the RANSE-VPP tends to predict slightly larger heel and leeway angles. This might be due to differences between the treatment of rudder forces and yaw balancing in conventional VPP and RANSE-VPP. It should be noted that for deep downwind courses, the leeway angles produced are in good agreement with boat behavior experienced on the water, while the same does not hold for the conventional VPP's output. This puts a good light on the virtual rudder model used for the RANSE-VPP.

Results for boat speeds correlate rather well with conventional VPP data. On average, the deviation from conventional VPP results is smaller than $3\%U_B$. However, there are always some areas in which deviations are higher. In most cases, these differences occur for highly loaded sailing states in which the righting moment plays an important role. Here RANSE-VPP has the advantage that it determines all effects contributing to the righting moment by taking into account influence of heel, pitch and waves through the rigid body motion module.

In general, the RANSE-VPP has been shown to work well. Problems like influence of heeling angle variations on grid resolution have been mastered and the VPP could be run highly automated. The implemented boat speed optimization algorithm gave similar results for reasonable $flat$ values compared with the other VPPs.

The work presented here gives a working solution for the task of creating a VPP with a hydrodynamic model based on a integrated and fully coupled RANSE simulation. However, this is can only be a first step and opens possibilities for further research work. Since no measured full scale data was available, the question whether the RANSE-VPP gives more accurate results than the conventional VPPs has to remain open. Therefore, further research should be pointed towards validation of the VPP. In the author's opinion, this could only be done versus full-scale measurements. Such a validation of VPP results is challenging, since the acquisition of accurate of real time boat data is problematic. For example, these data obviously takes into account effects due to sea state. VPP results, on the other hand, are calculated for calm water conditions and are therefore somewhat idealized. Research in the RANSE-VPP model itself could be directed towards reduction of the grid induced limitations on heel angle changes. Here, improvement of overset grid techniques might present an advancement. Finally, implementation of an unsteady sail force model would allow for maneuvering and seakeeping simulations.

10

CONCLUSIONS AND RECOMMENDATIONS

10.1. CONCLUSIONS

The present work has been initiated to improve the accuracy of traditional velocity prediction of sailing yachts. To this end, it was decided to link the hydrodynamic model directly to a flow simulation. By taking into account aerodynamic forces from a sail force model, one is able to directly evaluate the hydrodynamic forces at the actual boat state of the yacht for a given wind condition. It was assumed that this way interpolation errors in the hydrodynamic model could be avoided and secondary effects due to actual boat orientation taken into account. Furthermore, it seemed possible to save time and effort by reducing the necessary number of investigations.

Literature gives several methods to evaluate hydro- and aerodynamic forces acting on a sail boat. In this thesis a viscous flow solver based on RANSE was chosen to evaluate the hydrodynamic forces within the VPP because the model is able to handle the yacht traveling in displacement, semi-displacement or planing mode without additional effort which is not the case for all inviscid methods. Coupling of aero- and hydrodynamic forces is possible by treating the forces coming from the sails as external force vectors. This coupling is hard to achieve within towing tank tests. Finally, the RANSE flow solver is promising in terms of accuracy. However, there are also some disadvantages. The computational effort for viscous flow simulations is many times higher than that for inviscid CFD. Towing tank testing is also quicker but one has to take into account the time for model building and the increased effort which an aerodynamic force coupling would imply. This coupling could practically only be achieved in a circulation tank, which are

often restricted in size and therefore accuracy. Therefore, the RANSE simulation was chosen as the best compromise between all available methods.

For the aerodynamic force model of the VPP the situation is somewhat different. Also it is in principal possible to evaluate sail forces using CFD, the variety of possible trim parameters possible to find an optimum sail trim is very challenging. Since this force evaluation has to be done frequently whilst the VPP searches for hydrodynamic and aerodynamic force equilibrium, this is extremely time consuming. The alternative is to use a sail force model. Literature gives several different models, with the *implicit* sail force model being the best compromise between effort and accuracy. In this thesis an implicit sail force model of Hazen type was chosen. Although also it is in principal possible to use any available implicit sail force model within the RANSE-VPP, the Hazen type model was chosen to allow better comparison with the available conventional VPP which use the same model.

After first attempts to evaluate yacht hydrodynamics using RANSE simulations, severe problems with free surface resolution occurred. These problems, which are sometimes referred to as *numerical ventilation*, are a known problem for RANSE free surface simulations using the VOF method. They are most often encountered when the investigated body features a blunt bow and a small acute angel with the calm water line. To address this problem, several different free surface modeling techniques for RANSE solvers have been reviewed regarding their theoretic background. From this investigation, VOF method still evolved as the most promising method. Furthermore, the problem could be traced back to an interface smearing due to the use of low order advection schemes and a possible solution was developed. This solution approach has been tested in Section 7.1.2 and has been found to produce sharp free surface resolution for cases which seek a steady state solution as it is the case for the RANSE-VPP.

The RANSE-VPP uses a sail force vector to find equilibrium of aero- and hydrodynamic forces. The sail force vector is updated every time step depending on true wind speed V_T and angle β_T as well as current boat state. The sail force model used is of quasi-steady type with some extensions for sail induced heel and pitch damping. Within this model, sail trim to optimize speed is mimicked by variations of the global trim parameters. Evaluation of these trim parameters has been identified as one of the main drivers of computational effort, since it implies the search for a new aero- and hydrodynamic force equilibrium every time a new trim parameter is applied to the simulation. Therefore, a optimizing algorithm based on bracket and parabolic search has been implemented which evaluates trim parameters as few times as possible.

A further obstacle for the RANSE-VPP has been resolution of fluid-body interaction within the computational grid. While this topic is well researched for small, random motions or rotational motion inside a turbomachine, large motions still pose a problem. This problem is magnified by the grid density needed for a sharp resolution of the free surface interface. Here especially large differences in heeling angles proved to be problematic. Different techniques to resolve yacht motion have been investigated in Chap-

ter 6. The insights gained from this investigation led to an approach based on complete grid motion with vertical refinements in the area of the free surface to resolve heel motion. Nonetheless, heeling motion had to be restricted to +/- 7° making it necessary to approximate the expected heeling moment before using the RANSE-VPP. Although this solution is not ideal, it proved to be the only realistic option currently available.

With the modeling of the RANSE-VPP and the selection of the different components finished, a formal verification and validation of the hydrodynamic part of the model has been conducted. This proved to be very insightful regarding grid density and the influence of free surface resolution. It was shown that insufficient resolution of the free surface can lead to a significant underestimation of the resistance due to smaller wave resistance. The results of the EFD were reproduced with CFD to an accuracy of about 1% which is inside the resolution of towing tanks. Further simulations over the complete Froude range as well as yaw sweeps showed deviations from EFD to be a bit larger, up to 3 - 4%. Nonetheless, the verification and validation study allows the conclusion that modern viscous CFD methods can match the accuracy of towing tank tests if conducted with the necessary care.

After the successful testing of the hydrodynamic model, simulations using RANSE CFD have been performed to reproduce the test matrix of the towing tank data. Both EFD and CFD data sets have been processed to gain input for a conventional VPP. The velocity polars as well as the respective boat states have been compared. Differences have been found to be largest for high wind speeds which correlates to differences in resistance curve and side force coefficients f_{H0}.

Finally, the RANSE-VPP has been used to create results at the same true wind conditions as the conventional VPP. Comparison of velocity polars in general showed that maximum difference between RANSE-VPP and results from EFD and CFD based VPP occurred for low wind speeds on downwind course. Here maximum difference in boat speed U_B is up to 20% for $V_T = 5$ m/s and $\beta_T = 170°$. For higher wind speeds maximum difference reduces to 3 - 4%U_B. Average difference on downwind courses is between 4% and 0.1% of U_B. In contrast to downwind course, maximum differences on upwind courses occurred for high wind speeds and ranged up to 7%U_B in reaching conditions $\left(100 \leq \beta_T \leq 120\right)$. The average differences for upwind course are the same as for downwind, ranging again from 4% to 0.1%U_B.

Differences in VMG did not exceed 2.5% in upwind conditions. Differences in downwind conditions are a larger with 7.8%VMG in lightwind conditions. However, the latter can be correlated with differences in leeway which have been depicted more realistic by the RANSE-VPP. A thorough validation of the results proved difficult, especially since full-scale results have not been available. Use of such data would also be difficult because of the influence of sea state and could be a point for further research work. Since in most cases, differences between RANSE-VPP and conventional VPP results are of an order of magnitude which is on the verge what is measurable on a boat, this will be challenging. At this stage, this work presents a first implementations of a RANSE-VPP. Also first results

look promising, it cannot be finally judged if reducing linearisation and interpolation by using the RANSE-VPP increases accuracy of results.

When reviewing the whole work done throughout this thesis, it can be concluded that one of the major improvements drawn from this work is the increased resolution of the free surface. This led to an increased accuracy of the free surface RANSE simulation with respect to towing tank results. The RANSE-VPP showed good results but revealed some problems inherent to the system. The biggest problem for the RANSE-VPP, besides resolution of heel angle and optimizing for boat speed, is that it is valid only for one specific sail set. In contrast to hydrodynamic coefficients gained from numerical or experimental towing tank procedures which can be applied to various sail sets, the whole testing using RANSE-VPP has to be redone if performance information for other sail combinations are wanted. Another problem is the resolution of heeling motion with a moving grid. Due to grid size restrictions this approach is only feasible for a small heel angle range, making it necessary to have a good approximation of heeling moment to be expected. While giving good results, the approach certainly is too cumbersome for engineering practice. However, with increase in computational power and further developments in overset grid techniques this might change in the future.

Besides the problems stated above, RANSE-VPP can be an interesting choice for special cases. For example, if only a few sailing points, like maximum upwind and downwind VMG, are of interest, RANSE-VPP can be used to decrease computational effort. Another application which could be of interest is the evaluation of multihull performance. Since these boats travel at a fixed righting moment and therefore heel angle, resolution of heel angles is not mandatory. This significantly reduces computational effort and therefore makes RANSE-VPP a choice which can be considered.

10.2. RECOMMENDATIONS

From the problems encountered and insights gained during this thesis, the following recommendations are made for further research on an integrated VPP and its associated topics:

- To improve the confidence in prediction of hydrodynamic forces on a yacht, further formal verification and validation studies should be performed against experimental towing tank data. To enhance confidence, these studies should be conducted as double blind trials. A possible candidate for these studies could be the experimental data of the DSYHS, which are now publicly available at `http://dsyhs.tudelft.nl`.
- The overall operability of a RANSE-VPP could be enhanced by removing the heel angle range constraint. This could be achieved by using overset grid techniques which would allow for arbitrary motion on a background grid. Also the computational effort for overset grid technique is currently too high, it seems to be a very

good option for the future. Therefore, further grid motion developments should be targeted into that direction. This would also be advantageous if one would like to include maneuvering and seakeeping into the simulation.

- To prepare for maneuvering and seakeeping, an unsteady sail force model should be developed or implemented to remove the quasi-steady approach used during this work. Some effort has been made recently by various researchers in the field of yacht fluid dynamics to develop such a model. However, given the complexity of the topic, developing and validating an unsteady sail force model is a still field for future research.

A

SAIL FORCE MODELS

Since the main focus of this thesis is to directly couple the hydrodynamic model of a VPP to a flow solver, it is most important to have a sail force model which can be compared to a conventional VPP. The absolute accuracy of this sail force model is of minor importance, because as long as one knows that hydrodynamic model and coupling is correct, the sail force model can be exchanged at will. Therefore, the *Kerwin* sail force model was used during this thesis. The model, which has been described in Section 3.2.4 is the starting point of almost all quasi-static semi-empirical sail force models. However it shows some deficiencies regarding modeling of induced drag. In this section two alternative ways to evaluate aerodynamic forces, the *Jackson* model and the *Fossati* model, are described. Both approaches are aimed at a more realistic modeling of sail twist and resulting increase induced drag and lowering of center of effort.

A.1. JACKSON MODEL

In order to address the deficiencies of the depowering model of the Hazen sail force model, Jackson [115, 46] introduced a new parameter called $twist$. The goal of the new model, which is developed for upwind sails, was to explicitly model the relationship between induced drag C_{Di}, lift C_L and vertical center of effort ZCE. Its basic equations are

A

$$C_L = C_{Lmax}(\beta_A)\, reef^2\, flat, \tag{A.1}$$

$$C_{Di} = CE\, C_{Lmax}^2(\beta_A)\, flat^2\, reef^2\,(1 + c\, t^2), \tag{A.2}$$

$$C_{Ds} = c_s C_{Lmax}^2(\beta_A)\, reef^2\, flat^2, \tag{A.3}$$

$$C_D = C_{Dp}(\beta_A)\, reef^2 + C_{Ds} + C_{Di}, \tag{A.4}$$

$$CE = KPP + \frac{1}{\pi\, H_{eff}^2}, \tag{A.5}$$

$$t = 1 - \frac{ZCE}{ZCE_{opt}}, \tag{A.6}$$

with t as the trim parameter $twist$ and c as the twist weight function. The parameter t is 0 for $ZCE = ZCE_{opt}$. Any deviation from this optimum spanwise loading results in a drag penalty which is give by t^2 in the induced drag formulations. The twist weight function c has to be derived from experiments. Jackson [46] explains that in experiments conducted by Jones [140] values of $c = 8$ and $ZCE_{opt} = 0.42$ were found, which is in good agreement with aerodynamic theory. It has to be noted that these experiments have not been conducted for sails. Compared to the Hazen-model, the Jackson-Model splits up the drag into an additional component C_{Ds} which accounts for separation drag. Separation drag is assumed to arise due to flow separation from the surface of a lifting surface. The scalar c_S is the separation constant. Since it is difficult to separate parasitic profile drag and separation drag, they are commonly expressed together as the viscous drag. According to Kerwin [3], common c_S values are 0.016 for a upwind sail set (mainsail + jib) and 0.019 for a downwind sails (main sail + spinnaker). In [115] Jackson reports that wind tunnel experiments showed twist weight function c and ZCE_{opt} for sails to be smaller than the values derived by by Jones [140]. Nonetheless, he was able to achieve good agreement with wind tunnel tests and therefore concluded that the sail force model was well capable of capturing additional induced drag due to twisted trim. Fossati [141] however, reported differences in fitting wind tunnel data to the models expressions due to the onset of separation. Here the model showed a somewhat ambiguous behavior therefore Fossati suggested a new model which will be described below.

The Jackson model shows an interesting approach towards a more realistic modeling of depowering. It is currently in use but has not become a world wide standard. The reasons are most probably the additional effort to derive the twist weight function and a missing (published) verification and validation of the formulations which would increase the confidence in the model.

A.2. FOSSATI MODEL

As described above, current sail force modeling suffers from a number of deficiencies. The parameter $flat$ is used to model the effect of twist on induced drag. However, the modeling is no correct since it neglects the influence of twist on the vertical center of

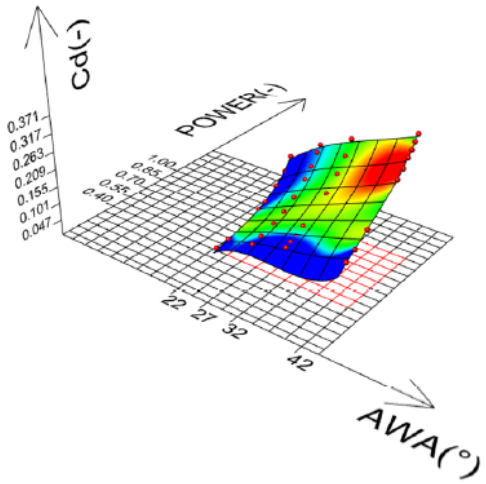

Figure A.1: Surface of Drag Coefficent over Apparent Wind Angle and trim parameter $power$ (Source: Fosati et al. [141])

effort ZCE. The parameter $reef$ has an impact on ZCE but is more a geometrical than an aerodynamic factor. The main criticism on $reef$ is that it changes geometry by scaling all sails equally instead of replacing a foresail whilst keeping the main. Sometimes $reef$ is used to emulate twist. Doing so is simply wrong since $reef$ adds no drag penalty but equally reduces C_D and C_L. Using the parameter $twist$ as introduced by Jackson [46] is an interesting approach. However, it is currently not often seen in practice.

With the deficiencies of the current sail force models in mind, Jackson et al. [142] proposed a model which is completely based on wind tunnel results. In particular the empiric approaches of the various semi-empirical models to emulate depowering and its effect on induced drag are abandoned. Instead drag and lift coefficients as well as the vertical center of effort are modeled as *surfaces*. Besides the mentioned variables, these surfaces also depend on apparent wind angle β_A and on a new parameter called $power$.

Fossati et al. [141] published a further development of the model. The surfaces are now modeled as parametric *Bezier Surfaces*, allowing to evaluate the position vectors of the surface control points as functions of apparent wind angle β_A and $power$. Furthermore, they propose to include the sailplan characteristics which have the main influence on sail aerodynamics, for example jib overlap or mainsail roach.

Figure A.1 illustrates the method on the example of the drag coefficient.

$$C_L; C_D; ZCE = f\left(\beta_A, power\right). \tag{A.7}$$

The basic idea behind the $power$ parameter is that the main reason for depowering and thus deviating from an optimum trim is the need to reduce heeling moment.

Therefore $power$ is defined as

$$power = \frac{C_{Mx}(\beta_A)}{C_{Mx,Max}(\beta_A)}. \tag{A.8}$$

With $C_{Mx}(\beta_A)$ as the current and $C_{Mx,Max}(\beta_A)$ the maximum heeling moment coefficient. The VPP can than use the $power$ parameter as trim variable to optimize boat speed. A problem of this approach is that it has to take into account non-optimum trims. This possibly leads to an increased effort for wind tunnel testing. However, normal wind tunnel testing procedures are based on an iterative approach to find the optimum. Therefore, non-optimum trims should be available anyway, but perhaps not covering the needed data space. This will have to be investigated in the future. In the current stage, the model seems to be in a preliminary state. However, it introduces a very interesting approach which shows potential for future VPP implementations.

REFERENCES

[1] K. S. M. DAVIDSON. **Some experimental studies of the sailing yacht**. In *Stevens Institute of Technology, SNAME annual Transaction*, USA, 1936. 4, 5, 9

[2] J. E. KERVIN, B. W. OPPENHEIM, AND J. H. MAYS. **A Procedure for Sailing Performance Analysis Based on Full Scale Log Entries an Towing Tank Data**. In *Report, Massachusetts Institute of Technology; Department of Ocean Engineering*, New London, Connecticut, USA, 1974. 4, 13

[3] J. E. KERVIN. **A velocity prediction program for occan racing yacht**. In *MIT Irving Pratt Ocean Race Handicapping Project*, USA, 1978. 4, 13, 40, 47, 51, 172

[4] J. E. KERWIN AND J. N. NEWMAN. **A Summary of the H. IRVING PRATT Ocean Race Handicapping Project**. In *4th Chesapeake Sailing Yacht Symposium*, Annapolis, MD, USA, 1979. 4, 13, 51

[5] C. A. MARCHAJ. *Sail Performance, Theory and Practice*. Adlard Coles Nautical, London, 1996. 5, 39

[6] F. FOSSATI, S. MUGGIASCA, I. M. VIOLA, AND A. ZASSO. **Wind Tunnel Techniques for Investigation and Optimization of Sailing Yacht Aerodynamics**. In *2nd High Performance Yacht Design Conference*, RINA, Auckland, NZ, 2006. 5, 39

[7] O. MÜLLER AND K. GRAF. **Der Twist-Flow Windkanal der Yacht Research Unit Kiel**. In *26th Symposium on Yacht Design and Construction*, Deutscher Boots- und Schiffbauerverband, Hamburg, GER, 2005. 5

[8] J. H. MILGRAM. **Naval Architecture Used in Winning the 1992 America's Cup Match**. In *Centennial Meeting*, SNAME, NewYork, 1993. 7

[9] J. H. MILGRAM, D. B. PETERS, AND D.N. ECKHOUSE. **Modelling IACC Sail Forces by Combining Measurements with CFD**. In *11th Chesapeake Sailing Yacht Symposium*, Annapolis, MD, USA, 1993. 7

[10] Y. MASUYAMA AND T. FUKASAWA. **Full Scale Measurement of Sail Force and the Validation of Numerical Calculation Method**. In *13th Chesapeake Sailing Yacht Symposium*, Annapolis, MD, USA, March 1997. 7

[11] K. HOCHKIRCH. *Entwicklung einer Messyacht zur Analyse der Segelleistung im Orginalmassstab (Design and Construction of a Full-Scale Measurement System for the Analysis of Sailing Performance)*. PhD thesis, Technische Universität Berlin, 2000. 7

[12] K. HOCHKIRCH AND H. BRANDT. **Fullscale Hydrodynamic Force Measurement on the Berlin Sailing Dynamometer**. In *14th Chesapeake Sailing Yacht Symposium*, Annapolis, MD, USA, 1999. 7

[13] F. FOSSATI, S. MUGGIASCA, I. BAYATI, AND C. BERTORELLO. **Innovation Hub Sailing Yacht Lab project**. In *3rd International Conference on Innovation in High Performance Sailing Yachts*, Lorient, France, June 2013. 7

[14] I.M. VIOLA AND R. FLAY. **Pressure Distributions on Sails Investigated Using Three Methods: On-Water Measurements, Wind-Tunnel Measurements and Computational Fluid Dynamics**. In *20th Chesapeake Sailing Yacht Symposium*, Maryland, USA, March 2011. 7

[15] B. AUGIER, P. BOT, AND F. HAUVILLE. **Experimental Full Scale Study in Yacht Sails and Rig Under Unsteady Sailing Conditions and Comparison to Fluid Structure Interaction Unsteady Models**. In *20th Chesapeake Sailing Yacht Symposium*, Maryland, USA, March 2011. 7

[16] J. MAUSOLF, J. DEPARDAY, K. GRAF, H. RENZSCH, AND C. BÖHM. **Photogrammetry Based Flying Shape Investigation of Downwind Sails in the Wind Tunnel and at Full Scale on a Sailing Yacht**. In *20th Chesapeake Sailing Yacht Symposium*, Maryland, USA, March 2011. 7

[17] M. CAPONNETTO, A. CASTELLI, P. DUPONT, B. BONJOUR, P.-L. MATHEY, S. SANCHI, AND M. L. SAWLEY. **Sailing Yacht Design using Advanced Numerical Flow Techniques**. In *14th Chesapeake Sailing Yacht Symposium*, Annapolis, MD, USA, 1999. 8

[18] H. J. RICHTER, K. C. HORRIGAN, AND J. B. BRAUN. **Computational Fluid Dynamics for Downwind Sails**. In *16th Chesapeake Sailing Yacht Symposium*, Annapolis, MD, USA, 2003. 8

[19] K. GRAF AND H. RENZSCH. **RANSE Investigations of Downwind Sails and Integration into Sailing Yacht Design Processes**. In *2nd High Performance Yacht Design Conference*, RINA, Auckland, NZ, 2006. 8

[20] H. RENZSCH, O. MÜLLER, AND K. GRAF. **FLEXSAIL - A Fluid Structure Interaction Program for the Investigation of Spinnakers**. In *International Conference on Innovation in High Performance Sailing Yachts*, Lorient, France, 2008. 8

[21] K. RENZSCH, H.AND GRAF. **Fluid Structure Interaction of Spinnakers - getting closer to reality**. In *2nd International Conference on Innovation in High Performance Sailing Yachts*, Lorient, France, 2010. 8

[22] K. GRAF, C. BÖHM, AND H. RENZSCH. **CFD- and VPP-Challenges in the Design of the New AC90 Americas Cup Yacht**. In *19th Chesapeake Sailing Yacht Symposium*, Annapolis, MD, USA, March 2009. 9

[23] D. TRICHMARCHI, S. R. TURNOCK, D. J. TAUNTON, AND D. CAPELLE. **The use of shell elements to capture sail wrinkles and their influence on aerodynamic loads**. In *2nd International Conference on Innovation in High Performance Sailing Yachts*, Lorient, France, June 2010. 8

[24] M. DURAND, F. HAUVILLE, , P. BOT, B. AUGIER, Y. ROUX, A. LEROYER, AND M. VISONNEAU. **Unsteady Numerical Simulations of Downwind Sails**. In *2rd International Conference on Innovation in High Performance Sailing Yachts*, Lorient, France, June 2010. 8

[25] M. DURAND, C. LOTHBODE, F. HAUVILLE, A. LEROYER, M. VISONNEAU, R. FLOCH, AND L. GUILLAUME. **FSI Investigation on Stability of Downwind Sails with an Automatic Dynamic Trimming**. In *3rd International Conference on Innovation in High Performance Sailing Yachts*, Lorient, France, June 2013. 8

[26] I. CAMPBELL. **A Comparison of Downwind Sail Coefficients from tests in different Wind Tunnels**. In *3rd International Conference on Innovation in High Performance Sailing Yachts*, Lorient, France, June 2013. 9

[27] J. GERRITSMA, R. ONNINK, AND A. VERSLUIS. **Geometry, Resistance and Stability of the Delft Systematic Yacht Hull Series**. In *7th HISWA Symposium*, Amsterdam, NL, 1981. 10

[28] J. GERRITSMA, J. A. KEUNING, AND A. VERSLUIS. **Sailing Yacht Performance in Calm Water and in Waves**. In *11th Cesapeake Sailing Yacht Symposium*, Annapolis, MD, USA, 1993. 10

[29] J. GERRITSMA, R. ONNINK, A. VERSLUIS, AND A. VAN GULIK. **The Bare Hull Resistance of the Delft Systematic Yacht Hull Series**. In *HISWA Symposium*, Amsterdam, NL, 1996. 10

[30] J. A. KEUNING AND U. B. SOMMENBERG. **Developments in Velocity Based on the Delft Systematic Yacht Hull Series**. In *International Conference on the Modern Yacht*, RINA, 1998. 10

[31] J. A. KEUNING AND M. KATGERT. **A Bare Hull Resistance Prediction Method Derived from the Results of the Delft Systematic Yacht Hull Series Extended to Higher Speeds**. In *International Conference on Innovation in High Performance Sailing Yachts*, Lorient, France, 2008. 10

[32] W. BEUKELMAN AND J. A. KEUNING. **The Influence of Fin-Keel Sweep-back on the Performance of Sailing Yachts**. In *5th HISWA Symposium*, Amsterdam, NL, 1975. 10

[33] J. A. KEUNING. **Wake Measurements on a 3.20 meter Sailing Yacht Model**. Report Nr. 698, Delft Shiphydromechanics Laboratory, Delft, 1985. 10

[34] J. GERRITSMA AND J. A. KEUNING. **Further Experiments with Keel-Hull Combinations**. In *1st Tampa Bay Sailing Yacht Symposium*, St.Petersburg, USA, 1986. 10

[35] J. A. KEUNING AND G. KAPSENBERG. **Wing-body Interaction on a Sailing Yacht**. In *12th Cesapeake Sailing Yacht Symposium*, Annapolis, MD, USA, 1995. 10

[36] C. W. BOPPE, B. S. ROSEN, AND J. P. LAIOSA. **Stars & Stripes '87; Computational Flow Simulation For Hydrodynamic Design**. In *8th Chesapeake Sailing Yacht Symposium*, Annapolis, MD, USA, 1987. 11

[37] M. CAPONNETTO. **A Review on Il Moro di Venezia Design**. In *11th Chesapeake Sailing Yacht Symposium*, Annapolis, MD, USA, 1993. 11

[38] B. S. ROSEN, J. P. LAIOSA, W. H. DAVIS, AND D. STAVETSKI. **SPLASH Free-Surface Flow Code Methodology for Hydrodynamic Design and Analysis of IACC yachts**. In *11th Chesapeake Sailing Yacht Symposium*, Annapolis, MD, USA, 1993. 11

[39] E. N. TINOCO, A. E. GENTRY, P. BOGATAJ, E. G. SEVIGNY, AND B. CHANCE. **IACC Appendage Studies**. In *11th Chesapeake Sailing Yacht Symposium*, Annapolis, MD, USA, 1993. 11

[40] K. GRAF AND E. WOLF. **CFD investigations and Design Integration for Sailing Yachts**. In *1st High Performance Yacht Design Conference*, RINA, Auckland, NZ, 2002. 11

[41] G. COWLES, N. PAROLINI, AND M. L. SAWLEY. **Numerical Simulation using RANS-based Tools for America's Cup Design**. In *16th Chesapeake Sailing Yacht Symposium*, Annapolis, MD, USA, 2003. 11

[42] R. AZECUETA. *Computation of Turbulent Free Surface Flow around Ships Floating Bodies*. PhD thesis, TU Hamburg-Harburg, 2001. 11

[43] C. BÖHM AND K. GRAF. **Advancements in Free Surface RANSE Simulations for Sailing Yacht Applications**. In *3rd International Conference on Innovation in High Performance Sailing Yachts*, Lorient, France, June 2013. 11

[44] E. C. SCHLAGETER AND J. R. TEETERS. **Performance Prediction Software for IACC Yachts**. In *11th Chesapeake Sailing Yacht Symposium*, Annapolis, MD, USA, 1993. 13

[45] A. CLAUGHTON. **Developments in the IMS VPP Formulations**. In *14th Chesapeake Sailing Yacht Symposium*, Annapolis, MD, USA, March 1999. 13, 51

[46] P. S. JACKSON. **An Improved Upwind Sail Model for VPPs**. In *15th Chesapeake Sailing Yacht Symposium*, Annapolis, MD, USA, March 2001. 13, 49, 50, 171, 172, 173

[47] J. TEETERS, R. RANZENBACH, AND M. PRINCE. **Changes to Sail Aerodynamics in the IMS Rule**. In *16th Chesapeake Sailing Yacht Symposium*, Annapolis, MD, USA, 2003. 13, 51

[48] K. GRAF AND C. BÖHM. **A New Velocity Prediction Method for Post-Processing of Towing Tank Test Results**. In *17th Chesapeake Sailing Yacht Symposium*, Annapolis, MD, USA, March 2005. 13, 55

[49] A. CLAUGHTON, F. FOSSATI, S. MUGGIASCA, AND D. BATTISTIN. **Changes and Development to Sail Aerodynamics in the ORC International Handicap Rule**. In *20th HISWA Symposium*, Amsterdam, NL, 2008. 13, 51

[50] J. A. KEUNING, K. J. VERMEULEN, AND E. J. DE RIDDER. **A Generic Mathematical Model for the Maneuvering and Tacking of a Sailing Yacht**. In *17th Chesapeake Sailing Yacht Symposium*, Annapolis, MD, USA, 2005. 14

[51] Y. MASAYUMA, T. FUKASAWA, AND H. SASAGAWA. **Tacking Simulation of Sailing Yachts - Numerical Integration of Equation of Motion and Application of Neural Network Technique**. In *12th Chesapeake Sailing Yacht Symposium*, Annapolis, MD, USA, 1995. 14

[52] J. NIELSEN. *Timing of the Pre-Start Manoeuvre for an America's Cup Yacht*. Master's thesis, KTH Royal Institute of Technology, 2006. 14

[53] J. R. BINNS, K. HOCHKIRCH, F. DEBORD, AND I. A. BURNS. **The Development and use of Sailing Simulation for IACC Starting Manoeuvre Training**. In *3rd High Performance Yacht Design Conference*, RINA, Auckland, NZ, 2008. 14

[54] Y. ROUX, S. HUBERSON, F. HAUVILLE, J.P. BOIN, M. GUILBAUD, AND M. BA. **Yacht Performance Prediction: Towards a numerical VPP**. In *1st High Performance Yacht Design Conference*, RINA, Auckland, NZ, Decembre 2002. 14

[55] E. JAQUIN, Y. ROUX, P.-E. GUILLERN, AND B. ALESSANDRINI. **Toward numerical VPP with the full coupling of hydrodynamic and aerodynamic solvers for ACC yacht**. In *17th Chesapeake Sailing Yacht Symposium*, Annapolis, MD, USA, March 2005. 14

[56] Y. ROUX, A. LEROYER, J. RAYMOND, AND F. HAUVILLE. **Strongly coupled VPP and CFD RANSE code for Sailing Yacht Performance Prediction**. In *3rd High Performance Yacht Design Conference*, RINA, Auckland, NZ, Decembre 2008. 14

[57] R. KORPUS. **Performance Prediction without Empiricsm: A RANS-Based VPP and Design Optimization Capability**. In *18th Chesapeake Sailing Yacht Symposium*, Annapolis, MD, USA, March 2007. 14, 50

[58] B. MASKEW AND F. DEBORD. **Upwind Sail Performance Prediction for a VPP including "Flying Shape" Analysis**. In *19th Chesapeake Sailing Yacht Symposium*, Annapolis, MD, USA, March 2009. 14

[59] H. HANSEN. *Enhanced Wind Tunnel Techniques and Aerodynamic Force Models for Yacht Sails*. PhD thesis, University of Auckland, 2006. 15, 39, 49

[60] T. SARPKAYA AND M. ISAACSON. *Mechanics of wave forces on offshore structures*. Van Nostrand Reinhold, 1981. 21

[61] R. WILSON, P. CARRICA, AND F. STERN. **URANS simulations for a high-speed transom stern ship with breaking waves**. *International Journal of Computational Fluid Dynamics*, **20**:105 – 125, 2006. 21

[62] J. WACKERS, B. KOREN, H. C. RAVEN, A. VAN DER PLOEG, A. R. STARKE, G. B. DENG, P. QUEUTEY, M. VISONNEAU, T. HINO, AND K. OHASHI. **Free-Surface Viscous Flow Solution Methods For Ship Hydrodynamics**. *Archives of Computational Methods in Engineering*, **18**:1 – 41, 2011. 21, 22, 24, 38

[63] J.H. FERZIGER AND M. PERIC. *Computational Methods for Fluid Dynamics*. Springer, New York, 2002. 22, 23, 75, 77, 99

[64] O. UBBINK. *Numerical predictions of two fluid systems with sharp interfaces*. PhD thesis, Imperial College of Science, Technology & Medicine. University of London, 1997. 22, 31

[65] J. WACKERS. *Surface capturing and multigrid for steady free-surface water flows*. PhD thesis, Delft University of Technology, 2007. 22, 31

[66] R.M. COLEMAN AND H.J. HAUSSLING. **Nonlinear waves behind an accelerated transom stern**. In *Procceedings of the 3rd Intrnational Conference on Numerical Ship Hydrodynamics*, Paris, France, 1981. 23

[67] DI MASCIO, R. A. MUSCARI, AND R. BROGLIA. **Computation of flow past the US Navy Combatant DTMB5415 by a Godunov-type scheme**. In *Gotenburg 2000 - A Workshop on Numerical Ship Hydrodynamics*, Gothenburg, Sweden, 2000. 23

[68] J. FARMER, L. MARTINELLI, AND A. JAMESON. **A fast multigrid method for solving the nonlinear ship wave problem with a free surface**. In *Proceedings of the 6th International Conference on Numerical Ship Hydrodynamics*, Iowa, USA, 1993. 23

[69] E.G. PATERSON, R.V. WILSON, AND F. STERN. **General-Purpose Parallel Unsteady RANS Ship Hydrodynamics Code: CFDSHIP-IOWA, IIHR Report No.432**. Technical report, Iowa Institute of Hydraulic Research, The University of Iowa, 2003. 23

[70] T. SUNDELL. **Computations of the free-surface flow around a ship using NS solver FINFLO, Technical Report M206, VALB279**. Technical report, VTT Manfufacturing Technology, Finnland, 1997. 23

[71] B. ALESSANDRINI AND G. DELHOMMEAU. **Simulation of three-dimensional unsteady viscous free surface flow around a ship model**. *International Journal for Numerical Methods in Fluids*, **19**(4):321–342, 1994. 23

[72] B. ALESSANDRINI AND DEL. **A fully coupled Navier-Stokes solver for calculations of turbulent incompressible free surface flow past a ship hull**. *International Journal for Numerical Methods in Fluids*, **29**:125 – 142, 1999. 23

[73] B. ALESSANDRINI AND G. DELHOMMEAU. **A multigrid velocity-pressure-free surface elevation fully coupled solver for calculation of turbulent incompressible flow around a hull**. In *Proceedings of the 21st Symposium on Naval Hydrodynamics*, **19**, pages 321–342, Trondheim, Norway, 1996. John Wiley & Sons, Ltd. 23

[74] N. HIRATA AND T. HINO. **An efficient algorithm for si,ulating free-surface turbulent flows around an advancing ship**. *Journal of the Society of Naval Architects of Japan*, **185**:1–8, 1999. 23

[75] C. O. E. BURG, K. SREENIVAS, D. G. HYAMS, AND B. MITCHELL. **Unstructured nonlinear free surface simulations for the fully-appended DTMB Model 5415 series hull including rotaing propulsors**. In *Proceedings of the 24th Symposium on Naval Hydrodynamics*, Fukuoka, Japan, 2002. 23

[76] C. O. E. BURG, K. SREENIVAS, D. HYAMS, AND B. MITCHEL. **Unstructured Nonlinear Free Surface Flow Solutions: Validation and Verification**. In *32nd AIAA Fluid Dynamics Conference and Exhibit*, St.Louis, Missouri, June 2002. 23

[77] M. HOEKSTRA. *Numerical Simulation of ship stern flows with a space-marching Navier-Stokes method*. PhD thesis, Delft University of Technology, 1999. 23

[78] M. HOEKSTRA AND L. ECA. **PARNASSOS: An efficient method for ship stern flow calculation**. In *Proceedings of the 3rd Osaka Colloquium on Advanced CFD Applications to Ship Flow and Hull Form Design*, Osaka, Japan, 1998. 23

[79] A. VAN DER PLOEG, M. HOEKSTRA, AND L. ECA. **Combing accuracy and efficiency with robusteness in ship stern flow computation**. In *23rd Symposium on Naval Hydrodynamics*, Val de Rueil, France, 2000. 23

[80] H. C. RAVEN AND A. R. STARKE. **Efficient methods to compute steady ship viscous flow with free surface**. In *Proceedings of the 24th Symposium on Naval Hydrodynamics*, Fukuoka, Japan, 2002. 23

[81] H. C. RAVEN, A. VAN DER PLOEG, A. R. STARKE, AND L. ECA. **Towards a CFD-Based Prediction of Ship Performance - Progress in Predicting Full-Scale Resistance and Scale Effects**. *International Journal of Maritime Engineering*, **RINA Trans. 150**:(A4), 2008. 23

[82] F H HARLOW AND J E WELCH. **Numerical calculation of time-dependent viscous incompressible flow of fluid with free surface**. *Physics of Fluids*, **8**(12):2182–2189, 1965. 26

[83] M SUSSMAN, P SMEREKA, AND S OSHER. **A Level Set Approach for Computing Solutions to Incompressible Two-Phase Flow**. *Journal of Computational Physics*, **114**(1):146–159, 1994. 26

[84] M. VOGT AND L. LARSSON. **Level set methods for predicting viscous free surface flows**. In *Proceedings of the 7th International Symposium on Numerical Ship Hydrodynamics*, Nantes, France, 1999. 26

[85] J. YANG, N. SAKAMOTO, Z. WANG, P. CARRICA, AND F. STERN. **Two Phase Level-Set/Immersed-Boundary Cartesian Grid Method for Ship Hydrodynamics**. In *9th International Conference on Numerical Ship Hydrodynamics*, Michigan, USA, 2007. 26

A

[86] A. CURA HOCHBAUM AND C. SHUMANN. **Free Surface viscous flow around ship models**. In *Proceedings of the 7th International Symposium on Numerical Ship Hydrodynamics*, Nantes, France, 1999. 26

[87] D. G. DOMMERMUTH, M. SUSSMAN, R.F. BECK, T. T. O'SHEA, D. C. WYATT, K. OLSON, AND P. MACNEICE. **The numerical simulation of ship waves using cartesian grid methods with adaptive mesh refinement**. In *25th Symposium on Naval Hydrodynamics*, St. Johns, Canada, 2004. 26

[88] YUSUKE TAHARA, ROBERT V. WILSON, PABLO M. CARRICA, AND FREDERICK STERN. **RANS simulation of a container ship using a single-phase level-set method with overset grids and the prognosis for extension to a self-propulsion simulator**. *Journal of Marine Science and Technology*, **11**:209–228, 2006. 10.1007/s00773-006-0231-8. 27

[89] R. V. WILSON, P. M. CARRICA, AND F. STERN. **Steady and unsteady single-phase level-set method for large amplitude ship motions and maneuvering**. In *Proceedings of the 25th symposium on naval hydrodynamics*, New Foundland, Canada, 2004. 27

[90] PABLO M. CARRICA, ROBERT V. WILSON, AND FRED STERN. **An Unsteady Single-Phase Level Set Method for viscous Free Surface Flows**. Technical report, IIHR - Hydroscience and Engineering, The University of Iowa, 2005. 27

[91] PABLO M. CARRICA, ROBERT V. WILSON, RALPH W. NOACK, AND FRED STERN. **Ship motions using single-phase level set with dynamic overset grids**. *Computers & Fluids*, **36**(9):1415 – 1433, 2007. 27

[92] HIRATA NOBUYUKI AND HINO TAKANORI. **An Efficient Algorithm for Simulating Free-Surface Turbulent Flows around an Advancing Ship**. *Journal of the Society of Naval Architects of Japan*, (185):1–8, 1999-06. 27

[93] A. DI MASCIO, R. MUSCARI, AND R. BROGLIA. **Computation of free surface flows around ship hulls by a level-set approach**. In *Proceedings of the 8th international symposium on numerical ship hydrodynamics*, Busan, Korea, 2003. 27

[94] C HIRT AND B NICHOLS. **Volume of fluid (VOF) method for the dynamics of free boundaries1**. *Journal of Computational Physics*, **39**(1):201–225, 1981. 28

[95] B. P. LEONARD. **Simple high-accuracy resolution program for convective modelling of discontinuities**. *International Journal for Numerical Methods in Fluids*, **8**(10):1291–1318, 1988. 30, 31

[96] H. JASAK, H. G. WELLER, AND A.D. GOSMAN. **High Resolution NVD Differencing Scheme for Arbitrarily Unstructured Meshes**, 1998. 31

[97] S. MUZAFERIJA AND M. PERIC. *Computation of free surface flows using interface-Tracking and interface-capturing methods*, chapter 2, pages 59–100. Computational mechanics publications. WIT Press, Southampton,, nonlinear water wave interaction edition, 1999. 31, 33, 34, 99

[98] S. MUZAFERIJA AND M. PERIC. **Computation of Free-Surface Flows using the Finite-Volume-Method and Moving Grids**. *Numerical Heat Transfer, Part B: Fundamentals*, **32**(4):369–384, 1997. 33, 99

[99] S.MUZAFERIJA, M.PERIC, P.SAMES, AND T.SCHELLIN. **A Two-Fluid Navier-Stokes Solver to Simulate Water Entry**. In *Twenty-Second Symposium on Naval Hydrodynamics*, Washington D.C:, 1999. 33, 99

[100] LARS LARSSON, FREDERICK STERN, AND VOLKER BERTRAM. **Benchmarking of Computational Fluid Dynamics for Ship Flows: The Gothenburg 2000 Workshop**. *Journal of Ship Research*, **47**(1):63 – 81, March 2003. 36

[101] LARS LARSSON, FREDERICK STERN, AND MICHEL VISONNEAU. *Gothenburg 2010, A Workshop on Numerical Ship Hydrodynamics*. Chalmers University of Technology, 2010. 36

[102] LARS LARSSON, FREDERICK STERN, AND MICHEL VISONNEAU. **CFD in Ship Hydrodynamics - Results of the Gothenburg 2010 Workshop**. In *MARINE 2011, IV International Conference on Computational Methods in Marine Engineering*, Lisbon, Portugal, 2011. 36

[103] F. FOSSATI. *Aero-Hydrodynamics and the Performance of Sailing Yachts*. 1st Ed. International Marine/McGraw-Hill, Camden, ME, 2009. 39, 119

[104] F. FOSSATI, G. MOSCHINI, AND D. VITALONE. **Experimental Technique for the Determination of Forces Acting on a Sailboat Rigging**. In *14th Chesapeake Sailing Yacht Symposium*, Annapolis, MD, USA, 1999. 39

[105] I. H. ABOTT AND A. E. VON DOENHOFF. *Theory of Wing Sections*. Dover Publications, New York, 1959. 39

[106] S. F. HOERNER. *Fluid Dynamic Drag*. Hoerner Fluid Dynamics, Brick Town, N. J., USA, 1965. 39

[107] S. F. HOERNER. *Fluid Dynamic Lift*. 2nd Ed., Hoerner Fluid Dynamics, Brick Town, N. J., USA, 1985. 39

[108] F. BETHWAITE. *High Performance Sailing: Faster Racing Techniques*. Adlard Coles, 2nd edition, March 2011. 41, 43, 44

[109] F. FOSSATI AND S. MUGGIASCA. **Experimental Investigation of Sail Aerodynamic Behaviour in Dynamic Conditions**. *Journal of Sailboat Technology*, **02**:1–41, 2011. 47

[110] F. FOSSATI, F. MARTINA, AND S. MUGGIASCA. **Experimental Database of sail performance and flying shapes in upwind conditions**. In *International Conference on Innovation in High Performance Sailing Yachts*, Lorient, 2008. 47

[111] F. FOSSATI AND S. MUGGIASCA. **Sail aerodynamic behaviour in dynamic conditions**. In *19th Chesapeake Sailing Yacht Symposium*, Annapolis, Maryland, 2009. 47

[112] F. C. GERHARDT, R. FLAY, AND P. J. RICHARDS. **Unsteady aerodynamic phenomena associated with sailing upwind in waves**. In *3rd High Performance Yacht Design Conference*, Auckland, 2008. 47

[113] F. C. GERHARDT. *Unsteady Aerodynamics of Upwinf-Sailing and Tacking*. PhD thesis, University of Auckland, 2010. 47

[114] C. A. MARCHAJ. **Wind Tunnel Tests on a 1/4 scale Dragon rig**. Suyr report 14, Southampton University, 1963. 49

[115] P.S. JACKSON. **Modelling the aerodynamics of upwind sails**. *Journal of Wind Engineering and Industrial Aerodynamics*, **63**(1 - 3):17 – 34, 1996. 49, 171, 172

[116] A. H. DAY. **Sail Optimisation for Maximal Speed**. *Journal of Wind Engineering and Industrial Aerodynamics*, **63**:131 – 154, 1996. 50

[117] S. E. EUERLE AND D. S. GREELEY. **Towards a Rational Upwind Sail Force Model for VPPs**. In *11th Chesapeake Sailing Yacht Symposium*, Annapolis, MD, USA, 1993. 50

[118] G.S. HAZEN. **A Model of Sail Aerodynamics for Diverse Rig Types**. In *New England Yacht Symposium*, New London, Connecticut, USA, 1980. 51

[119] C. L. POOR AND N. SIRONI. **The international Measurement System. A Description of the New International Rating System.** In *11th International HISWA Symposium on Yacht Design and Yacht Construction*, Amsterdam, 1990. 51

[120] P. VAN OOSSANEN. **Predicting the speed of Sailing Yachts**. *SNAME, transactions*, **101**(12):337 – 397, 1993. 51

[121] ORC. *ORC VPP Documentation 2012*. Offshore Racing Congress, 2012. 51, 69

[122] A. CLAUGHTON, J. F. WELLICOME, AND A. SHENOI. *Sailing Yacht Design: Practice*. Longman, 1998. 59

[123] S.A. HARVALD. *Resistance and Propulsion of Ships*. Krieger Publication Company, Florida, USA, 1992. 60

[124] W. H. PRESS, S. A. TEUKOLSKY, W. T. VETTERLING, AND B. P. FLANNERY. *Numerical Recipes in C++ - The Art of Scientific Computing*. Cambridge University Press, 2nd edition, 2002. 64, 70

[125] A. CLAUGHTON, J. F. WELLICOME, AND A. SHENOI. *Sailing Yacht Design: Theory*. Longman, 1998. 69

[126] K. GRAF, M. PELZ, V. BERTRAM, AND H. SÖDING. **Added Resistance in Seaways and its Impact on Yacht Performance**. In *18th Chesapeake Sailing Yacht Symposium*, Annapolis, MD, USA, 2007. 69

[127] Y. XING-KAEDING. *Unified Approach to Seakeeping by a RANSE method*. PhD thesis, TU Hamburg-Harburg, 2006. 84

[128] M. PERIC AND E. SCHRECK. **Advances in Simulation for Marine Engineering**. In *2nd Asian Symposium on Computational Heat Transfer and Fluid Flow*, Jeju, Korea, October 2009. 86

[129] ITTC. *ITTC Recommended Procedures and Guidelines; Uncertainty Analysis in CFD; Verification and Validation.* International Towing Tank Conference, 2008. 97, 103, 104, 105, 122

[130] V. ANDRILLION AND B. ALESSANDRINI. **A 2D+T VOF Fiully Coupled Formulation for Calculation of Breaking Free Surface Flow**. In *Proceedings of the 24th Symposium on Naval Hydrodynamics*, 2003. 99

[131] FRED STERN, ROBERT WILSON, AND JUN SHAO. **Quantitative V&V of CFD simulations and certification of CFD codes**. *International Journal for Numerical Methods in Fluids*, **50**(11):1335–1355, 2006. 103

[132] FRED STERN, ROBERT V. WILSON, HUGH W. COLEMAN, AND ERIC G. PATERSON. **Comprehensive Approach to Verification and Validation of CFD Simulations—Part 1: Methodology and Procedures**. *Journal of Fluids Engineering*, **123**(4):793–802, 2001. 103, 105

[133] F. STERN, R. WILSON, H. W. COLEMAN, AND E. PATERSON. **Verification and Validation of CFD Simulations**. Technical report, Iowa Institute of Hydraulic Research, 1999. 105, 106

[134] R. WILSON AND F. STERN. **Verification and Validation for RANS Simulation of a Naval Surface Combatant**. In *Standards for CFD in the Aerospace Industry, 2002 AIAA Aerospace Sciences Meeting*, 2002. 106

[135] JOE LONGO AND FRED STERN. **Uncertainty Assessment for Towing Tank Tests With Example for Surface Combatant DTMB Model 5415**. *Journal of Ship Research*, **49, No.1**:55–68, March 2005. 113

[136] KAI YAN, FENG ZHAO, CHENG SHENG WU, AND LEI YANG. **Numerical and experimental uncertainty analysis for the prediction of resistance and wave profile of a surface ship model**. In *8th International Conference on Hydrodynamics*, 2008. 113

[137] FRANK DEBORD. **Hydrodynamic Performance Prediction for Grand Prix Sailing Yachts**. Presentation at Stevens Institute. 113

[138] H. PEGEL. *Validierung eines hydromechanischen Modells für Mehrrumpfboote mittels RANSE-Strömungssimulation.* Master's thesis, University of Applied Sciences Kiel, 2013. 116

[139] P. VAN OOSSANEN. **America's Cup Yachts - Recent Design Developments**. In *The Modern Yacht Conference*. RINA, March 2003. 152

[140] R.T. JONES. **The spanwise distribution of lift for minimum induced drag of wings having a given lift and a givien bending moment**. TN 2249, NACA, 1950. 172

[141] F. FOSSATI, S. MUGGIASCA, AND I. M. VIOLA. **An Investigation of Aerodynamic Force Modelling for IMS rule using Wind Tunnel Techniques**. In *19th International HISWA Symposium on Yacht Design and Yacht Construction*, Amsterdam, 2006. 172, 173

[142] P. JACKSON, P. J. RICHARDS, AND H. HANSEN. **An investigation of Aerodynamic Force Modelling for Yacht Sails using Wind Tunnel**. In *Proceedings of the 2nd High Performance Yacht Design Conference*, Auckland, February 2006. 173

SUMMARY

One of the most important tools in today's sailing yacht design is the Velocity Prediction Program (VPP). VPPs calculate boat speed from the equilibrium of aero- and hydrodynamic flow forces. Consequently their accuracy is linked to the accuracy of the aero- and hydrodynamic data used to represent a yacht. These data are usually derived from Experimental Fluid Dynamics (EFD) or Computational Fluid Dynamics (CFD) results and processed by means of linearisation and interpolation to represent the actual sailing state of the yacht. This interpolation is a potential source of inaccuracy. Furthermore, viscosity related effects are often estimated by simplified theoretical or empirical models potentially neglecting complex physical phenomena.

This thesis has been initiated to investigate a method to improve the accuracy of velocity prediction programs for sailing yachts. After theory review it was decided to link the hydrodynamic model directly to a RANSE flow simulation in order to avoid linearisation and interpolation errors associated with traditional VPPs. By taking into account aerodynamic forces from a sail force model, one is able to directly evaluate the hydrodynamic forces at the actual boat state of the yacht for a given wind condition. It was assumed that this way, interpolation errors in the hydrodynamic model could be avoided and secondary effects due to actual boat orientation taken into account. The aerodynamic forces are coupled to the hydrodynamic model via a rigid body motion solver. They are modeled as external forces on the rigid body yacht and updated according to changes of boat state. The force are modeled with a *implicit* sail force model as the best compromise between effort and accuracy.

Adapting the hydrodynamic model to the needs of direct VPP calculation proved challenging. First, free surface modeling around yacht hulls is examined. It was found, that resolution of free surface suffers from extensive smearing of the interface, leading to an underprediction of wave resistance. The problem was traced back to the use of low order advection schemes and a possible solution was developed. This solution approach has been tested and was found to produce sharp free surface resolution for cases which seek a steady state solution as it is the case for the RANSE-VPP.

A further obstacle for the RANSE-VPP is the resolution of fluid-body interaction within the computational grid. Especially large heeling motions together with the necessary grid density for a sharp free surface resolution are problematic. Review of various body motion approaches led to complete grid motion with vertical refinements in the area of the free surface to resolve heel motion.

With the modeling of the RANSE-VPP and the selection of the different components finished, a formal verification and validation of the hydrodynamic part of the model has been conducted. This proved to be very insightful regarding grid density and the influence of free surface resolution. It was shown that insufficient resolution of the free surface can lead to a significant underestimation of the resistance due to smaller wave resistance. The experimental data were reproduced with CFD to an accuracy which is inside the resolution of towing tanks.

After the successful testing of the hydrodynamic model, conventional velocity predictions have been performed to serve as comparison data for the RANSE-VPP. Simulations using RANSE CFD have been conducted to reproduce the test matrix of the towing tank data. Both EFD and CFD data sets have been processed to gain input for a conventional VPP. The resulting velocity polars as well as the respective boat states have been compared. Largest differences between EFD and CFD based data were found for high wind speeds.

Finally, the RANSE-VPP has been used to create results at the same true wind conditions as for the conventional VPP. Comparison of velocity polars in general showed only modest deviations, with maximum differences between RANSE-VPP and results from EFD and CFD based VPP occurring for low wind speeds on downwind courses. A thorough validation of the results proved difficult, especially since full-scale results have not been available. At this stage, this work presents a first implementations of a RANSE-VPP. Also first results look promising, it cannot be finally judged if reducing linearisation and interpolation by using the RANSE-VPP increases accuracy of results.

One of the major improvements drawn from this work is the increased resolution of the free surface. This led to an increased accuracy of the free surface RANSE simulation with respect to towing tank results. The RANSE-VPP showed good results but revealed some problems inherent to the system. The main problem for the RANSE-VPP, besides resolution of heel angle and optimizing for boat speed, is that it is valid only for one specific sail set. In contrast to hydrodynamic coefficients gained from numerical or experimental towing tank procedures, which can be applied to various sail sets, the whole testing using RANSE-VPP has to be redone if performance information for other sail combinations are wanted.

Improvements of the method as well as possible points for further research could be advancements in the body motion approach and validation with full-scale measured performance data. A better body motion approach would have to allow for large changes in heel angle without sacrificing free surface resolution. A problem for proper validation of the RANSE-VPP will be the influence of sea state on data acquisition. Since in most cases, differences between RANSE-VPP and conventional VPP results are of an order of magnitude which is on the verge what is measurable on a boat, the whole validation will be challenging.

SAMENVATTING

Het Velocity Prediction Program (VPP) is één van de meest gebruikte hulpmiddelen, ten behoove van hedendaags ontwerp van zeiljachten. Vanuit het evenwicht van aëro- en hydrodynamische krachten, wordt de scheepsnelheid berekend. Met als gevolg, dat de accuraatheid van de berekeningen gerelateerd is, aan die van de aëro- en hydrodynamische gegevens, die het jacht reprensateren. Deze gegevens worden gebruikelijkerwijs verkregen, via Experimental Fluid Dynamics (EFD) of Computational Fluid Dynamics (CFD), waarbij de actuele jacht en zeil data wordt berekend, via linearisaties en interpolaties. Deze interpolaties zijn een potentiele bron van onnauwkeurigheden. Bovendien worden complexe fysische verschijnselen verwaarloosd, omdat visceuze effecten vaak geschat worden, door versimpelde theoretische en empirische modellen.

Dit proefschrift is aangevangen, met als doel een methode te onderzoeken, die de nauwkeurigheid van Velocity Prediction Programs (VPP's) voor zeiljachten verhoogd. Na de literatuur studie is besloten, om het hydrodynamische model direct te kopellen aan een RANSE aëro-simulatie. Met als gevolg dat de linearistatie en interpolatie onnauwkeurigheden, inherent aan traditionele VPP's, voorkomen worden. Eerst worden de aërodynamische krachten verkregen via een zeil-krachten-simulatie. Waarna deze voor elke wind invalshoek, direct gemodelleerd worden op de actuele staat van het schip. Thans aangenomen in deze methode is, dat interpolatie fouten in het hydrodynamische model nu vookomen kunnen worden en tweede orde effecten, met betrekking tot de orientatie van het jacht meegomen worden. De koppeling van deze aërodynamische en hydrodynamische krachten verloopt via het oplossen van bewegingsvergelijkingen voor starre lichamen. Dus de hydrodynamische krachten worden gemodelleerd als externe krachten op het jacht, welke is gemodelleerd als star lichaam, terwijl de hydrodynamische krachten constant worden bijgewerkt naar veranderingen in de staat van het jacht. De krachten worden impliciet berekend, aangezien dit het beste compromis gaf tussen nauwkeurigheid en kosten.

Het bleek een ware beproeving, om het hydrodynamische model af te stemmen, aan de behoeften van de directe VPP berekening. Als eerste werd het vrije vloeistof oppervlak, rond de romp van het jacht geëvalueerd. Uit de bevindingen bleek, dat de resolutie van het vrije vloeistof oppervlak behoorlijk was uitgesmeerd, over de interface, met onderschatting van de golfweerstand als gevolg. De aard van het probleem bleek te liggen, in het gebruik van een advectie schema van lage orde. Hiervoor is een mogelijke oplossing ontwikkeld. Na testen bleek, dat deze oplossing scherpe vrije vloeistof resoluties gaf, voor gevallen welke moeten resulteren in een steady state oplossing, kenmerkend voor RANSE-VPP berekeningen.

De resolutie van de interactie, tussen vloeistof en lichaam (structuur) in het berekenings rooster, ontaarde zich in een volgend obstakel voor de RANSE – VPP. In het bijzonder grote helende bewegingen, ontpopte zich problematisch, dit omdat rooster dichtheid een vereiste is, voor het verkrijgen van een scherpe vrije vloeistof oppervlak resolutie. Bestudering van verschillende hellende bewegings methodieken, hebbben geleid tot, volledige rooster bewegingen met veticalle verfijningen in het vrije vloeistof oppervlak gebied, om het probleem rond hellingshoeken op te lossen.

Nu het modelleren van RANSE-VPP en selecteren van verschillende componenten is afgerondt, kan een formele verificatie en validatie van het hydrodynamische deel van het model worden uitgevoerd. Dit proces bleek zeer veel inzicht te geven, in rooster dichtheid en invloed van de vrije vloeistof resolutie. Hier bleek, dat onvoldoende resolutie van het vrije vloeistof oppervlak kan leiden, tot een kleinere golfweerstand, met significante onderschatting van de totale weerstand als gevolg. De experimentele data werd gereproduceerd met CFD tot een nauwkeurigheid welke binnen de resolutie van sleeptanks valt.

Na het succesvol testen van het hydromechanische model, zijn conventionele snelheids voorspellingen uitgevoerd, die dienen as vergelijkings materiaal voor RANSE-VPP. Om de test matrix met sleeptank gegevens te reproduceren, zijn RANSE CFD simulaties uitgevoerd. Zowel EFD en CFD datasets zijn bewerkt, om te gebruiken als invoer voor het conventionele VPP. Waarna, zowel de de verschillende polaire snelheids diagrammen, als de bijbehorende jacht toestanden met elkaar zijn vergeleken. Voor hogere wind snelheden zijn de grootste verschillen tussen EFD en CFD gevonden.

Uiteraard, is de RANSE-VPP gebruikt, om voor dezelfde ware wind hoeken resultaten te generen als conventionele VPP's. Vergelijkingen tussen polaire snelheidsdiagrammen lieten in het algemeen alleen kleine afwijkingen zien, met maximum verschillen, tussen RANSE-VPP en resultaten van EFD en CFD gebasseerde VPP resultaten, optredend voor lage wind snelheden en voor de windse koersen. Een grondige validatie van de resulaten bleek moeilijk, vooral omdat ware-grootte experimenten niet beschikkbaar waren. In dit stadium, legt dit proefschrift, voor het eerst implementaties van een RANSE-VPP voor. De eerste resultaten zijn veelbelovend, maar het kan nog niet worden beoordeeld of de bewerkstelligde reducties in linearisaties en interpolaties, door gebruik te maken van RANSE-VPP, inderdaad leiden, tot een toegenomen nauwkeurigheid van de resultaten.

Een van de grootste verbeteringen die voortkomt uit dit proefschrift is de toegenomen resolutie van het vrije vloeistof oppervlak. Dit leidde tot een toegenomen nauwkeurigheid van het vrije vloeistof oppervlak RANSE simulatie, in vergelijking met sleeptank resultaten. In het algemeen liet de RANSE-VPP goede resultaten zien, maar bracht ook enige problemen inherent aan de methode aan het licht. Het grootte probleem for RANSE-VPP, naast de hellingshoek resolutie en jacht-snelheid optimalisatie, is dat de geldigheid gelimiteerd is tot één specifieke set zeilen. In tegenstelling tot de via numerieke en experimentele sleep tank proeven verkregen hydrodynamische coefficienten, welke kunnen worden toegepast op verschillende sets zeilen. Met als gevolg dat de vol-

ledige RANSE-VPP simulaties overnieuw gedaan moeten worden, als de prestaties van een andere set zeilen worden gevraagd.

Zowel verbeteringen in de methode als aanbevelingen voor vervolg onderzoek, zijn het aanbrengen van vorderingen in de lichaam-bewegings methode en validatie met ware grootte gegevens. Een betere lichaam-bewegings methode zal grotere veranderingen in de hellingshoek moet toelaten zonder daarbij de resolutie van het vrije vloeistof oppervlak te benadelen. Een probleem voor validatie met ware grootte metingen is de invloed van zeegang op de ware grootte data metingen. Dit komt, omdat in de meeste gevallen de verschillen tussen RANSE-VPP en de conventionele VPP's een orde grootte hebben, die op een varend jacht, op het randje van het meetbare liggen. Dat maakt een ware-grootte validatie een ware uitdaging.

ACKNOWLEDGEMENTS

First of all, I would like to express my gratitude to Kai Graf of Yacht Research Unit Kiel and University of Applied Sciences Kiel. He introduced me to the fascinating world of fluid dynamics and his enthusiasm to apply scientific methods to sailing yachts has been a great source of inspiration for me. He also gave me the the chance to work in a scientific environment, which finally led to this thesis which was partly sponsored by the background research of Yacht Research Unit Kiel.

I would also like to thank my supervisor René Huijsmans from Delft University of Technology for the time and effort he spent in guiding me through this work. He gave me the freedom to develop my own research, but guided my in scientific work and often pointed me towards new theoretical approaches. Further thanks go to my co-promoter Mark Gerritsma for his support and guidance.

Furthermore, I would like to thank my colleagues at Yacht Research Unit Kiel, especially Hannes Renzsch, Janek Meyer and Hannes Pegel, for many inspiring and fruitful discussions. Special thanks also go to Adrian va Hoeve for translating the summary into Dutch.

Finally, I would like to thank my wife Bettina for many discussions and advice and all her support.

CURRICULUM VITÆ

Christoph Böhm was born on August 20th 1976 in Essen, Germany. He attended secondary school at the Markgraf-Georg-Friedrich Realschule in Heilsbronn, graduating in 1995. Afterwards, he started an apprenticeship as joiner, finishing it with his skilled worker's examination in 1997. Subsequently, he returned to school to obtain his technical diploma for university entrance. After military service and voyaging as a mate and boatswain on the topsail schooner Thor Heyerdahl, he commenced his study of Naval Architecture at University of Applied Sciences Kiel in 2000. He completed his diploma 2004 and started working at the Yacht Research Unit Kiel, specializing in Ship Hydromechanics.

He was actively involved in projects for international sailing campaigns, like the Yacht Research Unit Kiel's flow investigations for the 32th America's Cup. Besides project work, his main tasks were development and improvement of CFD techniques for yacht hydrodynamics. On this work, he published regularly at the relevant conferences.

In 2009 he commenced a PhD research appointment at the section Ship Hydromechanics and Structures of the Delft University of Technology. The research project was aimed at the development of new velocity prediction procedure for sailing yacht, which addresses some problems of current contributions on this topic. The results of this work are presented here. For one aspect of this thesis, the improvement of free surface simulations around sailing yachts, he was awarded the KOMPASS 2013, a prize for innovative, maritime, scientific work from Schleswig-Holstein.

During PhD study, he continued working at Yacht Research Unit Kiel, being involved in its contribution to the Shared Design Package for the 34tth America's Cup. He was asked to give lectures at the University of Applied Sciences Kiel and taught resistance and propulsion and drawing of ship lines. From 2011 to 2013 he led the INTERREG financed R&D project PerforManD, which had the goal to develop a performance monitoring system for small yacht and dinghies in order to enhance the skills of dinghy sailors. The project received the *Deutsch-Dänische Innovationspreis 2014*, a prize for innovative German-Danish projects.

LIST OF PUBLICATIONS

JOURNAL PUBLICATIONS

1. **C. Böhm and K. Graf**, Coupling of RANSE-CFD with VPP methods: From the Numerical Tank to Virtual Boat Testing, *International Journal of Small Craft Technology*, RINA, 2011.

OTHER PUBLICATIONS

9. **C. Böhm and K. Graf**, Advancements in Free Surface RANSE Simulations for Sailing Yacht Applications, In *Proceedings of the INNOV'Sail13*, Lorient, France, 2013.

8. **C. Böhm, R. Brehm, J. Meyer, L. Duggen and K. Graf**, A Measurement System for Performance Monitoring on Small Sailing Dinghies, In *Proceedings of the 21th Chesapeake Sailing Yacht Symposium*, Annapolis, MD, USA, 2013.

7. **C. Böhm and K. Graf**, RVPP: Sailing Yacht Performance Prediction fully integrated into a RANSE based flow code, In *Proceedings of the 20th Chesapeake Sailing Yacht Symposium*, Annapolis, MD, USA, 2011

6. **J. Mausolf, J. Deparday, K. Graf, H. Renzsch and C. Böhm**, Photogrammetry Based Flying Shape Investigation of Downwind Sails in the Wind Tunnel, In *Proceedings of the 20th Chesapeake Sailing Yacht Symposium*, Annapolis, MD, USA, 2011

5. **C. Böhm and K. Graf**, Coupling of RANSE-CFD with VPP methods: From the Numerical Tank to Virtual Boat Testing, In *Proceedings of the INNOV'Sail10*, Lorient, France, 2010

4. **K. Graf, C. Böhm and H. Renzsch**, CFD- and VPP-Challenges in the Design of the New AC90 Americas Cup Yacht, In *Proceedings of the 19th Chesapeake Sailing Yacht Symposium*, Annapolis, MD, USA, 2009

3. **C. Böhm and K. Graf**, Validation of RANSE simulations of a fully appended ACCV5 design using towing tank data, In *Proceedings of the INNOV'Sail08*, Lorient, France, 2008

2. **C. Böhm and K. Graf**, RANSE Calculation of Laminar-to-Turbulent Transition Flow around Sailing Yacht Appendages, In *Proceedings of the 18th Chesapeake Sailing Yacht Symposium*, Annapolis, MD, USA, 2007

1. **K. Graf and C. Böhm**, A New Velocity Prediction Method for Post-Processing of Towing Tank Test results, In *Proceedings of the 17th Chesapeake Sailing Yacht Symposium*, Annapolis, MD, USA, 2005